THE EFFECTS OF STATIC AND DYNAMIC STRAIN AGEING ON THE FRACTURE TOUGHNESS OF LOW CARBON STEELS

A thesis presented for the degree of

Doctor of Philosophy

in

Mechanical Engineering

in the University of Canterbury

by

CHEW CHONG NGAI

December, 1979

To my wife Yvette

SYNOPSIS

Advancement in Linear Elastic Fracture Mechanics has resulted in the concept and standardised experimental determination of a new fracture parameter, namely, the plane strain Critical Stress Intensity Factor (K_{IC}). Unfortunately, this experimental technique has been shown to be generally inapplicable to low alloy structural steels except at artifically induced quasi-static test conditions i.e. by using unrealistically large test specimens, or by testing at low temperatures. Consequently, alternative fracture parameters and analytical techniques have been developed to extend the concept of K_{IC} to ductile materials. Although several claims of successful technique were reported, the standardisation of these procedures is still being awaited. Furthermore, the various recommended test procedures have stipulated the use of the fatigue crack as an artificial flaw without ascertaining the possible embrittlement effect caused by the strain ageing of the inherent fatigue crack-tip plastic zone.

The applicability of the Crack Opening Displacement test technique in three low carbon steels has been established experimentally. It was found that size independent fracture toughness parameter could be determined by using relatively small specimens. The fracture toughness was observed to change abruptly over a narrow range of temperature where the transition of fracture mode occur. The "shelf" levels of the fracture toughness showed good agreement with the predictions made by the contemporary models

of fracture behaviour. The experimental data also confirmed the existence of empirical correlations between the Charpy Impact Energy (C_v) and the Critical Stress Intensity Factor (K_{IC}).

The embrittlement effects caused by the strain ageing of the fatigue crack-tip plastic zone has been investigated by using two Grade 275 steels of different strain ageing propensity. It was found that strain ageing produced a small but definite increase in the Fracture Mode Transition Temperature. A model based on the basic theories of fracture behaviour and the influences of strain ageing on tensile properties was proposed to qualitatively predict the observed change in Fracture Mode Transition Temperature.

The COD testing of a Pressure Vessel steel at elevated temperature confirmed the embrittlement influences of dynamic strain ageing. The fracture toughness was observed to decrease substantially in the temperature range of 150^{o}C to 350^{o}C. This drop in fracture toughness can be explained by the postulation that the basic microvoid coalescence mechanism is affected by the increase in strain hardening rate associated with dynamic strain ageing - a postulation supported by the current experimental data.

ACKNOWLEDGEMENTS

I wish to express my gratitude to Professor L.A. Erasmus for his continual interest and supervision of this project. His encouragement, suggestions and concern are deeply appreciated.

I would also like to thank Mr J.S. Smaill, my associate supervisor, for his invaluable advice and assistance; and Professor D.C. Stevenson, Head of the Mechanical Engineering Department, for the use of facilities for this project.

I am also deeply appreciative to my father for his interest and support; to my wife who is also responsible for the meticulous typing, for her understanding and to the other members of my family for their encouragement.

My sincere thanks also go to the technical staff of the Department of Mechanical Engineering who have provided assistance during the execution of this project; in particular to the workshop team led by Mr E. Retallick; to Misses J.M. Shelton and A.L. Scott; and to Messrs M.J. Flaws, C.R. McDonald, C.D. Knudsen, D. Somerville and T.L. Bird.

This project was partially assisted by the financial grants provided in the forms of the Todd Motor Research and the Mercer Memorial Scholarships. These are gratefully acknowledged.

CONTENTS

LIST OF FIGURES

LIST OF TABLES

LIST OF PHOTOGRAPHS

NOMENCLATURE

SYMBOL	DESCRIPTION
a	Flaw size (crack length)
b_o	Equilibrium atomic spacing
B	Thickness of fracture Toughness test specimen
c	"Notional" crack length
C_o	Carbide thickness
$(COD)_{critical}$	Critical Crack Opening displacement at instability
d	grain size
d_g	grain diameter
D_o	Initial specimen diameter
D_i	Instantaneous specimen diameter
D_{pin}	Load pin displacement
E	Young's modulus of elasticity
G	Energy release rate
G_{crit}	Critical energy release rate
G_{IC}	Plane strain critical energy release rate
J	J-Integral
J_{IC}	Plane strain critical J-Integral
k_Y	Slope of the Hall-Petch relationship
k_Y^s	Slope of the shear Hall-Petch relationship
K	Stress intensity factor
K_{crit}	Critical stress intensity factor

SYMBOL	DESCRIPTION
K_{IC}	Plane strain critical stress intensity factor
K_Q	Apparent fracture toughness
K_s	Strengthening coefficient
ℓ_f	Critical length parameter
ℓ_{fi}	Average non-metallic inclusion spacing
L	Total length of the linear intercept method
M_t	Net elastic response of the test specimen, grips and test machine
N_i	Number of intercepts
P_l	Normalised instability load
P_F	Fracture load
P_i	Instantaneous load
P_Q	Instability load
r	Radius of the plane stress plastic zone
s	Slot-width
s_c	Critical slot-width
t	Ageing time at temperature T
t_r	Ageing time at ambient temperature T_r
T	Ageing temperature
T_c	Transition temperature
T_r	Ambient Temperature
$\tilde{T}$	Traction vector

SYMBOL	DESCRIPTION
u_{11}	Local displacement in the tensile direction of Mode I opening
$\bar{u}$	Displacement vector
U	Potential energy
U_e	Elastic energy
U_o	Energy required to separate a pair of isolated atoms to infinity
U'	Area under the load-load point displacement curve for the calculation of J_c and J_{IC}
v	Average velocity of dislocations
W	Width of the fracture toughness test specimen
W_e	Work done between successive load-deflection curves of J-Integral test
W'	Strain energy density
W - a	Uncracked ligament length of fracture toughness test specimen
X_o	Characteristic distance of cleavage fracture
$Y(\frac{a}{W})$	Compliance function
ΔY	Change in flow stress due to strain ageing
δ	Crack opening displacement
δ_c	Critical crack opening displacement at instability
δ_i	Critical crack opening displacement at the initial stable crack extension
δ_{IC}	"Plane strain" critical crack opneing displacement
Δ_{crack}	Load point displacement
ε_f	Uniaxial tensile fracture strain

SYMBOL	DESCRIPTION
ε_{fi}	Critical crack-tip strain (also known as notched ductility)
ε_F	Fracture plastic strain
ε_P	Plastic strain
ε_{P_i}	Instantaneous plastic strain
$\overline{\varepsilon}_P$	Crack-tip plastic strain
$\dot{\varepsilon}$	Machine strain rate
$\dot{\varepsilon}_e$	Elastic strain rate
$\dot{\varepsilon}_P$	Plastic strain rate
λ	Wavelength
μ	Shear modulus of elasticity
ν	Poisson's ratio
ρ'	Dislocation density
ρ'_o	Average density of unlocked dislocation
γ	Surface energy
γ_F	Surface energy of ferrite
γ_P	Energy expended in the plastic work necessary to produce unstable crack extension
σ	Stress
σ_{11}	Local tensile stress of Mode I opening
σ_{12}	Shear stress (Mode II opening)
σ_{13}	Shear stress (Mode III opening)
σ_{app}	Applied stress

SYMBOL	DESCRIPTION
σ_c	Critical tensile stress required to create dislocations from locked source
σ_F	Fracture stress
σ_f	Flow stress at fracture
σ_i	Instantaneous stress
σ_{if}	Critical interface strength
$\sigma_{i,f}$	Friction stress at fracture
σ_i^*	Temperature independent friction stress
σ_{max}	Maximum stress
σ_n	Normal stress
σ_u	Ultimate tensile stress
σ_{LY}	Lower yield stress
σ_Y	Yield stress
$\sigma_L(\frac{a}{W})$	Plastic Collapse stress
$\Delta\sigma$	Stress increment required to maintain a given dislocation density
σ_{flow}	Flow stress
$\sigma_{flow_{as\ fatigued}}$	Flow stress of the as-fatigued COD test specimen
$\sigma_{flow_{pre\text{-}strained}}$	Flow stress of pre-strained material
$\sigma_{flow_{5\%}}$	Flow stress at 5% pre-strain
σ_{local}	Local crack-tip tensile stress

SYMBOL	DESCRIPTION
$\sigma_{LY_{as\ rolled}}$	Lower yield stress of as-rolled material
$\sigma_{LY_{strain\ aged}}$	Lower yield stress of strain aged material
$\sigma_{Y_{as\ fatigued}}$	Yield stress of the as-fatigued COD test specimen
$\sigma_{Y_{aged}}$	Yield stress of aged material
τ_{app}	Applied shear stress
τ_c	Critical shear stress required to create dislocations from locked source
τ_{eff}	Effective applied shear stress
τ_i	Shear lattice friction stress
τ_Y	Shear yield stress
τ_o	Resolved shear stress corresponding to limit velocity

CHAPTER ONE

INTRODUCTION

During the past two decades advances in technology have made it necessary to produce materials of improved strength. These high strength materials are finding an increasing range of application, especially in the aerospace industry where heavy emphasis is placed on the minimum-weight design concept. Unfortunately, the usage of these high-strength materials has been accompanied by a succession of fatigue and 'static' failure, some of which were catastrophic. In 1969, the U.S. Air Force was directed to develop structural fracture resistance test procedure after the crash of a F-111A military aircraft[1]. This marked the beginning of the first sophisticated application of fracture mechanics.

The problems associated with the use of progressively stronger materials lie with their lower flaw size tolerance. The concept of flaw tolerance had been predicted as early as 1920 by Griffith whose crack propagation model essentially stated that an existing crack would propagate spontaneously only if in doing so, the total energy of the system was reduced[2]. The Griffith's crack propagation concept was verified experimentally with glass as the test material; and it was found that the fracture stress, σ_F, could be related to the surface energy, γ, by the relationship

$$\sigma_F = \left(\frac{E\gamma}{4a}\right)^{\frac{1}{2}} \qquad (1.1.)$$

where a is the flaw size

E is the modulus of elasticity.

However, Griffith's work did not receive due attention at that time because the popular structural materials in the decades between 1920 and 1960 were of relatively low strength by today's standard and consequently could tolerate large flaws without fracturing catastrophically. However, with increasing emphasis being placed on higher strength, the critical flaw size has been reduced continually. This trend can be inferred from the data of Griffith's experimental work shown in Table 1.1. where it can be seen that progressively higher strength was accompanied by the reduction in tolerable flaw size. This trend of reducing flaw tolerance had gone by unnoticed with the absence of suitable theoritical parameters and test methods.

The traditional method of assessing the fracture toughness is the notched bar impact test. This test measures the level of energy absorbed by the test specimen during the cleavage/ductile fracture transition. Unfortunately, this method has inherent limitations which may be summarised as:

(a) The inability to provide a quantitative parameter which characterise the material's resistance to fracture for design analysis.

(b) The unrealistic test conditions in relation to service enviroment.

(c) To a lesser degree, the different interpretation of the definition of the transition temperature which is usually used as a fail-safe measure.

Rupture Stress ($lb\text{-}in^{-2}$)	Flaw Size (in)
864	0.15
623	0.27
482	0.54
366	0.89

Table 1.1. Griffith's Experimental Data On The Bursting Stress Of Cracked Spherical Glass Bulbs[2]

The initial development of the fracture toughness test technique focused its attention on macroscopic Linear Elastic Fracture Mechanics (LEFM). The theoretical concepts of LEFM define the fracture parameter as the size independent plane strain Critical Stress Intensity Factor, K_{IC}, and K_{IC} is related to the fracture stress, σ_F, and the flaw size, a, by the relationship

$$K_{IC} = \sigma_F (\pi a)^{\frac{1}{2}} \qquad (1.2)$$

Subsequent experimental development led to the standardisation of the K_{IC} test technique basing on compliance measurements of standard test specimens[3, 4]. Unfortunately, the compliance measurement method can tolerate only an extremely small degree of plastic yielding. Consequently, the applicability of LEFM test methods is limited to quasi-brittle condition which effectively confines the normal ambient temperature application of the test method to very high strength materials where the yield strength is in the vicinity of $800MN\text{-}m^{-2}$. In lower strength materials such as structural steels, the LEFM technique is applicable only when artificial quasi-brittle condition was induced either by lowering the test temperature or by using expensive and unrealistically large test specimens.

Since LEFM test methods have proved to be unsuitable for K_{IC} measurement of low strength ductile materials, considerable attention has been focused on the development of alternative methods for the experimental measurement of a size independent fracture toughness parameter. These efforts have led to the development of the "General Yield Fracture Mechanics" (GYFM) concept which provides relatively simple alternative parameters and test techniques for the measurement of K_{IC}. The two popular GYFM parameters are:

(a) The Crack Opening Displacement (COD)

(b) The J-Integral Concept

The COD, like the LEFM K_{IC}, focuses attention on the crack-tip region. It defines the critical fracture criterion as a function of the flow stress at the crack-tip, usually taken to be the yield stress, σ_Y, and the "opening" of the crack-tip at the instance of separation so that

$$G_{IC} = \sigma_Y (COD)_{critical} \tag{1.3}$$

Later work showed that for a strain hardening material[5, 6, 7],

$$G_{IC} = M\sigma_Y (COD)_{critical} \tag{1.4}$$

where G_{IC} is the plane strain critical energy release rate

M is a constant and $1 < M < 2$.

Currently, the exact value of M is still ambiguous. However, it is important to note that the original, less sophisiticated model provides a conservative estimate.

The J-Integral method focuses attention away from the crack-tip region, and is defined as a path independent integral taken around the crack-tip. It has been interpreted as the potential energy difference between two identically loaded bodies having slightly different crack lengths so that for unit thickness[8],

$$J = -\frac{\partial U}{\partial a} \tag{1.5}$$

where U is the potential energy of the system

a is the crack length

and the critical fracture criterion is represented by the plane strain critical J-Integral so that[9]

$$J_{IC} = \frac{K_{IC}^2}{E}(1 - \nu^2) \qquad (1.6)$$

where K_{IC} is the plane strain Critical Stress Intensity Factor

E is the modulus of elasticity

ν is the Poisson's ratio

Thus, two alternative parameters which can be determined experimentally have been proposed and their practical applicability verified. Later reports indicated that the LEFM and GYFM parameters can be related by the equation[10, 11]

$$J_{IC} = \frac{K_{IC}^2}{E}(1 - \nu^2) = M\sigma_Y (COD)_{critical} \qquad (1.7)$$

Apart from the two above mentioned GYFM parameters, several alternative techniques which analyse the LEFM 'invalid' load-displacement K_{IC} test record have been developed and their successful applications supported by experimental data[12, 13, 14]

In spite of this abundance of feasible post-yield fracture toughness test and analysis technique, the fragmented nature of the research has resulted in the absence of any standardised test procedure. There remain several areas of ambiguity regarding the definition of the critical fracture event and the size dependence of the two alternative GYFM parameters.

Reports suggesting that the fracture toughness parameters can be related to the fracture models depicting the micro-fracture mechanisms of both cleavage[15, 16, 17] and ductile[18, 19, 20] failure have also been published. The cleavage fracture model states that spontaneous propagation of the existing fatigue crack

of a fracture toughness test specimen occurs only when the tensile fracture stress, σ_F, is exceeded over a "characteristic" distance, X_o, ahead of the crack-tip so that

$$K_{IC} = \sigma_F (2\pi X_o)^{\frac{1}{2}} \tag{1.8}$$

This characteristic distance was reported to be 1 to 2 grain diameters in dimension[16, 17]. However, it has also been suggested that Equation (1.8) is applicable in low strength steel only when the average grain diameter exceeds 40 μm[16], but a later investigation showed that Equation (1.8) remained valid in low strength steels even when the average grain diameter was as small as 8.3 μm[17]. Further contradiction has arisen from reports which state that the fatigue cracks of fracture toughness test specimens merely act as stress concentrators and that the spontaneous propagation of the crack must occur by the nucleation of micro-cracks at the fatigue crack-tip[15, 16, 17]. This implies that the fracture toughness test measures the energy required for both the nucleation and subsequent propagation of the crack, and contradicts an earlier report that the fracture toughness test only measures the energy required for crack propagation[21]. Thus, by using low carbon steels with suitable grain sizes, the grain-size limit of Equation (1.8) can be ascertained by performing the fracture toughness tests at -196°C. The micro-cleavage mechanism can also be inferred from these results.

The two ductile fracture models of notched specimens relate the critical COD to inherent material properties[18, 19, 20]. The more popular non-metallic inclusion based model states that[18, 19]

$$(COD)_{critical} = \varepsilon_{fi} l_{fi} \qquad (1.9)$$

where ε_{fi} is the critical crack-tip strain, also known as the notched ductility

l_{fi} is the average non-metallic inclusion spacing

The notched ductility may be measured experimentally by the slope of a graph of critical COD versus slot-width of the notch, usually approximated as equivalent to twice the notch root radius[22].

The second model relates the critical COD to the ferrite grain diameter, d_g, by the equation[20]

$$\ln \frac{(COD)_{critical}}{2\, d_g} = 0.2\varepsilon_f \qquad (1.10)$$

where ε_f is the uniaxial tensile fracture strain

This model assumes that the grain boundary carbide particles play a significant role in the micro-void coalescence mechanism. Since the average non-metallic inclusion spacing usually does not relate to the grain size, it is useful to ascertain the applicability of these two ductile fracture models to low carbon steels.

An important factor which has been overlooked by the various LEFM and GYFM K_{IC} test techniques is the embrittlement effect of strain ageing. In all the recommended test techniques[3, 4, 5 9], the "flaw" is introduced by fatigue cracking. Although it has been recommended that the stress intensity during the fatigue cracking process be kept below a critical level[3, 4, 23], the various fatigue crack propagation models[24, 25, 26, 27] suggest that it is inevitable that a small, plastically damaged area will be formed

at the fatigue crack-tip. Thus, strain ageing of the fatigue crack-tip plastic zone may produce significant changes in the fracture toughness of materials with strong strain ageing tendencies since the various fracture toughness parameters are measured at the crack-tip area and are therefore sensitive to localised changes in the material properties. Strain ageing of a more severe nature has been investigated by Burdekin[28]. In this investigation, notched specimens were pre-strained by bending to open the notch root by 0.15 mm before closing with a reverse bend to the original dimension. The specimens were then aged at 250°C. Subsequent COD testing showed that the fracture mode transition temperature increased dramatically from -55°C in the parent material to 10°C in the strain aged condition. The importance of any embrittlement effect caused by strain ageing at the fatigue crack-tip should consequently be investigated.

The application of fracture toughness testings at elevated temperature is also of practical interest especially for Pressure Vessel steels. The explosion in 1974 of a Pressure Vessel normally operated at elevated temperature occurred in Wellington, New Zealand. In the subsequent inquiry, the metallurgical soundness of the culprit vessel steel was questioned. One fact which emerged from this inquiry was the absence of information on the elevated temperature fracture toughness of the Pressure Vessel steel. As dynamic strain ageing can occur at temperature between 100°C and 350°C, it is almost certain that the fracture toughness in this temperature range will be adversely affected. Hence, this investigation will include elevated temperature fracture toughness testings

of the material obtained from the Pressure Vessel involved in the above accident.

The objectives of this thesis are therefore to establish:

(a) The feasibility of a fracture toughness test procedure for low carbon steels

(b) The existence of the plastic zone at the fatigue crack-tip

(c) The effect of ambient temperature strain ageing on the fracture toughness of low carbon steels

(d) Information on the changes of fracture resistance in the "blue-brittle" temperature range of 100°C to 350°C

It is obvious that the selected method of fracture toughness testing should be able to focus attention on the problem area, namely the crack-tip area, using economical and realistic specimens. Although the LEFM K_{IC} test can be used for testing low strength structural steel at -196°C for the purpose of establishing the relationship between K_{IC} and fracture stress, σ_F, given in Equation (1.8), its applicability at higher temperature, even as low as -80°C is doubtful. The COD test appears to be the most attractive alternative parameter and recent reports on the feasibility of experimentally measuring the thickness independent J_{IC} with small test specimens[10, 29, 30] appear encouraging. Hence, by establishing the minimum specimen size required to obtain the thickness independent critical COD, the "plane strain" Critical

Stress Intensity Factor, K_{IC}, may be estimated and compared with the Charpy V-notched Impact Energy, C_v, using empirical K_{IC}-C_v relationships, for low alloy steels published elsewhere[31, 32, 33].

PART 1

FRACTURE TOUGHNESS TESTINGS OF LOW CARBON STEELS

CHAPTER TWO

LINEAR ELASTIC FRACTURE MECHANICS

2.1 Ideal Fracture Strength

The ideal fracture strength of a material, when viewed microscopically, involves the breaking of atomic bonds. By assuming the approximate atomic stress-strain relationship of an isolated pair of atoms (Figure 2.1) to be a half sine wave (Figure 2.2) so that:

$$\sigma = \sigma_{max} \sin(2\pi \frac{x}{\lambda}) \qquad (2.1.1)$$

the work required to separate the two atoms to infinity is represented by the total area under the stress-strain curve. Since the energy (U_o) required to separate a pair of atoms to infinity in a crystalline solid can be equated to twice the surface tension (γ) of unit area of a free surface of the appropriate plane of the solid, that is:

$$+U_o = 2\gamma \qquad (2.1.2)$$

the area under the atomic stress-strain curve can also be equated to 2γ. Thus,

$$\frac{\lambda}{2\pi} \sigma_{max} \{ - \cos(\frac{2\pi x}{\lambda}) \}_o^{\frac{\lambda}{2}} = 2\gamma \qquad (2.1.3)$$

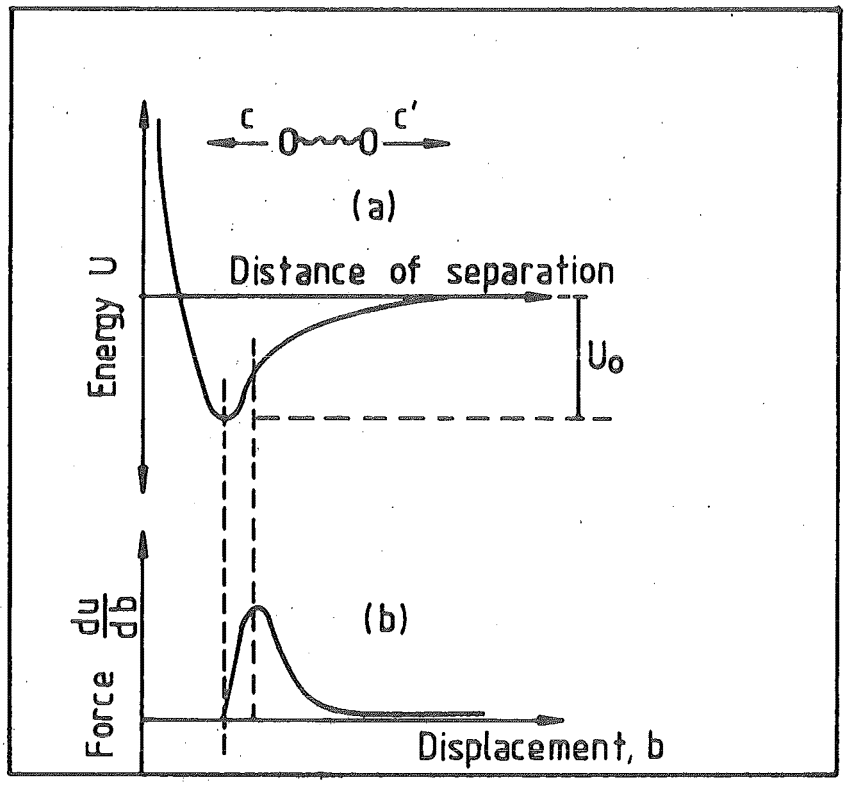

FIG 2·1 (a) BONDING ENERGY AS A FUNCTION OF DISTANCE OF SEPARATION

(b) FORCE DISPLACEMENT CURVE

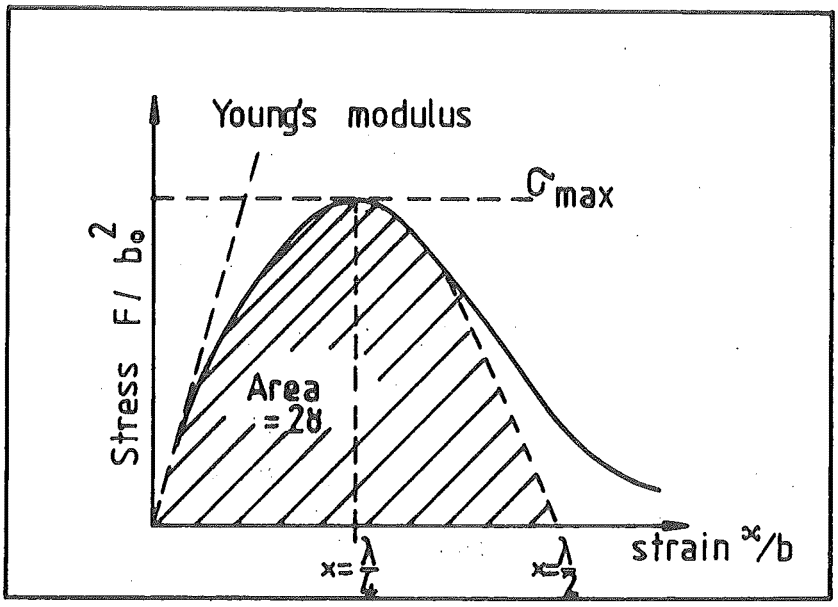

FIG 2·2 ATOMIC STRESS STRAIN CURVE.

For a very small displacement, Equation (2.1.1) may be written as

$$\sigma = \sigma_{max} \, 2\pi \frac{x}{\lambda} = E \frac{x}{b_o} \qquad (2.1.4)$$

Substituting for λ in Equation (2.1.3) yields

$$\frac{\sigma_{max}^2 \, b_o}{E} (2) = 2\gamma \qquad (2.1.5)$$

Hence, the ideal fracture strength may be expressed as

$$\sigma_{max} = \left(\frac{E\gamma}{b_o}\right)^{\frac{1}{2}} \qquad (2.1.6)$$

Equation (2.1.6) has been derived by considering the energies of interaction between pairs of atoms across the fracture plane. It is possible to derive similar expressions for the fracture stress by considering the interaction energies between an atom and all its neighbouring atoms and differentiating these to determine more accurate forms of atomic force-displacement curves. Such interaction energies have been expressed as Morse potentials[34] of the form:

$$U_{(b - b_o)} = U_o \{ e^{-s(b - b_o)} - 2e^{-s(b - b_o)} \} \qquad (2.1.7)$$

where s is the reciprocal of the "range" of the inter-atomic forces

In other cases[35], the interatomic forces have been given as functions of the form

$$F = \text{Constant} \{ \left(\frac{b_o}{b}\right)^m - \left(\frac{b_o}{b}\right)^n \} \qquad (2.1.8)$$

where m and n are dependent on the type of bonding

The exponent m is representative of the repulsive forces while the exponent n is dependent on the attractive forces. However, as the interatomic potentials are often not well defined, it becomes necessary to accept pseudo-potential functions of the forms given in Equation (2.1.7) to evaluate the various constants. The pseudo-potentials may then be used to calculate the atomic stress-strain curve. The net inference[36] of these results is that the fracture stress of a crystalline solid is of the magnitude 0.1E

2.2 Effects Of Cracks

The theoretical strength of a crystalline solid, as expressed in the previous section, has seldom been observed in real life. In fact, the observed strengths of crystals are found to be lower than 0.1E by about two orders of magnitude. Griffith[2] was the first to suggest an explanation by recognising that a macroscopically homogeneous test sample may contain small defects in the forms of cracks, or atomic deformation processes which could nucleate cracks, or inhomogeneity of composition. Griffith then analysed the fracture in such a cracked-body by energy-balance considerations. Briefly, Griffith's analysis stated that the introduction of a crack into a body strained between fixed grips would alter the total energy of the body in two ways:

(i) The energy is increased owing to the energy of the two crack faces; if the surface tension is Υ, the increase is given by $S = 2\gamma a$ per unit thickness where $2a$ is the crack length

(ii) The stored elastic strain energy is decreased due to the presence of stress-free areas above and below the crack. This decrease in stored elastic energy, U_e, per unit thickness is given by

$$U_e = -\tfrac{1}{2} \frac{\pi\sigma^2 a^2}{E} \qquad \text{(plane stress)} \qquad (2.2.1)$$

$$U_e = -\tfrac{1}{2} \frac{\pi\sigma^2 (1 - \nu^2) a^2}{E} \qquad \text{(plane strain)} \qquad (2.2.2)$$

where ν is the Poisson's ratio

Therefore, in plane stress, the total change in energy due to the presence of the crack is given by

$$W = S + U_e = 2\gamma a - \frac{\pi\sigma^2 a^2}{2E} \qquad (2.2.3)$$

Equation (2.2.3) may be visualised graphically in Figure 2.3. It is obvious that the energy passes through a maximum and then decreases with increase in crack length. Griffith considered the change in energy as the crack of length a was extended by a small amount δa and established a critical energy criterion - below which no crack extension occurs. Thus, differentiating Equation (2.2.3) yields

$$\frac{\partial}{\partial a} \left(2\gamma a - \frac{\pi\sigma^2 a^2}{2E}\right) = 2\gamma - \frac{\sigma^2 \pi a}{E} \qquad (2.2.4)$$

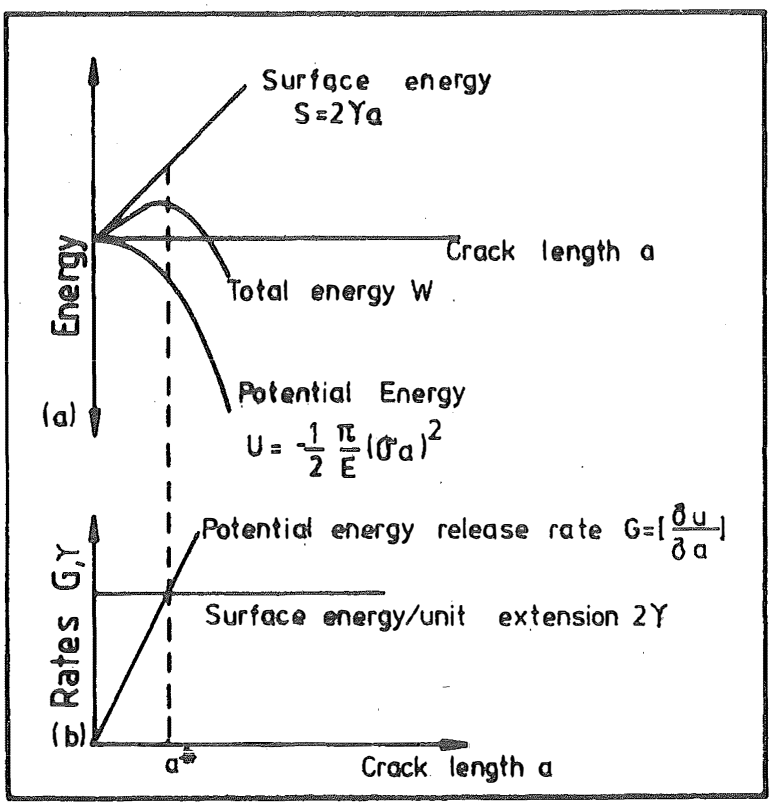

FIG 2·3 (a) VARIATION OF ENERGY WITH CRACK LENGTH

(b) VARIATION OF ENERGY RATES WITH CRACK LENGTH

a^* is the critical Griffith crack length

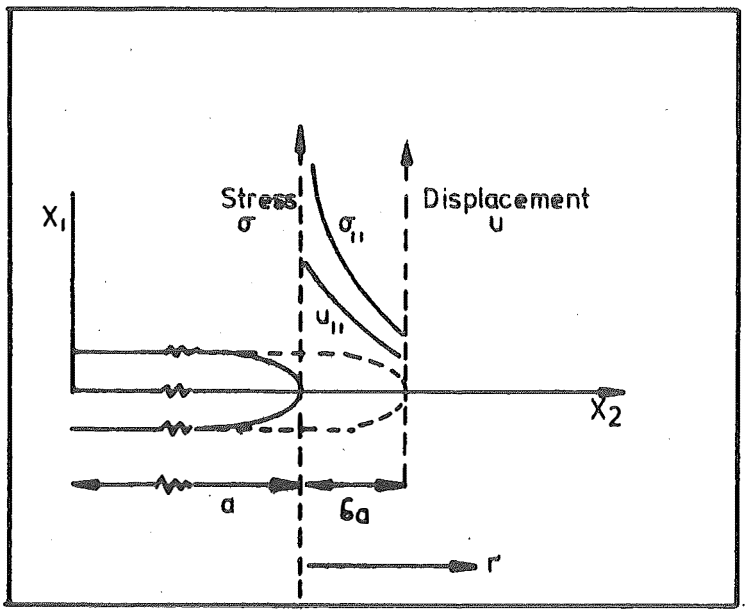

FIG 2·4 CALCULATION OF G FROM WORK DONE BY CRACK TIP STRESS FIELD

At the critical point (fracture), $\sigma = \sigma_F$, $\frac{\partial}{\partial a}(\quad) = 0$

$$2\gamma = \frac{\sigma_F^2 \pi a}{E} \tag{2.2.5}$$

Thus, in plane stress

$$\sigma_F = \left(\frac{2E\gamma}{\pi a}\right)^{\frac{1}{2}} \tag{2.2.6}$$

and in plane strain,

$$\sigma_F = \left\{ \frac{2E\gamma}{\pi(1 - \nu^2)a} \right\}^{\frac{1}{2}} \tag{2.2.7}$$

However, the Griffith expressions for critical fracture represent only a necessary but not a sufficient condition for failure. The Griffith expressions consider only the thermodynamics of the body and ignore the conditions at the crack-tip. For instance, a blunt crack-tip may not have sufficient concentrated stress to separate the atomic bonds.

2.3 Stress Intensity Factor

Irwin[37] showed that in order to state the fracture criteria, it is not necessary to conduct a stress analysis for the entire body. Instead, it is sufficient to describe only the crack-tip stresses. Such a crack-tip region is small compared with the body but is sufficiently large with respect to atomic dimensions to enable the applications of Linear Elastic Theory.

By visualising a crack as shown in Figure 2.4, where the stress distribution ahead of a half-crack of length a and the displacement distribution within a half-crack of length a + δa are both shown, the Westergaard's Solution[38] may be applied to yield

$$\sigma_{11} = \frac{\sigma x_2}{(x_2^2 - a^2)^{\frac{1}{2}}} \qquad (2.3.1)$$

and in plane strain

$$u_{11} = 2(1 - \nu^2) \frac{\sigma}{E} \{ (a + \delta a)^2 - x_2^2 \}^{\frac{1}{2}} \qquad (2.3.2)$$

By writing $r = x_2 - a$, Equations (2.3.1) and (2.3.2) may be written as

$$\sigma_{11} = \frac{\sigma (\pi a)^{\frac{1}{2}}}{(2\pi r)^{\frac{1}{2}}} = \frac{K}{(2\pi r)^{\frac{1}{2}}} \qquad (2.3.3)$$

$$u_{11} = 2(1 - \nu^2) \frac{\sigma}{E} (2a)^{\frac{1}{2}} (\delta a - r)^{\frac{1}{2}} \qquad (2.3.4)$$

The change in energy in the body as a whole may be evaluated by calculating the work done by the surface forces across the length δa when the crack is closed from a + δa to length a[37]. The energy change is given by the expression

$$G\delta a = \int_0^{\delta a} \sigma_{11} \, u_{11} \, dr \qquad (2.3.5)$$

where the thickness is assumed as unity,

and G is the energy release rate.

Substituting for σ_{11} and u_{11} yields

$$G\delta a = 2(1 - \nu^2) \frac{\sigma^2 a}{E} \int_0^{\delta a} \left(\frac{\delta a - r}{r}\right)^{\frac{1}{2}} dr \qquad (2.3.6)$$

since the crack is assumed to be elliptical, r may be written as $r = \delta a \sin^2 \omega$. Equation (2.3.6) may be evaluated to yield

$$G\delta a = \frac{\sigma^2 \pi a}{E} (1 - \nu^2) \delta a \qquad (2.3.7)$$

Thus

$$G = \frac{\sigma^2 \pi a}{E} (1 - \nu^2) \qquad (2.3.8)$$

By defining the Stress Intensity Factor as

$$K = \sigma(\pi a)^{\frac{1}{2}} \qquad (2.3.9)$$

Equation (2.3.8) may be written as

$$G = \frac{K^2(1 - \nu^2)}{E} \qquad (2.3.10)$$

similarly in plane stress, it may be shown that

$$G = \frac{K^2}{E} \qquad (2.3.11)$$

Thus, at fracture for Mode-I opening[39], the Griffith criterion in plane strain may be expressed as

$$G_{IC}da = 2\gamma da = \frac{K_{IC}^2}{E} (1 - \nu^2) da \qquad (2.3.12)$$

for unit thickness

The expressions relating to the energy release rate and the Stress Intensity Factor (Equations (2.3.10) and (2.3.11)) have very general and important applications in the field of Fracture Mechanics. For example, assuming that a half-crack of length a situated in an infinite body was subjected to a tensile stress (Mode I opening), to a shear stress (Mode II sliding), and to an anti-plane strain shear stress (Mode III opening), the actual crack-tip stresses which would do work would be σ_{11} (Mode I), shear σ_{12} (Mode II) and shear σ_{13} (Mode III). These would be characterised by the Stress Intensity Factors K_I, K_{II} and K_{III} respectively. Work would be done only if these stresses move in their appropriate directions and the expressions for the energy release rate per unit thickness would be

$$G = \lim_{\delta a \to 0} \frac{1}{\delta a} \int_0^{\delta a} (\sigma_{11}u_{11} + \sigma_{12}u_{12} + \sigma_{13}u_{13})\, dr \quad (2.3.13)$$

Evaluating as before, and assuming plane strain conditions for Modes I and II, yields

$$EG = (1 - \nu^2)K_I^2 + (1 - \nu^2)K_{II}^2 + (1 + \nu)K_{III}^2 \quad (2.3.14)$$

or in plane stress

$$EG = K_I^2 + K_{II}^2 + (1 + \nu)K_{III}^2 \quad (2.3.15)$$

Thus, the use of Stress Intensity Factors has reduced an otherwise complicated situation to one of only relatively simple mathematical model.

The Stress Intensity Factor may be modified to take the form

$$K = Y \sigma_{app} (a)^{\frac{1}{2}} \qquad (2.3.16)$$

where Y is a dimensionless parameter which accounts for the different loading systems and different crack configurations. Values of Y have been evaluated for many situations. A useful recent edition has been compiled by Cartwright and Rooke[40].

2.4 Quasi-Brittle Fracture

The Griffith analysis and the Linear Elastic Theory of cracks have both been devised for elastic media. Consequently, they are applicable to very brittle materials only. Modifications are obviously needed to enable their applications to more ductile materials commonly used in structural engineering. Irwin et al[41] conducted experiments on the fracture at room temperature of large, thin sheets of aluminium containing central cracks and found that the fracture stress, σ_F, could be expressed as

$$\sigma_F = \left(\frac{E.\text{constant}}{\pi a} \right)^{\frac{1}{2}} \qquad (2.4.1)$$

The constant, however, was found to be much greater than the surface energy of the material.

Independently, Orowan[42] and Irwin[43] suggested that the energy released in these specimens[41] was largely dissipated by producing plastic flow around the crack-tips, so that the critical values at

fracture were apparently much greater than 2γ. However, it was found that the amount of plastic work in the crack-tip region which preceded unstable crack extension was independent of the initial crack length and therefore a measure of the material's characteristic resistance to fracture. More importantly, the amount of plastic flow at instability was very much smaller in extent than either the crack length or the width of the sheet. Consequently, as far as the macroscopic energy release rate was concerned, methods of linear elasticity could still be used to relate crack-tip events to the applied stress.

Orowan re-wrote the Griffith criterion as[42]

$$\sigma_F = \left\{ \frac{E(2\gamma + \gamma_p)}{\pi a} \right\}^{\frac{1}{2}} \qquad (2.4.2)$$

where γ_p is energy expended in the plastic work necessary to produce unstable crack extension.

Since $(\gamma_p + 2\gamma) >> 2\gamma$

$$\sigma_F = \left(\frac{E\gamma_p}{\pi a}\right)^{\frac{1}{2}} \qquad (2.4.3)$$

Irwin, however, used the critical value of strain energy release rate at which unstable crack propagation occurs in his expression of fracture stress[43]. This critical strain energy release rate, G_{crit}, provided a convenient parameter to include all supplementary energy dissipating terms, in addition to the work required to fracture the lattice. The constancy of G_{crit}, and hence its use as a measure of a material's resistance to fracture, will be found to depend critically on experimental testing conditions.

However, for situations where small amounts of local plastic flow precede crack extension, which is generally termed "quasi-brittle" behaviour, the critical value can always be related to the failure stress by linear-elastic methods. Irwin's parameter, G_{crit}, provides a measure for fracture toughness. The development of fracture toughness testing since Irwin's initial work has been to define experimental conditions under which reproducible toughness measurements relevant to service applications can be measured in laboratory tests.

Irwin's expression for G_{IC} and K_{IC} are of the form[43]

$$\sigma_F = \left\{ \frac{EG_{IC}}{\pi(1 - \nu^2)a} \right\}^{\frac{1}{2}} \qquad (2.4.4)$$

$$K_{IC} = \left\{ \frac{EG_{IC}}{(1 - \nu^2)} \right\}^{\frac{1}{2}} \qquad (2.4.5)$$

The plastic zone at the crack-tip will obviously alter the stress distribution. A first approximation of the extent by which the plastic zone modifies the stress distribution is obtained[44] by assuming that small scale yielding at the crack-tip produces a "notional" crack of length $(a + 2r_y)$ in plane stress[45]. The fracture stress, σ_F, is expressed as

$$\sigma_F = \frac{EG_{IC}}{\pi a \left\{ 1 + \frac{1}{2} \left(\frac{\sigma_{app}}{\sigma_Y}\right)^2 \right\}} \qquad (2.4.6)$$

where σ_{app} is the applied stress

σ_Y is the yield stress

r_y is the radius of the crack-tip plastic zone

and the tip of the "notional" crack is located at the centre of the plastic zone. In terms of stress intensity,

$$K_{crit} = \sigma_F \{ \pi a (1 + \frac{\sigma_F^2}{2\sigma_Y^2}) \}^{\frac{1}{2}} \qquad (2.4.7)$$

where K_{crit} is the critical Stress Intensity Factor

A similar conclusion can be reached if the fracture stress is related to the plastic zone size calculated from Dugdale's model where the critical Stress Intensity Factor, K_{crit}, is expressed as[46]

$$K_{crit} = \sigma_F \{ \pi a (1 + \frac{\sigma_F^2 \pi a^2}{16\sigma_Y^2}) \}^{\frac{1}{2}} \qquad (2.4.8)$$

It is now possible to conclude that the Equations (2.4.7) and (2.4.8) should be used if $\frac{\sigma_F}{\sigma_Y} > 0.4$. For ratio of $\frac{\sigma_F}{\sigma_Y} > 0.8$, it is possible to substitute for more accurate values of r_Y (from Dugdale's model) into the expression for the "notional" crack and hence obtain relationships between K_{IC} and σ_F up to general yield. The validity of the equivalent elastic concept becomes doubtful at high values of $\frac{\sigma_F}{\sigma_Y}$ and such relationships need to be treated with caution.

2.5 The Effect of Specimen Thickness on Fracture Toughness

Previous discussions have indicated that the elastic stress analysis around a crack has reached a sufficiently high level of sophistication and this has resulted in considerable emphasis being

placed on the development of efficient and simple experimental methods that can be employed to determine fracture properties.

Krafft et al investigated the effects of specimen thickness on fracture toughness by using an age hardened aluminium alloy (7075-T6)[47]. Using Krafft et al's results, Srawley and Brown[48] and Tetelman and McEvily[49] showed that a large variation in toughness was obtained as indicated in Figure 2.5.a

The toughness curve may be conveniently divided into three regions:-

(i) Region A

In region A, the specimens are very thin and tend to show increasing toughness with thickness. The load-displacement curve (see Figure 2.5.b) is linear up to fracture and the fracture profile is completely slant. Cottrell[50] and Knott[51] proposed a model where the stress state at the crack-tip is essentially plane stress and an anti-plane strain mechanism (K_{III}) is responsible for crack extension. Using Bilby et al's method for calculating the size of plastic zones and displacements in Mode III deformation[52], Knott showed that the criterion for first crack extension, provided that the extent of screw dislocation pile-up ahead of the crack is small, may be written as[51]

$$\tau_{app} = \left(\frac{2^{\frac{3}{2}} \mu \tau_Y B}{\pi a} \right)^{\frac{1}{2}} \qquad (2.5.1)$$

where τ_{app} is shear stress

τ_Y is shear yield stress

μ is shear modulus

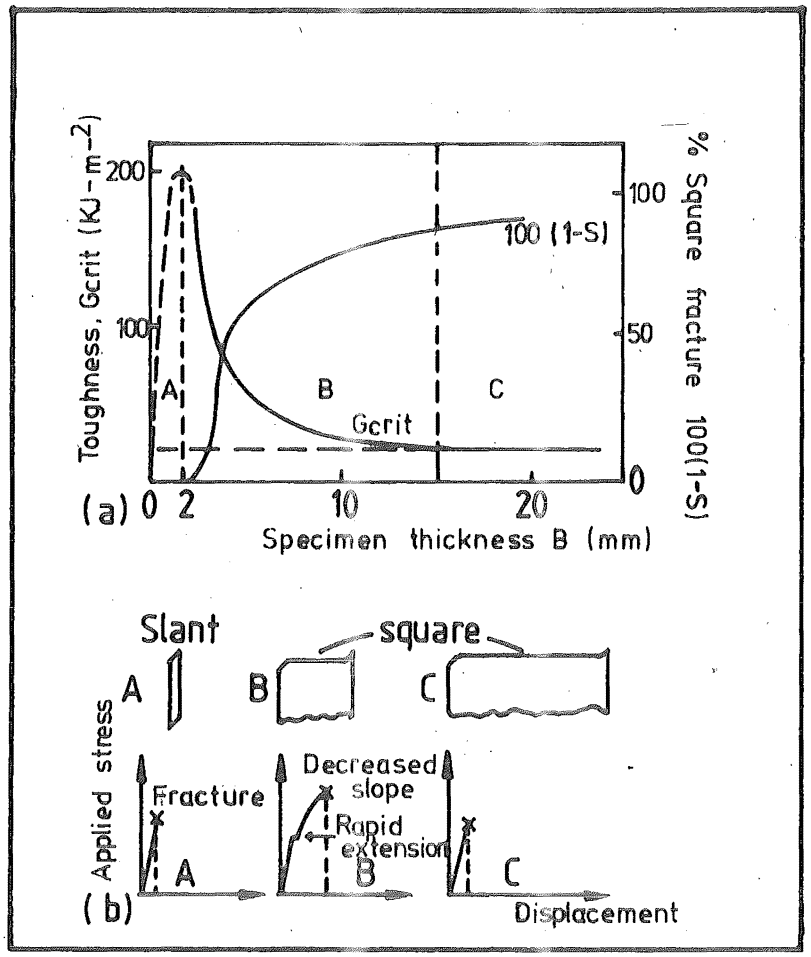

FIG 2·5 (a) VARIATION OF TOUGHNESS WITH THICKNESS OF 7075 ALLOY (Al-Zn Mg)-T_6

(b) FRACTURE PROFILES AND STRESS-DISPLACEMENT CURVES TYPICAL OF REGIONS A, B AND C.

B is specimen thickness

By rewriting Equation (2.5.1) in terms of the associated tensile stress and Young's modulus,

$$\sigma_{app} = \left\{ \frac{2^{\frac{3}{2}} E \sigma_Y B}{\pi a (1 + \nu)} \right\}^{\frac{1}{2}} \qquad (2.5.2)$$

This expression gives the condition for instability. Hence a maximum applied load is obtained and the critical Energy Release Rate, G_{crit}, may be written as

$$G_{crit} = \frac{2^{\frac{3}{2}} \sigma_Y B}{(1 + \nu)} \simeq 2\sigma_Y B \qquad (2.5.3)$$

This definition of G_{crit} predicts a very steep linear increase with thickness, which is generally held adequate to represent the experimental results in this region of the curve.

(ii) Region C

In region C, total instability occurs at loads corresponding to a virtually constant toughness value and the fracture appearance is almost completely square, with a very small proportion of slant profile at the edges. The central region of such a thick specimen is assumed to be deforming under approximately plane strain conditions. When yielding occurs around the crack-tip, high constraints are set up, and a tri-axial stress state is developed. This stress state enhances the initiation of fracture. Linear Elastic Fracture Mechanics describe the fracture process in this region adequately.

Recent development of techniques utilising LEFM for plane strain fracture toughness testing will be discussed in Section 2.6.

(iii) Region B

In this region, the fracture behaviour is more complicated. The fracture surface profile of such a specimen will show the formation of some square features in the centre of the specimen thickness at an applied stress σ_{app}.

However, the square fracture does not occupy a sufficiently high proportion of the thickness such that much of the load is borne by the side ligaments of the cross-section and that total instability does not occur at the stress σ_{app}. The load-displacement curve shows a sudden crack extension for constant, or even decreasing, load if the square fracture tunnels ahead and fractures rapidly. This phenomenon is known as a 'pop-in'. If the square does not advance rapidly, its presence will be detected only by a change in the compliance of the test specimen.

The criterion for final instability has not been firmly established, although the following postulations have been proposed. They are:-

(i) At the thin end of the range, the initial square fracture occupies only a small proportion of the thickness cross-section. As it tunnels forward, the plastic zone size becomes large with respect to the plate thickness. The through-thickness stress is relaxed and final instability is achieved at a load P_F

which is sufficiently large to operate a sliding mechanism for separation.

(ii) At the thick end of the range, the side ligaments bear a much smaller proportion of the total load applied to the test specimen and so final instability follows the initiation 'pop-in' more readily. The fracture profile at instability is a mixture of slant and square.

The behaviour observed in this intermediate range gives rise to doubts concerning the applicability of the Griffith-Irwin relationship as the failure criterion. Krafft et al recognised the problem and proposed a treatment in the form of R-curve analysis[53].

Form the above discussions, it is obvious that the plane strain fracture toughness G_{IC}, or in the form of K_{IC}, is the only value suitable for use as a representative design parameter. Any use of other fracture toughness values will present an over-optimistic prediction. However, an exception must be allowed for thin sheets, which are used extensively in aerospace industry. The need for high strength to weight ratio in such cases renders it desirable to assess G_{crit} values using specimens of similar thickness to the actual service structures. Nevertheless, the plane strain critical value of G_{IC} is the parameter over which researchers have displayed avid interests during the past two decades. Their efforts have led to the standardisation of plane strain fracture toughness testing methods.

2.6 Plane Strain Fracture Toughness (K_{IC}) Testings

The main objective of plane strain fracture toughness testings is to make reproducible assessments of the lower limit of the critical fracture toughness of a material. From discussions in the previous section, it is obvious that several restrictions need to be observed to produce plane strain, quasi-brittle fracture conditions.

Early researchers concentrated their efforts in designing suitable loading systems, specimen geometries and methods of analysing the experimental data[54, 55]. Naturally, initial results revealed large scatter of information, even for tests performed on the same materials. Subsequently, the American Society for Testings and Materials set up a committee (Committee E 24) on "Fracture Toughness Testings of Metals" to co-ordinate and correlate the various efforts of the many researches conducted in the United States. The committee's effort led to the eventual adoption of some of the testing methods as an ASTM Standard[3]. A similar committee under the title of "Fracture Toughness Committee" was also set up by BISRA and it also standardised the K_{IC} testings[4]. Both the ASTM and BSI recommended similar testing procedures.

Briefly, the recommended methods of testings are:-

(i) A slow bend test which involves the opening of a pre-existing fatigue crack by a three-point loading system.

(ii) A tension test which involves the eccentric loading and hence opening of a pre-existing fatigue crack.

A test record consists of an autographic plot of the output from the force sensing device versus the output from a double-cantilever displacement gauge which monitors the mouth-opening displacements across the crack. The fracture toughness value is then calculated by determining the critical load P_Q from the load-displacement plot and then substituting it into the equation[3, 4,56]

$$K_Q = \frac{P_Q}{BW^{\frac{1}{2}}} Y \left(\frac{a}{W}\right) \qquad (2.6.1)$$

where K_Q is the apparent Critical Stress Intensity Factor

B is the specimen thickness

W is the specimen width

a is the crack length

The function $Y(\frac{a}{W})$ varies with different specimen geometries and its values are normally tabulated for standard specimen types. The validity of K_Q as the critical plane strain fracture toughness parameter is governed by the criteria

$$a, \quad (W - a), \quad B \geq 2.5 \left(\frac{K_Q}{\sigma_Y}\right)^2 \qquad (2.6.3)$$

When the above criteria are satisfied, the K_Q is accepted as K_{IC} the conservative, size independent critical stress intensity factor. Thus, under plane strain fracture

$$a , \quad (W - a), \quad B \geq 2.5 \left(\frac{K_{IC}}{\sigma_Y}\right)^2 \qquad (2.6.3)$$

The crack length restriction as stated above effectively rules that the radius of the plane strain plastic zone, r_{IY} , at fracture must

be less than $0.02a$[51].

The K_{IC} validity criteria are obviously very restrictive. However, their necessity has been verified[56, 57].

2.7 Effects Of Temperature On K_{IC}

The effects of temperature on K_{IC} are shown most strongly in relatively low-strength structural steels. Non-ferrous alloys and very high-strength steels show rather small variations of toughness with temperatures up to $100^{o}C$. Similar trends are also observed in the traditional notched-bar impact tests. Results from K_{IC} testings on low-alloy medium strength steels indicates a steep rise in K_{IC} values over a small range of temperature (Figure 2.6)[58, 59].

2.8 Effects Of Strain Rate On K_{IC}

Moderate increases in strain rate have small effects on K_{IC}. Results from a semi-killed steel are shown in Figure 2.7[60]. It can be seen that an order of magnitude increase in loading rate is required to decrease K_{IC} by 10%. However, at very high strain rates (ahead of a running crack, for example) it is possible for the deformation to occur so fast that the heat generated by plastic flow cannot be fully dissipated into the bulk of the specimen. The temperature ahead of the propagating crack may then be raised substantially. Under such an "adiabatic condition", the toughness of the region just ahead of the crack-tip may increase substantially.

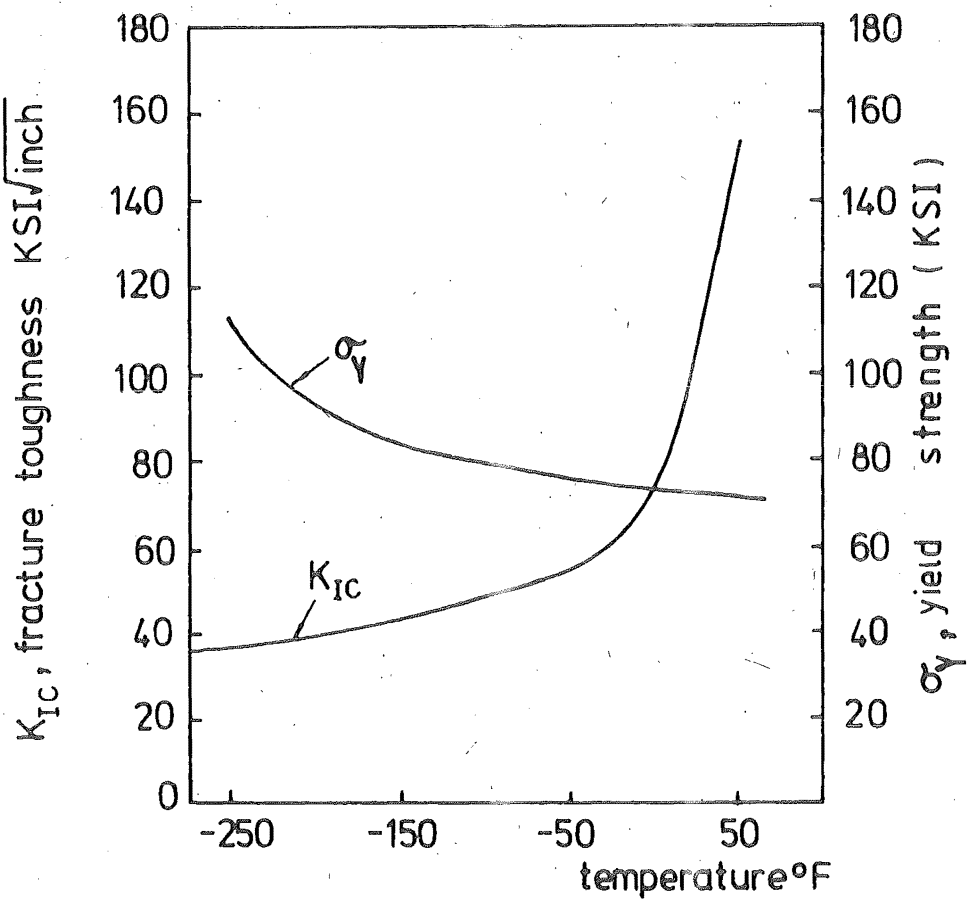

FIG. 2·6 TEMPERATURE DEPENDENCE OF THE K_{IC} FRACTURE TOUGHNESS OF A 12in. THICK A533 GRADE B CLASS 1 PLATE. (Ref. 58, 59)

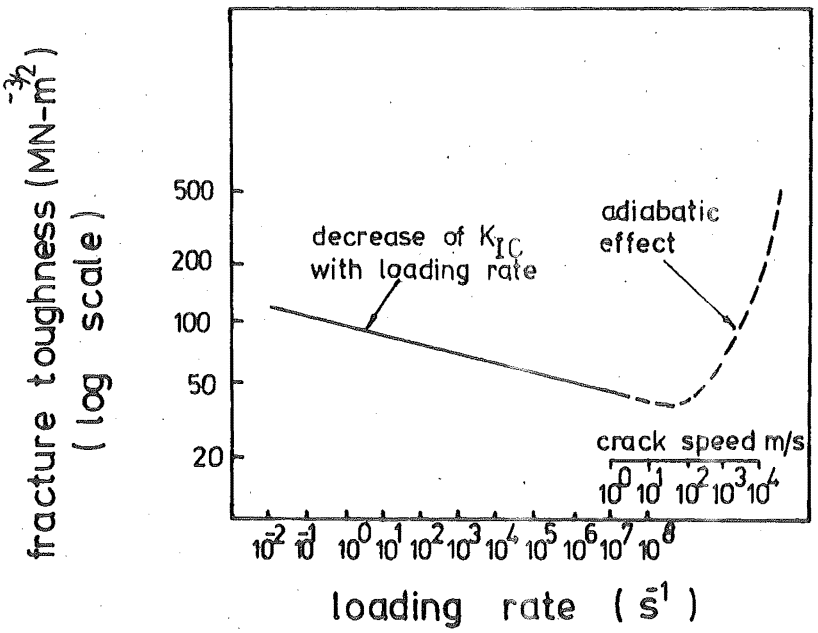

FIG. 2·7 VARIATION OF FRACTURE TOUGHNESS WITH LOADING RATE IN A SEMI-KILLED STEEL (Ref. 60)

2.9 Summary

The effects of flaws on the fracture toughness of a material have been given their due recognition over the past two decades. Sufficient theoretical development has firstly enabled mathematical treatments and subsequently standardising of testing methods of a cracked model. Unfortunately, the K_{IC} validity criteria have restricted the applications of LEFM to brittle, high-strength materials because unrealistically large specimens would be required for the valid assessments of K_{IC} for lower-strength materials. This effectively eliminated the use of LEFM in most structural steels.

CHAPTER THREE

FRACTURE MECHANICS OF LOW STRENGTH MATERIALS

3.1 Introduction

Linear Elastic Fracture Mechanics has been developed mainly for high-strength materials. Naturally, its possible application to structural materials is of great interest to engineers. Unfortunately, the limitations of plane strain K_{IC} testings eliminated the possible realistic applications of Linear Elastic Fracture Mechanics to medium and low strength materials. This is so because for tough materials, a valid K_{IC} test usually requires large specimen dimensions or very low testing temperatures. Consequently, attention has been focused on alternative measurements of K_{IC} under conditions relevant to the material's service applications. These efforts culminated in the proposal of two separate parameters which describe the fracture toughness of ductile materials. These are the Crack Opening Displacement (COD) at fracture and the critical value of a quasi-"strain energy release rate" known as the critical J-Integral (J_{IC}).

Apart from the two new parameters, several methods which analyse load-displacement curves extending into the post-yield regime were proposed. These methods claim to provide valid measures of K_{IC}.

3.2 The Crack Opening Displacement

3.2.1 Theoretical Concepts

When a cracked specimen reaches general yield condition, deformation at the crack-tip will be extensive and complex. Consequently, the crack-tip stress or strain field cannot be characterised by a single-valued parameter such as the applied load in the standard K_{IC} testing method. Independently, Wells[61] and Cottrell[62] considered the amount of crack opening prior to crack extension as a parameter which might characterise the crack-tip region's strain field for a given set of conditons.

Wells observed that the tip of a machined slot opened with a nearly-square ended contour during plastic deformation[61]. Using Irwin's estimate to determine the extent of plastic zone to represent the "notional" elastic crack-tip[44], he showed that COD is analogous in concept to a critical crack extension force which can be related to K_{IC} through the yield stress σ_Y and Young's modulus E. The Westergaard's solution[38] may be used to give the displacement u_{11} in the X_1-direction (Figure 3.1) at the elastic-plastic interface of the extended "notional" crack as[63]

$$u_{11} = \frac{2K(2\pi r_Y)^{\frac{1}{2}}}{\pi E} \qquad (3.2.1)$$

where K is the Stress Intensity Factor

and r_Y is the plane stress plastic zone's radius, its value being

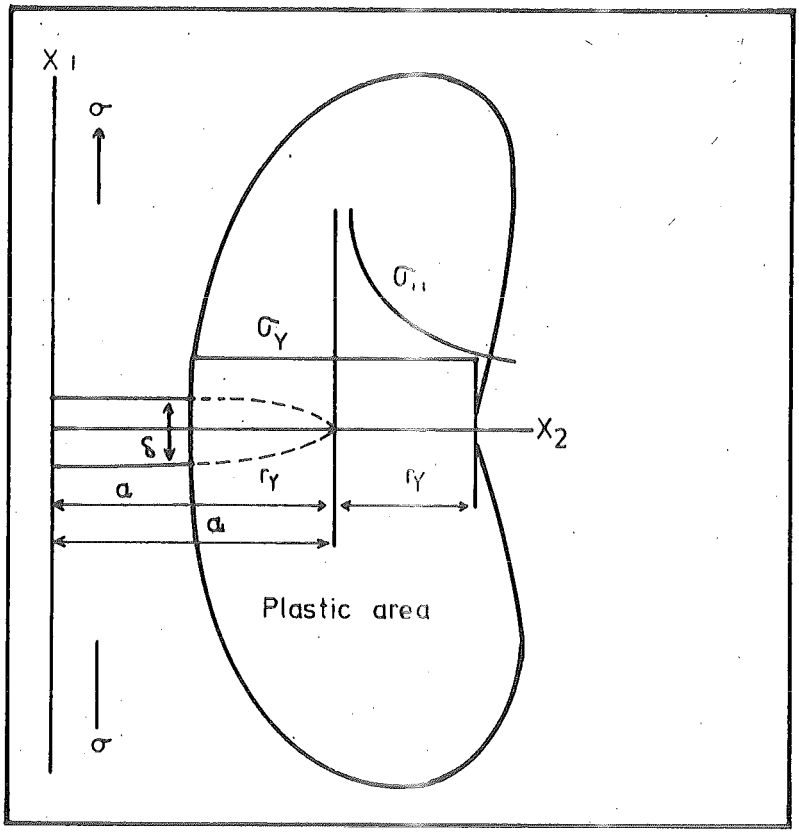

FIG 3·1 CRACK TIP STRESS FIELD

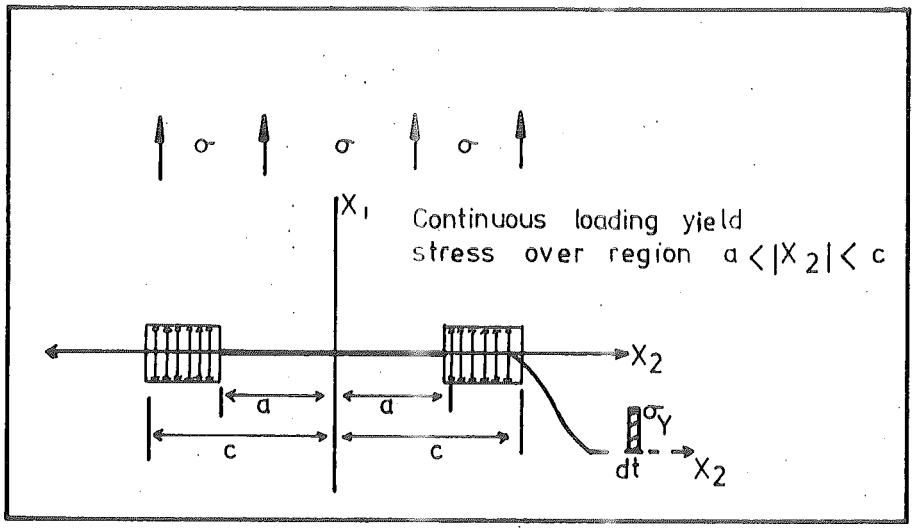

FIG 3·2 SPREAD OF PLASTICITY FROM A CRACK: DUGDALES MODEL, BASED ON WESTERGAARD'S STRESS FUNCTION

given by the expression[41]

$$r_Y = \left(\frac{1}{2\pi}\right) \left(\frac{K}{\sigma_Y}\right)^2 \qquad (3.2.2)$$

Noting that the total crack-tip COD is $\delta = 2u$, and using the above expression for r_Y, it can be shown that for plane stress

$$\delta\sigma_Y = \left(\frac{4}{\pi}\right) \left(\frac{K^2}{E}\right) = G \qquad (3.2.3)$$

where K is the Stress Intensity Factor for the condition of interest during crack-tip deformation.

Wells proposed that this concept could be extended to full plastic deformation where the concept of a local plastic zone has little meaning. The criterion for fracture was when the crack opening displacement, δ , reached some critical value, δ_c. Subsequent fracture experiments on bend and tension specimens produced data broadly consistent with the proposal, although agreement on a detailed level was incomplete[64].

Cottrell used the concept of COD to explain why small test specimens, cut from a large ship-plate which had fractured well before general yield in a brittle manner, now fractured well after general yield in a ductile manner when tested at the same temperature. He proposed that the plastic zone engulfed the whole cross-section of a small specimen before the COD reached the critical value at instability, δ_c, so leading to general yielding and ductile fracture whereas in large plate, δ_c was attained first and thus caused brittle fracture below the general yield stress.

Models of yielding at a crack-tip in terms of continuum mechanics were developed separately by Barenblatt[65], Vitvitskii and Leonov[66], and Dugdale[46]. Dugdale's simpler model (Figure 3.2) has been adopted widely in Yielding Fracture Mechanics. In his model, Dugdale represented the local plastic zones by a "notional" crack of length 2c subjected to the same real external stress (σ), but with additional internal closing stress of yield magnitude (σ_Y) acting over the length (c - a). Dugdale then used the stress functions of Muskhelishveli to obtain an equation describing this plastic zone size

$$\frac{c}{a} = \cos\left\{\frac{\pi}{2}\left(\frac{\sigma}{\sigma_Y}\right)\right\} \qquad (3.2.4)$$

Burdekin and Stone[64] derived from the above equation an expression for the opening of the crack as

$$\delta_c = \frac{8\sigma_Y a}{\pi E} \ln \sec\left\{\left(\frac{\pi}{2}\right)\left(\frac{\sigma}{\sigma_Y}\right)\right\} \qquad (3.2.5)$$

Similar forms of equations were obtained from the Dugdale model by Goodier and Field[67] and Hahn and Rosenfield[68] but their derivations have enjoyed less popularity.

Bilby, Cottrell and Swinden also proposed a model of yielding at the crack-tip by modelling the crack-tip and yield zone as arrays of dislocation[52]. This BCS model originally considered Mode III anti-plane strain shear by screw dislocations, and Mode II shear displacement by edge dislocations. However, by using suitably oriented edge dislocations, the model may be adapted to potray a

slit under tension with Mode I crack-tip displacement expressed in identical forms to Equations (3.2.4) and (3.2.5).

Thus, the BCS model and the Dugdale model are equivalent and they both reduce the problem to linear elasticity by using methods which allow yielding only in the plane of crack opening, and so constituting a plane stress state. This approach has been termed as a "strip-yield" model.

By expanding Burdekin and Stone's expression for COD yields[64]

$$\delta = \frac{\pi\sigma^2 a}{E\sigma_Y} \{ 1 + \frac{\pi^2}{24} (\frac{\sigma}{\sigma_Y})^2 + \ldots\ldots\ldots \} \qquad (3.2.6)$$

Since in LEFM the plane stress centre-cracked infinite plate solution yields

$$G = \frac{K^2}{E} = \frac{\pi\sigma^2 a}{E} \qquad (3.2.7)$$

it is obvious that for small applied stresses,

$$G = \sigma_Y \delta \qquad (3.2.8)$$

It is now generally accepted that

$$G = M\sigma_Y \delta \qquad (3.2.9)$$

where M is a plastic intensification factor which can be used to account for different stress states, specimen geometries and work-hardening.

The value of M varies from approximately 1 for conditions of plane stress and non-work-hardening materials[70, 71, 72], as assumed by the Dugdale and BCS models, to 2 where a crack-tip is highly restrained by a work-hardening material[5, 6]. For the BCS model under plane strain, Haigh et al[73] established that the relationship is:-

$$M\sigma_Y = 1.61\sigma_u \qquad (3.2.10)$$

while Tracey[7] reported that:

$$M = 1.84 \quad \text{for small scale yielding}$$
$$= 2 \quad \text{after general yield}$$

However, Sailor has shown that the value of M can reach 3.5 for materials with high strain hardening index[20]. This variability of M is likely to be caused by the fact that the theoretical treatment of COD does not take into account the effects of the variations of the in-plane and out-of-plane constraints. In theoretical treatments, M is expected to vary between 1 and 2[74] and the experimental correlations[5, 71, 72] fell within this range.

The compatibility between COD and LEFM, particularly between COD and fracture toughness K_{IC}, is readily demonstrated by using Equations (3.2.9) and (2.3.10) where in plane strain

$$G = M\sigma_Y\delta = \frac{K^2}{E}(1 - \nu^2) \qquad (3.2.11)$$

Hence, by using the appropriate values of M, full compatibility of the two concepts can be achieved[5].

Thus, the COD concept provides an alternative to the standard K_{IC} tests with the advantage of tolerance for a substantial amount of yielding. The COD model has been further developed by Heald et al[75] to predict fracture events in the post-yield regime. They adopted a simple fracture criterion $\delta = \delta_c$ and expressed the fracture stress in terms of the Griffith-Irwin equation[2, 43]

$$\sigma_F = \frac{K_{IC}}{(\pi a)^{\frac{1}{2}}} \qquad (3.2.12)$$

By further assuming the crack-tip material to be fully work-hardened at fracture and hence substituting the ultimate tensile stress, σ_u, in place of the yield stress, σ_Y, in the Equation (3.2.5), they derived the expression

$$\sigma_F = 2\pi\sigma_u \cos^{-1}\{\exp(-\frac{\pi K_{IC}^2}{8\sigma_u^2 a})\} \qquad (3.2.13)$$

Heald et al claimed that Equation (3.2.13) describes fracture over conditions ranging from LEFM to extensive yielding.

3.2.2 Practical Measurements Of COD

The main objective of a COD test is to measure the amount of crack-tip opening δ_c which is a characteristic of the mode of fracture. This involves obtaining values associated with the crack-tip region and detecting the onset of crack extension.

The first attempts to measure COD for a crack-like geometry were made using the paddle-type COD meter[64]. This method made use of a probe with a thin piece of steel at its end inserted as close as possible to the crack tip in the plane of the crack. The probe was lightly loaded in torsion and connected to a transducer, so that as the crack faces moved apart, the toes of the paddle continued to bear on the surfaces and the consequent rotation provided an electrical signal from the transducer which could be calibrated in terms of COD. This device has the advantage of measuring the crack opening directly. However, it could not be used in fatigue pre-crack test specimens.

An alternative method of COD measurement was the double-notched specimen[76]. In such a specimen, fatigue cracks of roughly similar length were produced at the end of the notches. The specimen was then fractured, and the COD at the unfractured pre-cracked notch was obtained by metallographic sectioning and direct measurement on the micrograph. This COD represents the critical value just prior to final instability. Unfortunately, this method does not provide a continuous record of the test.

Realising the inadequacy of the above two methods, efforts were directed at designing COD instrumentation which could be identical to those used in LEFM tests. Such a technique was developed in which the opening at the standard knife-edges mounted on a specimen was measured using a clip-on-extensometer. This opening was related to the crack-tip COD by prior calibration[77]. The calibration may be obtained experimentally or theoretically[78]. The theoretical

calibration assumes that the rigid ends of the specimen rotate about the neutral axis by sliding along a plastic hinge (Figure 3.3). The COD and the extensometer displacement, V_g, are related by the expression

$$\frac{\delta}{r(W - a)} = \frac{V_g}{z + a + r(W - a)} \qquad (3.2.14)$$

The position of the neutral axis varies with specimen geometry. It is usually shown to be located at a distance r(W - a) from the crack-tip. The values of the rotational constant, r, were initially reported to be 0.37 for four-point bend geometry and 0.40 for compact tension geometry[63]. However, these values were only valid for general yield conditions. The situation was slightly improved by the empirical solutions of Wells[79] which extend the range of theoretical calibration to encompass both the elastic and plastic regimes. Later investigations reported that the hinge-point location varies significantly with the degree of plasticity[81]. Thus, the previous methods of analysis may cause significant errors at low values of COD. However, further investigations resulted in the availability of analytical solutions for three-point bend[71] and compact tension[82] geometries. A proposal for standard COD testings was documented in 1972[23].

Unfortunately, the COD method may be imprecise in its definition of the point of failure. Unlike a linear elastic fracture event, the point of final instability in a COD test is occasionally preceded by varying amount of ductile crack extension. In such cases, it is a matter of interpretation as to whether the COD value at the initiation of fracture (δ_i) or at the maximum applied force on the

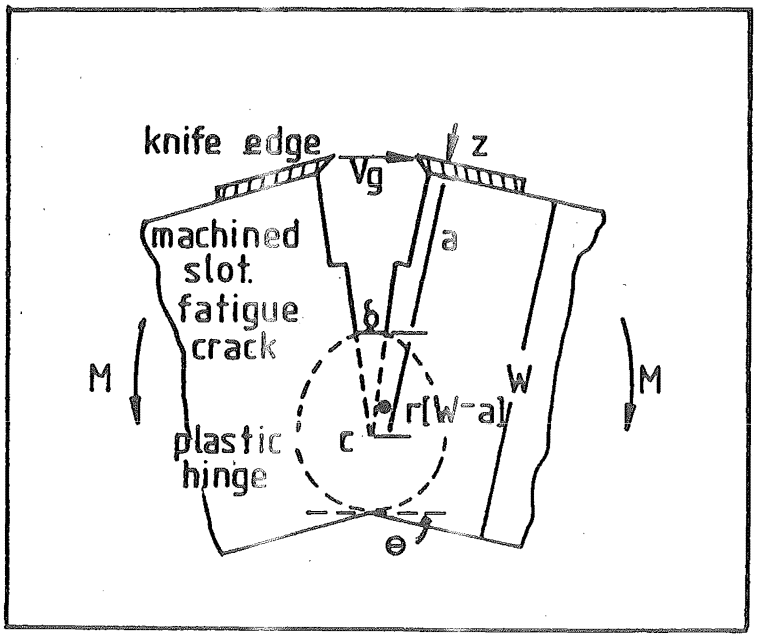

FIG 3·3 RELATIONSHIP BETWEEN CRACK OPENING DISPLACEMENT δ AND EXTENSOMETER DISPLACEMENT Vg

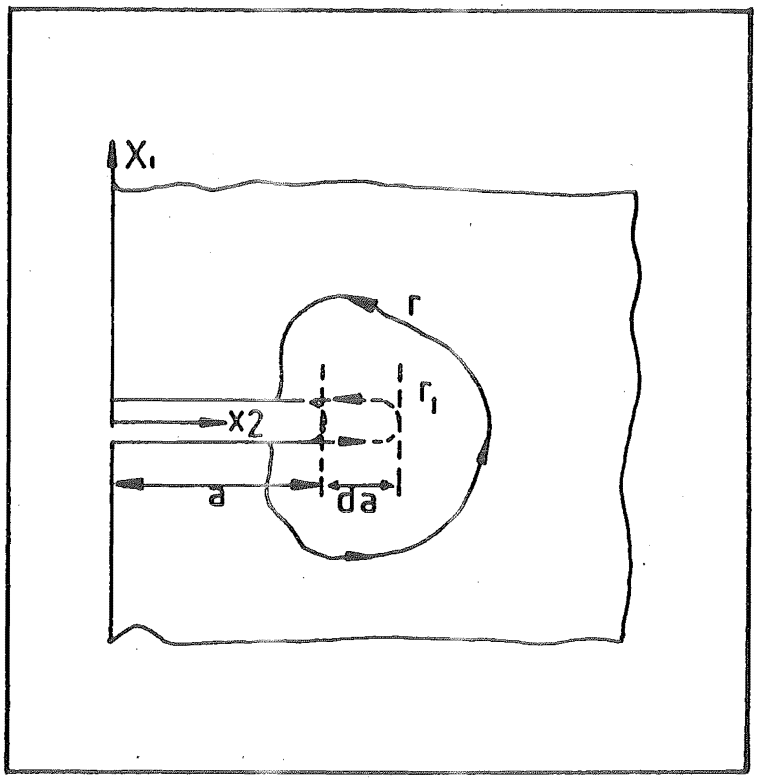

FIG 3·4 RELATIONSHIP BETWEEN CHANGE IN POTENTIAL ENERGY AND LINE INTEGRAL (Ref 8)

applied force-displacement curve (δ_m) is to be used. Experimental works[18, 83] had suggested that δ_i was a material constant while δ_m may depend on specimen dimensions and machine stiffness if the material displays a significant difference between δ_i and δ_m. Practical measurement of δ_i is difficult although several elaborate crack-initiation detection techniques have been reported[4, 11, 18, 71, 79, 84].

3.3 The Critical J-Integral Method

3.3.1 Theoretical Concept

The J-Integral as defined by Rice is a path independent energy line integral (Figure 3.4) where[8]

$$J = \int_{\Gamma} (W' \, dy - \tilde{T} \frac{\partial \bar{u}}{\partial x} \, dS) \qquad (3.3.1)$$

where W' is the strain energy density

$\tilde{T}$ is traction vector on the path Γ

$\bar{u}$ is the displacement vector

S is the arc length Γ

Γ is any contour anticlockwise around the crack from the lower to the upper crack face.

Thus, J is concerned with the difference between the strain energy and the work done in crack opening.

Energy line integrals describing the spread of plasticity at a notch have been developed earlier[85, 86]. However, Rice's definition is more popular because McClintok[87] combined it with contemporary

stress-strain solutions for a non-elastic crack-tip model[88, 89]. More importantly, Rice interpreted J as the potential energy difference between two identical loaded bodies having slightly different crack lengths[8]. Thus, J is the potential energy (U) release rate as a crack extends, such that for unit thickness

$$J = -\frac{\partial U}{\partial a} \qquad (3.3.2)$$

For elastic conditions, this is equivalent to G. However, the potential energy concept fails under conditions of plasticity because a large part of the energy is expended in plastic deformation rather than crack extension[70]. Nevertheless, in such cases, U is taken to be equivalent to W_e, the work done between successive load deflection curves as specimens with successively longer cracks are deformed to a given displacement or load. Thus for unit thickness,

$$J = -\frac{\partial W_e}{\partial a} \qquad (3.3.3)$$

where a is the crack length.

3.3.2 The J-Integral As A Failure Criterion

Based on the definition and energy interpretation of J-Integral, Begley and Landes proposed a critical value of J at the instance of crack-tip instability which could be measured experimentally since failure is controlled by near crack-tip deformation[9]. Experimental evidence supporting the above assumption was presented and showed

that for a given material, the value of J at failure was fairly constant between linear elastic and fully plastic conditions; and was equal to G_{IC} under plane strain conditions[9]. However, since the line energy integral is expressed only in two dimensions, the approach is, therefore, limited to problems of plane strain or generalised plane stress. Furthermore, the original derivation of J as a valid failure criterion was based on a deformation theory of plasticity rather than on the more appropriate incremental theory. Therefore restrictions have to be placed on the applicability of the critical J criterion because the final stress-strain states of real materials are dependent on the loading history. Thus, in a test, loading must always be monotonic because unloading is not permitted if the deformation theory of plasticity is to be a realistic approximation of elastic-plastic behaviour. This rules out the use of the maximum load as an instability criterion if the material exhibits significant degree of stable crack extension prior to final instability, as any crack extension will cause unloading near the crack-tip. However, limited load relaxation associated with slight crack extension and crack-tip blunting prior to instability is tolerated in the same way as plasticity in K_{IC} testings. Nevertheless, a rigorous validity criterion will limit critical J_c fracture criterion to the instance of initial crack extension rather than the final crack instability in materials which exhibit sub-critical stable crack extension.

3.3.3 Practical Evaluation Of The Critical J-Integral

The early experimental determinations of J were based on load-load point displacement curves using the energy rate concept

based on Equation (3.3.2)[9]. This is a tedious technique which uses Rice's potential energy difference concept, repeated for a range of crack lengths. It provides a calibration for J as a function of load point displacement for a given geometry, against which a given fracture test displacement can be compared, and the critical value of J (J_c or J_{IC}) could then be estimated. Bucci et al proposed a method for approximating J by curve fitting[90]. They used plastically adjusted LEFM analysis and plastic limit load solutions to estimate load-displacement curves, and in turn, J versus displacement curves. Results so obtained were satisfactory[9, 90]. Extensions to Bucci et al's proposal have been reported where a single load-displacement record was sufficient for the evaluation of J[91, 92]. For certain specimen configurations, it can be shown that[92]

$$J = \frac{2}{(W - a)} \int_0^{\Delta_{crack}} P \, d(\Delta_{crack}) \qquad (3.3.4)$$

where P is load per unit thickness

Δ_{crack} is load point displacement

(W - a) is dimension of the uncracked ligament

This leads to the expression

$$J_c \text{ , } J_{IC} = \frac{2U'}{B(W - a)} \qquad (3.3.5)$$

where U' is the area under the load-load point displacement curve up to the instance of initial crack-tip instability.

B is the specimen thickness.

Equation (3.3.5) has been shown to be applicable to deeply-notched three-point bend and compact tension specimens[92]. Deep notches ($\frac{a}{W} > 0.6$) were necessary to ensure that plasticity is confined to the uncracked ligament. Strictly speaking, the work of elastic deformation of an uncracked specimen has to be subtracted from the area under the load-load point displacement curve. However, Rice et al claimed that this elastic work is negligible for compact tension specimens or for cases where plastic displacement becomes very large compared to elastic contributions[92].

A more general method of assessing J_{IC} using the work of crack-tip instability has also been proposed[93]. In this case, J_{IC} was given by

$$J_{IC} = \frac{N_e U'_e}{B(W - a)} + \frac{N_p U'_p}{B(W - a)} \qquad (3.3.6)$$

where N replaces 2 in Equation (3.3.5)

and subscripts e and p refer to elastic and plastic components respectively.

Values of N were calculated for different geometries and different ratios of $\frac{a}{W}$[93]. This method obviously removes the restriction on notch-depth and the necessity to subtract the elastic energy of the uncracked specimen. Nevertheless, this approach still relies on the numerical equality of the energy absorbed up to the critical displacement with the values of J.

The restriction of monotonic loading in the determination of J_{crit} is presenting a problem in the assessment of low and medium

strength materials. Sub-critical crack growth often occurs in these specimens. Consequently, they lead to erroneous values of J_{crit}. Hence, it is important to detect the point of initiation of such slow crack growth which incidentally corresponds to the initial crack-tip instability. Unfortunately, the standard clip gauge instrumentation may not be able to detect slow crack growth adequately. Consequently, other methods such as the electrical potential technique need to be employed[3, 4]. Recent developments have led to more tangible methods of measurements. The multi-specimen, heat-tinting method to monitor crack growth used in conjunction with a resistance curve technique to assess J_{crit} was initially proposed[29]. However, this method has the inherent disadvantage of using multiple specimens. This problem was overcome by making repeated partial unloadings of a single specimen during testing, then using linear elastic compliance calculations to detect the onset of a certain crack extension[94]. This point was then identified on the load-load point displacement curve and then using Equation (3.3.5) to evaluate J_{IC}. It was claimed that the error in estimating the onset of crack growth was small and that the small unloadings were not detrimental. A more accurate method using the silicon rubber replication technique[71, 80] has been investigated[84] and it was found that the accurate determination of the crack-tip displacement at the onset of crack growth enabled the evaluation of J_{IC} using Equation (3.3.5).

3.3.4 Effects of Specimen Size

In applying J as a fracture criterion to large scale yielding problems, the ASTM plane strain size criteria, namely[3]

$$a,\ B,\ (W - a) \geq 2.5 \left(\frac{K_{IC}}{\sigma_Y}\right)^2$$

must be replaced by a new set of criteria and a new definition of local plane strain at the crack-tip. The region to which plane strain conditions exist now only needs to encompass the region at the crack-tip where the critical separation process is taking place. The set of new geometry criteria proposed was[30]

$$a,\ B,\ (W - a) \geq A\ \frac{J_{IC}}{\sigma_{flow}} \qquad (3.3.7)$$

where A is a constant.

The value of A was initially proposed to be 50. However, experimental investigations found that a value of A = 25 was sufficient[10,29] The flow stress, σ_{flow}, is usually taken as σ_Y although it has been interpreted as $\frac{1}{2}(\sigma_Y + \sigma_u)$[29]. Thus, the geometrical size criteria for J_{IC} is much less rigorous than those for the K_{IC} testings.

3.4 Relationship Between COD And J-Integral And The Differences In Their Usage

Both COD and J_{IC} attempt to characterise fracture events by parameters measured with model laboratory test specimens which may be related to the critical value of energy release rate when a large service structure breaks well before general yield. Both tests usually use small specimens where a substantial amount of yielding

precedes fracture. The COD focuses attention on the crack-tip region and is able to be related directly to the micro-mechanism of fracture in a region of area less than 0.01 mm^2. J_{IC} relates to a macroscopic work term or to crack-tip conditions, depending on the Γ-contour chosen. Since J is proportional to Δ_{crack}, the load point displacement, and Δ_{crack} is proportional to COD in the standard bend and compact tension specimens, J is in fact proportional to COD. This deduction can be verified by referring to the expression

$$G_{IC} = J_{IC} = \frac{K_{IC}^2}{E}(1 - \nu^2) \quad \text{(Ref. No. 9, 91)} \quad (3.4.1)$$

$$G_{IC} = M\sigma_Y\delta_{IC} \quad \text{(Ref. No. 70)} \quad (3.4.2)$$

where δ_{IC} is the "plane strain" critical COD

M is a constant

Thus, $$J_{IC} = M\sigma_Y\delta_{IC} \quad (3.4.3)$$

In the Dugdale COD model as currently used, $M\sigma_Y$ is equivalent to the restraining stress at the crack-tip. M is assumed to be constant. However, in more realistic assessments, M was found to vary[5, 6, 70, 71, 72, 74].

The COD is a simple concept, and its rapid development leading to a near standardised testing method makes it a practical approach in the assessments of fracture toughness parameters. Unfortunately,

it is often necessary to restrict the application of the critical value of COD found in laboratory tests to be representative of the thickness tested because of the oversimplification of the model. The J-Integral attempts to produce a more rigorous analytical treatment of yielding fracture mechanics. However, conflicting claims on the range of applicability of the J_{IC} fracture criterion have been reported[10, 95].

Nevertheless, both COD and J_{IC} provide a reasonable estimate of K_{IC} with the advantage of using specimens that are much smaller than those stipulated in the standard K_{IC} testing. The concept of K_{IC} may now be extended to be applicable to medium and low strength materials.

3.5 Load-Displacement Curve Analyses

Several methods have been developed in the analyses of load-displacement curves which extend into the post-yield regime. These methods were reported as being able to provide measures of fracture toughness values which can be related to K_{IC} or J_{IC} while using specimens of thickness that are invalid according to the ASTM standard[4]. These include the prediction of K_{IC} by

(a) energy consideration

(b) the curve fitting technique for load-displacement plots

(c) a semi-empirical method

3.5.1 The Equivalent Energy Method

This method provides a simple way to relate fracture in a small specimen to fracture in larger but geometrically similar models. The principles behind this technique have been discussed by Witt and Mager[12, 101], while further analytical investigations were conducted by Rice et al[92] and also by Begley and Landes[96].

The method considers the load-displacement curves of geometrically similar bodies of various sizes. If these curves are normalised by a size parameter such as the thickness B, they will fall on a universal load-displacement curve as shown in Figure 3.5[97]. Up to the point at which fracture occurs, the load-displacement plot of any specimen will lie on this curve. The curve also varies linearly with the applied load in the small scale yielding region, and the area under the curve reflects the energy input to the crack. In the fracture toughness testing of a thick specimen, failure will occur on the linear part of the curve. Tests on progressively smaller specimens will fail at increasingly higher normalised loads. Witt postulated that it is possible to predict K_{IC} of a material from an invalid test by considering the volumetric energy ratio[97]. Witt's estimate of K_{IC} is given by the expression

$$K_{IC} = \frac{P_1 \left(\frac{A_1}{A_2}\right)^{\frac{1}{2}} Y \left(\frac{a}{W}\right)}{BW^{\frac{1}{2}}} \qquad (3.5.1)$$

where P_1 is the normalised failure load of the specimen

A_1 is the area under the normalised curve up to failure

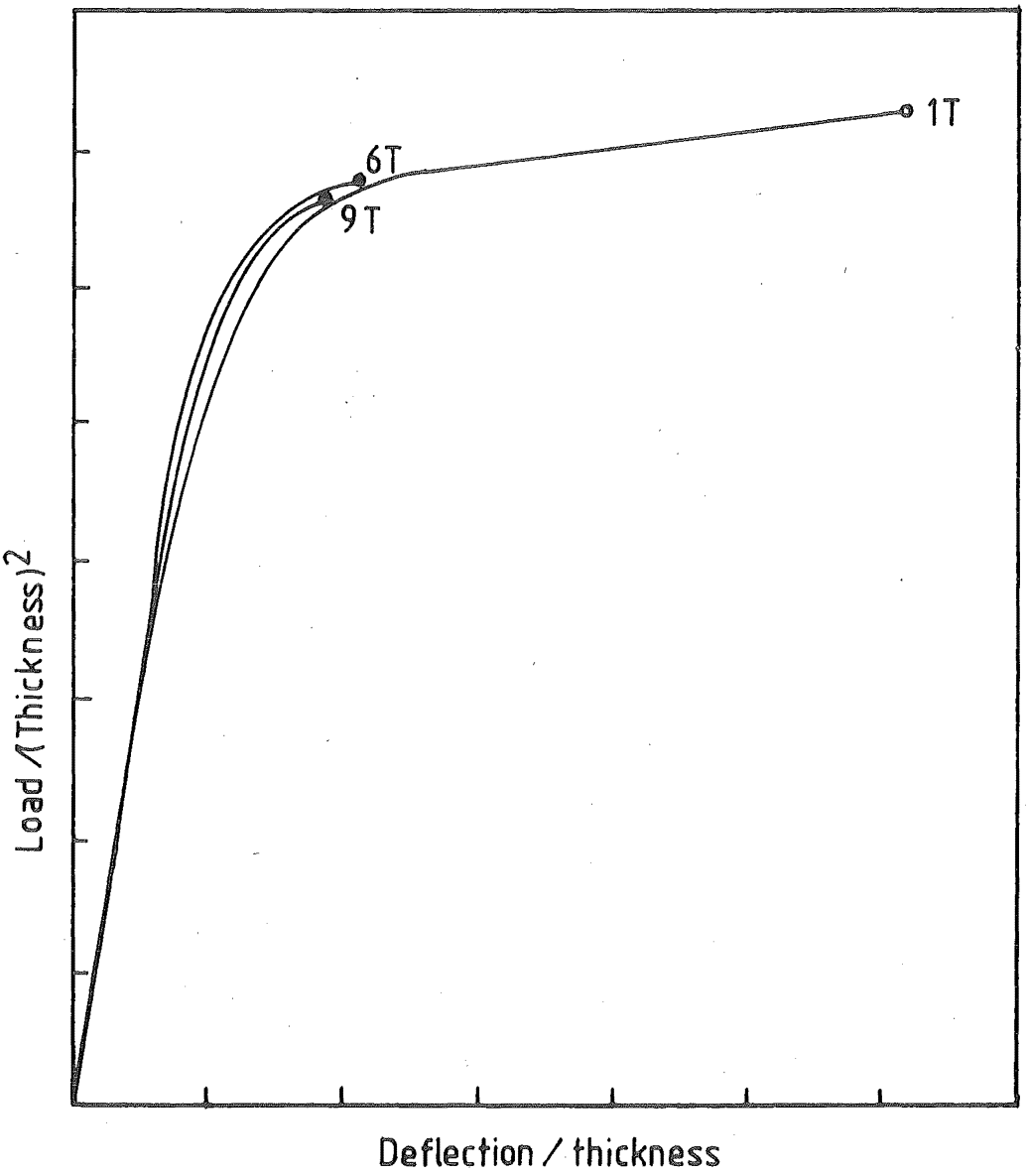

FIG 3·5 NORMALISED LOAD-DEFLECTION CURVES FOR 1T (1 inch thick), 6T AND 9T COMPACT TENSION SPECIMENS TESTED AT 200°F (ASTM A5 33, GRADE B CLASS 1 STEEL) (Ref 97)

A_2 is the area under the normalised curve up to the point where a valid K_{IC} is expected.

W is the specimen width

B is the specimen thickness

Y $(\frac{a}{W})$ is the standard compliance function in K_{IC} testings.

Experimental results showed that Witt's method can provide an estimate of K_{IC} which is within the acceptable limit of scatter as long as excess elastic deformation was not present[97, 98, 99]. Chell had further shown thatdeep notches ($\frac{a}{W} > .65$ for bend specimens, $\frac{a}{W} > .5$ for compact tension specimens) were essential in order to avoid unduly optimistic predictions of K_{IC}[100].

3.5.2 Load-Displacement Curve Fitting Method

This method was a development by Chell and Milne[13] on the original proposal by Adams and Munro[91]. A semi-empirical fracture formula is chosen so that it interpolates between linear elastic fracture mechanics and plastic collapse. This formula is then used to provide an approximation of J.

For a constant load test a relationship exists between J and the displacement D_{pin} at the load pins due solely to the crack. This may be written as

$$D_{pin} = B \frac{\partial}{\partial P} \int_o^a J \, da \qquad (3.5.2)$$

J was taken to be [13]

$$J = \frac{8}{\pi^2} E\alpha Y^2\left(\frac{a}{W}\right)\sigma_L{}^2\left(\frac{a}{W}\right) \ln \sec\left\{\frac{\pi\sigma}{2\sigma_L\left(\frac{a}{W}\right)}\right\} \qquad (3.5.3)$$

where σ is the applied stress

E is the modulus of elasticity

$\sigma_L\left(\frac{a}{W}\right)$ is the plastic collapse stress under plane stress condition

α is 0.5 for compact tension specimens

2 for bend specimens

$Y\left(\frac{a}{W}\right)$ is the standard compliance function of the test specimen

The plastic collapse load must first be guessed, from which J and D_{pin} are obtained and then fitted to the experimental load-displacement curve by an iterative process. The method considers only the plastic displacement and in doing so avoids the sources of error due to elastic displacement of the uncracked body. Results of experimental investigations indicated that the method provides a reasonable estimate of K_{IC}[13, 99, 100]. In some cases, it was claimed to be superior to the equivalent energy method[100].

3.5.3 Semi-Empirical Method

By modifying the semi-empirical post-yield fracture expression derived for a uniform tension specimen[102], Chell obtained the equation[14]

$$K_{IC}{}^2 = \frac{8}{\pi^2} aY^2\left(\frac{a}{W}\right)\sigma_L{}^2\left(\frac{a}{W}\right) \ln \sec\left\{\frac{\pi\sigma_F}{2\sigma_L\left(\frac{a}{W}\right)}\right\} \qquad (3.5.4)$$

where a is the crack length

$Y(\frac{a}{W})$ is the ASTM K_{IC} compliance function

$\sigma_L(\frac{a}{W})$ is the collapse stress of the system

σ_F is the fracture stress

Thus, by identifying $\sigma_L(\frac{a}{W})$ of the material concerned, a simple method of estimating K_{IC} is available. The plane strain collapse stress of popular specimen geometries had been previously derived[103]. For a three-point bend specimen[14, 103],

$$\sigma_L(\frac{a}{W}) = 2.18\ \sigma_u(1 - \frac{a}{W}) \qquad (3.5.5)$$

where σ_u is the Ultimate Tensile Stress

and for a compact tension specimen [14, 103]

$$\sigma_L(\frac{a}{W}) = A_1'\sigma_u(1 - \frac{a}{W}) \qquad (3.5.6)$$

where A_1' is 0.35 to 0.45 for most steels, depending on the work hardening characteristics

and $0.4 < \frac{a}{W} < 0.6$

Chell used the formula to analyse data from several invalid K_{IC} tests and found reasonable agreement with K_{IC} values obtained from valid tests[14]. However, as the method depends solely on the stress at fracture and not on a more sensitive parameter such as the load-displacement curve, a sensible and accurate knowledge of collapse stress is essential.

3.6 Summary

In order to overcome the unrealistic size criteria of the standard K_{IC} testings when applied to low strength materials, several proposals have been investigated.

The COD concept is a very attractive one as it involves relatively uncomplicated procedures in the measurement of a tangible parameter. However, the ambiguity in the definitions of critical load in cases where ductile fracture or sub-critical crack growth had occurred raises doubts about the extent of the range of applicability of the concept. However, extensive research has led to the claim that COD concept, although lacking rigorous analysis, could provide a workable parameter for the measurement of K_{IC} for engineering design purposes.

The J_{IC} fracture criterion attempts to provide a more rigorous argument than those of COD and focuses attention on macroscopic work terms in a region near the crack-tip. Although significant advances have been achieved in the theoretical analysis of J_{IC}, a comprehensive coverage of fracture events with varying degrees of yielding is still awaited. In experimental measurements, the J_{IC} criterion suffers handicaps similar to those of COD testings in the form of sub-critical crack growth and possibly ductile fracture. Nevertheless, the development of J_{IC} criterion is currently still in its infancy and further improvements are expected.

The various methods of load-displacement curve analysis appeared to provide good estimates of K_{IC} from invalid tests. Among these,

Chell's semi-empirical formula for estimating K_{IC} is very interesting as it measures the applied fracture stress and hence it may have overcome the problem associated with sub-critical crack growth.

It is obvious that assessments of K_{IC} from invalid tests are still inconclusive because of the lack of standardised testing procedures, which, in effect reflects on the absence of a comprehensive understanding of fracture process with significant quantity of yielding. However, the various proposals have been supported by favourable experimental evidence. Thus, it is logical to conclude that each method has its limited range of applications. The successful measurements of $K_{IC}$with the concepts of yielding fracture mechanics will depend very much on the discrete selection of testing procedures and methods of analysis.

CHAPTER FOUR

RELATIONSHIP BETWEEN FRACTURE TOUGHNESS AND MICRO-PARAMETERS

4.1 Cleavage Fracture

It is generally accepted that cleavage fracture of ferrite-pearlite low alloy steel occurs when the critical cleavage stress σ_F is exceeded locally[76, 104, 105]. The effects of yielding on cleavage stress was investigated by Low[106] who found that by fracturing low carbon steel specimens at -195°C, the cleavage fracture stress was coincident with the yield stress for coarse grain materials, and exceeded the yield stress for fine-grain materials (Figure 4.1). These observations reinforced the postulation that cleavage is induced by local yielding. Assuming that cleavage fractures are slip nucleated, several models have been suggested to describe the cleavage fracture mechanism.

Cottrell proposed a mechanism where two dislocations with Burger's vector of type $\frac{a}{2}\langle 1\,1\,1 \rangle$ interacted and formed a micro-crack with Burger's vector of type $a\langle 1\,1\,0 \rangle$. The final fracture condition of this model is given as[107]

$$\sigma_F \geq \frac{2\mu\gamma}{k_Y^s} d^{-\frac{1}{2}} \qquad (4.1.1)$$

where σ_F is the fracture stress

k_Y^s is the slope of the Hall-Petch Relationship

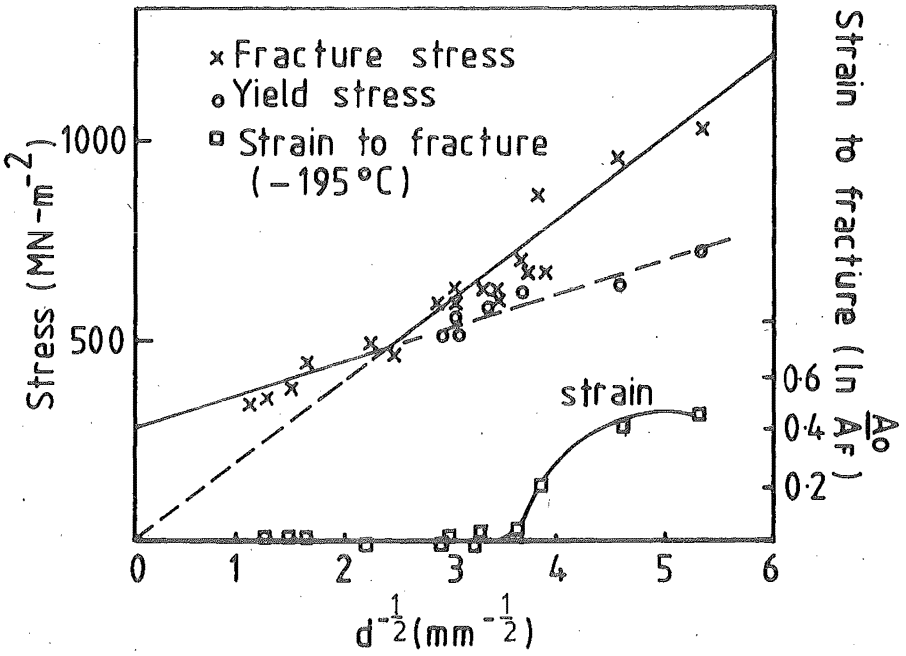

FIG 4·1 GRAIN SIZE DEPENDENCE OF THE YIELD AND FRACTURE STRESS OF A LOW CARBON STEEL AT -195 °C (Ref 106)

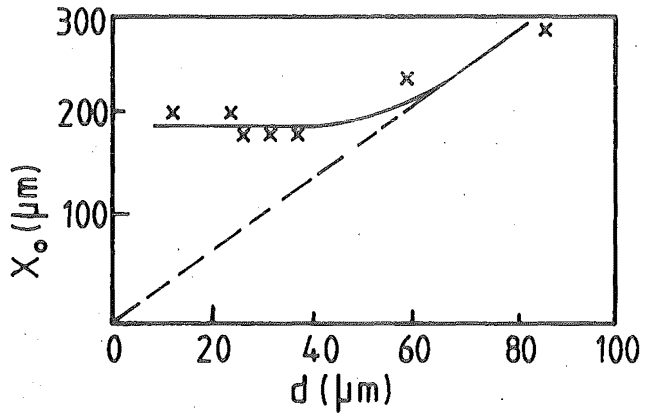

FIG 4·2 GRAIN SIZE DEPENDENCE OF THE "CHARACTERISTIC" DISTANCE OF A LOW ALLOY STEEL (Ref. 16)

μ is the shear modulus

d is the grain diameter

γ is the surface energy.

Thus, Cottrell's model relates the grain size, d, and the yield parameter, k_Y^S, to cleavage fracture stress, σ_F, and it appears to be a comprehensive model. However, McMahon and Cohen showed that Cottrell's model had omitted the effects of microstructural heterogeneities by showing that carbide size had a significant influence on the fracture mechanisms[108].

Smith proposed an alternative solution which incorporates the effects of carbide particles by modelling a situation where dislocations pile up against a grain boundary and initiate a crack nucleus at the adjacent grain boundary carbide[109]. Detailed consideration of energy changes enables the critical value of cleavage stress to be related to microstructural parameters by the equation

$$(\frac{C_o}{d})\sigma_F^2 + \tau_{eff}^2 \{ 1 + \frac{4}{\pi}(\frac{C_o}{d})^{\frac{1}{2}} \frac{\tau_i}{\tau_{eff}} \}^2 \geq \frac{4E\gamma_F}{\pi(1 - \nu^2)d} \qquad (4.1.2)$$

where E is the modulus of elasticity

τ_i is the lattice friction stress

τ_{eff} is the applied shear stress

γ_F is the effective surface energy of ferrite

C_o is the carbide thickness.

However, Evensen[110] pointed out that Smith's model could appear to contradict the experimentally observed grain size dependence of the cleavage fracture stress[76,104, 105, 106,111] by substituting τ_{eff} as

$$\tau_{eff} = \tau_Y - \tau_i = k_Y^s \, d^{-\frac{1}{2}} \qquad (4.1.3)$$

so that Equation (4.1.2) now becomes

$$C_o \sigma_F^2 + k_Y^{s\,2} \{ 1 + \frac{4\tau_i}{\pi k_Y^s} C_o^{\frac{1}{2}} \}^2 \geq \frac{4E\gamma_F}{\pi(1 - \nu^2)} \qquad (4.1.4)$$

This apparent conflict was partially resolved by Knott who suggested that the growth of both ferrite and grain boundary carbides is controlled by the same diffusion process so that the ratio $\frac{C_o}{d}$ will be approximately constant[112]. This suggestion was later verified by Curry and Knott[113] who showed that examination of the available experimental data in literature would reveal a general relationship between the ferrite grain size and the "largest observed" grain boundary carbide thickness.

A similar model was proposed by Almond et al who obtained the cleavage fracture stress as[114]

$$\sigma_F = \{ \frac{k_Y^2 d}{4C_o} + \frac{8\mu\gamma}{\pi(1 - \nu)C_o} \}^{\frac{1}{2}} - \frac{k d^{\frac{1}{2}}}{2C_o} \qquad (4.1.5)$$

The current popular model relating K_{IC} to σ_F assumes that the fracture stress is attained or exceeded over a "characteristic distance", X_o, ahead of the crack-tip when cleavage fracture occurs

so that[15, 16]

$$\sigma_F(2\pi X_o)^{\frac{1}{2}} \geq K_{IC} \qquad (4.1.6)$$

A graph of X_o versus d is shown in Figure 4.2[16]. The concepts of characteristic distance and the Smith's cleavage model were adopted to describe the critical fracture event at the crack-tip of coarse grain material (d > 40 μm) and it was found that X_o was of the order of 1 to 2 grain diameter in magnitude, but that X_o became grain-size independent for finer grain sizes (d < 40 μm)[16]. This conclusion is in contradiction with the later report that the K_{IC}-σ_F relationship shown in Equation (4.1.6) is applicable in a low strength steel of grain size ranging from 8.3 μm to 13 μm[17].

4.2 Ductile Fracture

In this section, the basic theories of microvoid coalescence will be reviewed before their application to COD testings are considered. As the general behaviour of ductile fracture involves the nucleation of microvoids around second phase particles and the subsequent growth of these voids to achieve final coalescence, the theoretical models describing ductile fracture usually consider the three different stages separately.

The nucleation process has been described separately by Argon et al[115] and Ashby[116] who both assumed interface decohesion as the void nucleating mechanism.

Argon's model suggests that the normal stress (σ_n) at the

interface between the parent matrix and the second phase particle must exceed a critical interface strength (σ_{if}) to facilitate void nucleation. Local work hardening is often necessary because σ_{if} usually exceeds σ_Y. Hence, it is possible to describe the nucleation condition in terms of critical macroscopic strain parameter ε_n.

Ashby's model suggests a dislocation mechanism that accounts for local work hardening and increase in flow stress at the second phase particle. The macroscopic nucleation strain is related to the interface tensile stress by considering the number of dislocation loops piling up against the particle.

However, cracking of second phase particles or inclusion has also commonly been observed to result in void formation. In such cases, the nucleation criterion could be described by the fibre loading model of Lindley, Oates and Richards[117].

The current popular models for the growth of voids at second phase particles include those of McClintok[118], Thomason[119], and Brown and Embury[19].

McClintok's model describes the effects of a hydrostatic stress field on the growth of an array of cylindrical voids. However, the model does not include a void coalescence mechanism. Instead, coalescence is assumed when the final void diameter attains the value of final intervoid spacing.

Thomason's model assumes the uniform deformation of the void arrays and the parent matrix until the attainment of local necking

condition in the intervoid ligaments. The condition for coalescence is expressed as a function of the interparticle spacing or the volume fraction of void particles.

The Brown-Embury model assumes that the voids elongate along the major strain axis. When the length of void attains the value of the average initial inter-particle spacing, unconstrained plastic flow along the planes of the maximum shear stress occurs, thus leading to coalescence and failure.

The common feature of these void-growth models is that they merely consider void coalescence in geometrical terms so that the growth strain is limited by the initial volume fraction of void particles. However, current evidence suggests that strain localisation occurs, especially in materials with low work hardening propensity, which results in lower ductility than those predicted by the geometrical models[120, 121].

The maximum COD of a material in a fracture toughness specimen is limited by the strain that can be sustained at the crack-tip. Consequently, the critical COD of ductile fracture is dependent on the initial notch root radius. This dependency has been shown to result in the existence of a constant ratio between the COD at crack-tip instability, δ_i, and the slot-width of the crack (usually taken as being equal to twice the notched root radius ρ), provided that a critical slot-width, s_c, is exceeded[18, 121]. Below s_c, the value of δ_i is constant. It has also been shown that when $s \geq s_c$, the constant ratio of $\frac{\delta_i}{s_c}$ may be defined as the

critical crack-tip strain usually known as the notched ductility ε_{fi}[22]. When ductile fracture is initiated ahead of a fatigue crack, similar value of ε_{fi} will have been attained over a critical length parameter (ℓ_f) of the material[18, 19], so that

$$\delta_i = \ell_f \times \varepsilon_{fi} \qquad (4.2.1)$$

The value of ℓ_f appears to be in good agreement with the initial MnS inclusion spacing[18].

However, evidence has also been presented by Sailor[20] who showed that the critical length parameter is dependent on the grain size for a range of steels with varying strengths. In this model, ℓ_f is related to the critical COD, δ_i, by the relationship:

$$\ln\left(\frac{\delta_i}{\ell_f}\right) = \bar{\varepsilon}_p \qquad (4.2.2)$$

where $\bar{\varepsilon}_p$ is the plastic strain at the physical crack-tip so that

$$\bar{\varepsilon}_p = 0.2\ \varepsilon_f \qquad (4.2.2.a)$$

where ε_f is the uniaxial tensile fracture strain.

Sailor showed that the critical length parameter of a ferritic steel was equivalent to twice the grain size.

CHAPTER FIVE

CONCEPT OF YIELD POINT

5.1 Yield Point Phenomena

In the tensile testing of non-ferrous metals or alloys, the typical load-extension curve usually shows a gradual transition from elastic to plastic deformation (Figure 5.1). In such cases, the terms "yielding", "yield-point" or "yield-stress" are often used to describe the onset of plastic deformation in the materials. It is now generally accepted that the 'yield-point' of these non-ferrous materials is better described by the stress required to produce a specific small strain e.g. 0.2%, and this is then referred to as the 0.2% proof stress for the material. In contrast, the load-extension curve for a low carbon steel displays a localised, heterogeneous transition from elastic to plastic deformation. (Figure 5.2). The load-extension curve follows an initial elastic relationship until a sudden drop in load signifies that the transition to plastic deformation has commenced. The stress corresponding to the abrupt decrease in load is termed the "upper yield stress" (σ_{UY}). Once the upper yield point is exceeded, the load extension plot then fluctuates about some approximately constant load value. The lowest stress value measured in this region is generally referred to as the "lower yield stress" (σ_{LY}), while the extension and the corresponding strain value occurring at this stress level is called the "yield point elongation" and the

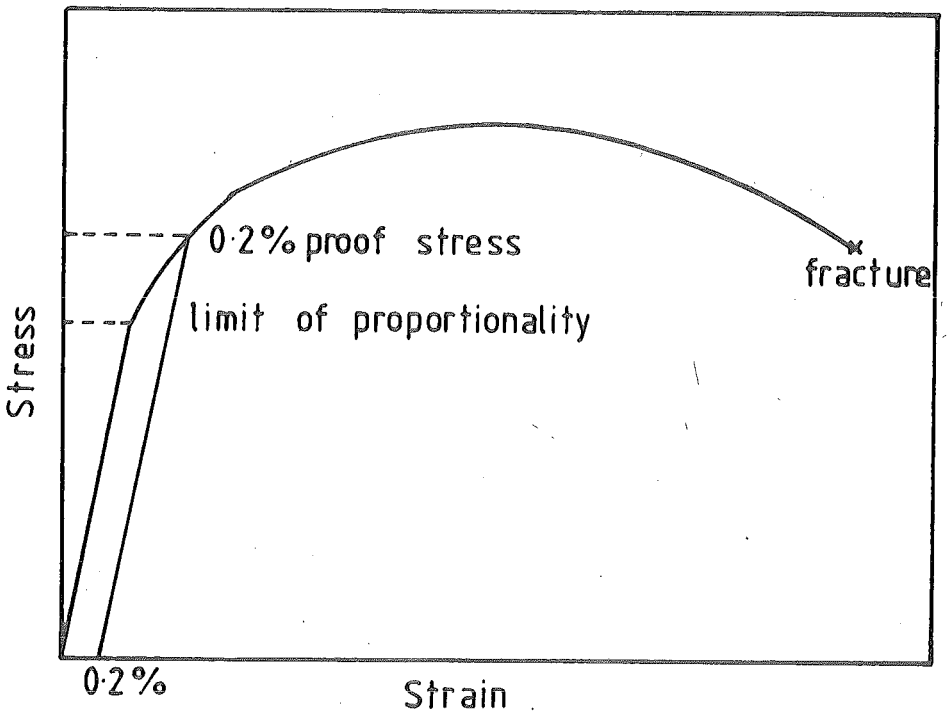

FIG 5·1 A TYPICAL STRESS-STRAIN CURVE FOR A NON-FERROUS METAL TESTED IN TENSION

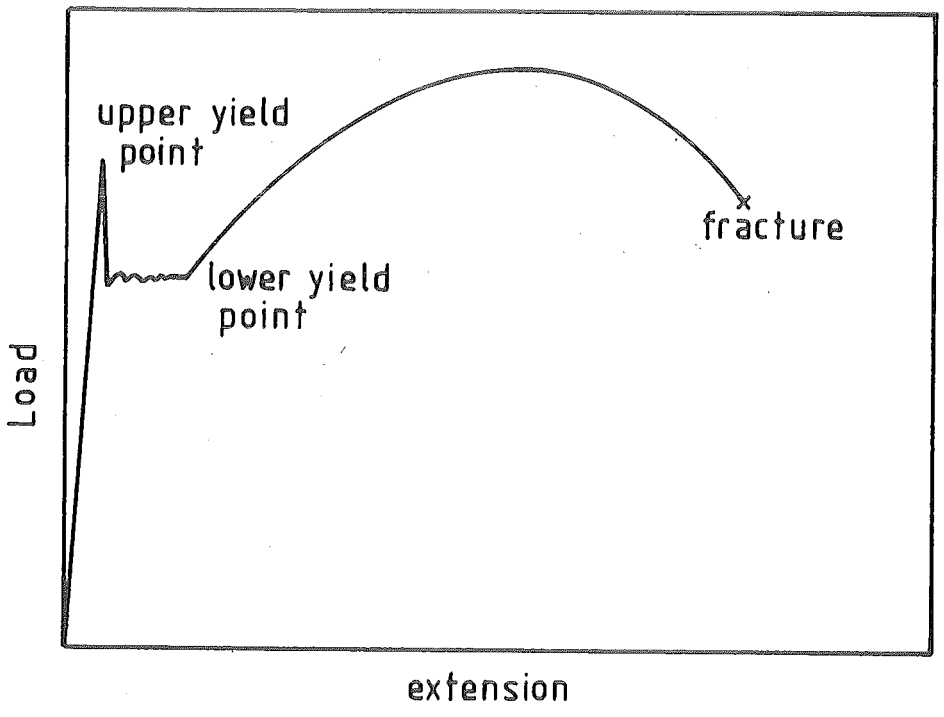

FIG 5·2 A TYPICAL LOAD EXTENSION CURVE FOR A LOW CARBON STEEL TESTED IN TENSION

"Luder strain" respectively. In this thesis, the term "yielding" and its related properties will generally refer to the discontinuous yielding of ferrous metals unless otherwise stated.

Macroscopically, the discontinuous yield point can be explained by the following mechanism.

At the upper yield point, a distinct band of plastically deformed metal appears at some points of stress concentration. This band is formed at approximately 45^{o} to the tensile axis and is known as a "Luder band". Subsequently, this region of plastic deformation propagates along the specimen gauge length, causing the yield point elongation. Several Luder bands are usually formed with the edge of each band acting as a further stress concentrator. As each plastically deformed band strain-hardens, further yielding and band propagation occurs until plastic deformation has spread along the full length of the test-piece. At this point, the test load increases again as the gauge length continues to elongate uniformly and normal strain hardening occurs.

The yield stress is affected by several factors such as the test machine stiffness, axiality of load application, strain rate and the geometry and surface finish of specimens[122].

5.2 Theoretical Models Of Yield Point

Currently, two theoretical models of yield point of low carbon steels are recognised. They are:

(i) the Cottrell-Bilby[123] model which attributes the cause of discontinuous yielding to unlocking of dislocations;

(ii) the more recent model of Hahn[124] which suggests that the mechanism responsible for discontinuous yielding is mobile dislocation nucleation at grain boundaries and points of stress concentration and their subsequent multiplication.

5.2.1 The Cottrell-Bilby Theoretical Model[123]

It has been well established that discontinuous yielding in mild steel is critically dependent on the quantity of interstitial carbon and nitrogen. The initial theoretical model of yielding proposed that an individual grain of ferrite matrix was surrounded by a thin film of cementite[125]. The cementite film restricted the deformation of the ferrite until the upper yield stress was reached. At this stress, the cementite film collapsed and the nucleus of a Luder's band spread across the specimen.

This theory was later replaced by the Cottrell-Bilby model[123]. This theory postulates that yielding occurs by the unpinning of dislocations from the interstitial atoms in solid solution with the ferrite matrix. These interstitials had earlier segregated to and locked the dislocations. In the ferrite matrix, the carbon and nitrogen interstitial atoms are located in interstitial sites which are too small and hence cause lattice strain. This strain energy can be relieved by the migration of the interstitial atoms to the

tensile region of edge dislocations where the lattice is itself dilated. Cottrell and Bilby estimated that a concentration of approximately 10^{-6} wt.% carbon was sufficient to place one carbon atom on each dislocation per atom plane, assuming the normally accepted dislocation density of 10^{8} line-cm^{-2} in annealed ferrite. This led to the inference of a binding energy of about 0.5 eV per atom plane. This energy level has to be overcome by the applied strain, assisted by the thermal activation energy, before yielding can occur. Later measurements by internal friction or by electrical resistivity techniques revealed that the number of atoms per dislocation plane was large, usually exceeding $10^{(126)}$. Consequently, it was suggested that the upper yield point corresponded to the stress level at which dislocations broke away from their "atmosphere" of interstitial atoms, multiply, and thus forming the first Luder's band.

The Lower Yield Stress was consequently defined as the stress required for the propagation of Luder bands along the specimen. If, on a microscopic scale, these dislocations pile up against a grain boundary, a large concentration of stress is produced in the nearby regions of the adjacent grain. A force of $(\tau - \tau_i)$ may be considered to have been transferred from a blocked slip band of length ℓ to the adjacent grain,

where τ is the applied shear stress

τ_i is the friction stress which opposes the glide of a dislocation in the slip band

By analogy between a slip band and a crack, linear elastic theory may be used to show that the stress at a distance r ahead of the blocked slip band is elevated to $\tau(\frac{\ell}{4r})^{\frac{1}{2}}$. Thus, assuming the existence of τ_c - the critical shear stress value required to create dislocations from the locked source, and taking r as the average distance between the end of the blocked slip band and the nearest locked dislocation sources in the adjacent grain, the elevated stress caused by the dislocation pile-up gives rise to yielding in the adjacent grain when

$$\tau_c = (\tau - \tau_i) (\frac{\ell}{4r})^{\frac{1}{2}} \qquad (5.2.1)$$

If $\ell = A_i' d$,

where d is the mean grain diameter

A_i' is a constant,

then Equation (5.2.1) can be written as

$$\tau_c = (\tau - \tau_i) (\frac{A_i' d}{4r})^{\frac{1}{2}} \qquad (5.2.2)$$

By assuming that the applied shear stress is equal to the lower yield stress, and converting all shear stresses to their corresponding tensile stresses, Equation (5.2.2) can be written as

$$\sigma_c = (\sigma_Y - \sigma_i) (\frac{A_i' d}{4r})^{\frac{1}{2}} \qquad (5.2.3)$$

or $$\sigma_Y = \sigma_i + k_Y d^{-\frac{1}{2}} \qquad (5.2.4)$$

where $$k_Y = 2\sigma_c (\frac{r}{A_i'})^{\frac{1}{2}} \qquad (5.2.4.a)$$

Equation (5.2.4) is generally known as the Hall-Petch equation where σ_i and k_y are material constants[127].

5.2.2 The Hahn Theoretical Model[124]

Later experimental work revealed that except for lightly aged steels ageing caused the value of k_y to increase to a saturation value k_y^o, which was independent of continual solute segregation and changes in test temperature[128]. This observation implied that dislocations were strongly locked by Fe_3C and Fe_4N, and that mobile dislocations were not generated by unpinning. Hence, it was postulated that it was possible that new dislocations were nucleated from sources in grain boundaries.

If yielding were dependent on the generation of new dislocations, which multiplied rapidly under the applied stress, it is possible to assume that the new dislocations can continue to move at a lower stress. This led to the theory by Hahn which analysed the yield point behaviour of iron and related b.c.c. metals[124]. Hahn assumed that most of the original dislocations remained locked by their precipitates, and that the dislocations responsible for slip were heterogeneously nucleated and multiplied rapidly. The abrupt yield drop was then considered to be a consequence of rapid multiplication of dislocations and the stress dependence of dislocation velocity.

In this model, the strain rate imposed by the machine $\dot{\varepsilon}$ must be matched by the elastic ($\dot{\varepsilon}_e$) and plastic ($\dot{\varepsilon}_p$) strain rate so that

$$\dot{\varepsilon} = \dot{\varepsilon}_e + \dot{\varepsilon}_p \qquad (5.2.5)$$

The elastic strain rate may be described in terms of the stress σ, and the modulus M_t, descriptive of the net elastic response of the test specimen, grips and the test machine, so that

$$\dot{\varepsilon}_e = \frac{1}{M_t} \frac{d\sigma}{dt} \tag{5.2.6}$$

The plastic strain rate may be expressed in terms of the Burger's vector b, the dislocation density ρ', and the average velocity of dislocations v, so that

$$\dot{\varepsilon}_p = 0.5\ b(f\rho')v \tag{5.2.7}$$

where f is a constant

0.5 b is the contribution of a single dislocation of unit length and unit velocity moving in a direction close to the maximum resolved shear stress

Studies[124] had shown that dislocation multiplication and straining may be described by a parabolic relationship of the form

$$\rho' = \rho'_o + R(\varepsilon_p)^h \tag{5.2.8}$$

where R and h are constants

ρ'_o is the average density of unlocked dislocations, i.e. those dislocations nucleated heterogeneously at inclusions or other discontinuities below the nominal stress level associated with significant dislocation mobility.

The stress dependence of dislocation velocity may be expressed as

$$v = \left(\frac{\tau}{\tau_o}\right)^{p_1} \tag{5.2.9}$$

where τ is the resolved shear stress and is approximately equal to $\frac{\sigma}{2}$

τ_o is the resolved shear stress corresponding to limit velocity

p_1 is a temperature dependent constant

If $\Delta\sigma$ is the stress increment required to maintain a given dislocation velocity, and if a simple linear hardening law is assumed so that

$$\Delta\sigma = m\varepsilon_p \tag{5.2.10}$$

It can be shown that

$$v = (2\tau_o)^{-p_1} (\sigma - m\varepsilon_p)^{p_1} \tag{5.2.11}$$

By combining Equations (5.2.5), (5.2.6), (5.2.7), (5.2.8) and (5.2.11), an expression relating flow stress, plastic strain and strain rate may be obtained as

$$\dot{\varepsilon} = \frac{1}{M_t}\frac{d\sigma}{dt} + 0.5\ bf(\rho'_o + R\varepsilon_p^{\ h})\ (2\tau_o)^{-p_1}\ (\sigma - m\varepsilon_p)^{p_1} \tag{5.2.12}$$

By neglecting the elastic contribution, Equation (5.2.12) may be reduced to

$$\sigma = m\varepsilon_p + 2\tau_o \left\{ \frac{\dot{\varepsilon}}{0.5\, bf(\rho'_o + R\varepsilon_p^{h})} \right\}^{\frac{1}{p_1}} \qquad (5.2.13)$$

Equation (5.2.13) thus describes a model which is totally rigid-plastic with an initial finite yield stress dictated by ρ'_o and $\dot{\varepsilon}$.

5.3 Summary

It is now possible to conclude that abrupt yield will occur in an ordinary cubic structured metal if:

(i) the initial number of mobile dislocations is low, and either

(ii) the grain boundaries are effective barriers to mobile dislocations, or

(iii) the internal stress opposing dislocation motion is sensitive to dislocation velocity.

Annealed polycrystalline low carbon steels normally satisfy all three of the above requirements. Consequently, it is obvious that the two models are complementary in the description of yield point behaviour.

CHAPTER SIX

STATIC STRAIN AGEING

6.1 General Characteristics Of Strain Ageing

When a low carbon steel specimen (in annealed, as-rolled or normalised state) is strained to a point A in the strain-hardening region (Figure 6.1), unloaded, and then retested immediately, the steel will deform approximately elastically up to the previous applied load at A, and will then continue to deform plastically with strain-hardening (curve a) as if the test has not been interrupted. The steel now behaves in a similar manner to any other metal where the dislocations are not pinned by atmosphere or precipitates.

However, if the same specimen is allowed to 'age' either at ambient or elevated temperature after it has been unloaded at point A before retesting in tension, the yield point returns at a higher stress (point B in curve b) than the flow stress at A of the non-aged steel. The steel is now said to have "strain aged". The return of the yield point after strain ageing is also accompanied by an increase in the tensile strength and a reduction in ductility. Other properties affected by strain ageing include the fracture toughness, fatigue strength, and the magnetic and electrical properties; these have been reviewed extensively by Baird[129]. Furthermore, during deformation of a mild steel specimen tested at temperatures around 150°C to 250°C, dynamic strain ageing

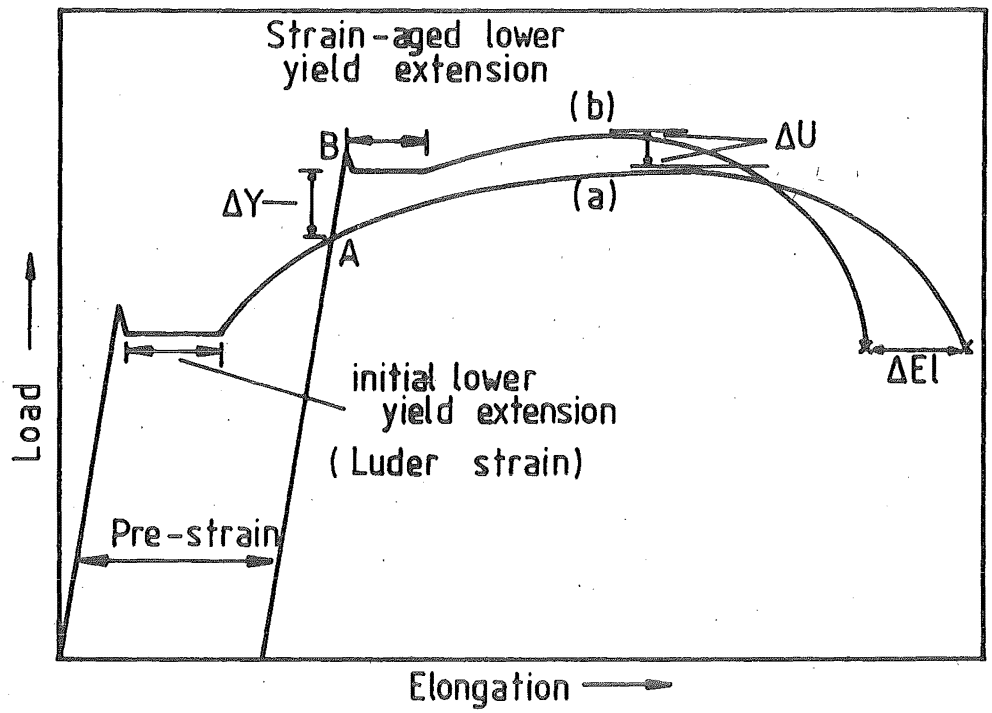

FIG 6·1 LOAD-ELONGATION CURVE FOR LOW-CARBON STEEL, STRAINED TO POINT A, UNLOADED AND THEN RESTRAINED IMMEDIATELY (curve a) AND RESTRAINED AFTER AGEING (curve b)

ΔY AND ΔU ARE CALCULATED ON ORIGINAL AREA

occurs. (See Chapter Nine.)

6.2 Mechanisms Of Strain Ageing

Strain ageing is effected by the segregation of interstitial atoms to the new dislocation sites formed by straining. Observations on the variation of tensile properties (Figure 6.2) have led to the postulation of a two-stage strain ageing process[130].

During the first stage, the interstitial solute atoms are assumed to migrate to the dislocation sites to form Cottrell's atmospheres and hence the magnitude of discontinuous yield is related to the density of these atmospheres. Yielding at this stage appears to be caused by the unpinning of these dislocations. Consequently, this stage only affects the Upper and Lower yield points and the Luder strain. The strain-hardening part of the stress-strain curve remains unaltered because straining beyond the Luder strain causes the dispersion of the Cottrell's atmosphere. If the interstitial solute content is very low, only this first stage of ageing can be observed. (Figure 6.3)

During the second stage, it is postulated that precipitates are formed by the continual segregation of interstitials to dislocation sites[130]. Since the dislocations were fully locked at the end of Stage I, the locking contribution is now not significantly increased and so the Luder strain is not affected during the second stage. However, the formation of precipitates raises the general level of the basic curve, and so raises the Lower Yield Stress and

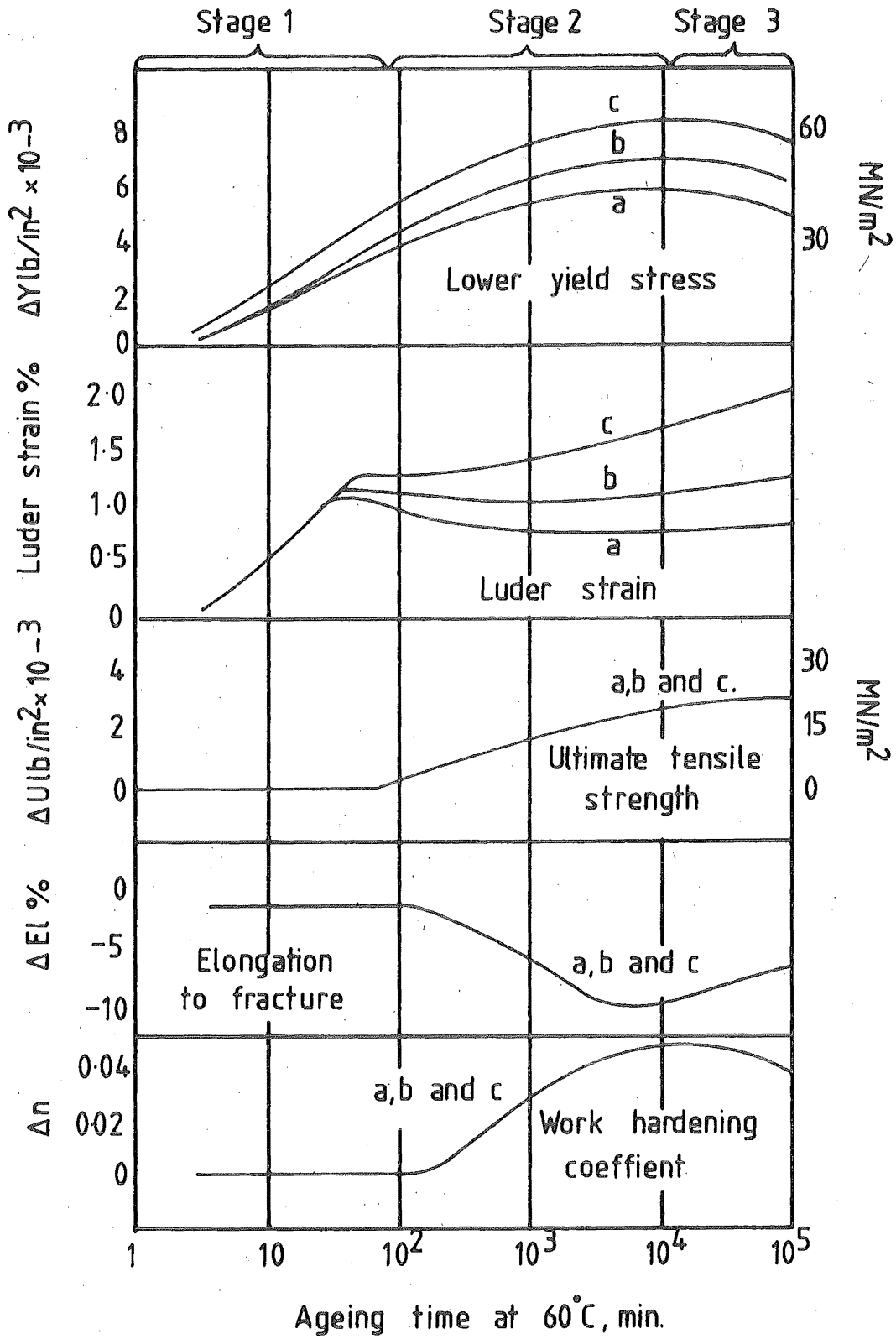

FIG 6·2 EFFECT OF AGEING TIME ON CHANGES IN TENSILE PROPERTIES DUE TO STRAIN AGEING (PRE-STRAIN 4%) IN LOW CARBON RIMMED STEELS HAVING GRAIN SIZES (GRAIN/mm²) OF (a) 50 (b) 195 (c) 1850 (Ref 130)

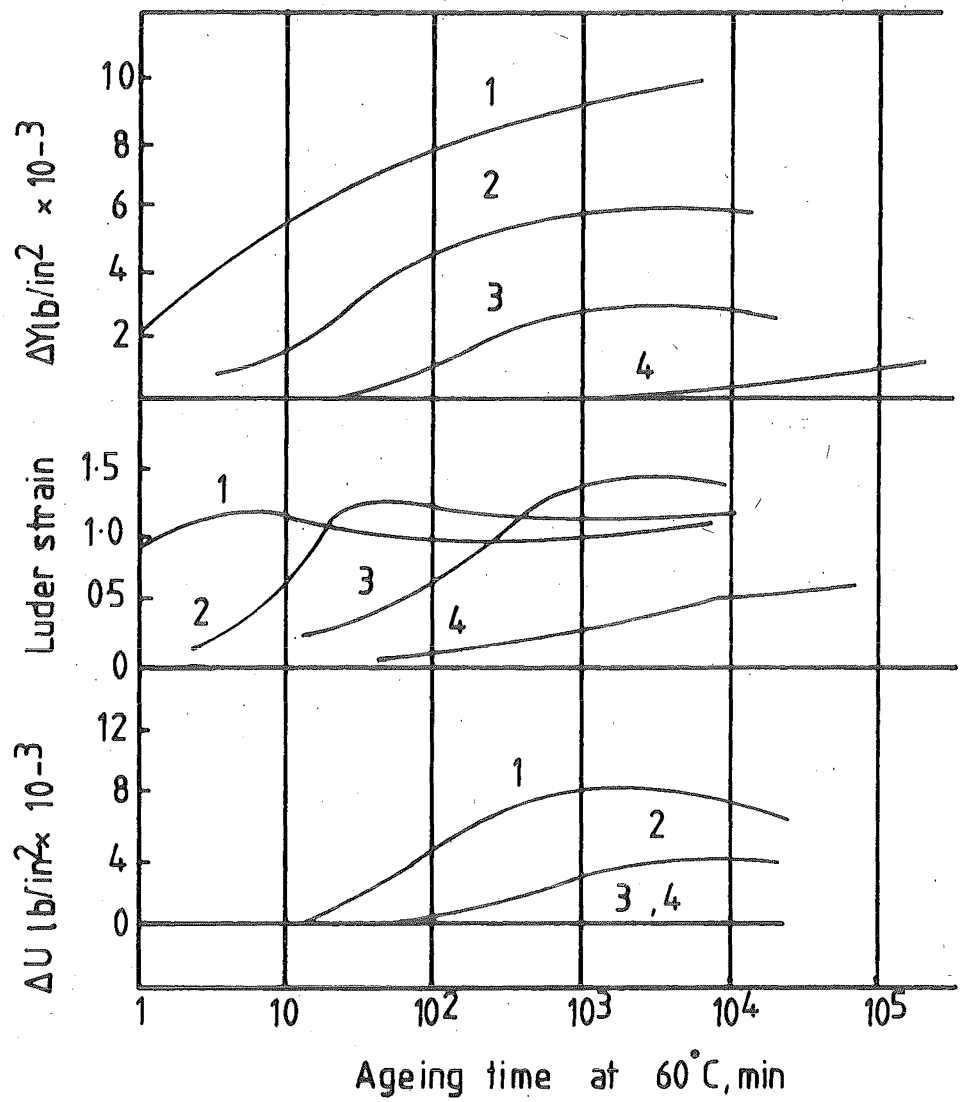

FIG 6-3 EFFECT OF INTERSTITIAL SOLUTE CONTENT ON CHANGES IN TENSILE PROPERTIES DUE TO STRAIN AGEING (PRE-STRAIN 4%) IN LOW-CARBON RIMMED STEEL INTERSTITIAL SOLUTE CONTENTS (1) 0·014% (2) 0·0022% (3) 0·0005% (4) 0·0002% (Ref 130)

the tensile strength. The corresponding increase in work hardening rate causes a reduction in the elongation at fracture (Figure 6.2). This stage is observed in most low carbon steels except those with extremely low interstitial solute contents (Figure 6.3). In his review on the kinetics of strain ageing, Baird[129] reported that Bullough and Newman's assumptions, namely,

" (i) that rod-like precipitate particles are formed along the dislocation cores, stabilised by a combination of chemical binding within the particles and elastic interaction within the dislocation strain field,

(ii) that the rate of transfer of solute across the interface into these precipitates becomes slower as segregation proceeds. "

could be used to obtain the Harper Equation which models the observed kinetics of strain ageing. The Bullough-Newman postulation of special precipitate formation has since been supported by the observation[131] that precipitates formed during the early stage of the second phase of strain ageing did not redissolve as readily as the precipitates formed by quench ageing on reheating. This observation implied that the former had a higher bonding strength.

Possibly in the later stage of strain ageing, further formation of discrete precipitates of carbides and/or nitrides on dislocation continued. On long ageing time and especially at high temperature,

these precipitates may coarsen and thus cause overageing as observed by Wilson and Russel[130] (Figure 6.2). Overageing causes a small decrease in tensile strength and yield stress, and a small rise in elongation at fracture.

6.3 Effects Of Ageing Temperature

Currently, there is considerable evidence that strain ageing of a low carbon steel at temperatures below 100°C is different in character from strain ageing above this temperature[129]. It has been known that ageing of a low carbon steel at lower temperatures is predominantly due to interstitial nitrogen. This postulation has been supported by the fact that when the nitrogen is combined with strong nitride formers, the steel displays negligible strain ageing effects when aged at temperatures below 100°C to 150°C[129, 132]. Above this temperature, some ageing is observed even in steels containing strong nitride formers[129], and is brought about by carbon.

The equation relating strain ageing at different temperatures has been derived as[133]:

$$\log_{10}\left(\frac{t_r}{t}\right) = A_H\left(\frac{1}{T_r} - \frac{1}{T}\right) - \log_{10}\left(\frac{T}{T_r}\right) \qquad (6.3.1)$$

where A_H is a constant

t_r is the ageing time at ambient temperature T_r in deg. K

t is the ageing time at elevated temperature T in deg. K.

The values of A_H have been shown to be 4400 for the diffusion of carbon atoms and 4000 for the diffusion of nitrogen[133]. These are very nearly similar values of A_H and suggest that the diffusion rate of carbon and nitrogen interstitials to dislocations should be nearly equal, which contradicts the experimental observation[129, 130]. Hence, the rate of diffusion does not satisfactorily explain the observed preference for nitrogen dislocation locking at low ageing temperature. However, the maximum solubility of nitrogen in ferrite is higher than that of carbon (Figure 6.4). Furthermore, the equilibrium solubility temperature of iron nitrides Fe_4N and $Fe_{16}N_2$ is lower and these precipitates consequently have lower stability than iron carbides[129]. The resolution of iron nitride therefore occurs more readily at lower ageing temperatures, thus providing a ready supply of interstitial nitrogen for dislocation locking.

From observations of the maximum solubility data of carbon in ferrite and also the greater stability of carbide precipitates (compared to iron nitrides), it may be deduced that carbon strain ageing in slowly cooled steels is negligible at temperatures below $100^{o}C$. This deduction has been supported by experimental observations[134]. There is now considerable evidence that sufficient resolution of iron carbides occurs in normally cooled steels at temperatures of $150^{o}C$ and above to cause appreciable strain ageing by carbon dislocation locking[135, 136]. However, carbon strain ageing may still occur at temperatures below $150^{o}C$ if the steel is

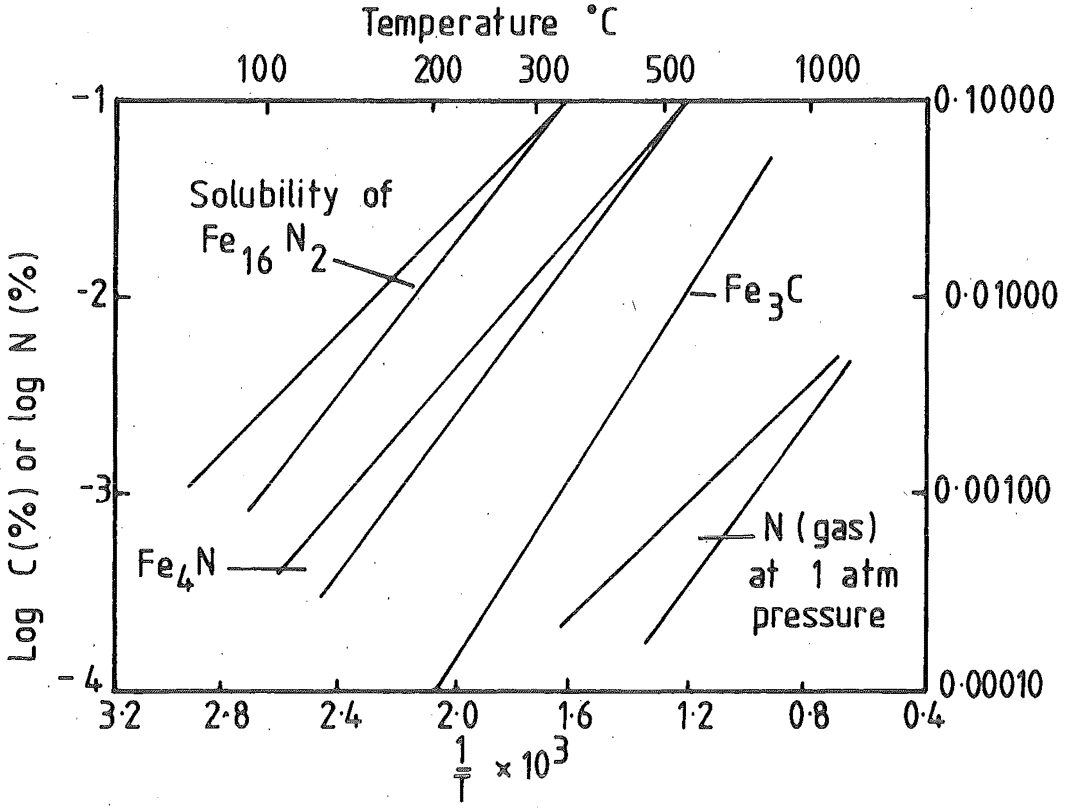

FIG 6·4 SOLUBILITIES OF NITROGEN AND CARBON IN IRON (Ref129)

super-saturated by rapid cooling from the austenite range.

6.4 Effect Of Strain Ageing On Tensile Properties

Tensile properties of low carbon steels have been observed to vary in two distinct stages on strain ageing.

(i) the first stage when dislocation locking is by "Cottrell atmosphere" during which only the yield point properties are affected;

(ii) the second stage when precipitation locking of dislocations occurs and ageing affects the Lower Yield Stress, tensile strength and elongation at fracture.

The effects of strain ageing on the grain-size dependency of yield properties as described by the Hall-Petch Equation (5.2.4) where

$$\sigma_Y = \sigma_i + k_Y d^{-\frac{1}{2}}$$

has been investigated[130]. Results (Figure 6.5) revealed that k_Y increased during the first stage of ageing while σ_i remained unchanged. On subsequent full ageing, σ_i increased but k_Y remained constant. These observations can be explained by the then favoured Cottrell-Bilby theory on yielding. The values of k_Y for the strain-aged state were also reported to be lower than the initial values of the annealed state. This was explained by the postulation that the

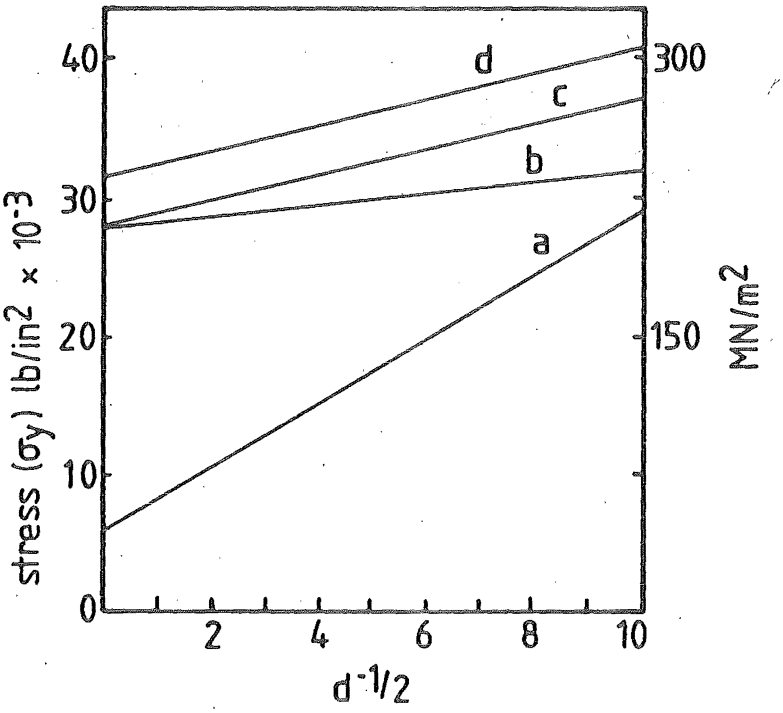

FIG.6.5. EFFECT OF STRAIN AGEING IN A LOW-CARBON STEEL ON THE RELATIONSHIP BETWEEN THE LOWER YIELD STRESS (σ_y) and $d^{-\frac{1}{2}}$; where 2d IS THE MEAN GRAIN DIAMETER.

(a) ANNEALED STEEL;

(b) STRAINED 4%;

(c) STRAINED 4% AND AGED TO THE END OF STAGE 1;

(d) STRAINED 4% AND FULLY AGED (10^4min. at 60°C).

(REF. 130)

values of r in Equation (5.2.4.a) are lower in the strain-aged state.

Later work by Wilson showed that[137]:

(a) The first stage of strain ageing is due to atmosphere locking of dislocations. The yield point behaviour during this stage is consistent with the Cottrell-Bilby theory on yielding, which suggests that mobile dislocations are generated at the yield-front by the unpinning process. Thus, for constant grain size, the increase in yield strength $\Delta\sigma_Y$ during this stage is dependent on k_Y, which in turn is close to being proportional to the dislocation atmosphere density.

(b) At the end of the first stage of ageing, continued solute segregation experienced a sudden drop in its effectiveness in raising the yield strength. At the same time, the Luder strain and k_Y became insensitive to continued solute segregation to dislocations. Yielding by unpinning is unlikely after the end of the first stage. Mobile dislocations are probably now being nucleated at grain boundaries, as suggested by Leslie and Keh[138]. The mobile dislocation nucleation process is similar to that of the annealed steel. However, an anomaly in the values of k_Y was observed during the second stage of ageing because

$$k_{Y_{aged}} \simeq 0.65\, k_{Y_{annealed}} \qquad (6.4.1)$$

This had been explained by assuming that pre-straining causes a reduction in the average local stress, σ_c , required to nucleate dislocations from grain boundaries. It was further suggested that the slow rise of k_Y to the saturation value of $k_{Y_{annealed}}$ on continued ageing may be caused by the long range diffusion of solute atoms from grain interiors to the "damaged" grain boundaries.

6.5 Effects Of Strain Ageing On Fracture Toughness

The effects of strain ageing on fracture toughness parameters such as K_{IC} , J_{IC} and COD are currently scarce due to the lack of systematic investigations. However, information on the transition temperatures obtained by the traditional notched bar impact tests has been widely employed to illustrate the qualitative effects of strain ageing on fracture resistance. Currently, the shift in the transition temperature has been accepted as a measure of the severity of embrittlement caused by strain ageing. Strain age embrittlement has been observed to be dependent on the amount of pre-strain and on the time and the temperature of the ageing treatment[139, 140, 141]. Assuming fully aged conditions were attained by artificially ageing at 100^{o}C for three hours, the shift in transition temperature was shown by Pussegoda and Erasmus to be dependent on the degree of pre-strain (see Figure 6.6.a)[141]. The shift

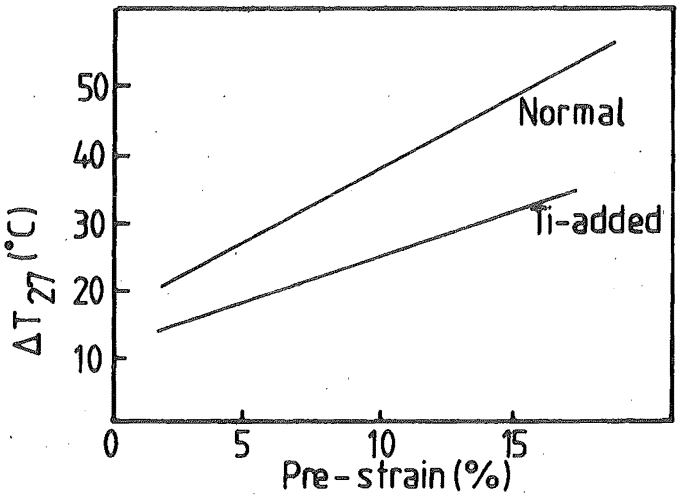

FIG 6·6a EFFECT OF PRE-STRAIN ON THE INCREASE IN THE CHARPY 27 JOULE IMPACT-TRANSITION TEMPERATURE (ΔT_{27}) DUE TO STRAIN AGEING IN NORMAL AND Ti-added GRADE 275 STEELS (Ref 141)

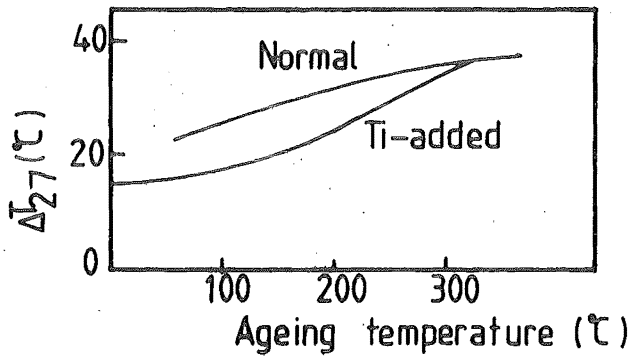

FIG 6·6b EFFECT OF AGEING TEMPERATURE ON THE INCREASE IN THE CHARPY 27 JOULE IMPACT TRANSITION TEMPERATURE (ΔT_{27}) DUE TO STRAIN AGEING IN THE NORMAL AND Ti-added GRADE 275 STEELS (Ref 141)

in the transition temperature of specimens that were pre-strained by 5% and soaked at temperature for one hour was also shown to be dependent on the ageing temperature (see Figure 6.6.b)[141]. These results also show that strain age embrittlement is sensitive to the free nitrogen content and that embrittlement can be alleviated by the addition of suitable nitride-forming elements such as titanium.

The theoretical analysis of the impact energy curve is still not well understood although Cottrell has derived an expression predicting that the transition from brittle to ductile fracture in a notched bar will occur when[142]

$$(\sigma_i d^{\frac{1}{2}} + k_Y)k_Y = A_3\mu\gamma \qquad (6.5.1)$$

where A_3 is the reciprocal of the stress intensification factor,

σ_i and k_Y are obtained from the Hall-Petch Equation of

$$\sigma_Y = \sigma_i + k_Y d^{-\frac{1}{2}}$$

Expressions for transition temperature have also been derived by Petch as[143]

$$A_4 T_c = \sigma_i^* + C - (\frac{4\beta\mu\gamma}{k} - k)d^{-\frac{1}{2}} \qquad (6.5.2)$$

where (i) σ_i^* is the temperature independent friction stress given by

$$\sigma_i = \sigma_i^* + C - A_5 T \qquad (6.5.2.a)$$

where A_5 is a constant

(ii) A_4 , C are constants

(iii) k is given by

$$\sigma_f = \sigma_{i,f} + kd^{-\frac{1}{2}} \qquad (6.5.2.b)$$

where σ_f is the flow stress at fracture and

$\sigma_{i,f}$ is the friction stress at fracture

(iv) μ is the shear modulus

and by Erasmus as[144]:

$$A_6 T_c = \sigma_i^* + C - \left(\frac{\beta\mu\gamma}{k_y} - k_y\right) d^{-\frac{1}{2}} \qquad (6.5.3)$$

where A_6 is a constant

The applicability of Cottrell's theory for fracture transition as expressed by Equation (6.5.1) has been investigated by Baird[129] using the results of Wilson and Russel[130]. By evaluating the left hand side of Equation (6.5.1), Baird found that its value was highest in the annealed state and lowest in the strained state, while ageing caused an increase from the lowest value. Assuming that the surface energy γ does not alter significantly during straining and subsequent ageing, Baird's evaluation of Equation (6.5.1) implied that the transition temperature should decrease after pre-straining and then increase during ageing but would not exceed the transition temperature of the annealed state. This conclusion is contrary to experimental observations of increase in the transition temperature after straining and a further increase during subsequent ageing[129, 139] (see Figure 6.7).

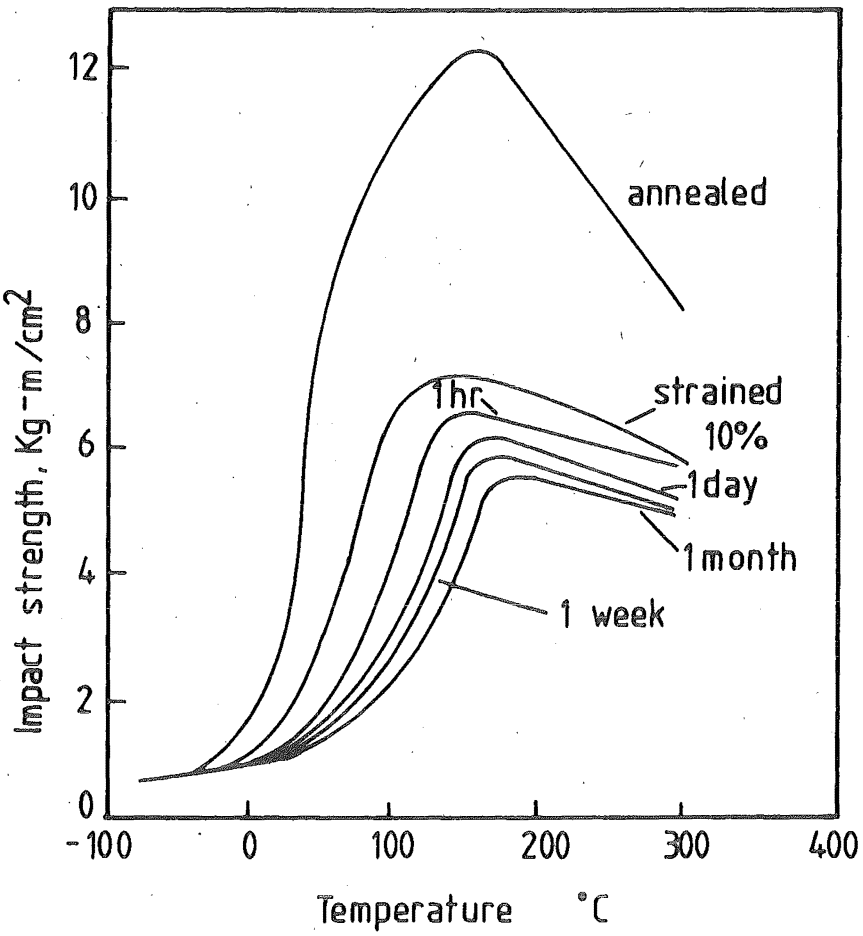

FIG 6·7 EFFECT OF STRAIN AGEING IN A BASIC BESSEMER STEEL ON THE IMPACT TRANSITION CURVE (PRE-STRAINED 10 % AND AGED AT 60°C) (Ref129)

It has been suggested that the value of γ may vary according to the expression[145]:

$$\gamma = A_7 k_y^{-q} \qquad (6.5.4)$$

where A_7 is a constant

q is a constant of value between 1 and 2

By substituting for γ as expressed above, Cottrell's criteria for fracture transition is even less compatible with the observed transition temperature increase on pre-straining although agreement on subsequent ageing may be improved.

Thus, even with the abundance of information on strain age embrittlement effects, the existing theories of fracture are still inadequate in elucidating the observed pattern of transition temperature changes. Discrepancy between theory and experimental data could have many sources. These may include:

(i) the empirical nature of impact testing methods,

(ii) the fracture theory of Cottrell does not account for the effects of second phase particles,

(iii) the behaviour of γ is not sufficiently understood,

(iv) the possibility of error[146] in using the equation[142]

$$\sigma_Y - \sigma_i = \frac{2na\mu}{l} \qquad (6.5.5)$$

to determine the number of pile-up dislocations necessary for the nucleation of the micro-crack in

the derivation of Equation (6.5.1).

The effect of strain ageing on the quasi-static fracture toughness obtained by the notched bend test was investigated by Burdekin[28]. The pre-strain treatment consisted of firstly bending the notched specimen to open the root of the notch by 0.15 mm and then closing it again with a reverse bend to the original dimension. This was followed by an artificial ageing treatment of soaking at 250°C for 30 minutes. Burdekin found that this strain age embrittlement treatment of the notch-tip area produced a dramatic effect on the fracture crack opening displacement (see Figure 6.8).

6.6 Control Of Strain Ageing In Steels

Since strain-ageing in steels is caused by the locking of mobile dislocations by interstitial carbon and nitrogen atoms, the reduction of strain ageing to tolerable levels obviously involves the reduction or the immobilisation of these intertitials. Currently, the popular methods of eliminating or reducing strain ageing include:

(a) Annealing in suitable gas mixtures to reduce the carbon and/or nitrogen contents. Moist hydrogen treatment removes both carbon and nitrogen but the resulting non-ageing steel has poor strength[147]. In contrast, dry hydrogen annealing removes only nitrogen and has little detrimental effect on the steel's strength[148].

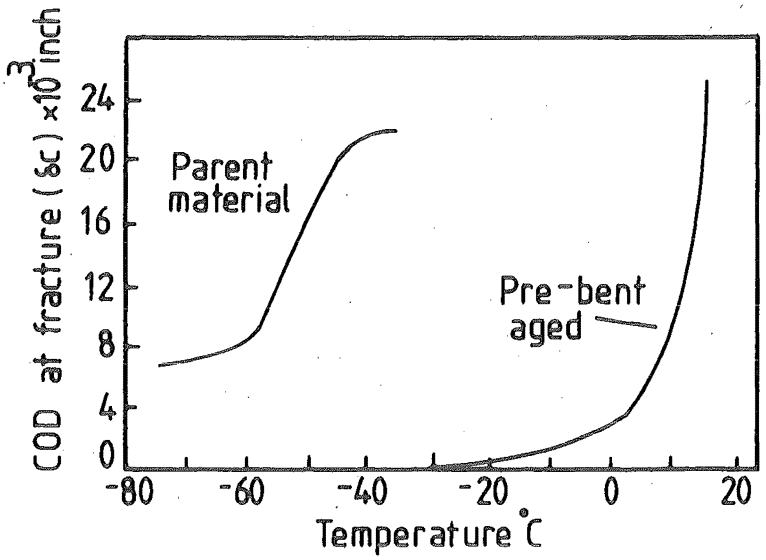

FIG 6·8 EFFECT OF STATIC STRAIN AGEING ON THE COD OF 3 IN. THICK NOTCHED BEND STEEL SPECIMENS (Ref 28)

(b) Reducing the concentration of "free" nitrogen with the use of suitable alloying elements combined with heat treatments to form the appropriate alloy nitrides. Vanadium is generally used as a nitriding element for rimmed steels whereas, boron, aluminium and titanium may be used in deoxidised steels.

(c) Refrigerating at cryogenic temperatures to retard the diffusion of interstitials. This method is obviously a temporary measure for short storage times and it has little commercial application.

(d) Manufacture of very low nitrogen steels by

(i) Vacuum degassing.

(ii) The L/D (Linz-Donawitz) Process[149].

6.7 Summary

The phenomenon of strain ageing of low carbon steels can now be explained as a two-stage process. The initial stage involves the locking of dislocations by Cottrell's atmosphere of nitrogen and carbon interstitials while the formation of "rod-like" precipitates on dislocations dominates the second stage. The theoretical analysis of the kinetics of strain ageing in steels have been reviewed extensively and the theories appear to describe the two stage mechanism adequately[129].

The effects of strain ageing on tensile properties and the impact fracture toughness of low carbon steels have been documented.

The theoretical treatments on the variations of various tensile properties are well established and appear to show good agreement with experimental evidence. However, the embrittlement effects, although widely recorded and acknowledged, still lack adequate theoretical explanations.

Overageing which occurred after long ageing time with the consequent "softening" of tensile properties has been reported. However, the fracture resistance does not display a similar tendency to "recover" after long ageing time[139].

Commercially, reduction of strain ageing of steels can be effected by annealing in dry hydrogen or by the manufacture of low nitrogen steel. The common alloying elements include chromium, vanadium, aluminium, boron and titanium.

CHAPTER SEVEN

EXPERIMENTAL PROCEDURES

In this chapter, the objectives and the experimental procedures for determining the fracture toughness of three low carbon steels will be presented; and unless otherwise stated, the results and the related discussions of this series of experiments will be presented in Chapter Eight.

The different experimental techniques used in this series of experiments are listed as follows:-

(i) The ASTM K_{IC} test for determining the fracture toughness at -196^{o} C.

(ii) The COD test for determining the minimum thickness of valid plane strain fracture toughness measurement.

(iii) The Crack Opening Displacement (COD) test for determining the temperature dependence of fracture toughness in the vicinity of the fracture mode transition temperature.

(iv) The Notched Ductility test.

(v) The Charpy V-notched impact test.

(vi) Optical and scanning electron microscope examination of the structure, fracture surface topography and the fatigue crack-tip plastic zone.

7.1 Experimental Objectives And The Preparation Of Steels

Three low carbon steels were selected for this series of experimental investigations and their chemical compositions are given in Table 7.1. The preparation of these steels and their experimental objectives are described as follows:-

(a) Steel A

This steel was supplied by Pacific Steel Ltd of Auckland, New Zealand. The raw stock was supplied as a 3 m long, 102 mm x 102 mm cross-section billet. The experimental objectives of this steel are summarised as follows:-

(i) To ascertain the effect of temperature on fracture toughness

(ii) To establish the influence of grain refinement caused by AlN precipitation[150, 151] on fracture toughness to assess AlN precipitation as a nitrogen reduction method

(iii) To ascertain the effects of strain ageing of the inherent crack-tip plastic zone on fracture toughness by testing the steel in the as-rolled and low active nitrogen conditions

(iv) To investigate the size criterion for the measurement of size independent "plane strain" fracture toughness by the COD method

Element	Steel A (Billet Steel)	Steel C (Pressure Vessel Steel)	Steel B (Grade 275 Steels)	
			Normal	Ti-added
C	.205	.205	.22	.22
Mn	.620	.95	.46	.46
Si	.120	.030	.10	.10
S	.041	.019	.031	.031
P	.026	.014	.010	.010
Ni	.11	.05	-	-
Cr	.10	.04	-	-
Mo	.01	.08	-	-
Cu	.22	.05	-	-
Sn	.031	-	-	-
V	.001	-	-	-
Ti	< .005	-	-	.039
Al	.03	-	-	-

Table 7.1 Chemical Composition Of Steels (% wt)

(v) To compare the experimental data with the predictions made by the micro-fracture models of cleavage[15, 16, 17] and ductile[18, 19, 20] failure.

For convenience of material handling, the steel billet was cut into 42 mm blocks and then divided into two groups. One group was subsequently subjected to an AlN precipitation heat treatment consisting of three cycles of heating to 950 ^{o}C and soaking at that temperature for two hours to ensure homogeneity before furnace cooling to 500 ^{o}C. At the end of the final cycle, the steel blocks were further furnace cooled to ambient temperature. Surface decarburisation of the steel was minimised by the use of a fuel-rich town gas curtain in the furnace. The second steel group remained untreated.

Nitrogen analyses were conducted to determine the amount of active Nitrogen present in the two steels. The method of Nitrogen analysis was that of the United Steel Company which includes the separate determination of Nitrogen as acid soluble and acid insoluble[152]. Since the soluble part consists mainly of Aluminium Nitride and active Nitrogen and that the Aluminium Nitride content can be determined by the Ester Halogen method[153], the active Nitrogen content may be estimated by the equation,

$$\%\ N_{active} = \%\ N_{as\ soluble\ nitride} - \%\ N_{as\ AlN}$$

Details of the Nitrogen analysis techniques are given in Appendix A.

The results of the Nitrogen analysis are shown in Table 7.2. It can be seen that the AlN precipitation treatment did not eliminate the presence of active Nitrogen completely but was successful in producing a steel of low Nitrogen and therefore low strain ageing propensity when compared to the as-rolled material.

For convenience, the two steels will be referred to as the "As-Rolled" and "Hi-AlN" Billet Steels.

(b) Steel B

Steel B was made from casts produced by the BEA process to conform to Grade 275 of NZ3402P/73. The cast and Nitrogen analyses are given in Tables 7.1 and 7.2 respectively.

The experimental objectives of this steel are as follows:-

(i) To establish the effects of strain ageing of the crack-tip plastic zone on fracture toughness.

(ii) To compare the experimental fracture toughness data with the predictions made by the micro-fracture models of crack propagation.

(iii) To compare the quasi-static fracture toughness, K_{IC} , with the Charpy Impact energy, C_v, so as to establish their empirical relationship.

By referring to Table 7.2, it can be seen that the addition of Titanium to the Normal Grade 275 steel had reduced the active

Material / Elements	Billet Steel		Pressure Vessel Steel	Grade 275 Steel	
	As Rolled	Heat Treated		Normal	Ti-added
$N_{soluble}$	.0047	.0047	.0030	.0051	.0004
$N_{Insoluble}$	.0006	.0006	.0010	.0009	.0061
N_{AlN}	.0002	.0038	.0002	.0002	.0001
N_{Active}	.0045	.0009	.0028	.0049	.0003

Table 7.2 Nitrogen Analysis (% wt)

Nitrogen content substantially and consequently resulted in two steels of different strain ageing tendency.

In the remainder of this thesis, the two groups of Steel B shall be referred to as the "Normal" and "Ti-added" Grade 275 Steels.

(c) Steel C

Steel C was obtained from a Pressure Vessel from Wellington which had been involved in a fatal accident. The chemical composition and Nitrogen analysis of this steel are again given in Tables 7.1 and 7.2 respectively.

The experimental objectives of this steel are summarised as:

(i) To compare the experimental fracture toughness data with the predictions derived from the micro-fracture models of crack propagation.

(ii) To empirically relate the quasi-static fracture toughness, K_{IC}, with the Charpy Impact Energy, C_v.

(iii) To determine the effects of dynamic strain ageing on the fracture toughness in Part 2 of this thesis.

This steel shall be referred to as the "Pressure Vessel Steel" in the remainder of this thesis.

7.2 Fracture Toughness Test

7.2.1 The ASTM K_{IC} Test[3]

The ASTM K_{IC} test was used to determine the fracture toughness of the Pressure Vessel and the Grade 275 Steels at -196°C for the purpose of establishing the validity of the predictions made by the cleavage fracture model[15, 16, 17] in the these steels.

(a) Specimen Preparation

The specimen selected was the compact tension type. This specimen design was chosen because it was the most economical from the material points of view. The specifications of the specimen are given in Figure 7.1. The specimen size selected for this series of tests was 10 mm thick and the crack plane orientation in relation to the direction of rolling of the raw stock is given in Table 7.3.

To facilitate the nucleation of the fatigue crack, a modified form of the chevron notch[3] was adopted (see Figure 7.3). The final crack starter was introduced by cutting the notch-tip with a metal file which had a thinned-down cutting edge with a root radius of approximately 60 μm. The fatigue cracking was conducted on an Amsler High Frequency Vibrophore(see Plate 7.1). The maximum load amplitude of the stress cycle was kept low so that the stress intensity during fatigueing would remain below 60% of the apparent fracture toughness, K_Q , as specified by the ASTM standard[3]. The

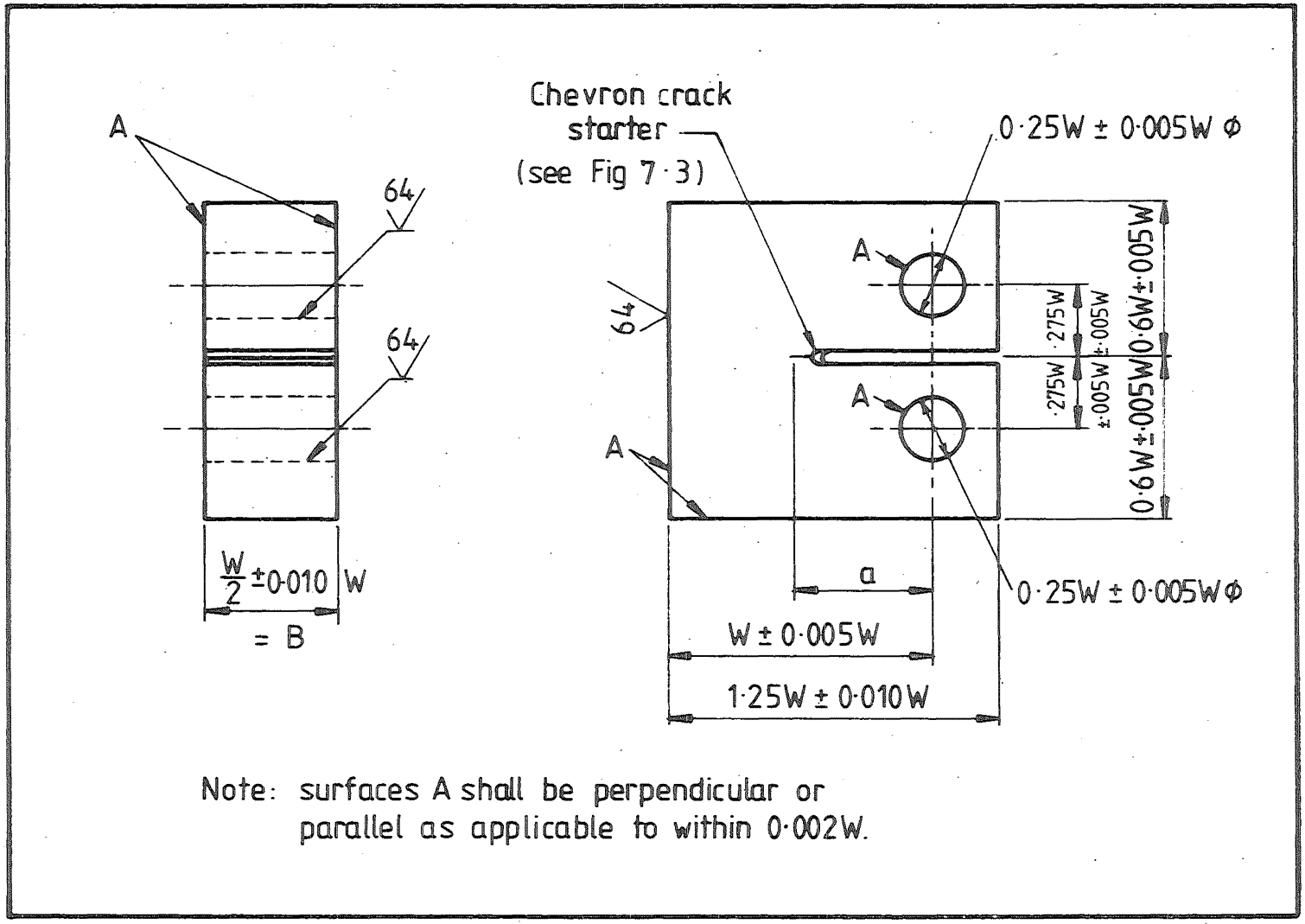

Note: surfaces A shall be perpendicular or parallel as applicable to within 0·002W.

FIG 7·1 THE ASTM COMPACT TENSION SPECIMEN[20]

Material	Specimen Thickness (mm)	Crack Plane Orientation *
Billet Steel	10	S-T
Pressure Vessel Steel	10	T-L
Grade 275 Steel	10	L-R

* See Figure 7.2

Table 7.3 Crack Plane Orientation Of The ASTM K_{IC} Test Specimens

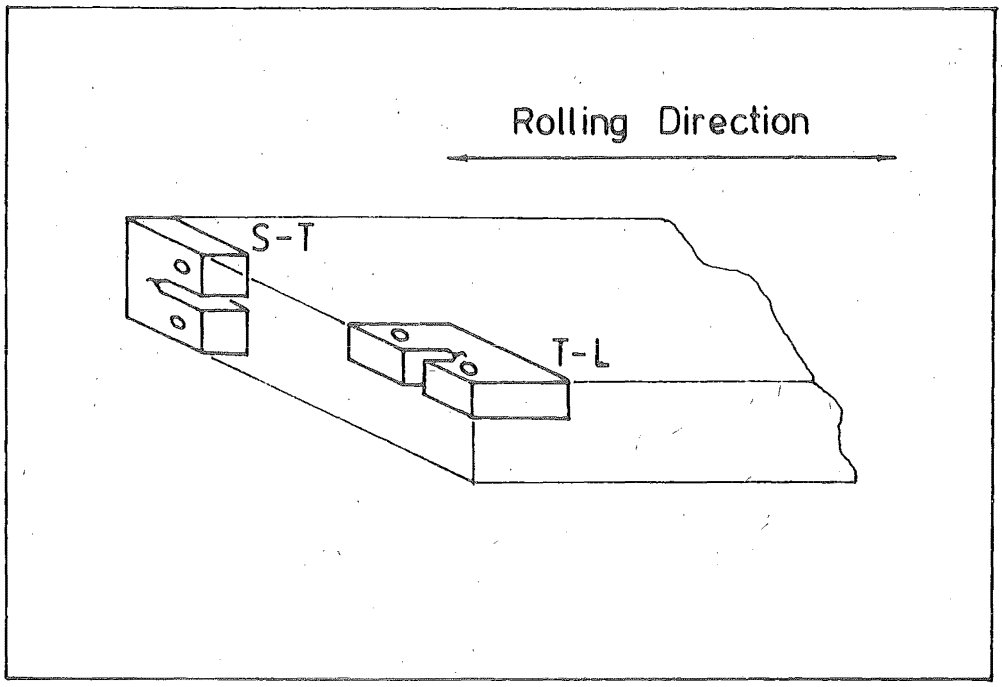

(a)

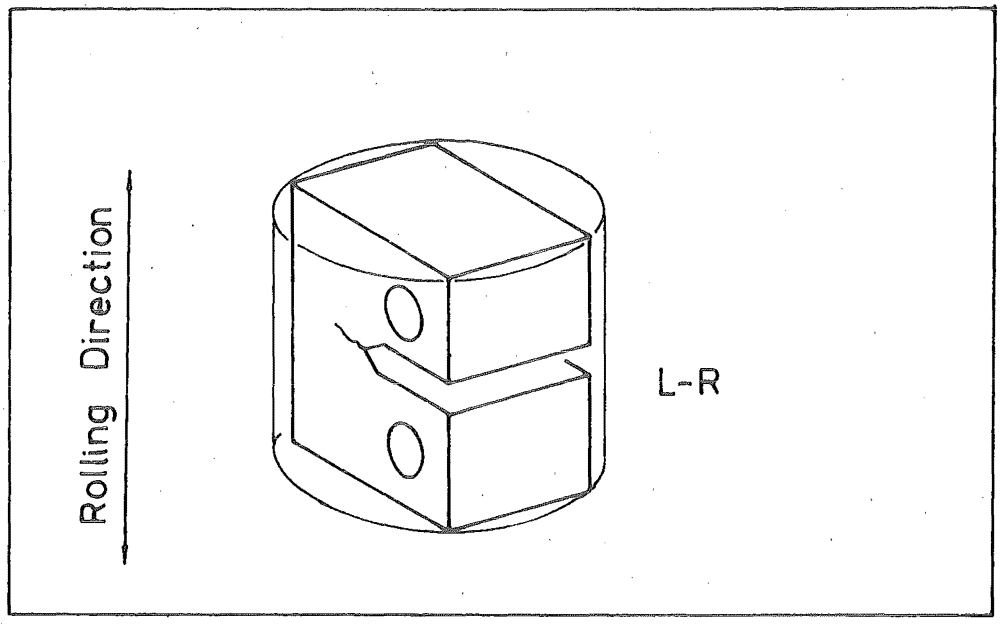

(b)

FIG. 7·2 CRACK PLANE IDENTIFICATION OF THE (a) PRESSURE VESSEL & BILLET STEEL SPECIMEN. (b) GRADE 275 STEEL SPECIMEN.

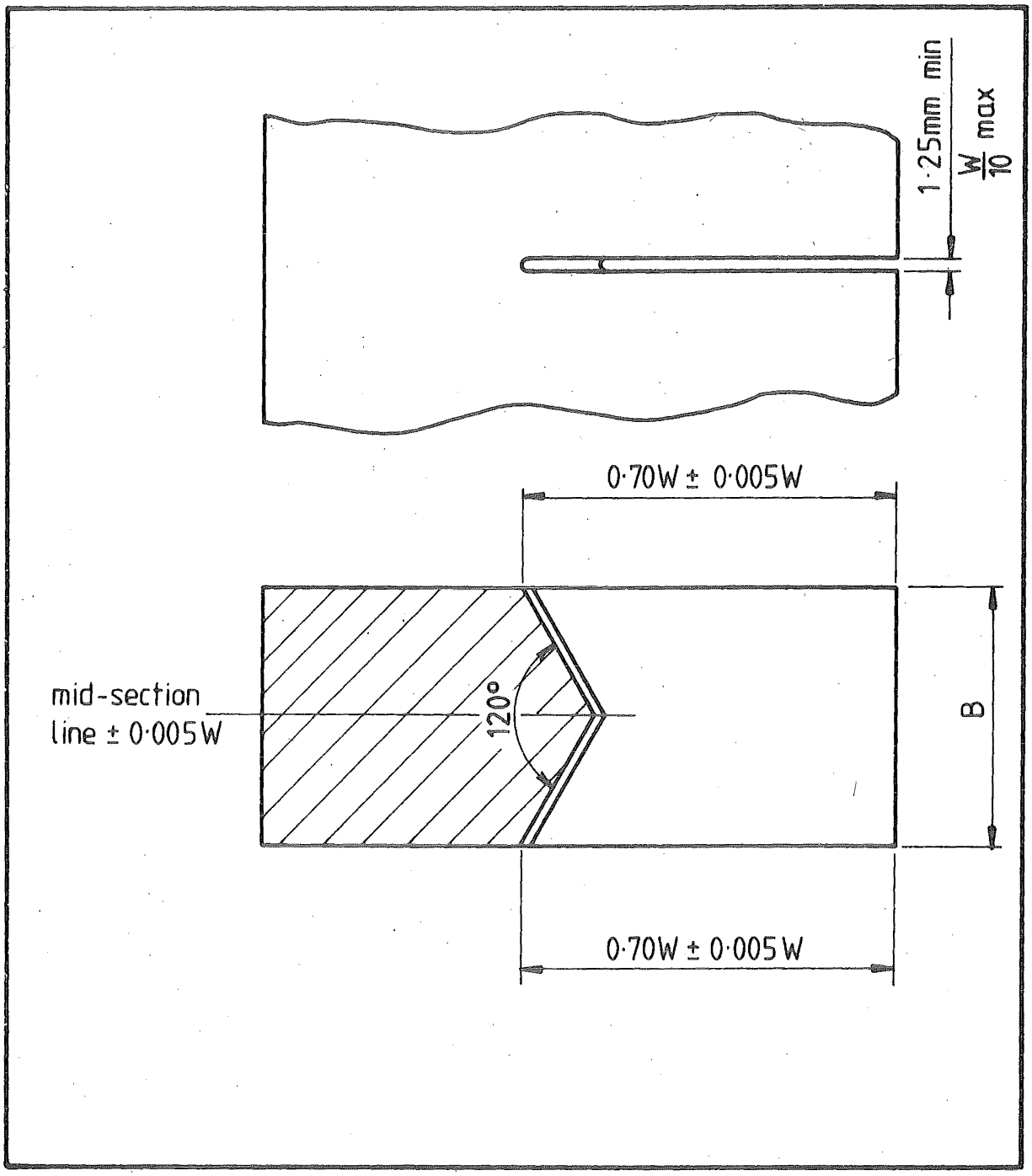

FIG 7·3 THE MODIFIED CHEVRON CRACK STARTER

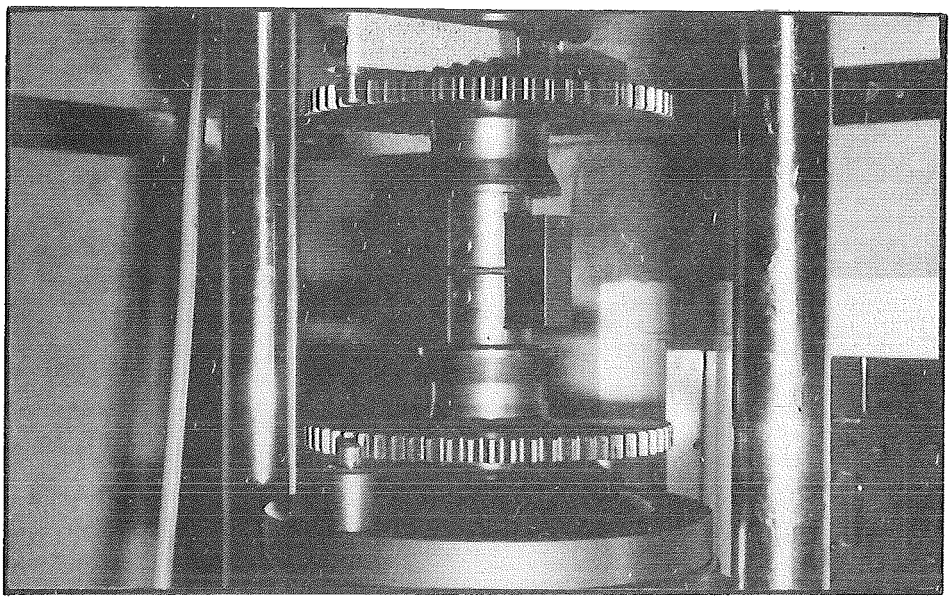

PLATE 7·1 FATIGUE CRACKING OF A COMPACT TENSION SPECIMEN ON THE AMSLER VIBROPHORE

load amplitude was further reduced during the final 20% of fatigue cycling. A brief summary of the fatigue cracking history is given in Table 7.4

The propagation of the fatigue crack was monitored visually with the aid of a magnifying glass so as to ensure that the ratio of crack length/specimen width, $\frac{a}{W}$, would fall within the range of 0.50 ± 0.05. Later examination of the fracture surfaces of broken specimens revealed that the above limit placed on the ratio $\frac{a}{W}$ was met adequately.

The cracked specimens of each of the two Grade 275 steels were sub-divided into two further groups. One group was tested immediately after fatiguing or where this was not possible stored at $-70^{o}C$ for a maximum of 48 hours while the other group was subjected to an ageing treatment of 30 hours at $80^{o}C$ before testing. The Pressure Vessel Steel specimens were tested in the as-fatigued condition.

(b) Test Procedure

The K_{IC} testing was conducted on an Instron 250 KN maximum capacity Universal Testing Machine. The test specimen was immersed in liquid Nitrogen in an Amsler Enviromental Test Chamber (Model number TV742). The test was conducted at a crosshead speed of 0.5 mm-min^{-1}. For the purpose of ensuring temperature homogeneity, the specimen was immersed in the coolant for a minimum of 15 minutes before the commencement of testing.

Material	Initial Maximum Load Amplitude (KN)	Final Load Amplitude (KN)	Approximate Number Of Stress Cycles (10^3)
Pressure Vessel Steel	1.5-1.8	1.0	500-1000
Normal Grade 275 Steel	1.5	1.0	500-1000
Ti-Added Grade 275 Steel	1.5	1.0	500-1200

Table 7.4 The Fatigue Cracking History Of The ASTM K_{IC} Test Specimens

(c) Analysis Of Results

The typical test record of these tests consisted of a graph of applied-force versus crosshead displacement, as shown in Figure 7.4. Although an extensometer was not used in these tests, no "pop-in" was observed indicating that the instability load, P_Q could be used to calculate the apparent fracture toughness value K_Q by using the equation

$$K_Q = \frac{P_Q}{BW^{\frac{1}{2}}} \{ 29.6(\frac{a}{W})^{\frac{1}{2}} - 185.5(\frac{a}{W})^{\frac{3}{2}} + 655.7(\frac{a}{W})^{\frac{5}{2}} - 1017(\frac{a}{W})^{\frac{7}{2}} + 638.9(\frac{a}{W})^{\frac{9}{2}} \} \quad (7.2.1)$$

where a is the crack length

W is the specimen width

B is the specimen thickness

The thickness dependence of K_Q was then assessed by using the size criterion

$$a, W - a , B \geq 2.5(\frac{K_Q}{\sigma_Y})^2 \quad (7.2.2)$$

where a is the crack length

W - a is the uncracked ligament length

B is the specimen thickness

σ_Y is the yield stress.

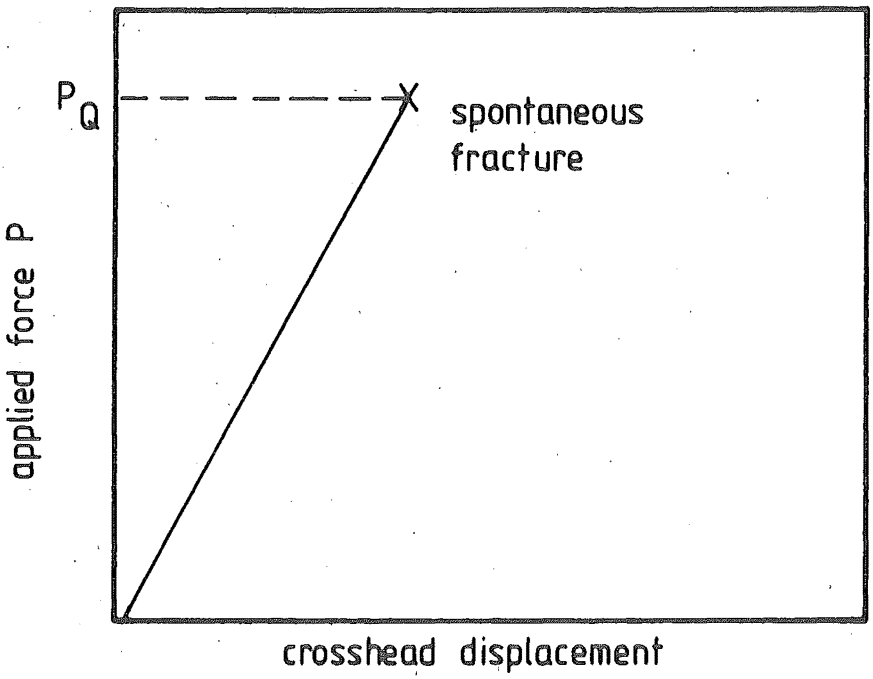

FIG 7·4 TYPICAL ASTM K_{IC} TEST RECORD

When the size criterion was satisfied, the apparent fracture toughness, K_Q , was accepted as the valid thickness independent "plane strain" fracture toughness, K_{IC} .

7.2.2 COD Test For Determining The Minimum Size Criterion

(a) Specimen Preparation

The specimens used in this experiment were of the compact tension type with thicknesses of 3, 4, 7, 10, 20 and 30 mm machined from the As-Rolled Billet Steel. The preparation of the 10, 20 and 30 mm thick specimens was similar to that described in Section 7.2.1.a with the crack plane being in the S-T direction (see Figure 7.2). The 3, 4 and 7 mm thick specimens were obtained by machining the uncracked ligament area of the fatigue cracked 10 mm thick specimens down to size so that they would fit the standard 10 mm test specimen grips. The specimens were tested at ambient temperature.

(b) Test Procedure

The specimens were tested on the Instron Universal Testing Machine and SIL-21 rubber was used to produce a replica of the crack-tip profile at regular load intervals, both prior to and after the attainment of maximum load. The mid-thickness section of each of these crack-tip replica were then examined under the Nikon (Model 6C) Shadowgraph

and the COD at the instance of initial stable crack extension measured.

The position of the crack-tip was determined by measuring the actual distance between the fatigue crack-tip and a reference point, usually taken at the chevron crack starter tip on the fracture surface of the broken specimen. Thus, a reasonably accurate assessment of the COD at the instance of initial stable crack extension regardless of whether it was sufficient to cause structural instability (i.e. at maximum load), could be made.

7.2.3 Crack Opening Displacement (COD) Test For Determining The Temperature Dependence Of Fracture Toughness

The purpose of this series of test was to establish the temperature dependence of fracture toughness in the vicinity of the fracture mode transition temperature. All three low carbon steels were tested in this manner.

(a) Specimen Preparation

The compact tension specimen type was chosen for this series of tests. The specimen and the fatigue crack starter specifications were similar to those given earlier in Figures 7.1 and 7.3 respectively. The range of specimen thickness and their crack plane orientations are

given in Table 7.5.

The fatigue cracking was conducted on the Amsler High Frequency Vibrophore. A brief summary of the fatigue cracking history is given in Table 7.6, while the detailed information is given in Appendix D. Precautions similar to those described in Section 7.2.1.a were followed to ensure that the ratio of $(\frac{a}{W})$ remained within 0.50 ± 0.05. The fatigue cracked specimens were either tested immediately after fatiguing or stored at $-70^{\circ}C$ for a maximum of 48 hours prior to testing to ensure a minimal degree of ageing. The Grade 275 and the Billet Steels were also aged prior to testing, for this ageing treatment the fatigue cracked specimens were soaked at $80^{\circ}C$ for 30 hours. However, the unexpected fracture behaviour of the Hi-AlN Steel (see Section 8.2) caused the abandonment of the initial plan to investigate the effect of strain ageing of the crack-tip plastic zone on the fracture toughness measurement of the Billet Steel.

(b) Test Procedure

The COD tests were conducted on the Instron Universal Testing Machine. For sub-ambient test temperatures, the test specimens were surrounded by a helical copper tube enclosed in a polystyrene enviromental chamber. Temperature control was effected by regulating the flow of liquid air

Materials	Specimen Thickness (mm)	Crack Plane Orientation*
Billet Steel	10, 20, 30	S-T
Pressure Vessel Steel	10	T-L
Grade 275 Steel	10	L-R

* See Figure 7.2

Table 7.5 The Range Of Specimen Thickness And The Crack Plane Orientation Of The COD Specimens

Material		Average Initial Maximum Load Amplitude (KN)	Average Final Load Amplitude (KN)	Approximate Number Of Stress Cycles (10^3)
Billet Steel	10 mm Thick	2-2.5	1.0	150-500
	20 mm Thick	9-11.0	3.0	100-500
	30 mm Thick	20-24	5.0	700-1000
Pressure Vessel Steel		2-3	1.0	100-700
Grade 275 Steel		2.5-3.0	1.0	100-600

Table 7.6 The Summary Fatigue Pre-Cracking History Of The COD Test Specimens

through the copper tube. The test equipment is shown in Plate 7.2.a.

The temperature of the test specimen was monitored by two Phillip PR64C213/60 Ni-NiCr thermocouples attached to the crack-tip region of both specimen surfaces. The possible existence of a through thickness temperature gradient had been investigated and these details are given in Appendix C. Prior to the commencement of the COD test, the specimen was soaked at the desired temperature for a minimum of 15 minutes to ensure steady state condition. The specimen was then tested at a crosshead speed of 0.5 mm-min^{-1}. The tests were conducted over a temperature range of -80^{o}C to 25^{o}C.

(c) The Monitoring Of Crack Opening Displacement

The crack opening displacement was measured indirectly with an Instron A384-1B clip-on type extensometer. As it was not feasible to attach the extensometer across the crack directly in the sub-ambient temperature COD tests, two Nilo low expansion extension arms were used (see Plate 7.2.b). The system was calibrated using a silicon rubber crack-tip replication technique[71, 80, 84] to determine the COD-extensometer displacement (V_g) relationship. Details of the calibration technique are given in Appendix B. In the actual COD tests, the extensometer was also calibrated against displacement recorder-pen of the

PLATE 7·2
(a) THE COD TEST EQUIPMENT

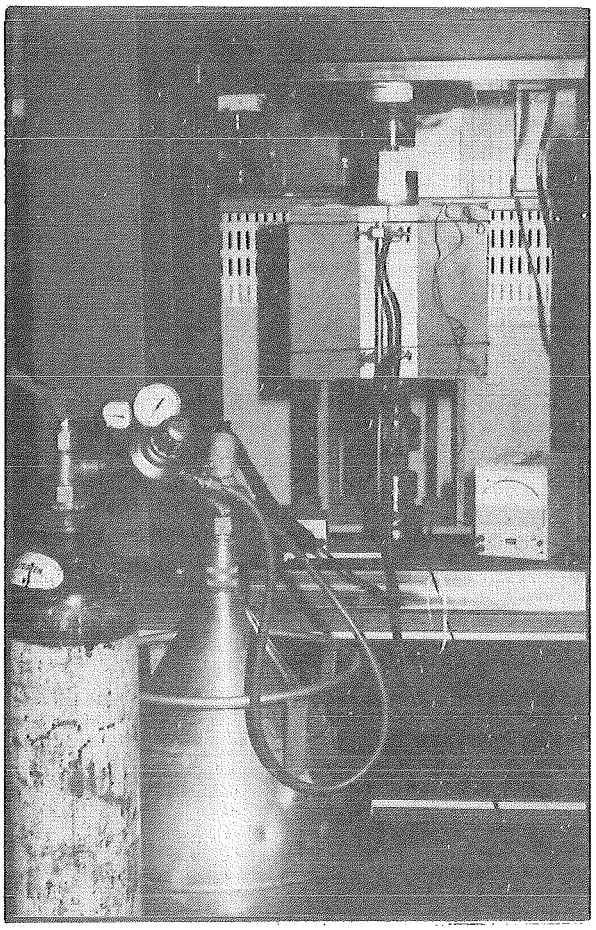

(b) THE EXTENSION ARMS OF THE COD CLIP-ON TYPE EXTENSOMETER

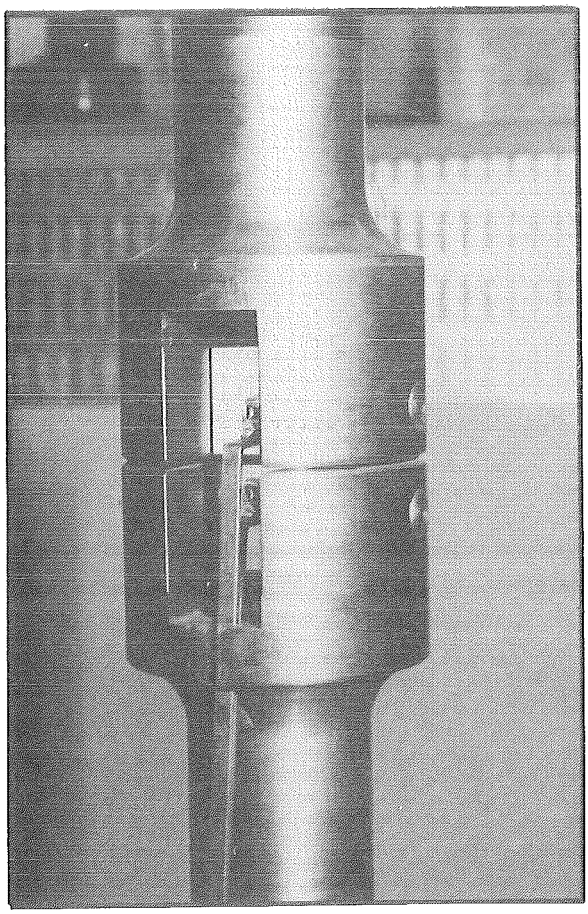

Instron Testing machine prior to every test or daily when more than one test was performed per day.

(d) Analysis Of Results

The typical COD test record was in the form of a graph of applied force (P) versus extensometer displacement (V_g). The critical value of V_g was determined in accordance to the method recommended in the BS-DD 19, which may be briefly described as:-

(i) The value of V_g at the instance of spontaneous instability provided that the maximum load had not been exceeded (see Figure 7.5.a)

or

(ii) The value of V_g at maximum load (see Figure 7.5.b).

The critical COD was then evaluated by referring to the experimental calibration. The raw data from this series of tests is given in Appendix E. It should be noted that the use of maximum load COD as a critical instability criterion could be inaccurate when sub-critical stable crack extension occurred prior to instability[18, 83]. In this series of experiments, this problem was surmounted by using the silicon rubber crack-tip replication technique[71, 80, 84] to determine whether the maximum load COD was a suitable instability criterion. The technique involved loading the COD specimen to

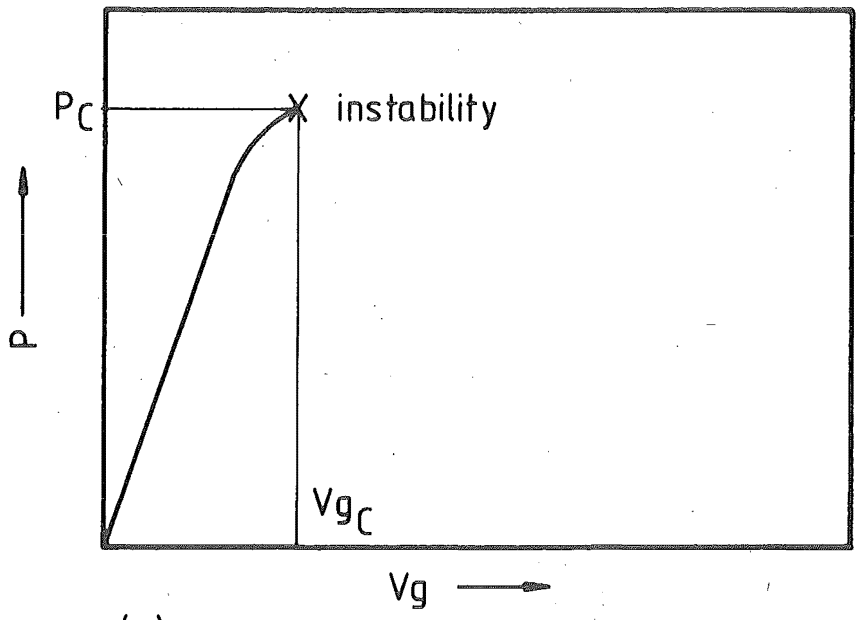

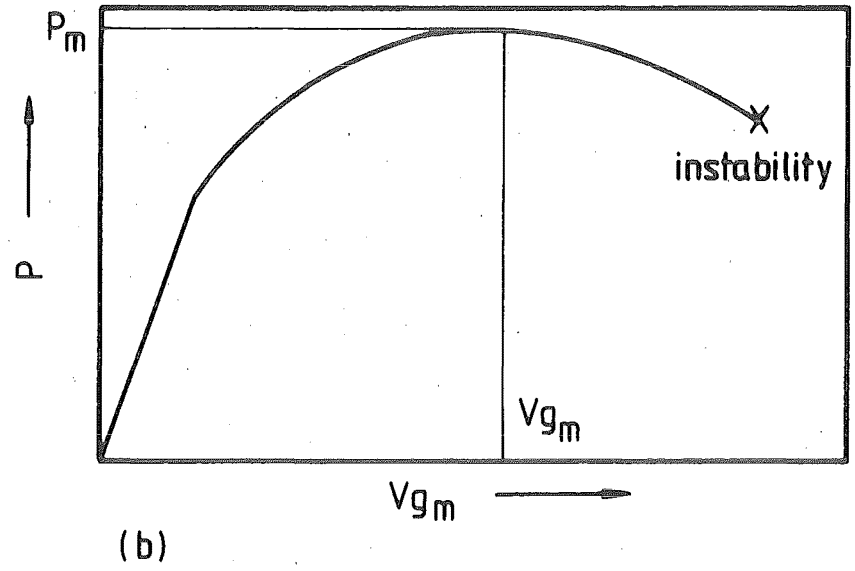

FIG 7·5 TYPICAL APPLIED FORCE-DISPLACEMENT RECORDS OF THE COD TEST

pre-determined load levels and then producing the crack-tip replica with the SIL-21 hardening rubber. The openings at the crack-tip were then examined and measured under a Nikon (model 6C) Shadowgraph in the manner described earlier in Section 7.2.2. The result of this investigation will be included in the next chapter.

7.2.4 Notched Ductility Test

This test was necessary to provide the notched ductility data for the comparison of experimental fracture toughness with the predictions made from the non-metallic inclusion fracture model[18, 19] in which the notched ductility, ε_{fi} , is related to the COD at the instance of initial crack extension, δ_i , by Equation (4.2.1)

i.e. $$\delta_i = \ell_f \times \varepsilon_{fi}$$

where ℓ_f is the average non-metallic inclusion particle spacing

The technique used in determining the notched ductility had been reported earlier[22]. The method involved measuring the instability COD of fracture toughness specimens with notches instead of fatigue cracks to obtain a graph of the critical COD at instability versus the slot-width of the notch. The slope of the linear part of this graph would provide a measure of the notched ductility.

The specimens used in this test were the 10 mm compact tension type machined from the Pressure Vessel and the Grade 275 Steels. Apart from the fatigue crack induced in the manner described in

Section 7.2.1.a, notches with slot-widths of 300, 650 and 950 μm were produced by using a jeweller's saw and hand-saw blades which had been pre-ground down to suitable thicknesses. These notches were cut with care to ensure that the notch front remained parallel to the front face of the specimen. A typical illustration of the notch profile produced in this manner is given in Plate 7.3. This photograph shows the side-on profile of a notch cut by the saw blade on a piece of mild steel plate examined under the Jeol JSM 35 Scanning Electron Microscope. The average values of the slot-width were measured from the replicas of the notch-tip prepared with the SIL-21 hardening rubber. The mid-thickness section of these replica was examined and measured under the Nikon (Model 6C) Shadowgraph to provide the slot-width values values given earlier.

The specimens were then tested on the Instron Universal Testing Machine and the COD at the instance of instability by stable crack extension measured from the SIL-21 rubber replica of the crack-tip obtained under load. The techniques of testing and locating the crack-tip were similar to those described earlier in Section 7.2.2.b.

7.3 Tensile Test

Three different series of tensile tests were performed with the following aims:-

(i) To establish the temperature dependence of the lower yield stress, σ_{LY} , of the three experimental steels used in the fracture toughness test.

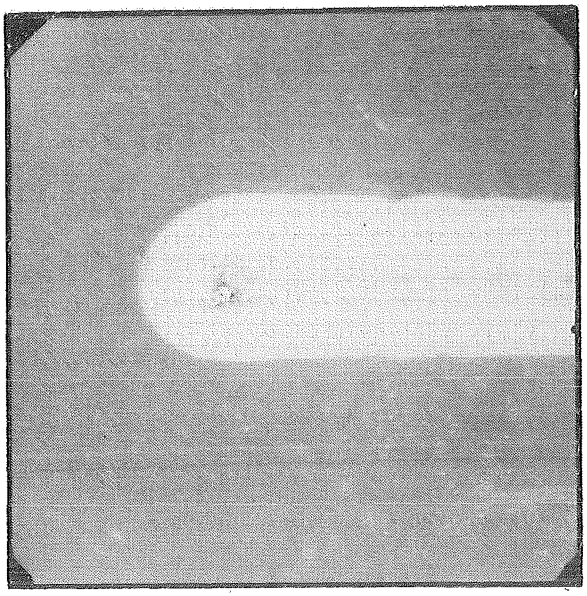

PLATE 7·3 TYPICAL SIDE-ON PROFILE OF THE NOTCH OF THE COD TEST SPECIMENS USED IN THE NOTCHED DUCTILITY TEST.
(magnification = 75
slot width = 300 μm)

(ii) To establish the true stress-true strain relationship:

$$\sigma = K_s \varepsilon^n \qquad (7.3.1)$$

where σ is the true stress

ε is the true strain

n is the hardening index

K_s is the strengthening coefficient

so as to establish the applicability of the Sailor's model of ductile fracture[20] which relates the COD at the instance of crack instability (δ_i), the uniaxial fracture strain ε_f and the average grain diameter, d_g by the Equation

$$\ln\left(\frac{\delta_i}{2d_g}\right) = 0.2\ \varepsilon_f \qquad (7.3.2)$$

(iii) To establish the tensile properties of the three steels at -196^{o}C for the purpose of investigating the applicability of the cleavage fracture model where the fracture toughness K_{IC} is related to the fracture stress, σ_F , by the Equation

$$\sigma_F(2\pi X_o)^{\frac{1}{2}} = K_{IC} \qquad (4.6.6)$$

where X_o is the "charecteristic" distance, reported to be 1 to 2 times the average grain diameter.

(iv) To ascertain the effect of strain ageing on the tensile properties of the Billet and the Grade 275 Steels measured at -196^{o}C so that the effects of strain ageing on K_{IC} and the tensile properties can be compared.

7.3.1 Specimen Preparation

The specimen design described below is common to all three series of tests. The dimensions of the tensile specimens were based on those of the No. 14A specimens of the Hounsfield Tensometer Tensile specimen handbook. Slight modification to the standard dimensions were introduced so that the specimens could be adopted for testing on the Instron Universal Testing Machine. The dimensions and the machining sequence of the tensile specimen are shown in Figure 7.6. The tensile specimens used in the -196^{o}C testing were given additional polishing and finish polished with Grade 600 emery paper to eliminate the notch effects of machining marks.

The specimens were machined from the raw stock in the direction relevant to the COD testing (see Figure 7.7).

7.3.2 Test Procedure

(a) Fracture Toughness Related Tensile Test

As stated earlier, the aim of these tests was to establish the lower yield stress, σ_{LY}, of the experimental

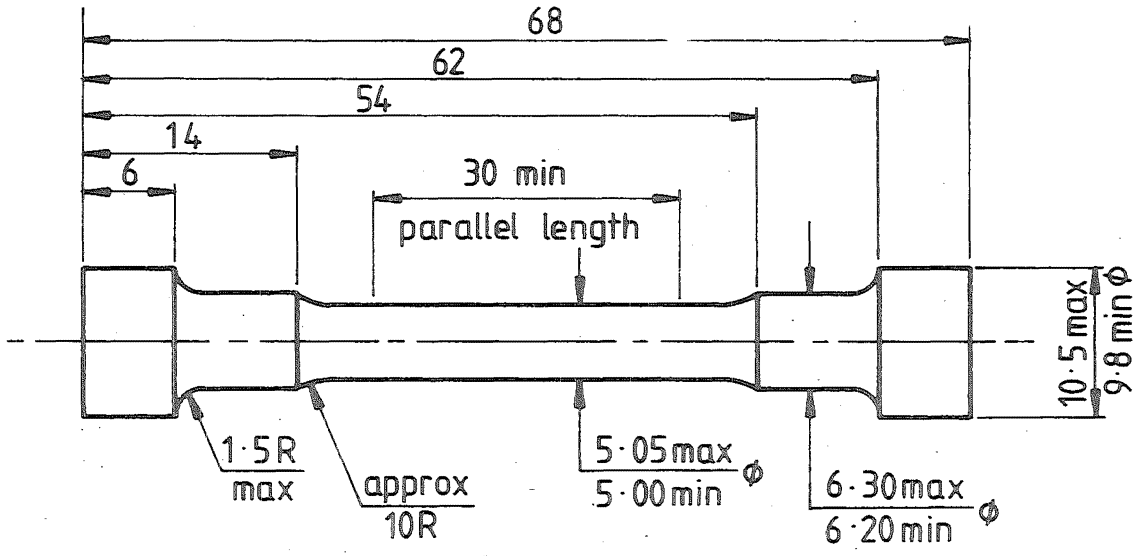

all dimensions in mm

Machining sequence of gauge length

(1) Finish turn to 5·125mm dia
(2) Grind to 5·025mm dia
(3) Finish grind to 5·00mm dia in two 0·0125mm cuts

FIG 7·6 TENSILE SPECIMEN

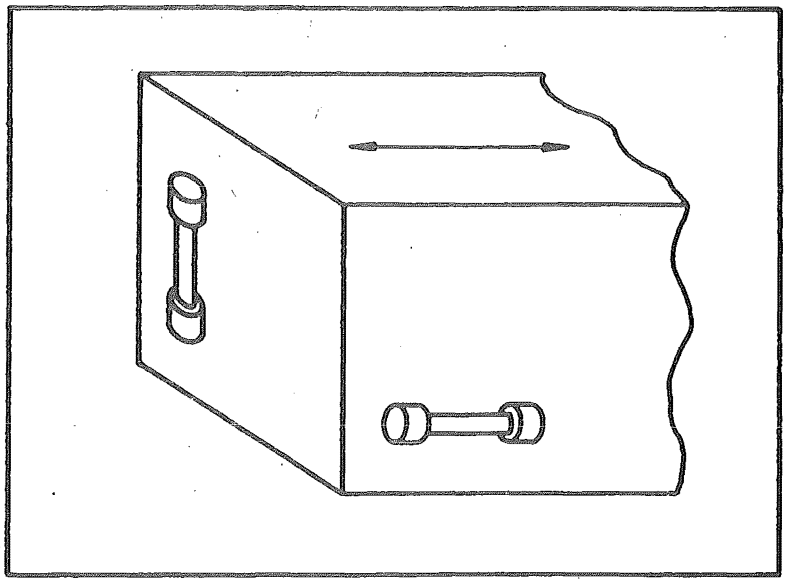

(a) the billet steel

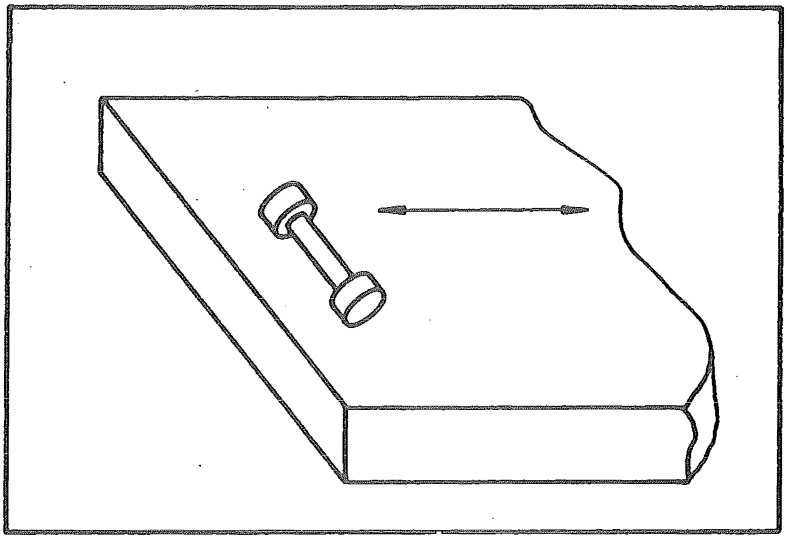

(b) the pressure vessel steel

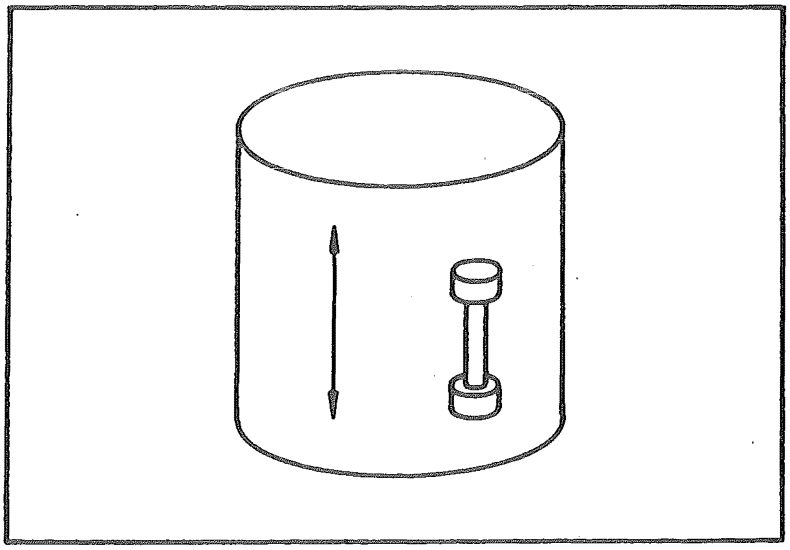

(c) the grade 275 steel

FIG 7·7 ORIENTATION OF TENSILE SPECIMENS (arrows indicate direction of rolling)

steels at temperatures relevant to the fracture toughness test. The lower yield stress needed for the ASTM low temperature K_{IC} test will be supplied by the test described later in Section 7.3.2.c.

This series of tests was conducted over the temperature range of $-90^{o}C$ to $25^{o}C$ on the Instron Universal Testing machine. As the specimens were tested over a range of sub-ambient temperature with the use of the polystyrene enviromental chamber (see Section 7.2.3.b), the use of extensometer was not feasible without elaborate modification. However, since the aim of these tests was to establish the lower yield stress, the test records of applied force versus cross-head displacement supplied adequate information. As in the COD testing, the test specimens were allowed to soak at the desired temperature for a minimum of 15 minutes to ensure steady state temperature. The temperature of the specimen was monitored by attaching a Phillip PR64C213/60 Ni-NiCr thermocouple on the gauge area of the specimen. The tests were performed at a cross-head speed of 0.5 $mm\text{-}min^{-1}$ to entail a strain rate of approximately 2.8×10^{-4} sec^{-1}.

In the analysis of the test results, it was found that the Hi-AlN Billet steel failed without any sign of yielding and with little plastic deformation (see Figure 7.8.b). The failure appeared to have occurred by tearing between the transverse non-metallic inclusion particles. As the

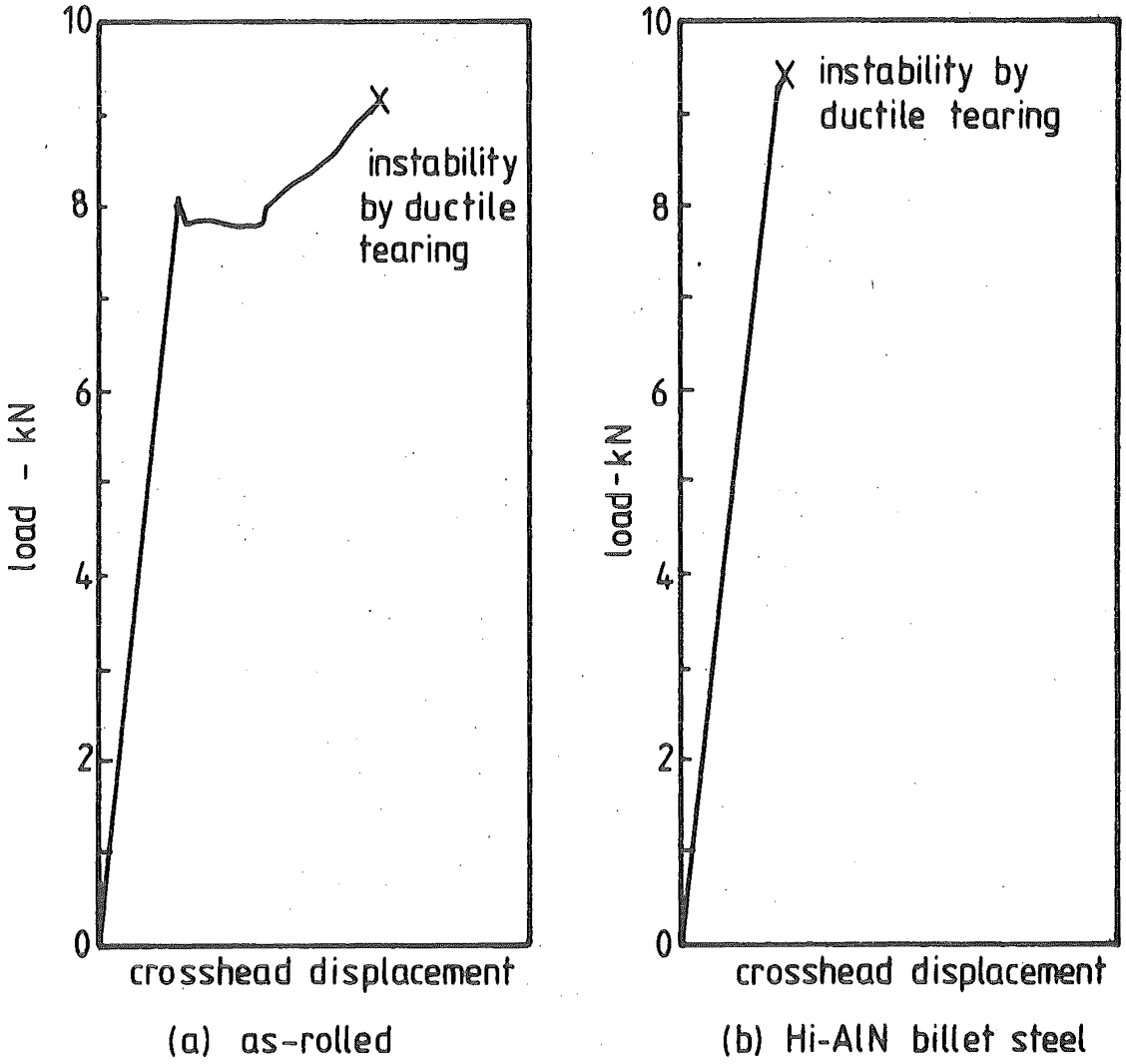

FIG 7·8 TYPICAL TENSILE TEST RECORDS

AlN precipitation heat treatment can cause grain refinement thus resulting in an elevated yield and flow stresses [150, 151], it was decided that the ambient temperature flow stress of the As-Rolled and the Hi-AlN Billet Steels in the orientation longitudinal to the rolling direction would be measured using similar tensile specimen design and test equipment. The flow stress of the Hi-AlN in the transverse direction was estimated by evaluating the "instability" stress determined by the applied force at the instance of instability.

(b) The True-Stress True-Strain Test

This series of tests was conducted at ambient temperature on an Avery type 7102 CCH Universal Testing Machine. The test technique involved the measurement of the instantaneous applied force, P_i , and the corresponding instantaneous specimen diameter, D_i . The instantaneous stress, σ_i , and the instantaneous plastic strain, ε_{P_i} , were calculated with the equations

$$\sigma_i = \frac{4P_i}{\pi D_i^2} \qquad (7.3.1)$$

$$\varepsilon_{P_i} = 2 \ln\left(\frac{D_o}{D_i}\right) \qquad (7.3.2)$$

where D_o was the initial specimen diameter.

Graphs of log σ_i versus log ε_{P_i} were then used to establish

the strain hardening index, n, and the strengthening coefficient, K_s . These graphs are given in Appendix F. The fracture strain, ε_f , was estimated by substituting the specimen diameter at fracture, D_F , in Equation (7.3.2). It should be noted that the Hi-AlN steel could not be used in this series of tests because of the unusual failure behaviour described in Section 7.3.2.a.

(c) The Liquid-Nitrogen-Temperature Tensile Test

These tests were performed on the Instron Universal Testing machine at a cross-head speed of 0.5 mm-min^{-1}. The desired specimen temperature of -196^{o}C was attained by immersing the test specimen and grips in liquid Nitrogen contained in the Amsler Enviromental Test Chamber (Model No. TV42). Once again, the use of extensometer was not feasible without elaborate modification to the standard grips. However, since the purpose of these tests was to measure the upper and lower yield stress and the fracture stress and strain, the test record of applied force versus cross-head displacement supplied adequate information (see Figure 7.9). Before the commencement of each test, the specimen was immersed in liquid Nitrogen for a minimum of 15 minutes to ensure temperature homogeneity.

The lower and upper yield stresses were calculated

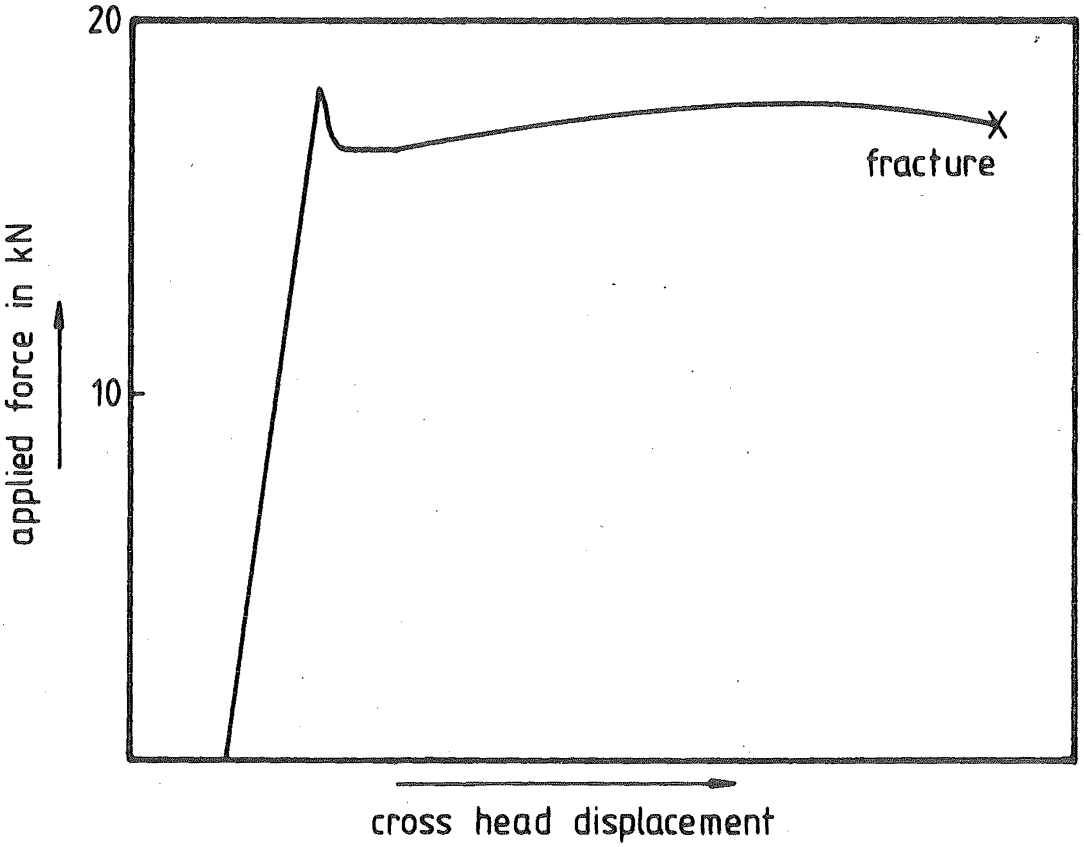

FIG 7·9 TYPICAL TENSILE TEST RECORD AT −196°C

in the usual manner from the test record. The fracture stress was estimated by using the load value, P_F , at fracture with the equation

$$\sigma_F = \frac{4P_F}{\pi D_F^2} \qquad (7.3.3)$$

where D_F is the specimen diameter at fracture

This was possible because of the brittle nature of the fracture. The fracture strain, ε_f , was estimated by the equation

$$\varepsilon_f = 2 \ln\frac{D_o}{D_F} \qquad (7.3.4)$$

where D_o is the initial specimen diameter

D_F is the fracture specimen diameter.

Specimens machined from the three experimental steels were tested in the above manner. However, in the Billet Steel the fracture occurred by decohesion at transverse non-metallic inclusion particles. Consequently, no meaningful data could be obtained from the testings of these steels.

In addition, the effect of strain ageing on the tensile properties measured at $-196^{o}C$ was also investigated using specimens machined from the two Grade 275 Steels pre-strained by 5%, 10% and 15% followed by an ageing treatment of 30 hours at $80^{o}C$.

7.4 Calculation Of K_{IC} From COD Test Results

Although the BS-DD 19/72 COD test procedure does not define a limit on the specimen size for the evaluation of thickness independent "plane strain" fracture toughness, it is possible to infer the value of such a limit indirectly from

(i) The plane-strain size limit for the J-Integral test, which was reported as[10, 29]

$$a \ , \ B \ , \ W - a \geqslant 25 \frac{J_{IC}}{\sigma_Y} \qquad (7.4.1)$$

where a is the crack length

B is the specimen thickness

W - a is the uncracked ligament length

J_{IC} is the "plane strain" critical J-Integral

σ_Y is the yield stress

and that J_{IC} is related to the plane strain Critical Stress Intensity Factor, K_{IC} , by the equation

$$\frac{K_{IC}^2}{E}(1 - \nu^2) = J_{IC} \qquad (7.4.1.a)$$

where E is the modulus of elasticity

ν is the Poisson's ratio.

and (ii) The report that for pre-fatigue cracked specimens[11]

$$\frac{K_{IC}^2}{E}(1 - \nu^2) = \sigma_Y \delta_c \qquad (7.4.2)$$

where δ_c is the critical COD at instability.

These two observations can be combined to yield a size limit for the COD test as

$$a \ , \ B \ , \ W - a \geq 25 \ \delta_c \qquad (7.4.3)$$

Thus, by using the maximum value of the experimental critical COD as the conservative value, the size criteria of the COD test could be predicted and compared with the experimental results obtained by the test described earlier in Section 7.2.2

The conservative value of K_{IC} were evaluated by using Equation (3.2.11) with M = 1 so that

$$\frac{K_{crit}^2}{E}(1 - \nu^2) = \sigma_{LY}\delta_c$$

where σ_{LY} is the lower yield stress

δ_c is the critical COD at instability

K_{crit} is the critical Stress Intensity Factor

E is the modulus of elasticity

By substituting the appropriate values of E and ν of low carbon steel, where[189]

$$E = 207 \times 10^3 \ MN\text{-}m^{-2}$$

$$\nu = 0.3$$

Equation (3.2.11) becomes

$$K_{crit} = 0.4769 \ (\sigma_{LY}\delta_c)^{\frac{1}{2}} \ MN\text{-}m^{-\frac{3}{2}} \qquad (7.4.4)$$

with σ_{LY} in $MN\text{-}m^{-2}$ and δ_c in μm

7.5 Charpy V-Notched Impact Test

The Charpy V-Notched Impact tests were performed with the aim of assessing the empirical correlation between the quasi-static fracture toughness K_{IC} and the Charpy V-notched impact energy, C_v .

(a) Specimen Preparation

The Charpy V-notched specimens were prepared from the Pressure Vessel and the Grade 275 Steels in accordance with the specifications of BS 131 Part II/1972. The orientation of the notch plane in relation to the rolling direction of the raw stock is shown in Figure 7.10. The Pressure Vessel specimens were tested in the as-rolled condition while each of the two Grade 275 Steels was divided into two groups; one group subjected to a 5% pre-strain and subsequently aged for 30 hours at 80^{o}C before testing and the other group tested in the as-rolled condition.

(b) Test Procedure

The tests were performed on an Avery Impact Testing machine with a striking energy of 298J and a strike velocity of 5 Ms^{-1} , in accordance with the BS 131 specifications. The specimens were cooled by immersion in a petroleum ether and dry ice mixture for sub-ambient temperature tests, while hot oil was used as the heating medium in elevated temperature tests. A minimum soak time of 15 minutes at the desired temperature was allowed

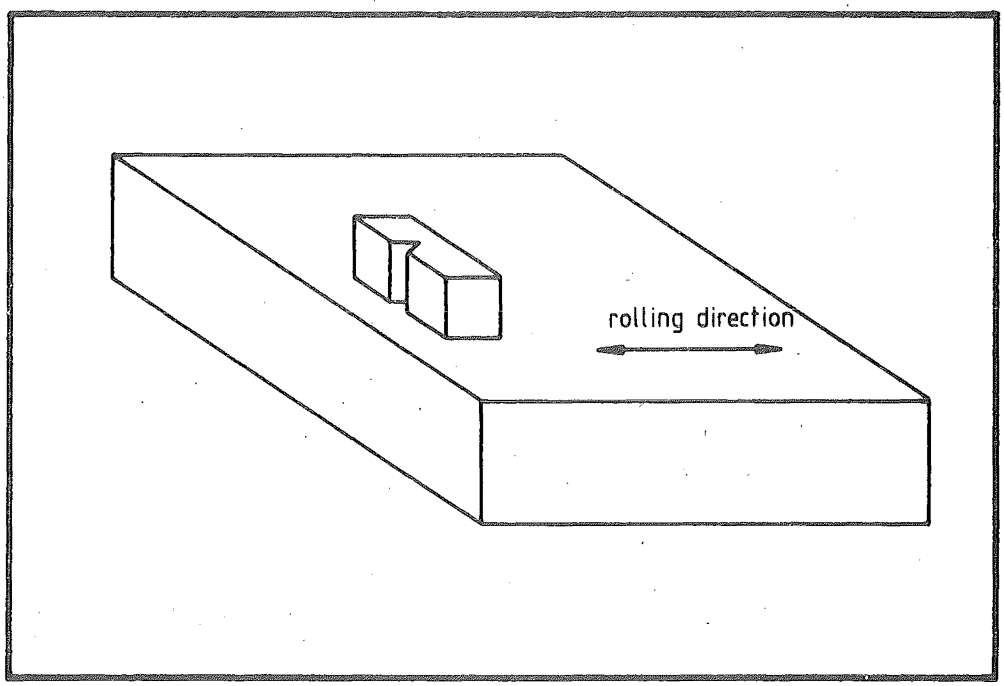

(a)

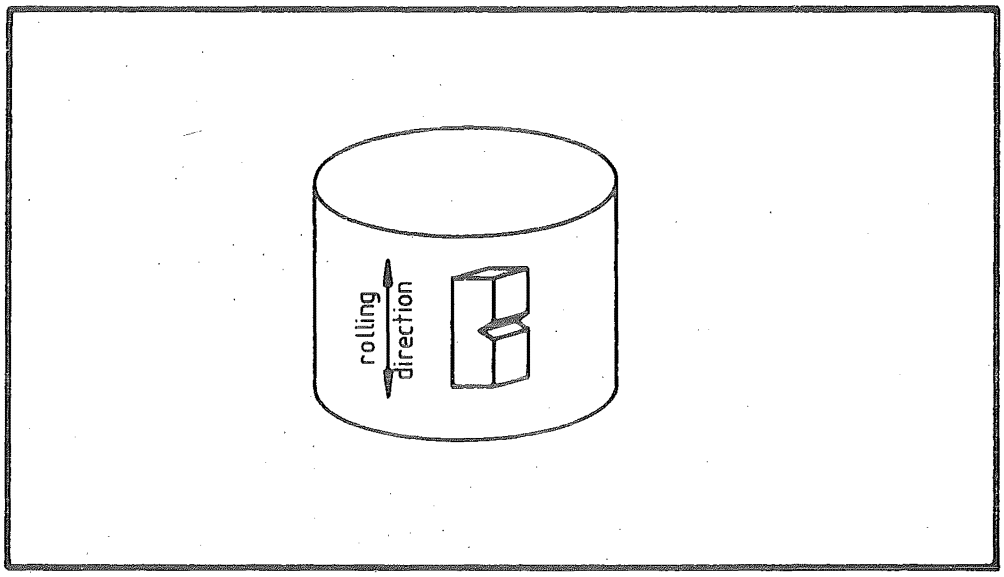

(b)

FIG 7·10 THE NOTCH PLANE ORIENTATION OF THE CHARPY SPECIMEN MACHINED FROM
a) the pressure vessel steel
b) the grade 275 steel

to ensure temperature homogeneity. The raw data of the Charpy tests are given in Appendix G.

7.6 Micro-Examination

Two types of micro-examination were performed. They were

(i) Optical microscope examination

(ii) Scanning electron microscope examination of the fracture surfaces of broken fracture toughness test specimens.

7.6.1 Optical Micro-examination

Optical micro-examination was needed to provide data for

(i) The average grain size of the experimental steels

(ii) The average inter-inclusion particle spacing of the experimental steels

(iii) The identity of the type of non-metallic inclusion particles.

The experimental technique involved the preparation of micro-specimen by polishing the relevant metal surface with suitable grades of emery paper in the usual manner and then finish polished with industrial diamond paste of ½ μm grit size. The specimen was then flushed with ethyl alcohol and washed with acetone in an ultrasonic cleaner before being examined and photographed under an

Olympus Optical Microscope at suitable magnification for the assessment of the average inter-inclusion particle spacing. The specimens were subsequently etched in 2% Nital solution for 15 to 30 seconds, flushed with ethyl alcohol and washed again in acetone in an ultra-sonic cleaner to provide micrographs for the purpose of grain size measurement and the identification of the type of non-metallic inclusion particle.

The grain size was estimated by the Linear Intercept method as illustrated in Plate 7.4. Briefly, this method involved drawing parallel straight lines of fixed total length, L , on the micrographs and then counting the number of intercepts, N_i , made by these lines with grain boundaries. The average grain diameter, d_g , was calculated as

$$d_g = \frac{L}{N_i \times (\text{magnification factor})} \qquad (7.6.1)$$

A minimum of 300 interceptions per micrograph was counted to ensure an accurate assessment of the grain diameter.

The parallel line intercept method could not be used to measure the inclusion spacing because of the small sizes of the inclusion particles. Instead, the inclusion spacings were estimated by a modification of the ASTM grain size measurement method[154]. This modified method measured the distance between intercepts made by drawing lines through the particles on the micrograph. Although this method may not possess the same degree of accuracy as the grain size measurement method or the data obtained by using the Quantimet

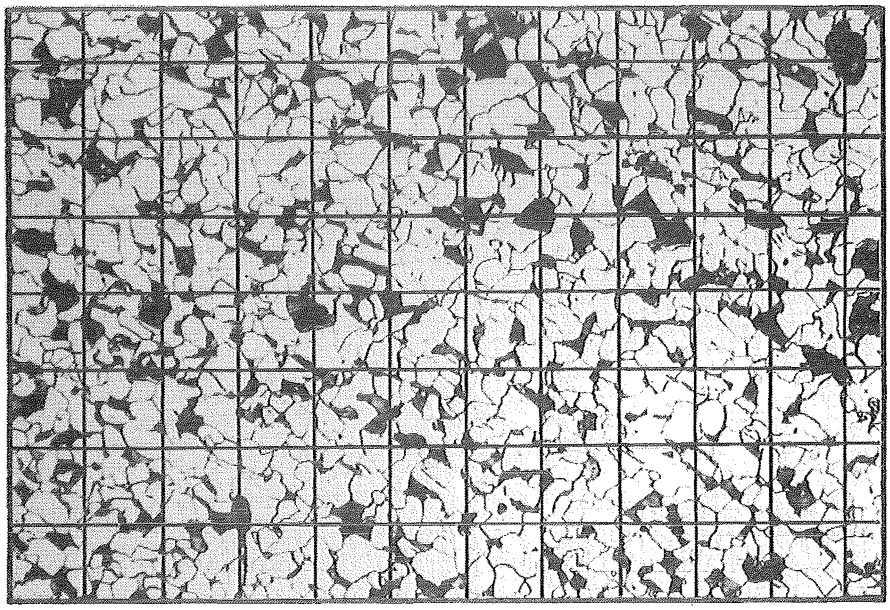

PLATE 7·4 TYPICAL EXAMPLE OF THE LINEAR INTERCEPT METHOD FOR GRAIN SIZE DETERMINATION.

microscope, a reasonably representative value was obtained by ensuring a minimum of 100 intercepts.

7.6.2 Scanning Electron Micro-Examination

The fracture surfaces of broken fracture toughness test specimens were examined under the Jeol JSM 35 Scanning Electron Microscope with main objective of determining the mode of separation at the instance of initial crack extension. In the cases of unusual fracture appearance and also when ductile fracture occurred, the chemical composition of the fracture surface was qualitatively assessed by the Energy Dispersion Analyser of the Jeol JSM 35 Scanning Electron Microscope.

7.7 Micro-Examination Of The Fatigue Crack-Tip Plastic Zone

10 mm thick compact tension specimens were prepared from a special high-Nitrogen-low-carbon steel for this examination. The chemical composition of this steel is given by wt-% as follows:

C	Si	S	P	Mn	Al_{sol}	N_{sol}
.060	.050	.043	.042	.210	.005	.012

The specimen was fatigue cracked with a maximum load amplitude of 2.5 KN until the ratio of crack length to specimen width, i.e. $\frac{a}{W}$ was approximately 0.5. On the completion of fatigue cracking, the specimen was subjected to an ageing treatment of 30 minutes at 250^{o}C. The aged specimen was then sectioned at mid-thickness by a

cut-off wheel to reveal the mid-thickness surface. This surface was then polished on coarse grade emery paper to remove a minimum of 0.5 mm of the top layer and subsequently polished in the usual manner before finishing off with diamond paste of 0.5 μm grit. The polished specimen was then etched by immersion in Fry's reagent for 10 seconds. The Fry's reagent used had the following composition

$CuCl_2$	HCl	H_2O
45 g	180 ml	100 ml

After etching, the specimen was flushed with ethyl alcohol and washed by acetone in an ultra-sonic cleaner. The specimen was then examined under the Olympus Optical Microscope and the Scanning Electron Microscope. Micrographs of the etched mid-thickness crack-tip area were prepared.

7.8 Summary

The objectives and the techniques of the experimental measurement of the fracture toughness and its related material properties of three low carbon steels have been presented. The results of these experiments will be presented and discussed in the next chapter.

CHAPTER EIGHT

RESULTS AND DISCUSSIONS

8.1 Accuracy Of Experimental Techniques

(a) Temperature Monitoring

As the temperature of the COD test specimens were not controlled by immersion in a liquid medium, it was necessary to assess the possible existence of a through-thickness temperature gradient in the test specimen. This uncertainty was investigated experimentally and the details are supplied in Appendix C. The results of this investigation, shown in Figure 8.1, revealed that within the relevant COD test temperature range of $-90^{o}C$ to $25^{o}C$, the maximum magnitude of through-thickness temperature variation was less than $1^{o}C$. This small temperature variation can be regarded as insignificant as far as the accuracy of the test temperature is concerned.

(b) Extensometer Calibration

The rubber crack-tip replication method was used to calibrate the extensometer with the actual crack opening displacement. This was necessary because the mounting of the extensometer on a pair of Nilo low expansion extension arms could have introduced a higher degree of uncertainty into the theoretical calibration methods which were originally proposed for direct extensometer mounting on the test specimen[23, 79]. The details of this experimental calibration are given in Appendix B and the results are shown in Figure

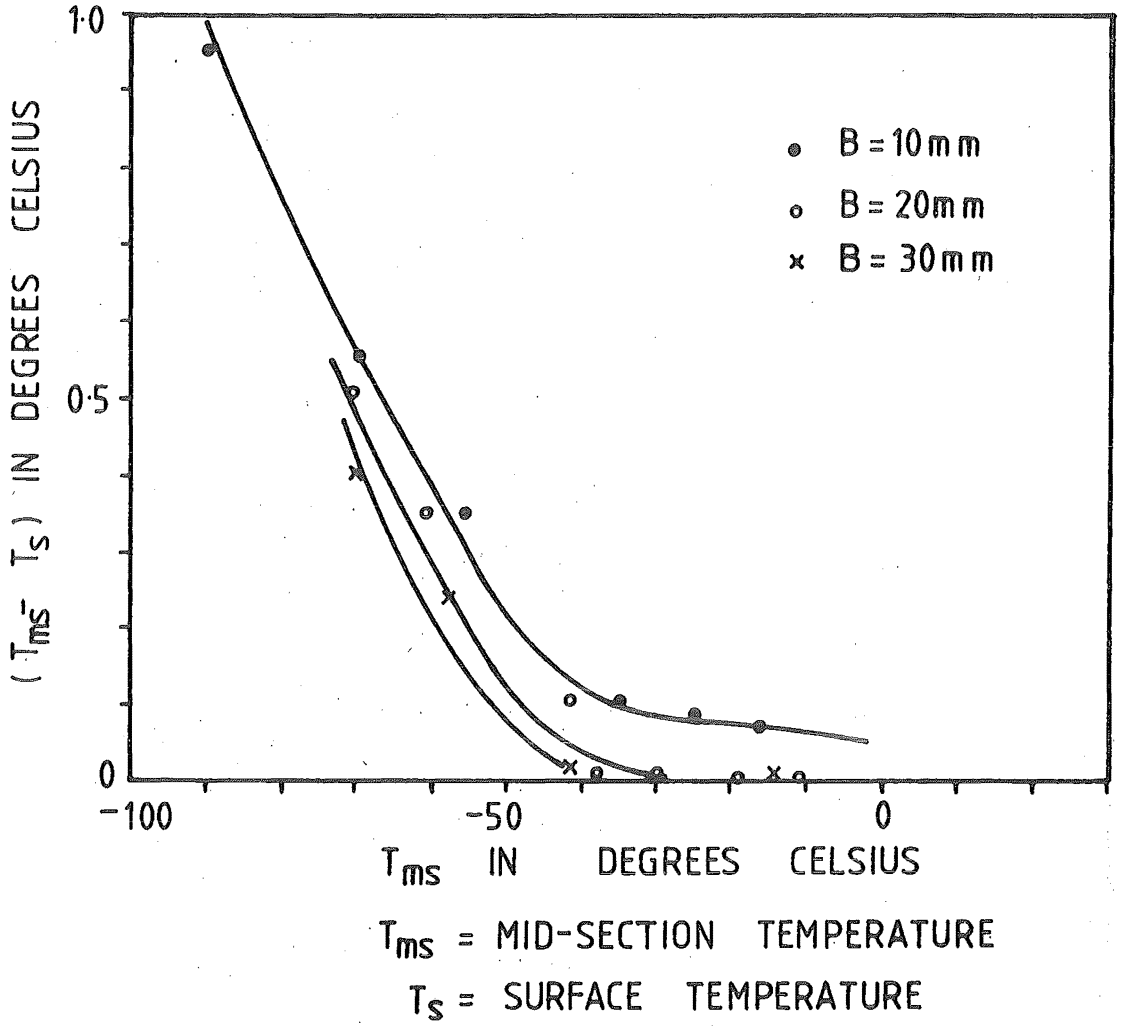

FIG. 8·1 GRAPH SHOWING THE THROUGH THICKNESS DIFFERENCE IN SURFACE AND MID-SECTION TEMPERATURES OF COD TEST SPECIMENS AFTER 15 MINUTES AT TEMPERATURE

8.2. The results confirmed earlier reports that the location of the "hinge-point" of rotation initially varied with small scale yielding before finally settling down at a fixed distance ahead of the crack-tip after large scale yielding[80, 81]. It can be seen that satisfactory calibration curves were obtained for the different sizes of experimental steel specimen and that the calibration of the 10 mm specimens was independent of the type of steels used. The results of further experimental calibration conducted with the Ti-added Grade 275 Steel with slot-width of:

(i) fatigue crack magnitude

(ii) 300 μm

and (iii) 650 μm

are given in Figure 8.3. It can be seen that the calibration was not affected by the variation of the slot-width. Consequently, the calibration curve of Figure 8.2 could be used for specimens with notches which were wider than the fatigue crack.

8.2 The Critical COD

The definition of the critical COD as the COD value measured at the initial instance of instability was found to be unambiguous when fracture occurred spontaneously without prior stable crack extension. However, when instability was either

(i) Spontaneous but preceded by sub-critical stable crack extension or

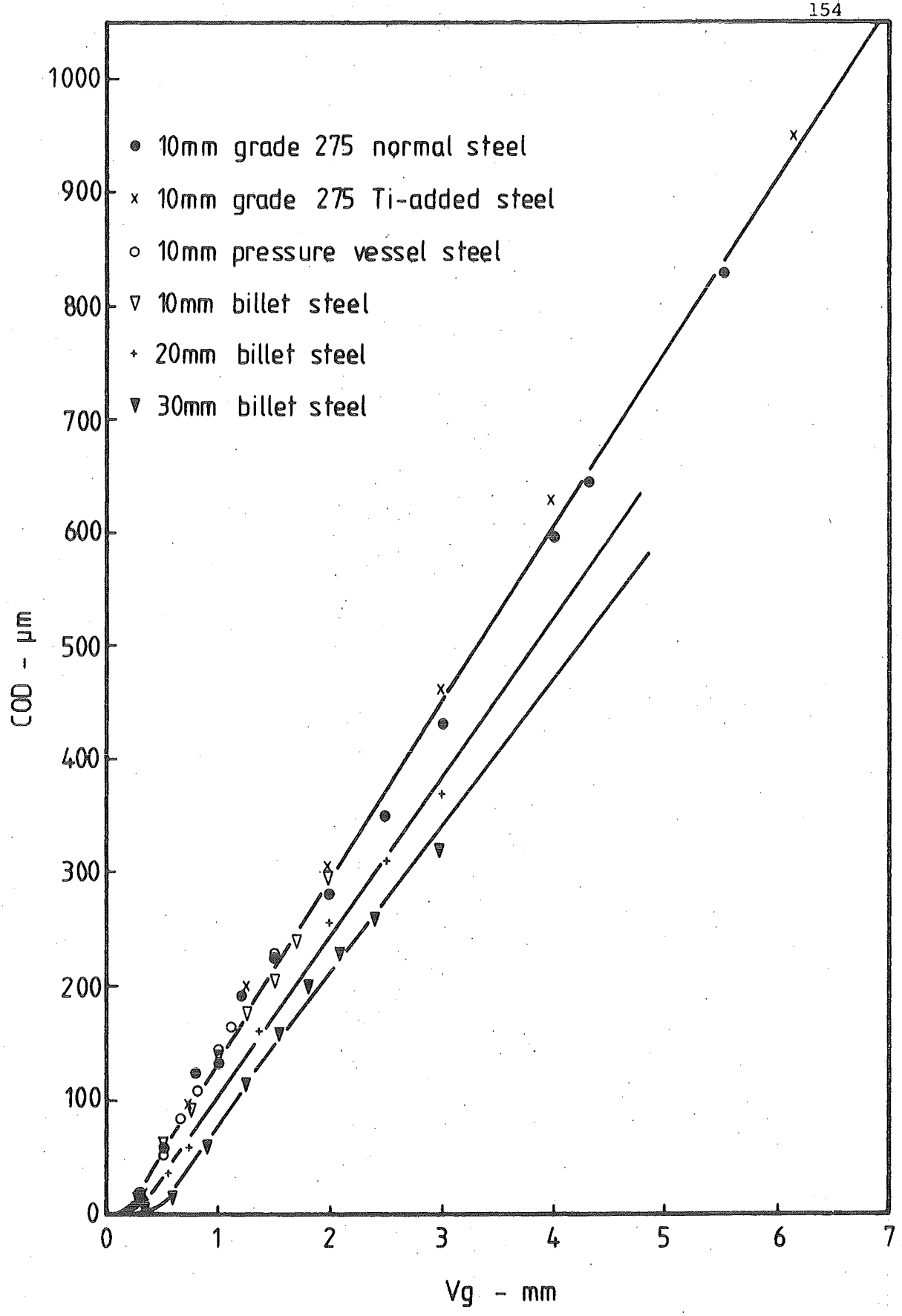

FIG 8·2 CALIBRATION OF FATIGUE PRE-CRACKED SPECIMENS

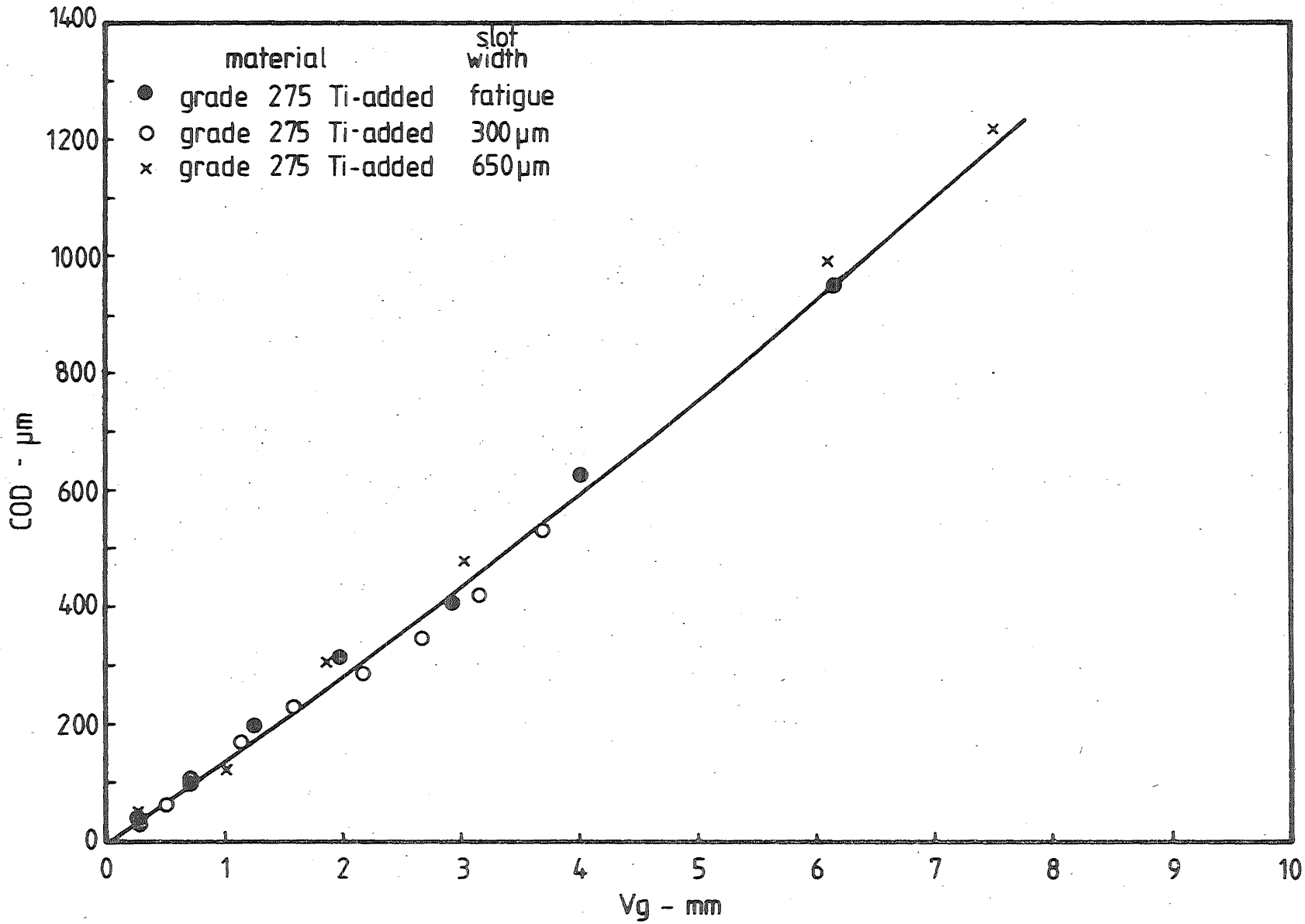

FIG 8·3 EFFECTS OF SLOT-WIDTH ON COD - Vg CALIBRATION

(ii) Defined as the attainment of maximum load instead of spontaneous instability,

the definition of the critical COD was found to be unclear. In this series of experiments, it was found that:

(i) In the Billet and Pressure Vessel Steels, the COD at the attainment of maximum load had to be used as the critical value when initial separation of the crack-tip material was by micro-void coalescence, i.e. when ductile crack extension was observed on the fracture surfaces of the broken specimens

(ii) In the Grade 275 Steels, initial stable crack extension by ductile tearing was observed in some specimens, before final instability by either spontaneous crack extension or defined by the attainment of maximum load.

In these cases, it was necessary to determine the critical COD measured at the instance of initial stable crack extension which is usually termed the initiation COD, δ_i . This was important because δ_i represents the COD value at which the crack-tip material became unstable. This initial crack extension COD could then be compared with the critical COD defined as the point of

(i) spontaneous instability with evidence of prior stable crack extension or

(ii) attainment of maximum load

so that the use of the latter two represents the critical event, i.e., the separation of the crack-tip material. This comparison was conducted experimentally by using the SIL-21 rubber to produce replica of the crack-tip in the manner described in Section 7.2.2.b. It was found that in the Billet and Pressure Vessel steels, the COD at the attainment of maximum load, δ_m , gave a good estimate of the COD at initial crack extension, δ_i , even when the final instability was spontaneous with ample evidence of sub-critical stable crack extension. However, in the Grade 275 Steel, stable crack extension was found to have occurred prior to the attainment of maximum load. Consequently in this steel the COD defined by either

(i) The COD at spontaneous instability with evidence of stable crack extension

or (ii) The COD at the attainment of maximum load

did not provide meaningful data as far as the instability of the crack-tip material was concerned. However, these definitions of COD could have limited significance because they coincide with the instability of the test specimen. These observations are illustrated in Plates 8.1 and 8.2. Hence, it was found that

(i) In the Billet and Pressure Vessel Steels, the maximum load COD, δ_m , and the COD at spontaneous instability, δ_c , provided information that corresponded to the instability of the crack-tip material and therefore did not need correction.

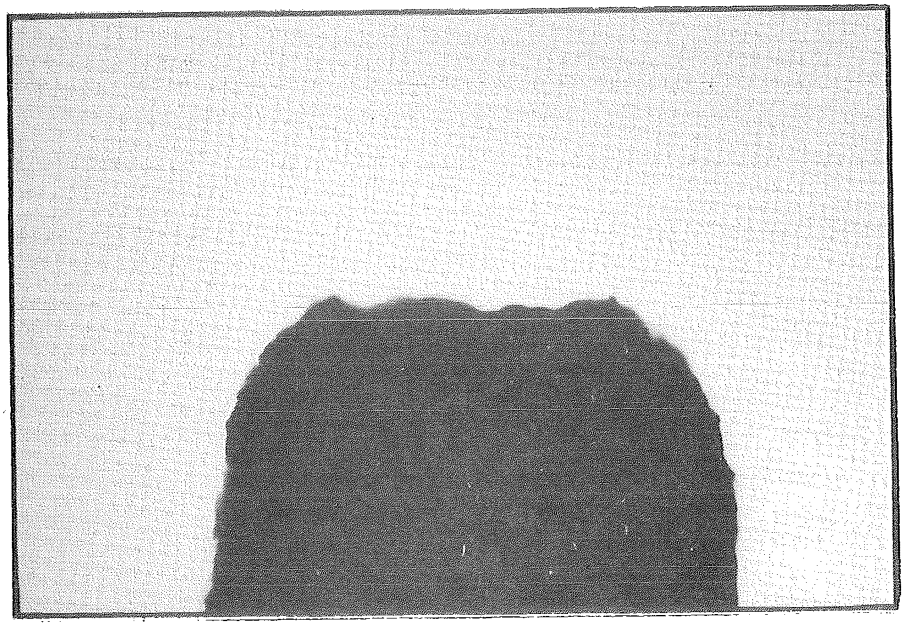

(a) at the attainment of maximum load (5·1kN) with COD = 330μm

(b) just past the maximum load (5·0kN) with COD = 400μm.

PLATE 8·1 CRACK TIP REPLICA OF A PRESSURE VESSEL STEEL COD TEST SPECIMEN WITH INITIAL SLOT-WIDTH = 300μm (×120)

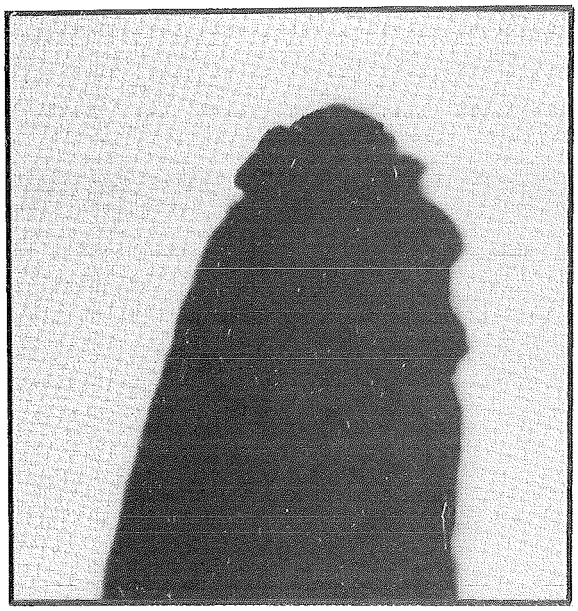

(a) just prior to crack-tip instability with COD = 276 μm, load = 5·7kN

(b) at crack-tip instability with COD = 347μm, load = 5·9kN

(c) at maximum load with COD = 580μm, load = 6·0kN.

PLATE 8·2 THE CRACK TIP REPLICA OF A NORMAL GRADE 275 STEEL COD TEST SPECIMEN OF INITIAL SLOT-WIDTH = FATIGUE CRACK. (×120)

(ii) In the Grade 275 Steel, the maximum load COD measured with evidence of sub-critical stable crack extension required correction. As the rubber crack-tip replication method could not be applied in sub-ambient temperature testing, an estimate of the initial crack extension COD level corresponding to micro-void coalescence was provided by the ambient temperature value. This value had to be added onto the results of the main COD testing described in Section 7.2.3

A possible explanation for the observed different behaviour of Grade 275 Steel from the other two experimental steels could lie with their crack plane orientation with respect to the direction of rolling of the raw material. The Billet and Pressure Vessel Steels were machined from the raw stock with the crack plane being parallel to the rolling direction, whilst the Grade 275 Steel specimen had its crack plan were perpendicular to the rolling direction (see Figure 7.2). Consequently, the morphology of the inclusion particles, expected to be predominantly MnS, can be schematically represented as shown in Figure 8.4, where the cross-sectional areas of the inclusion particles in the load-bearing direction of the Billet and Pressure Vessel steel specimens are larger than those of the Grade 275 steel specimens. This postulation was supported by the Scanning Electron Micrographs of the fracture surface of the broken COD test specimen of the three experimental steels shown in Plate 8.3. It can

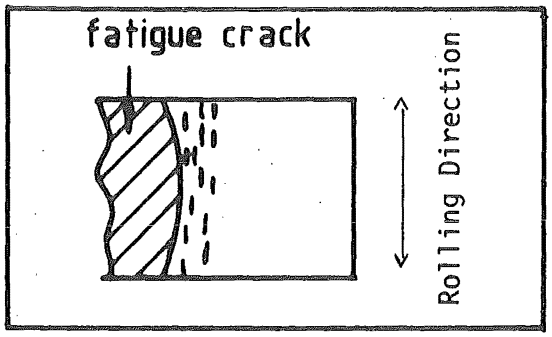

(a) Billet Steel

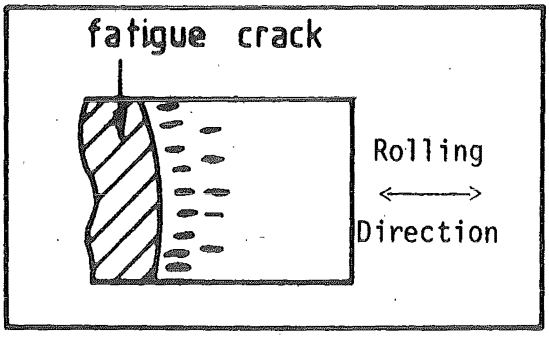

(b) P.V. STEEL

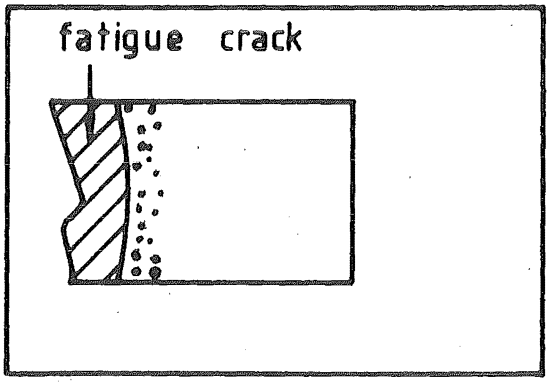

(c) GRADE 275 STEEL (crack plane perpendicular to direction of rolling)

FIG 8·4 MnS INCLUSION MORPHOLOGY IN THE CRACK PLANE

(a) stringers
(b) lenticules
(c) cross-section of stringers.

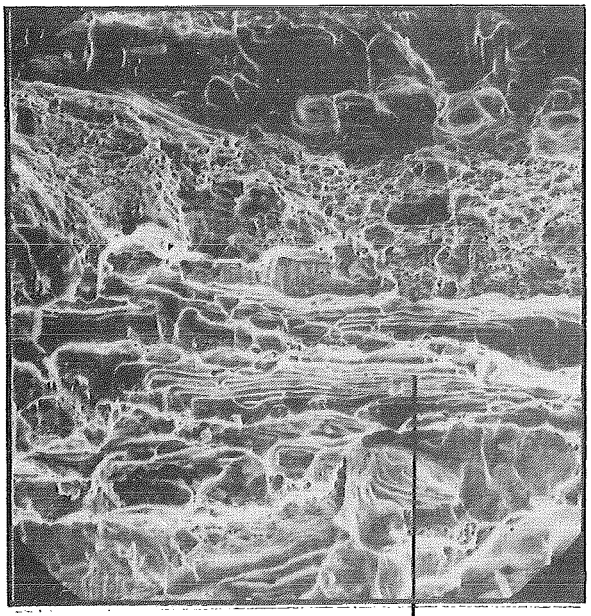

(a) the billet steel

ductile area

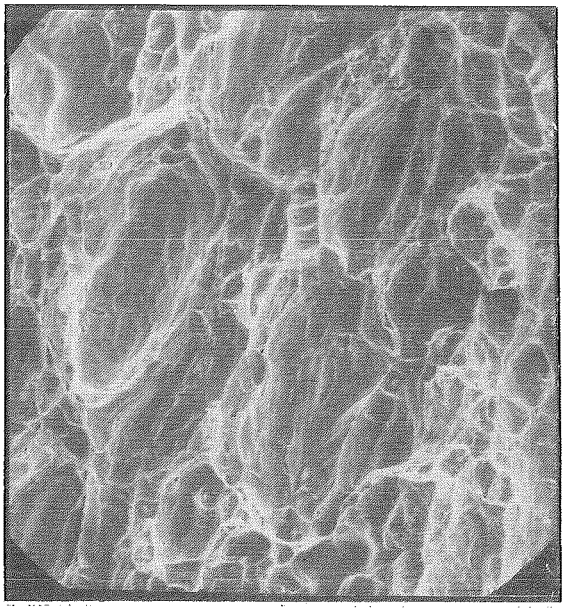

(b) the pressure vessel steel

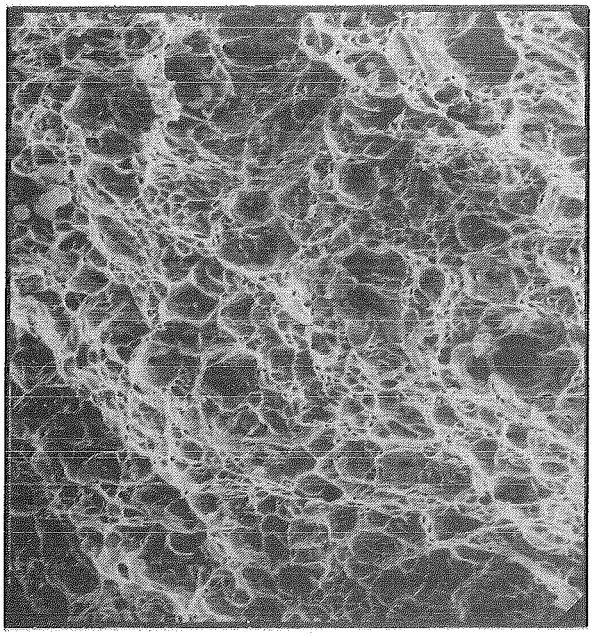

(c) the normal grade 275 steel

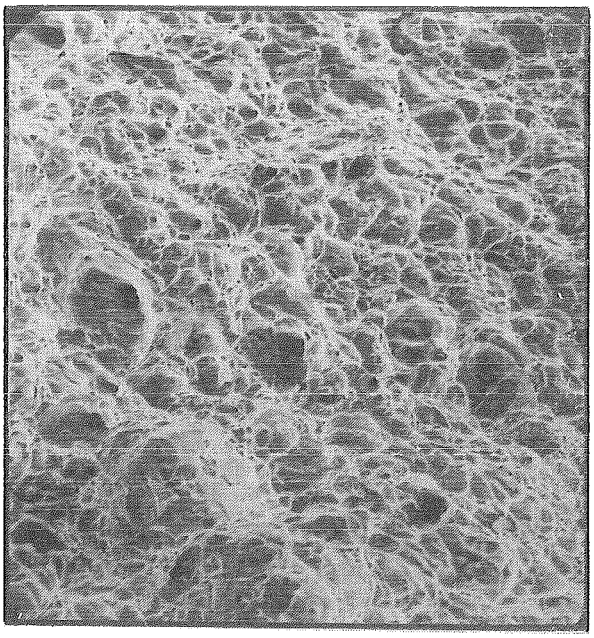

(d) the Ti-added grade 275 steel

PLATE 8·3 SCANNING ELECTRON MICROGRAPHS OF THE DUCTILE AREA OF THE FRACTURE SURFACES OF THE BROKEN COD TEST SPECIMENS

(×390)

be seen that the void size of the Grade 275 Steel was much smaller than those of the Billet and Pressure Vessel Steels. The Energy Dispersion X-Ray Analyses of these void areas are shown in Figures 8.5 to 8.8. The results of further examination by etching in 2% Nital solution are given in Plate 8.4. It can be seen that

(i) The voiding particles of the Billet Steel were Type II[155, 156] MnS "stringers"

(ii) The voiding particles of the Pressure Vessel Steel were type I[155, 156] MnS "lenticules"

(iii) The voiding particles of the Grade 275 Steel were type I[155, 156] MnS "stringers"

As the MnS inclusions had been reported to be the primary voiding particles during microvoid coalescence[18, 110], the different cross-sectional area of the load bearing MnS inclusion particles would result in the different reduction in area at the initial crack extension. This factor could have been responsible for the earlier observation that sub-critical crack extension occurred in the Grade 275 Steel, but not in the Billet or Pressure Vessel Steel because of the larger reduction in area suffered by the "transverse" specimens at the initial crack-tip instability.

In the COD testings of the Billet Steel specimens, the presence of large clusters of inclusion at critically sited areas, usually, just ahead of the crack front, had caused several invalid measurements. A typical example of the fracture surface of these speci-

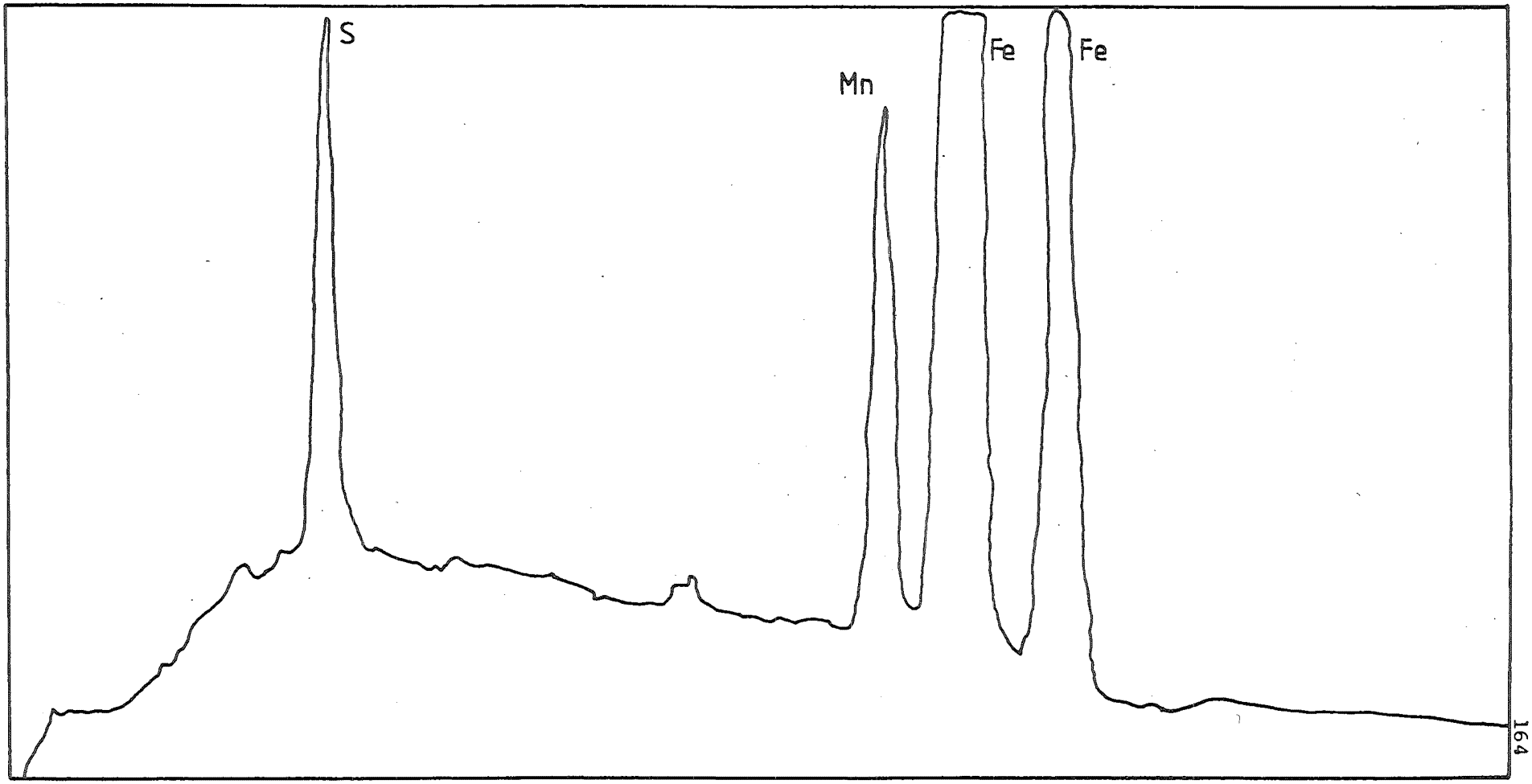

FIG. 8·5 THE ENERGY DISPERSION ANALYSIS OF THE VOID AREA OF A BILLET STEEL COD TEST SPECIMEN

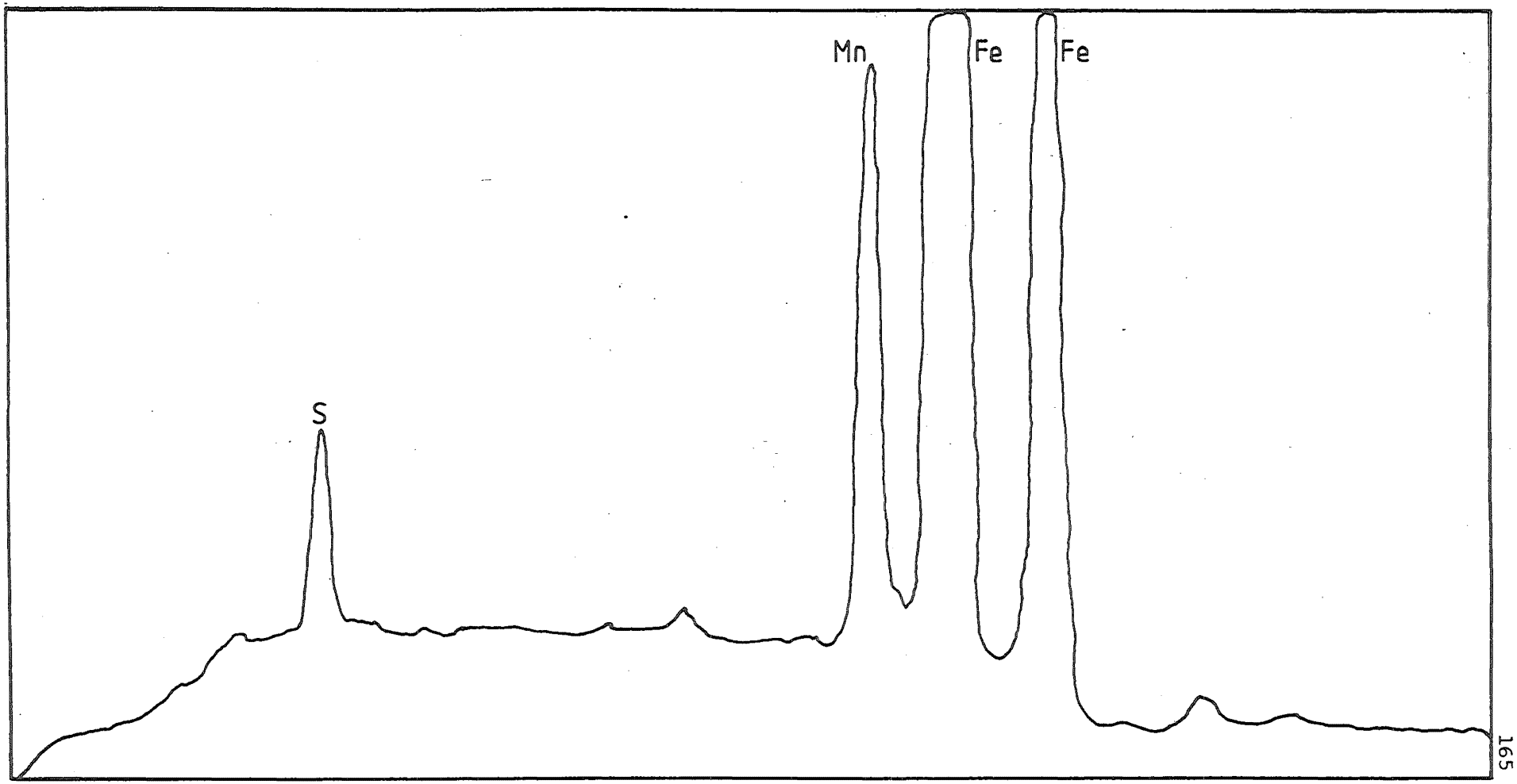

FIG 8·6 ENERGY DISPERSION ANALYSIS OF THE VOID AREA OF A PRESSURE VESSEL STEEL COD TEST SPECIMEN

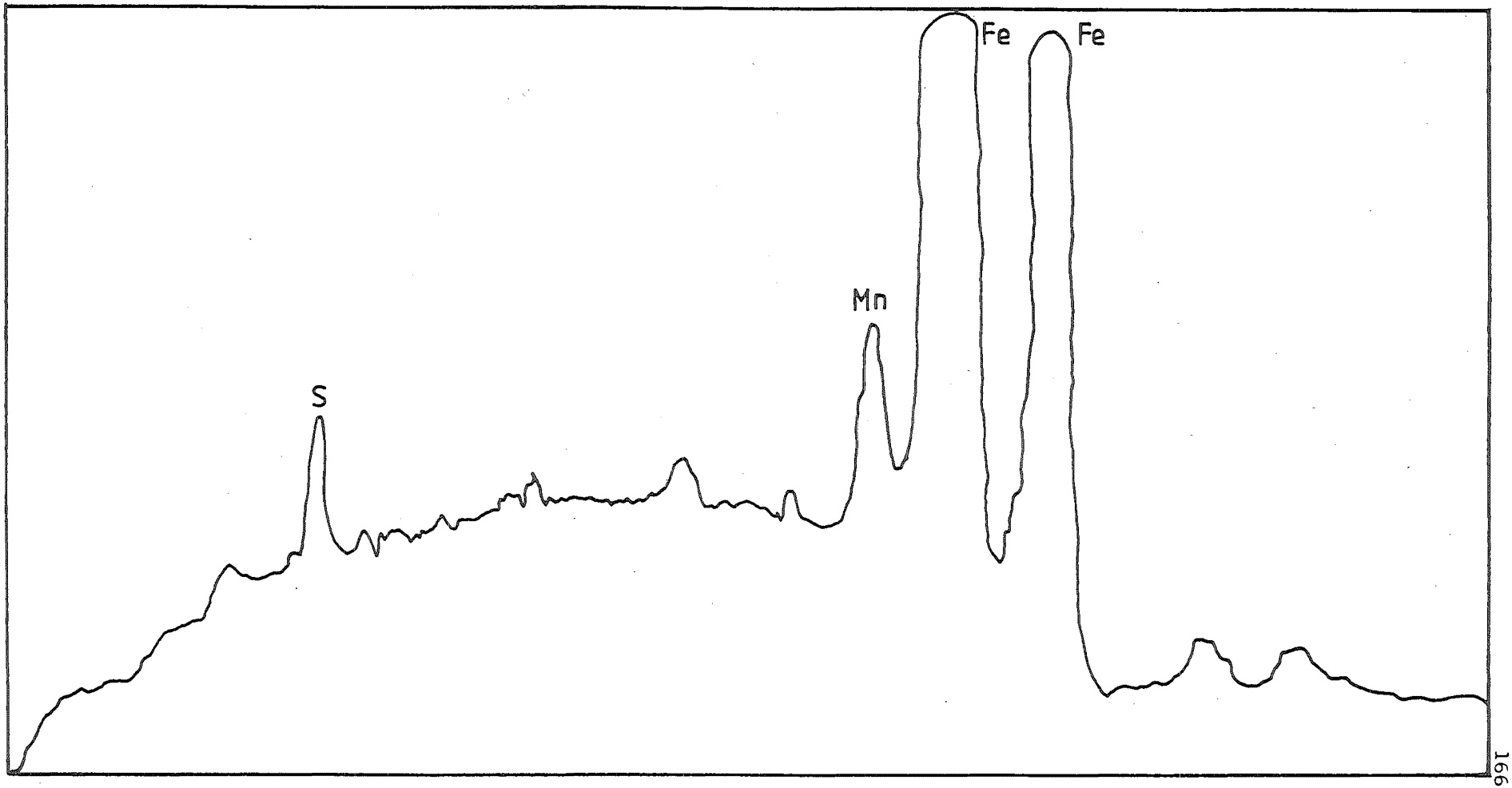

FIG 8·7 ENERGY DISPERSION ANALYSIS OF THE VOID AREA OF A NORMAL GRADE 275 STEEL COD TEST SPECIMEN

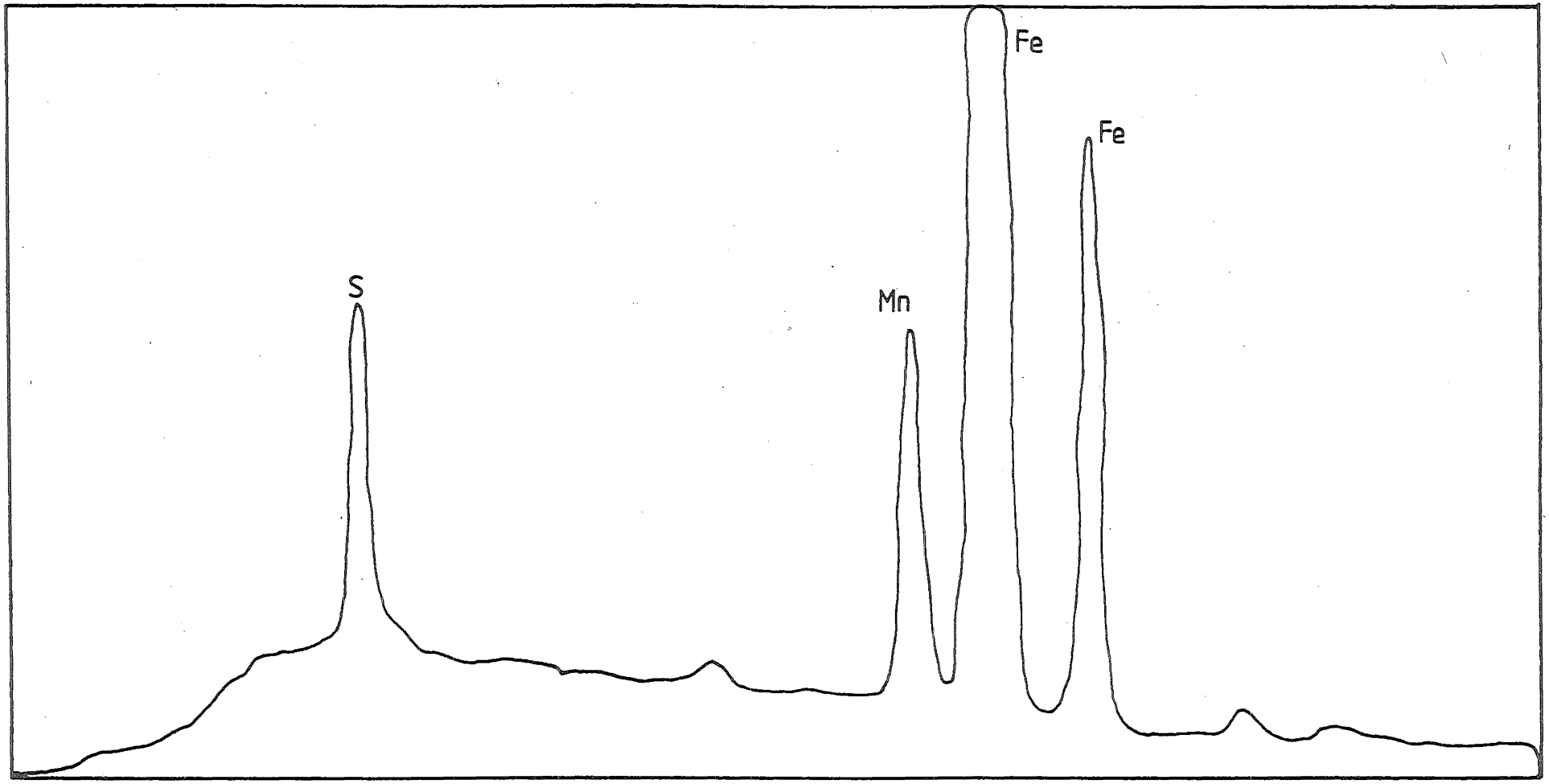

FIG 8·8 ENERGY DISPERSION ANALYSIS OF THE VOID AREA OF A Ti-added GRADE 275 STEEL COD TEST SPECIMEN

(a) billet steel (×2250) ⊙ rolling direction

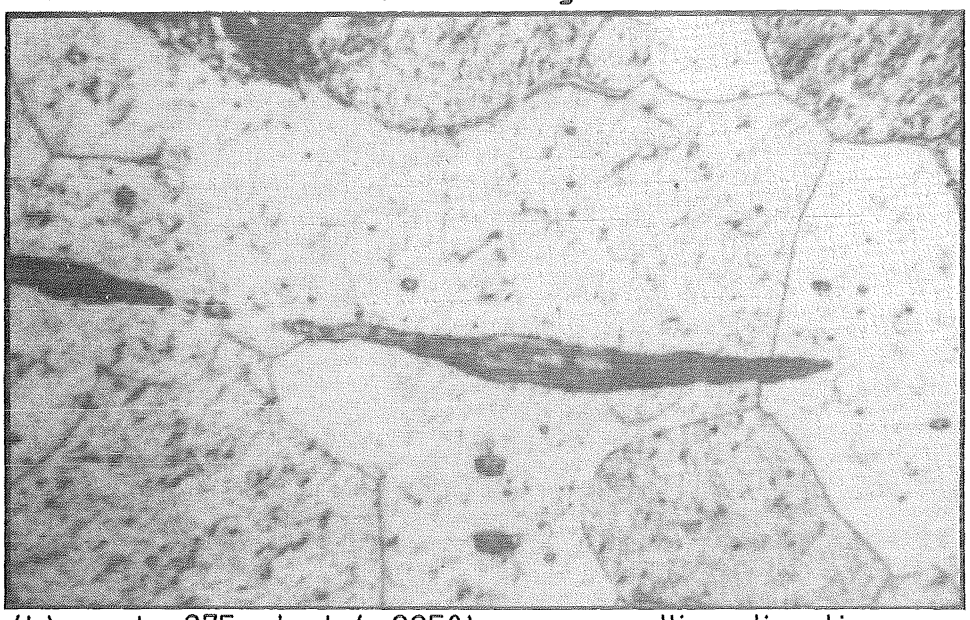

(b) grade 275 steel (×2250) ⟷ rolling direction

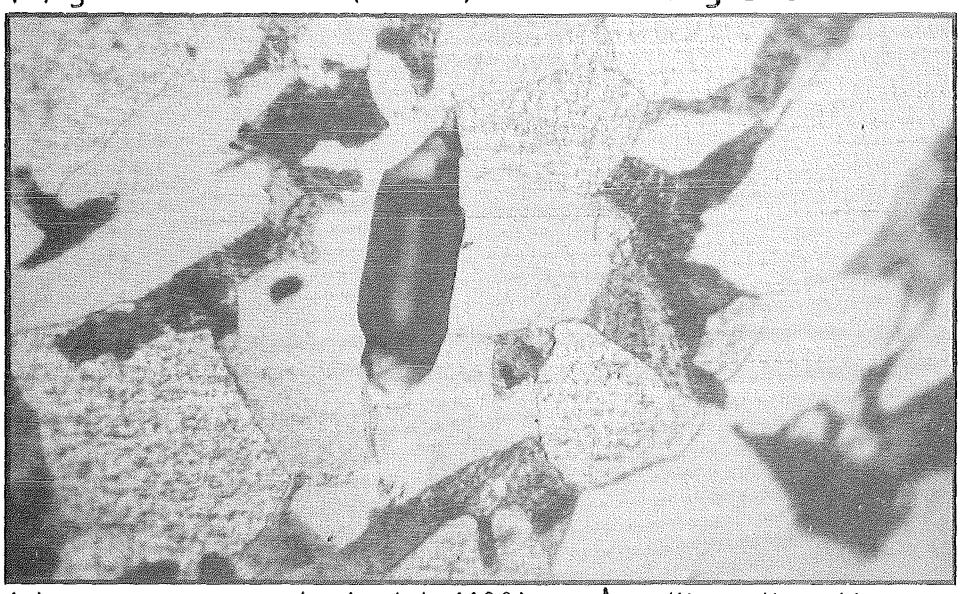

(c) pressure vessel steel (×1100) ↕ rolling direction

PLATE 8·4 MnS INCLUSIONS. (direction of rolling is indicated)

mens is shown in Plate 8.5. The chemical composition of the inclusion cluster was identified by the Energy Dispersion Analyser. These results given in Figures 8.9 to 8.11 show that the inclusions consisted mainly of MnS. The critical COD values of these specimens were found to be several times higher than normal. The close proximity of these inclusion cluster to the crack-tip had probably resulted in the measurement of the opening at these inclusions when decohesion between the ferrite matrix and the inclusion cluster occurred. Hence, the results obtained with these test specimens had to be considered as erroneous. This observation raised doubts on the applicability of the COD method in assessing the fracture toughness of such material because the fracture toughness measured with the "normal" test specimen may not represent the conservative level. Nevertheless, since these invalid COD values were higher than those obtained from "normal" test specimens, the "normal" fracture toughness value may still be used to impose a maximum flaw size for quality control purposes or to modify the critical design stress to allow for these large inclusion clusters.

8.3 The Thickness And Temperature Dependence Of Fracture Toughness Obtained By The COD Tests

The size criterion for valid ASTM K_{IC} test[3] was given as

$$a \text{ , } W - a \text{ , } B \geq 2.5 \left(\frac{K_Q}{\sigma_Y}\right)^2$$

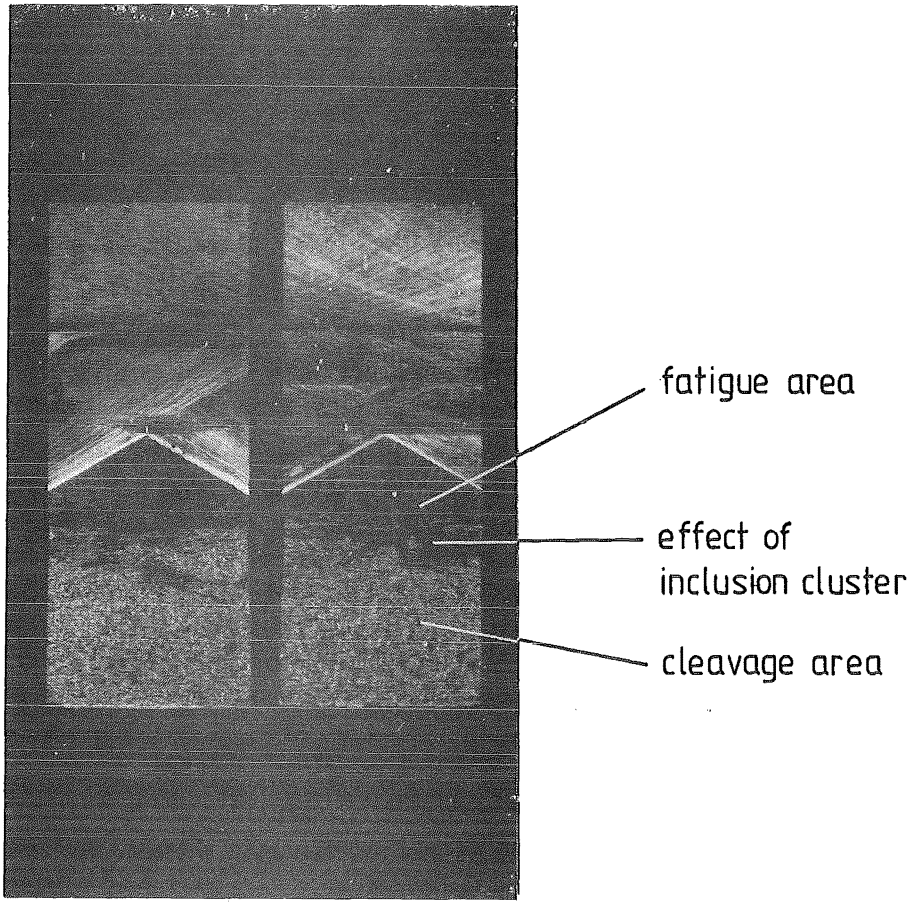

PLATE 8·5 FRACTURE SURFACE OF A 20mm AS-ROLLED BILLET STEEL SPECIMEN TESTED AT -55°C SHOWING THE EFFECT OF THE PRESENCE OF MnS INCLUSION CLUSTER AT THE CRACK TIP AREA.

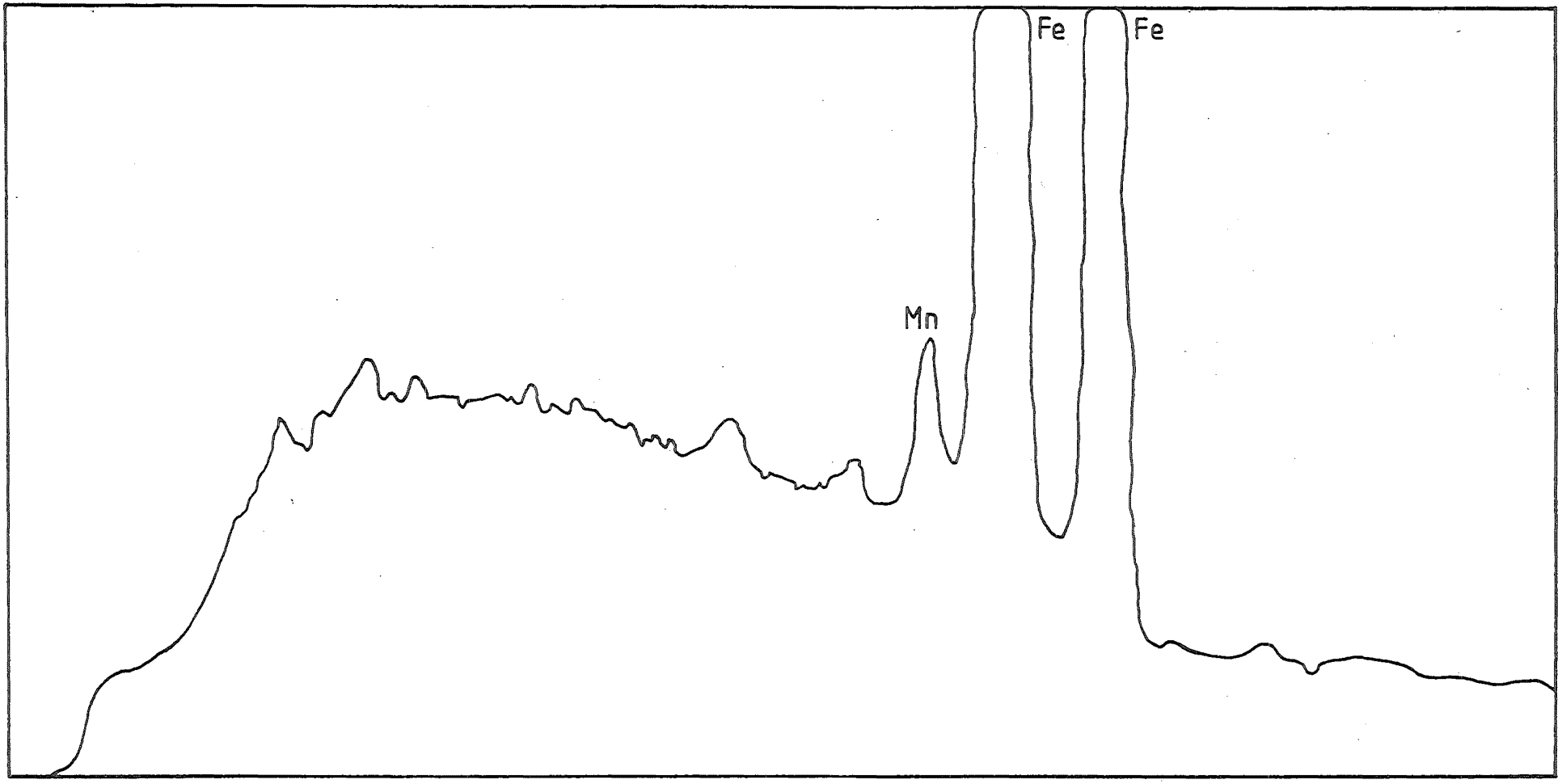

FIG 8·9 ENERGY DISPERSION ANALYSIS OF THE FATIGUE CRACK AREA OF PLATE 8·5.

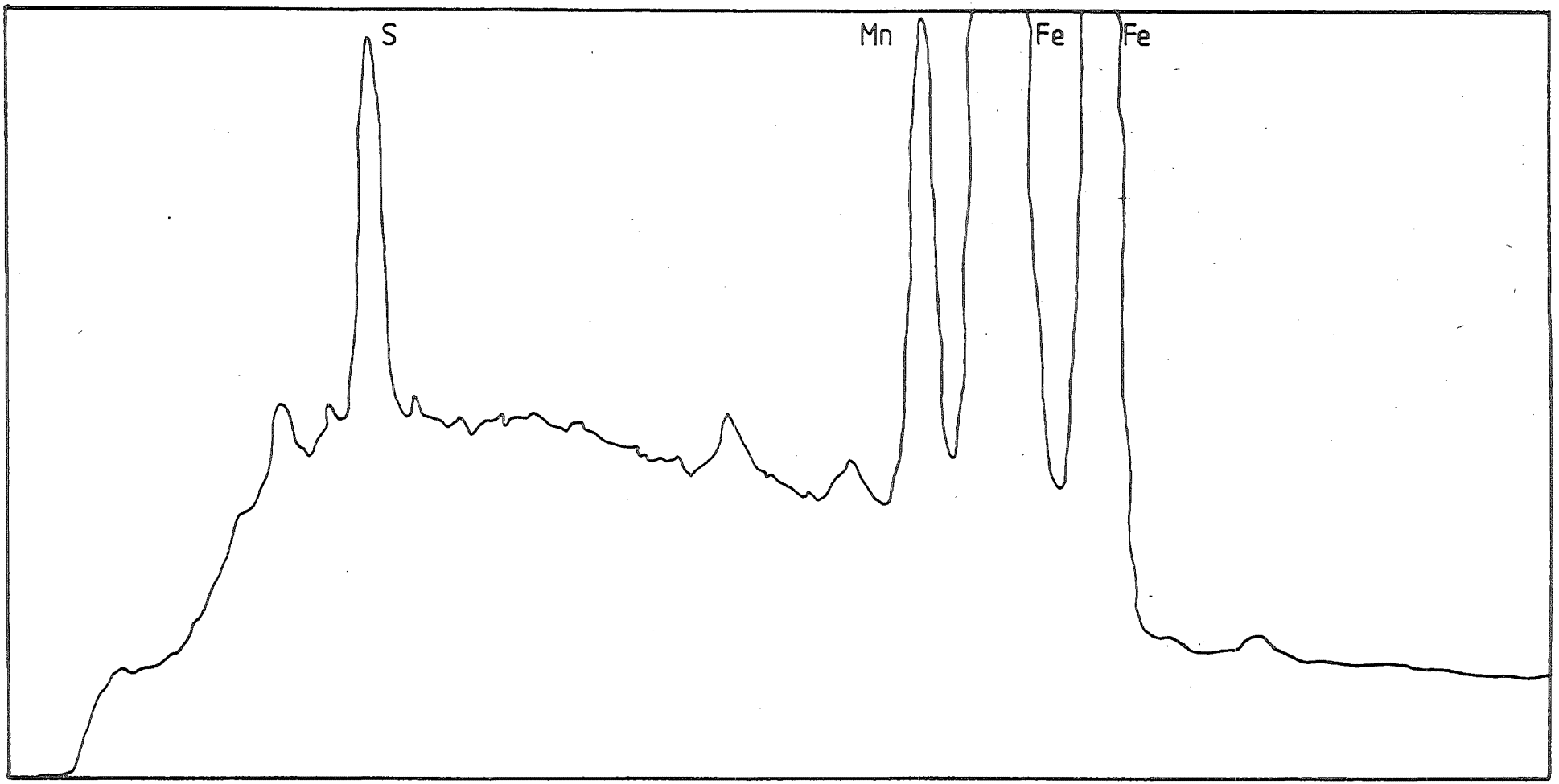

FIG 8·10 ENERGY DISPERSION ANALYSIS OF THE INCLUSION CLUSTER AREA OF PLATE 8·5

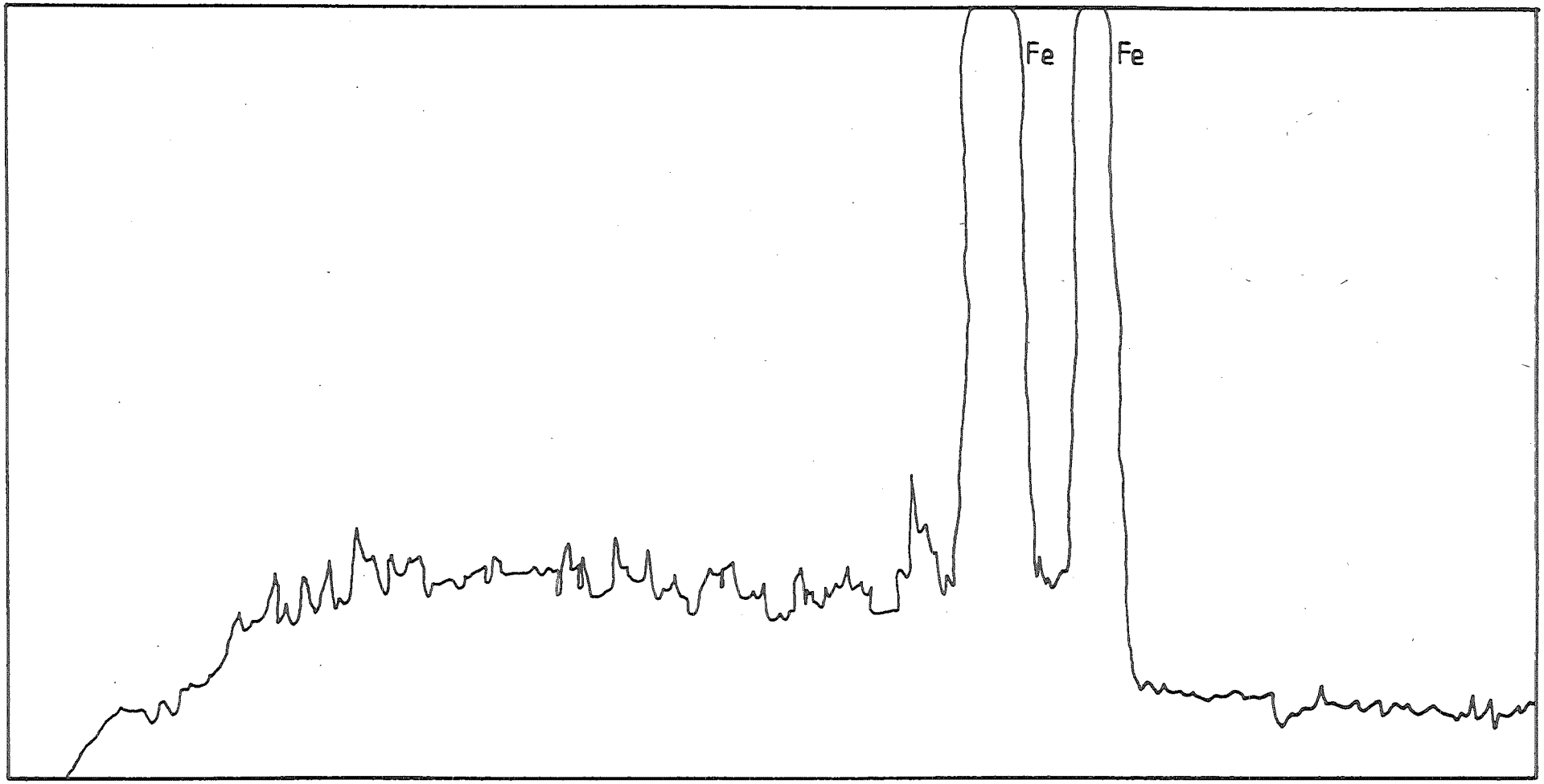

FIG 8·11 ENERGY DISPERION ANALYSIS OF THE CLEAVAGE AREA OF PLATE 8·5

where a is the crack length

W - a is the uncracked ligament length

B is the specimen thickness

K_Q is the apparent Critical Stress Intensity Factor

σ_Y is the yield stress.

Thus, by evaluating the apparent Critical Stress Intensity Factor of the largest specimen tested at the most brittle temperature, i.e. at the lowest end of the test temperature range of the COD tests by using Equation (7.2.1) where

$$K_Q = \frac{P_Q}{BW^{\frac{1}{2}}}\left\{ 29.6\left(\frac{a}{W}\right)^{\frac{1}{2}} - 185.5\left(\frac{a}{W}\right)^{\frac{3}{2}} + 655.7\left(\frac{a}{W}\right)^{\frac{5}{2}} - 1017\left(\frac{a}{W}\right)^{\frac{7}{2}} + 638.9\left(\frac{a}{W}\right)^{\frac{9}{2}} \right\}$$

where P_Q is the instability load

a is the crack length

B is the specimen thickness

W is the specimen width.

it was possible to determine whether the values of K_Q were valid according to Eqn. (7.2.2). The results showing the temperature dependence of COD of the three experimental steels are shown in Figures 8.12 to 8.16 and those showing the temperature dependence of the yield stresses of the three steels are given in Figures 8.17 to 8.19. Using data from these figures and also those supplied in Appendix E, the minimum specimen size, represented by the minimum thickness required for valid thickness independent "plane strain"

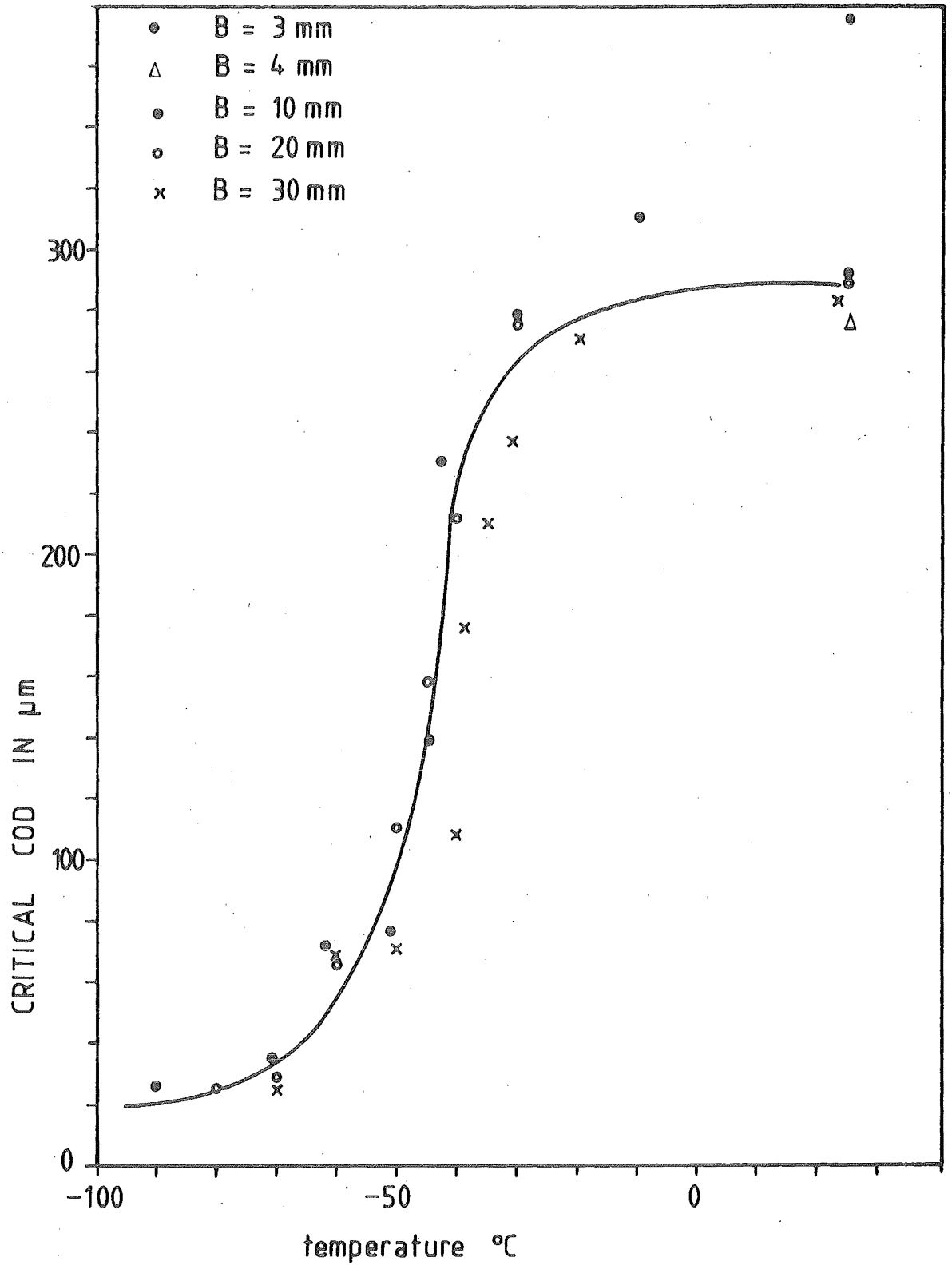

FIG 8·12 VARIATION OF CRITICAL COD WITH TEMPERATURE OF AS-ROLLED BILLET STEEL

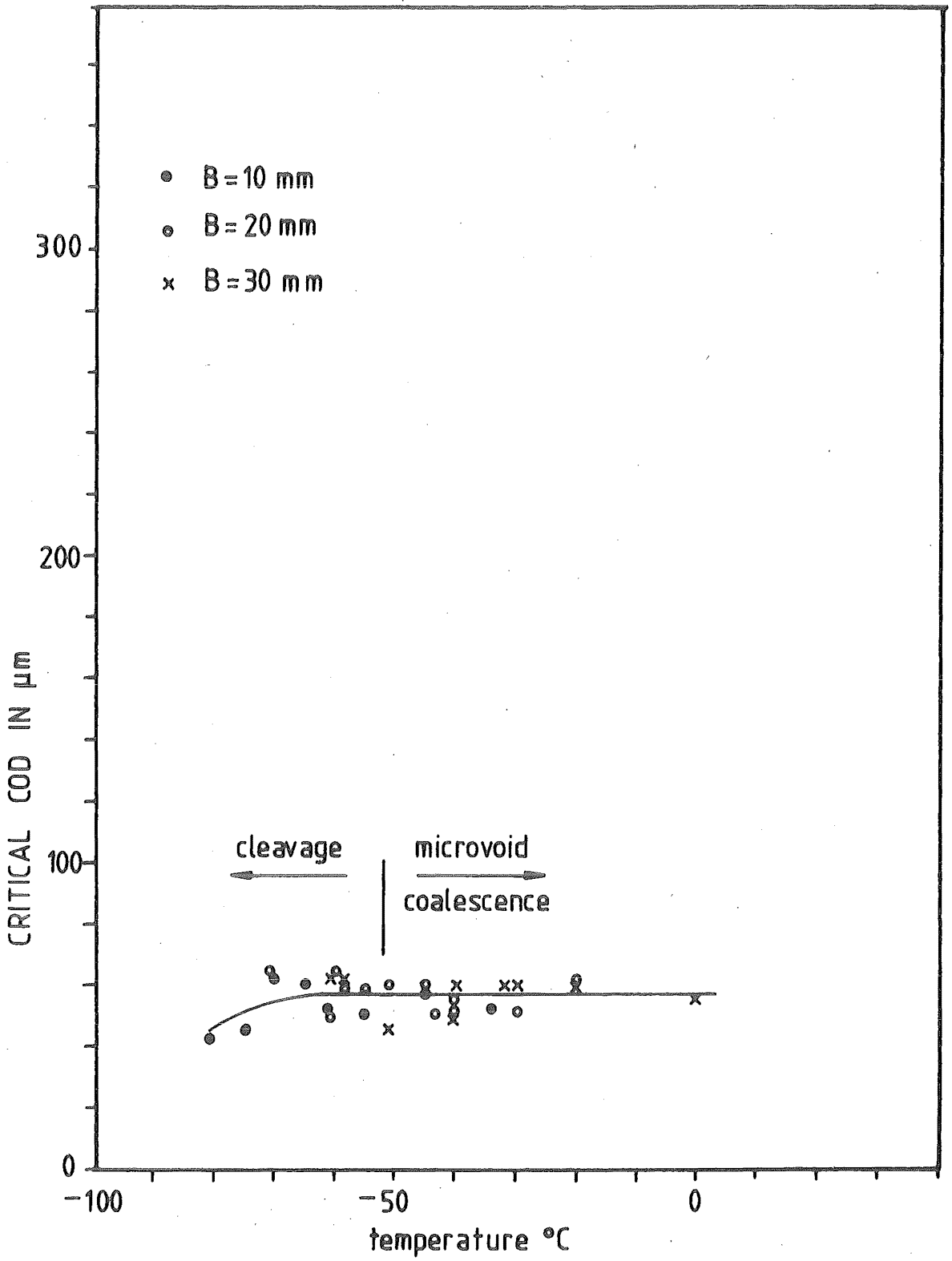

FIG 8·13 VARIATION OF CRITICAL COD WITH TEMPERATURE OF Hi-AlN BILLET STEEL

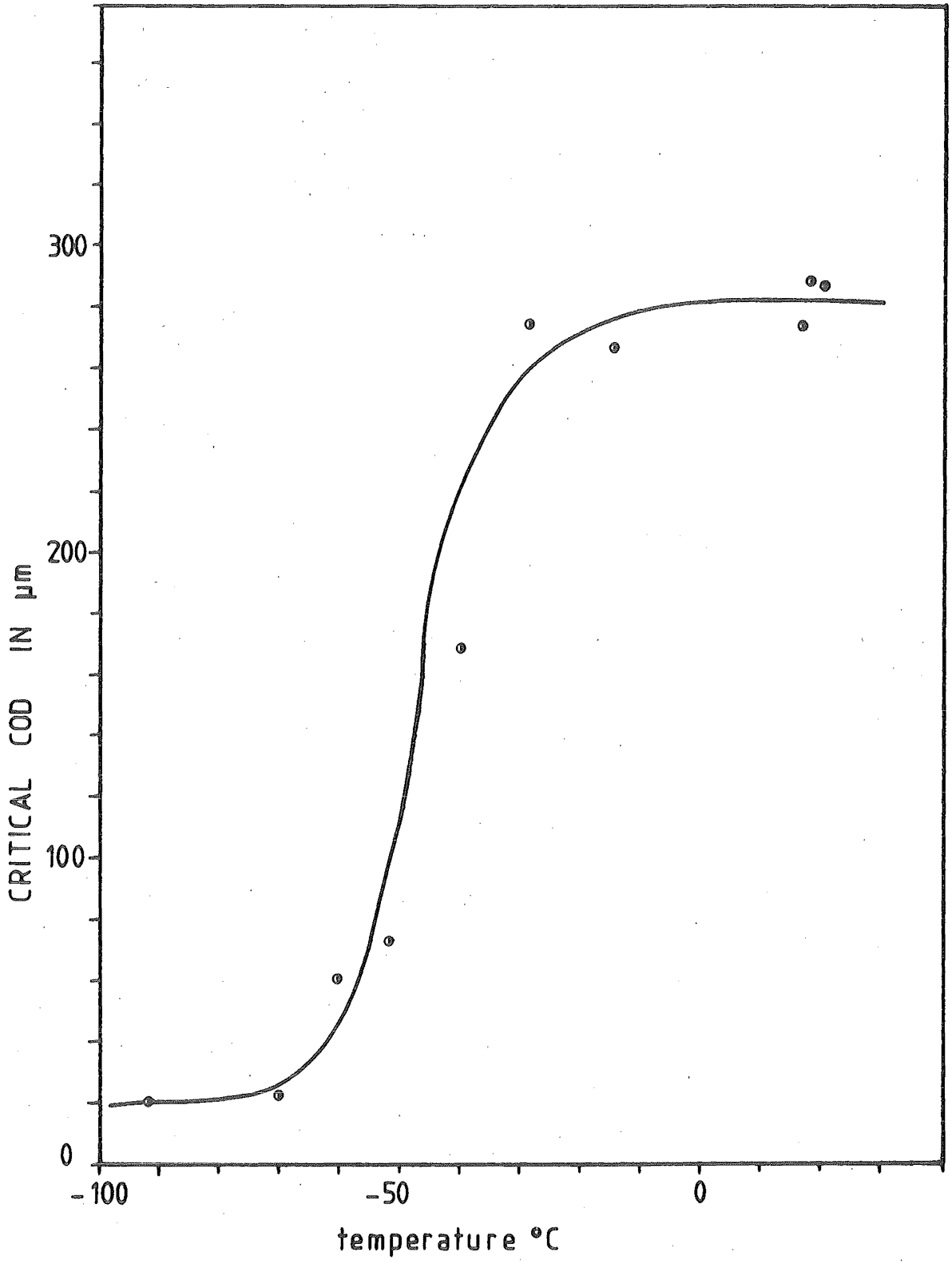

FIG 8·14 VARIATION OF CRITICAL COD WITH TEMPERATURE OF THE PRESSURE VESSEL STEEL

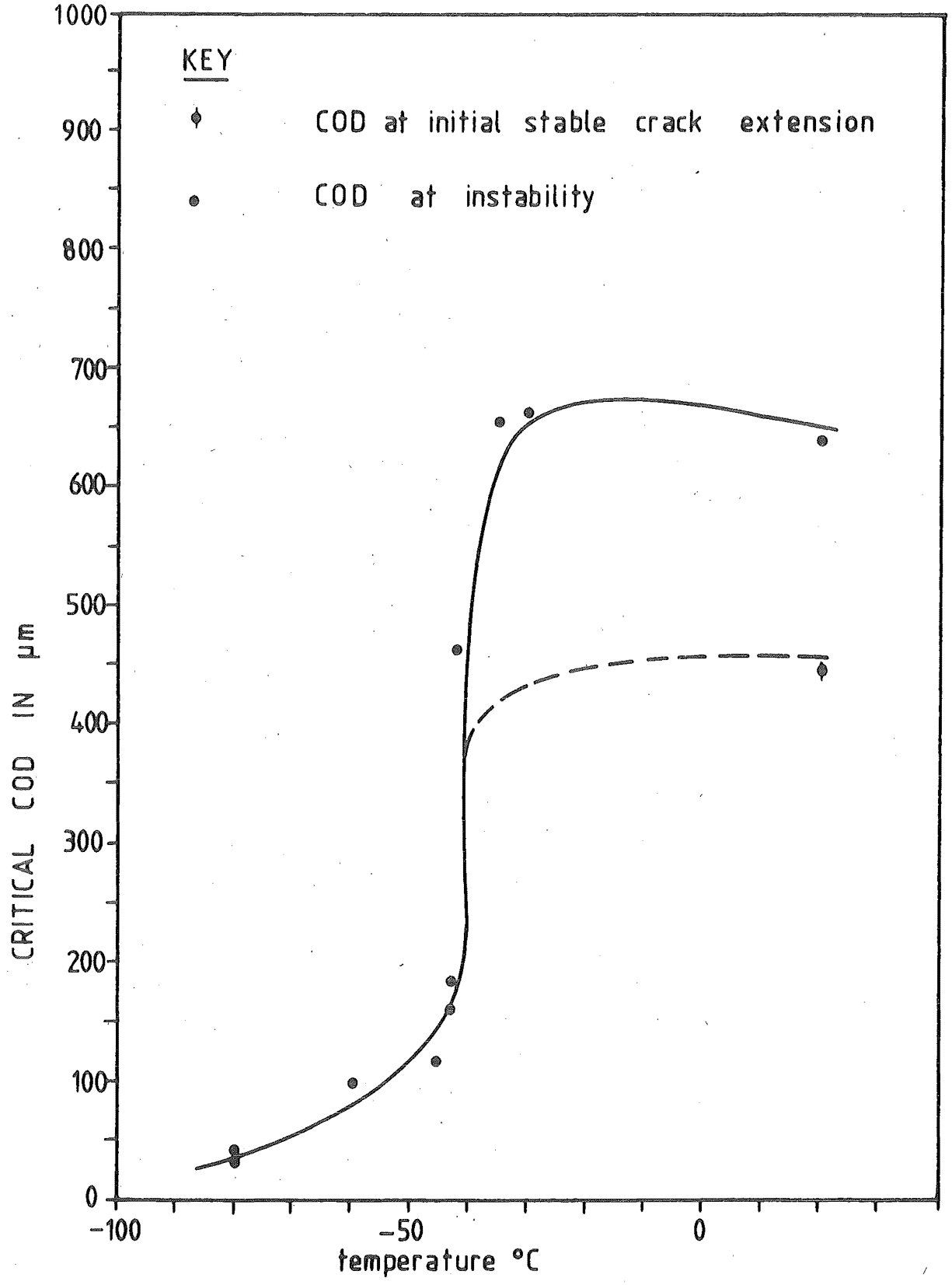

FIG 8·15 VARIATION OF CRITICAL COD WITH TEMPERATURE OF NORMAL GRADE 275 STEEL

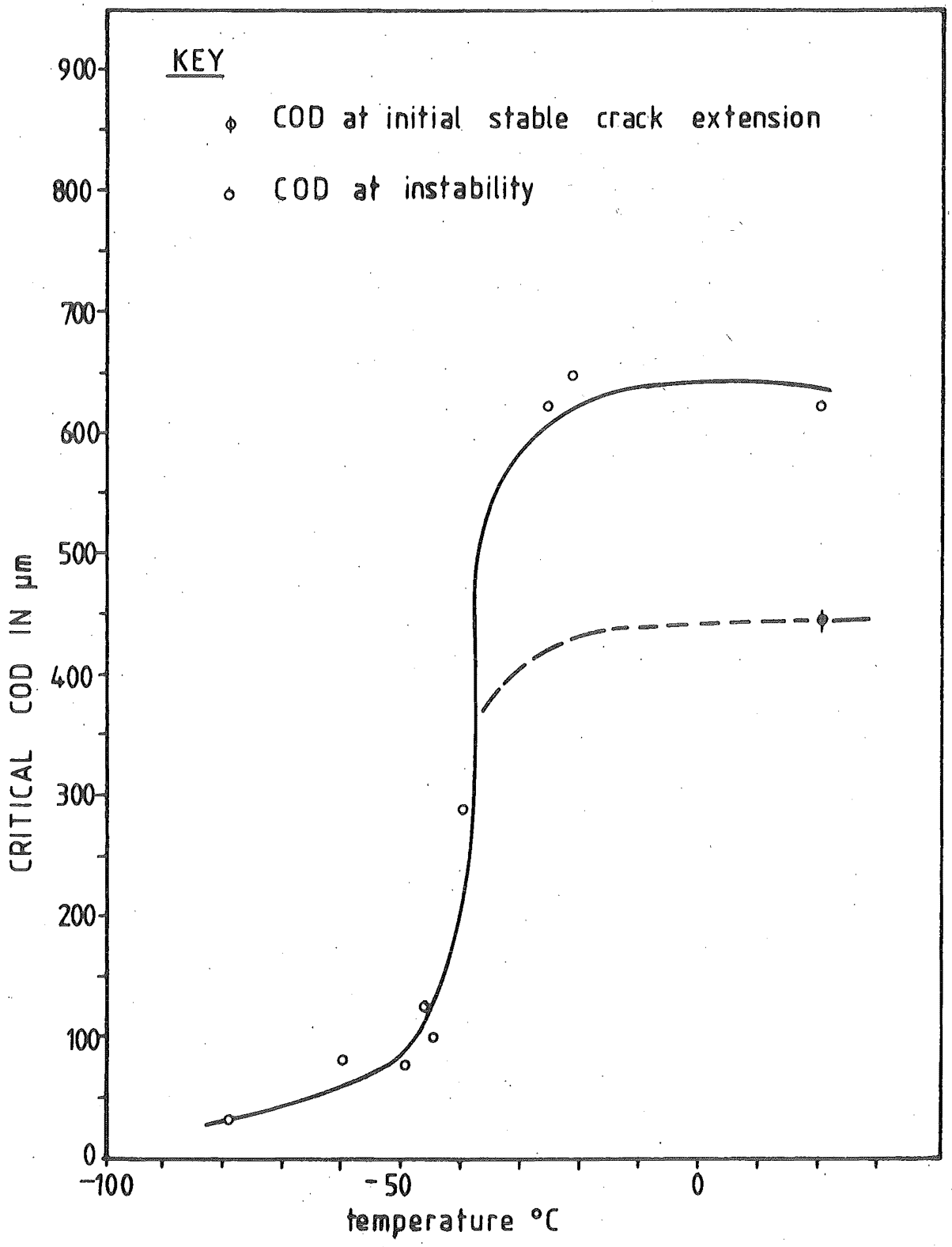

FIG 8·16 VARIATION OF CRITICAL COD WITH TEMPERATURE OF Ti-ADDED GRADE 275 STEEL

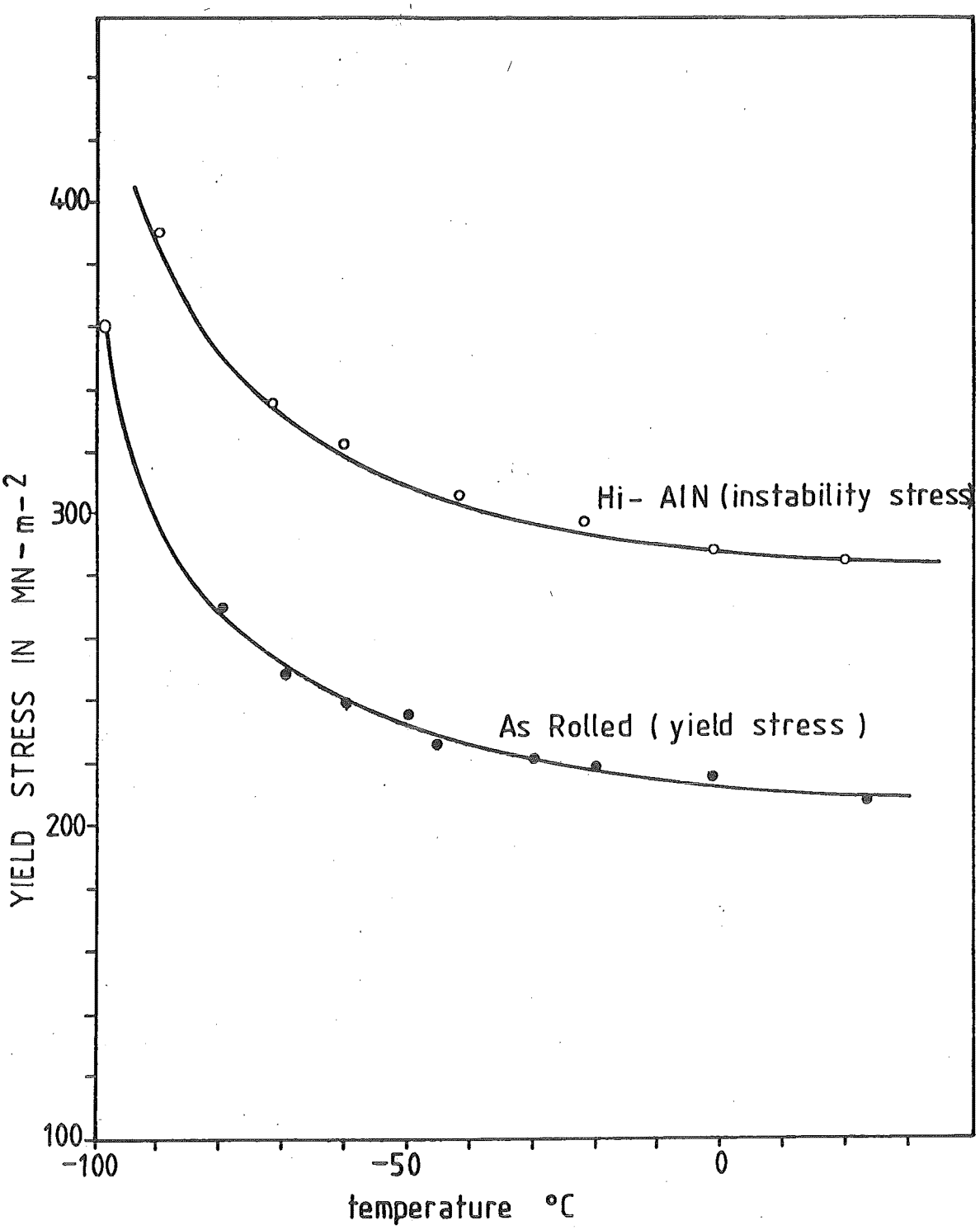

FIG 8·17 FLOW STRESS - TEMPERATURE RELATIONSHIP OF BILLET STEEL

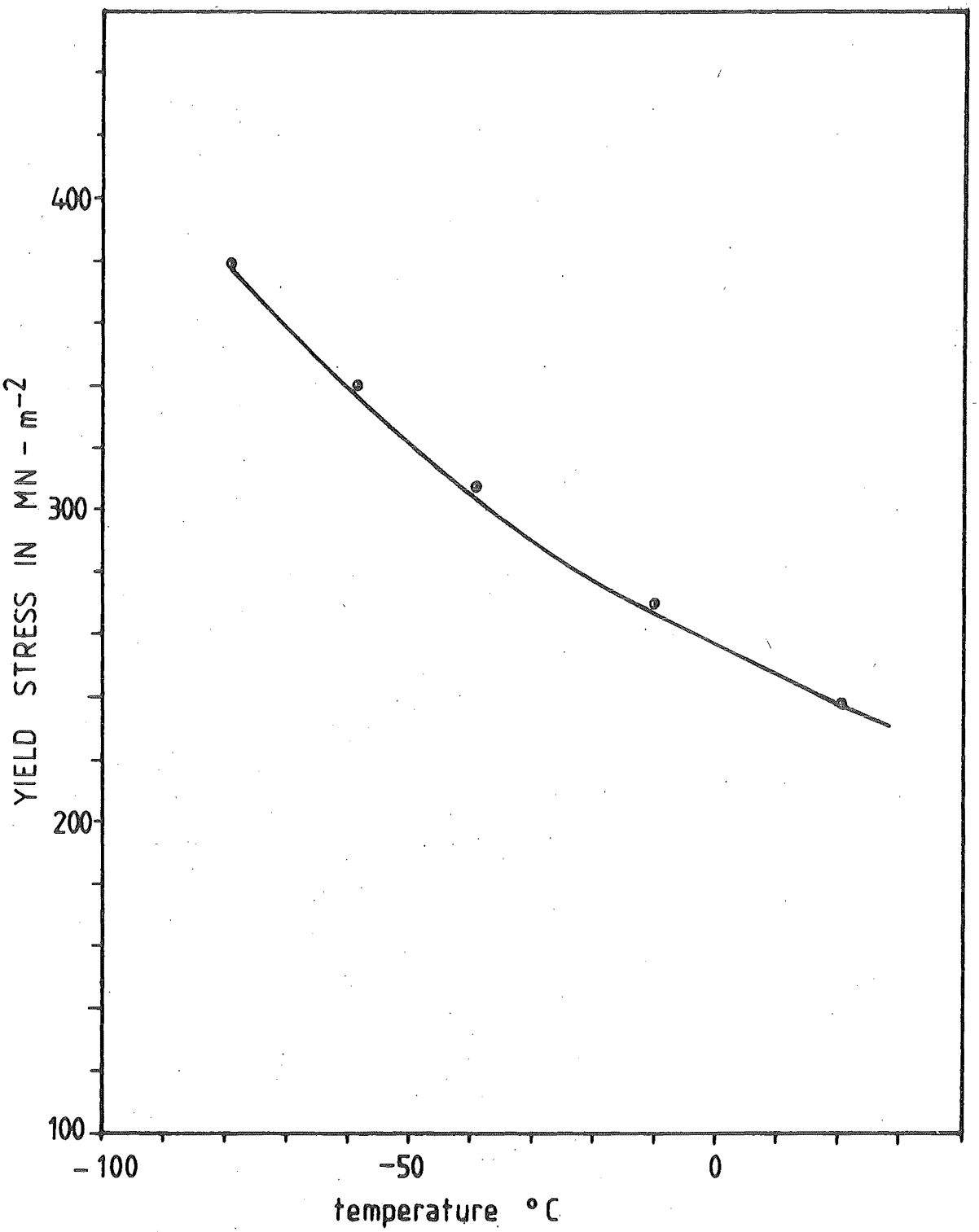

FIG 8·18 YIELD STRESS – TEMPERATURE RELATIONSHIP OF THE PRESSURE VESSEL STEEL

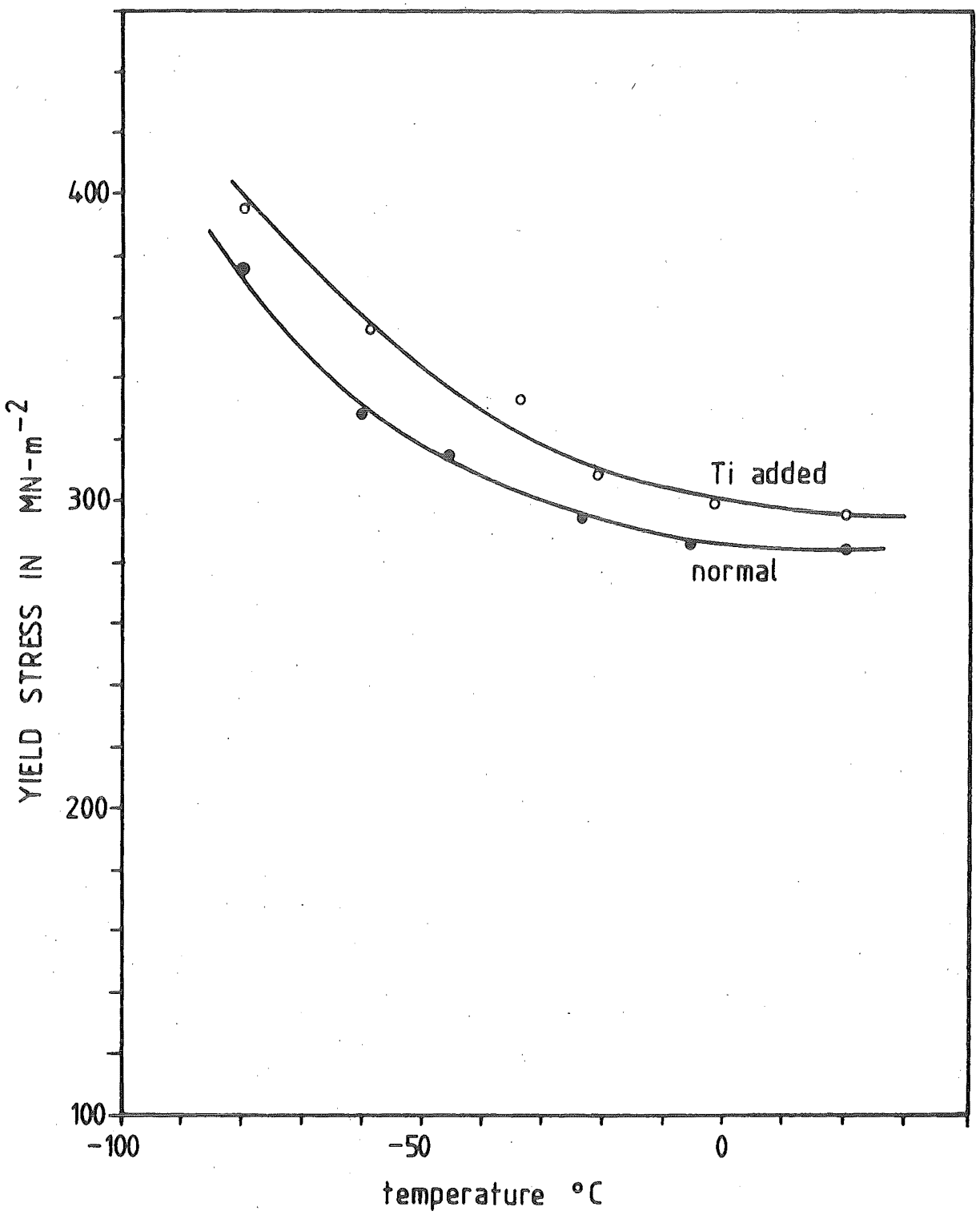

FIG 8·19 YIELD STRESS–TEMPERATURE RELATIONSHIP OF GRADE 275 STEEL

fracture toughness was calculated and the results are shown in Table 8.1. The use of the specimen thickness as a representative figure was possible because the relevant specimen dimensions, i.e. the crack length a, uncracked ligament length W - a and the specimen thickness B were specified to be nominally equal. It can be seen that even for the most brittle test condition, the specimen thickness B was still below the minimum plane strain specimen size given by $2.5\ (\frac{K_Q}{\sigma_Y})^2$. Hence, the standard ASTM K_{IC} test method was confirmed to be unsuitable for the fracture toughness testing of the experimental steels in the COD test temperature range.

An indication of the thickness independence of the COD test can be gauged from the results given in Figure 8.12. The specimen thickness of 10 mm was found to be sufficiently large to provide thickness independent fracture toughness value at both cleavage and ductile fracture because the critical COD of the 10, 20 and 30 mm thick specimens were similar at -70^{o}C and again at 25^{o}C. Larger scatter of results was observed in the vicinity of the transition temperature. However, this was not unexpected. Further investigation on the limit on specimen size for thickness independent COD-related fracture toughness were conducted with the As-Rolled Billet Steel specimens (see Section 7.2.2). This steel was used because it had the lowest yield stress and therefore should produce the conservative size limit if the ASTM size criterion of $2.5\ (\frac{K_Q}{\sigma_{LY}})^2$ was followed. The results of this investigation are

Steel Type	Test Temperature (^{o}C)	Apparent Fracture Toughness, K_Q ($MN\text{-}m^{-\frac{3}{2}}$)	Lower Yield Stress, σ_{LY} ($MN\text{-}m^{-2}$)	Minimum Specimen Thickness $B = 2.5\ (\frac{K_Q}{\sigma_{LY}})^2$ (mm)	Actual Specimen Thickness, B, (mm)
As-Rolled Billet	-70	85.7	238	324	30
Hi-AlN Billet	-60	90.4	328*	190	30
Pressure Vessel	-92	47.2	407	13.4	10
Normal Grade 275	-80	39.6	376	11.1	10
Ti-Added Grade 275	-80	43.5	395	12.1	10

* Instability Stress (see Section 7.3.2.a)

Table 8.1 Thickness Dependence Of The Apparent Fracture Toughness Calculated By The ASTM K_{IC} Test Method[3]

given in Figure 8.20. The fracture toughness, K_{crit} , was calculated using Equation (7.4.4) given as

$$K_{crit} = 0.4769 \, (\sigma_{LY} \delta_c)^{\frac{1}{2}} \ MN\text{-}m^{-\frac{3}{2}}$$

where σ_{LY} is the lower yield stress in $MN\text{-}m^{-2}$

δ_c is the critical COD in μm.

The fracture toughness results are given in Figure 8.21. These results showed that the fracture toughness became thickness independent when the specimen thickness, B , exceeded 7 mm. The corresponding value of the critical COD, defined as the COD at the instance of initial stable crack extension, δ_i , was found to be 300 μm (see Figure 8.20). Consequently, it can be shown that the thickness independence of fracture toughness required a minimum specimen thickness, B_{min} , given by

$$B_{min} \geq 23.3 \, \delta_i$$

This experimental limit on the minimum specimen thickness agreed well with the thickness limit predicted by using that of the J-Integral test method[10, 29] which was given in Equation (7.4.3) as

$$a \ , \ W - a \ , \ B \geq 25 \, \delta_c$$

where a is the crack length

W - a is the uncracked ligament length

B is the specimen thickness

δ_c is the critical COD at instability

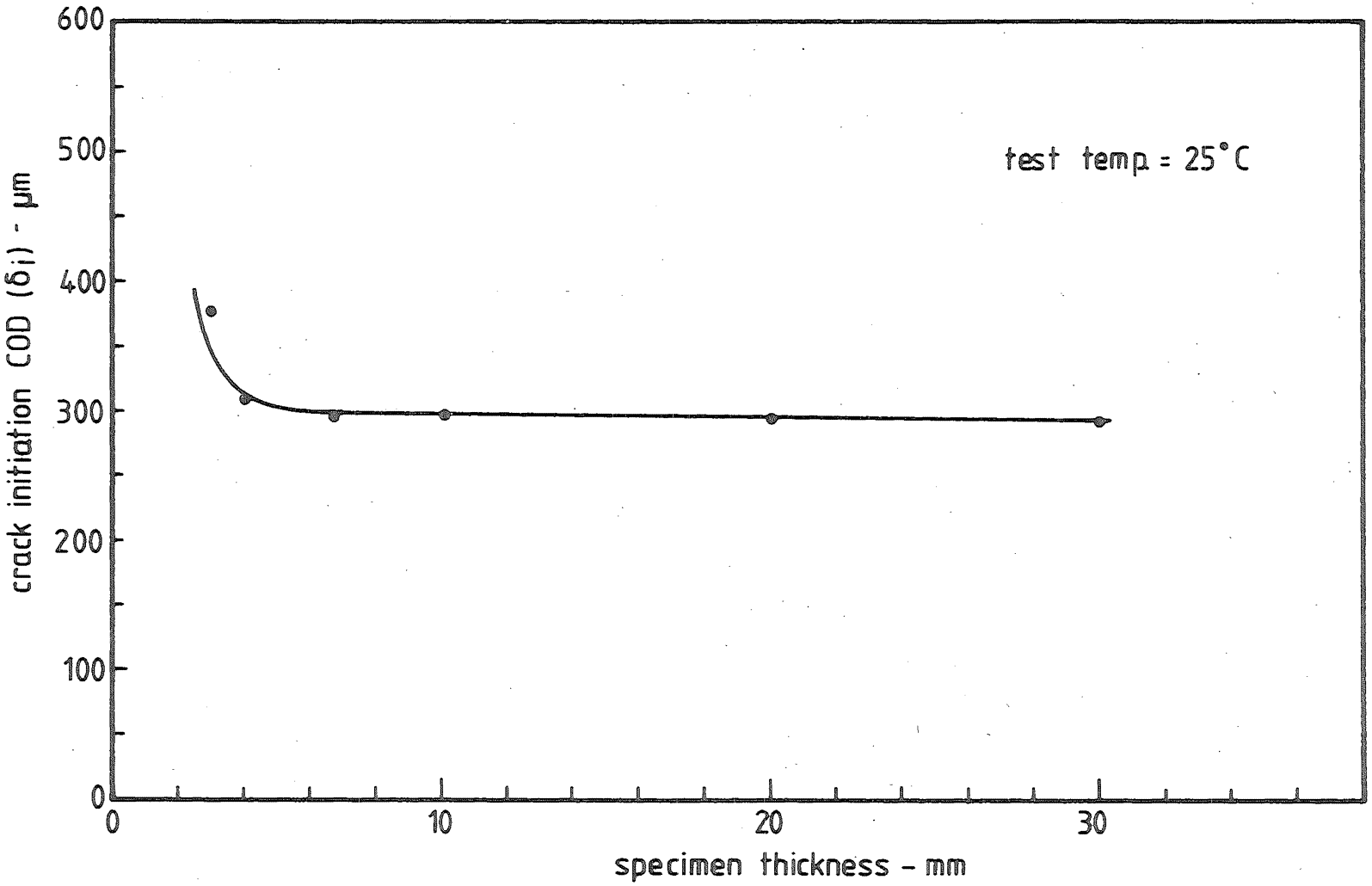

FIG 8·20 THICKNESS DEPENDENCE OF CRACK INITIATION COD OF AS-ROLLED BILLET STEEL.

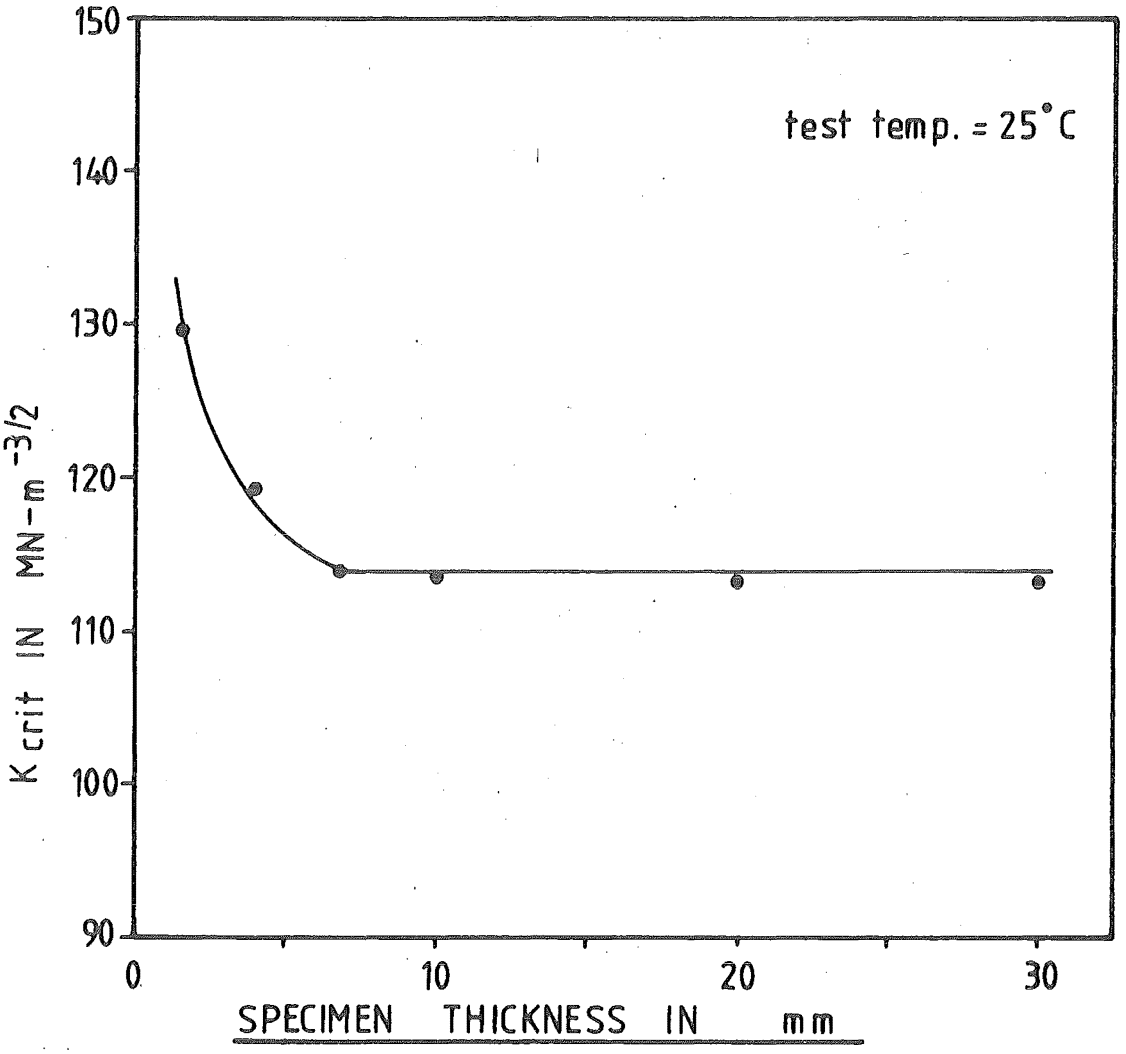

FIG 8·21 SPECIMEN THICKNESS DEPENDENCE OF K_{crit} OF AS-ROLLED BILLET STEEL

Although the effect of varying the crack length, a , and the uncracked ligament length, W - a , on the fracture toughness was not investigated, the standard nominal specification of a = W - a = B of the compact tension specimen had eliminated the necessity of further investigation in this direction as far as the use of this type of COD test specimen was concerned.

Hence, the experimental results of Figures 8.20 and 8.21 verified that the COD test can be used to obtain size independent "plane strain" fracture toughness experimentally provided that the standard specimen dimensions of the crack length a , the uncracked ligament length W - a and the specimen thickness B all exceeded a minimum limit defined as

$$a , W - a , B \geq 25 \delta_i$$

where δ_i is the COD at the instance of initial crack extension. The results of this experimental investigation agreed well with those of other research projects where the standard bend specimens were used[84, 157]. Thus, the COD test had been shown to be a practical and relatively economical alternative to the standard ASTM K_{IC} test[3] in the evaluation of the fracture resistance of low carbon steels.

The temperature dependence of the critical COD of the three experimental steels was also shown in Figures 8.12 to 8.16. Using these results and also the yield stress data given in Figures 8.17 to 8.19, the Critical Stress Intensity Factor data was

calculated using Equation (7.4.4)

$$K_{crit} = 0.4769 \ (\sigma_{LY} \delta_c) \ MN\text{-}m^{-\frac{3}{2}}$$

where K_{crit} is the Critical Stress Intensity Factor

σ_{LY} is the lower yield stress in $MN\text{-}m^{-2}$

δ_c is the critical COD in μm.

The calculated K_{crit} results are summarised in Figures 8.22 to 8.25. It should be noted that the micro-void coalescence fracture toughness levels were defined at the instance of initial crack extension, i.e. at the initial instability of the crack-tip material and not at final instability. This definition was more meaningful and was also necessary for the purpose of comparing the experimental results with the prediction made by the micro-fracture models[18, 19, 20]. When the critical COD defined at the instability of the specimen did not coincide with the initial crack-extension COD, both types of results were included for the purpose of comparison (see Figure 8.25). It can be seen that with the exception of the upper-shelf level, i.e. at micro-void coalescence of the Normal Grade 275 Steel, the fracture toughness, K_{crit}, of the three experimental steels can be shown to be size independent using the criterion

$$a \ , \ W - a \ , \ B \geqslant 25 \ \delta_c$$

The Upper-shelf COD value of the Grade 275 Steel was 450 μm. This was determined at the instance of initial crack-tip instability. The minimum specimen size required to produce thickness independent

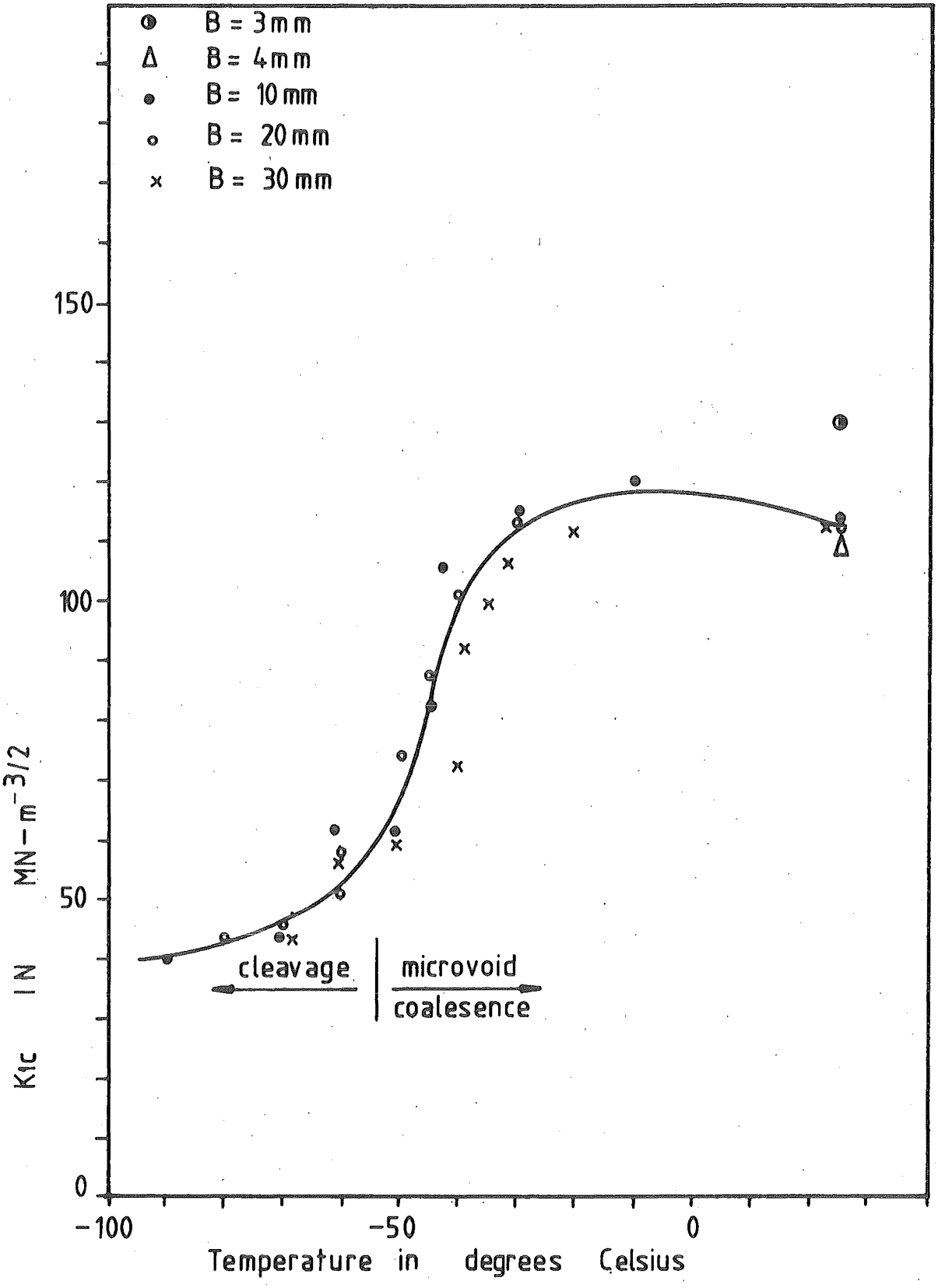

FIG 8·22 VARIATIONS OF K1c WITH TEMPERATURE OF AS – ROLLED BILLET STEEL.

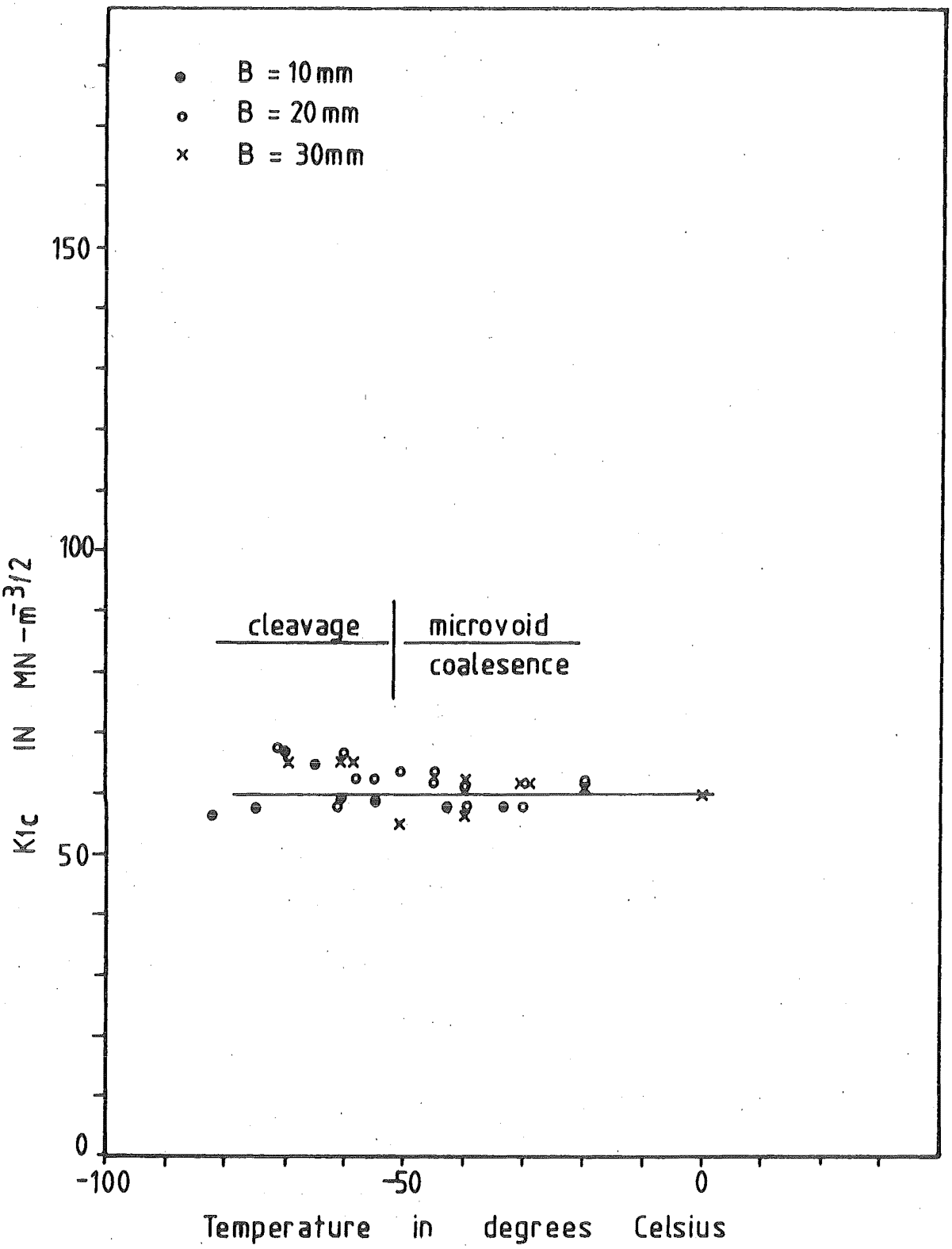

FIG 8.23 VARIATION OF K_{1c} WITH TEMPERATURE OF Hi-AlN BILLET STEEL.

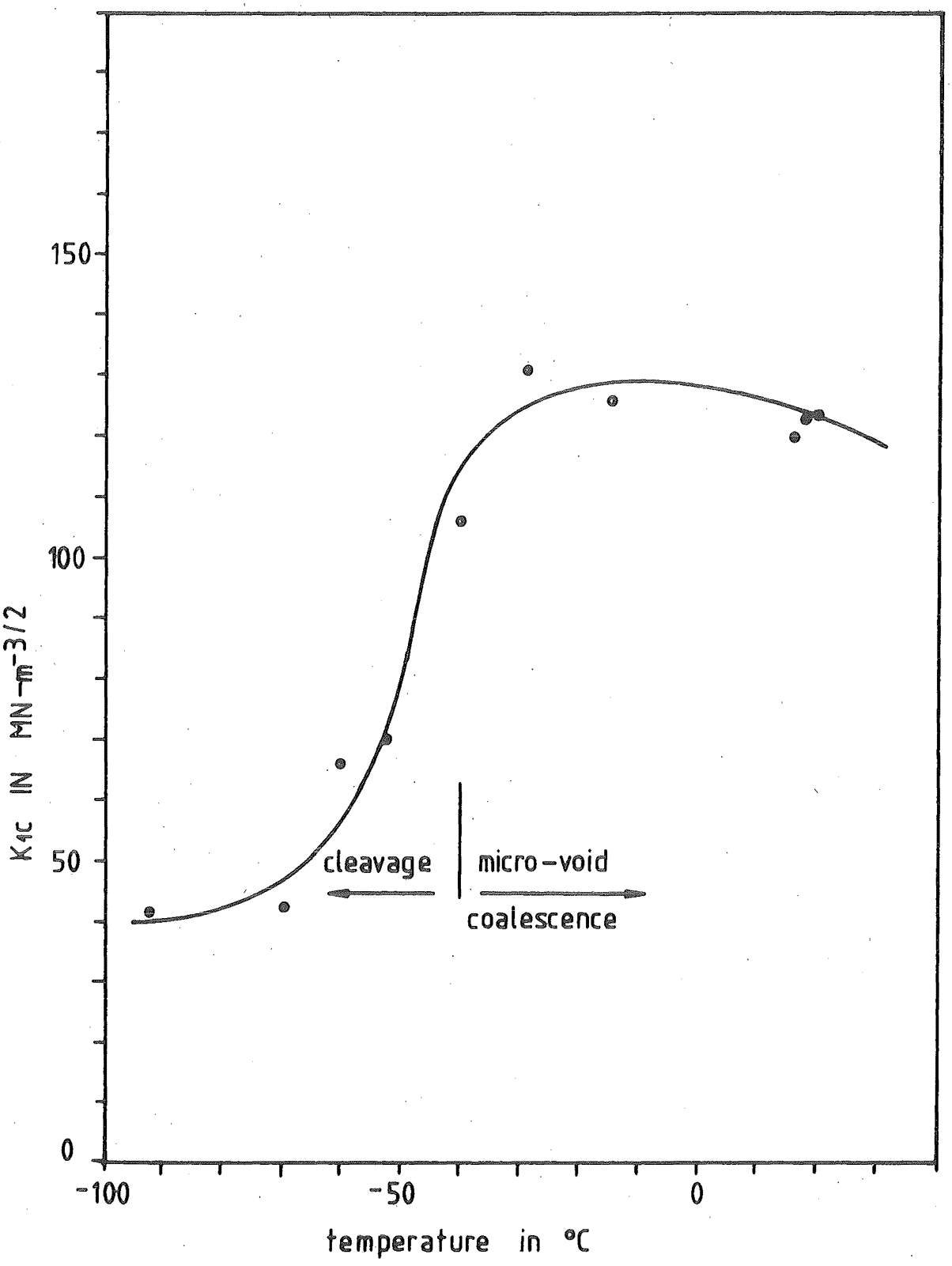

FIG 8·24 VARIATION OF K_{1c} WITH TEMPERATURE OF PRESSURE VESSEL STEEL

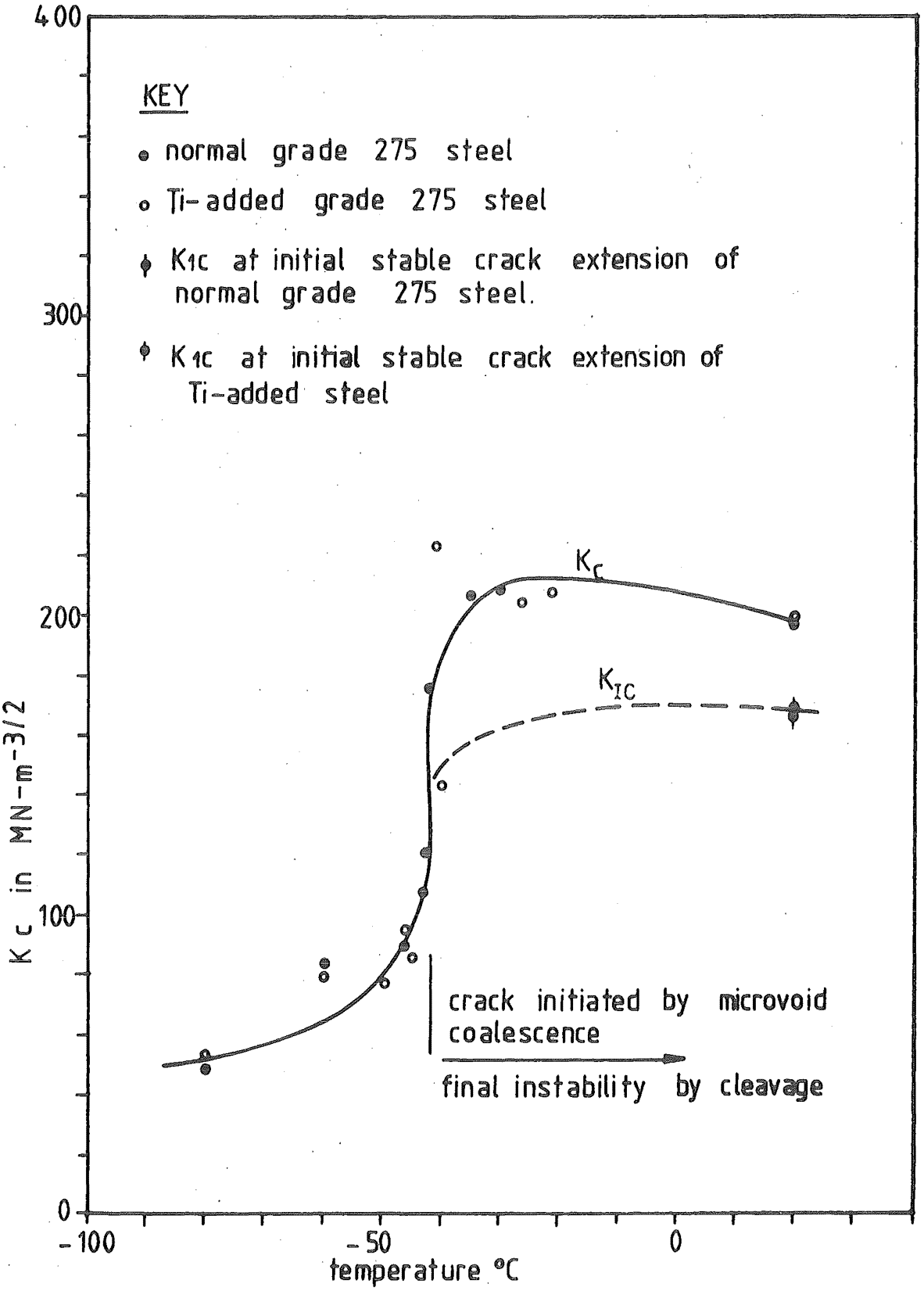

FIG 8.25 VARIATION OF K_c WITH TEMPERATURE OF GRADE 275 STEEL

fracture toughness data at this COD level would be 11.25 mm. Thus, the 10 mm thick specimen used in the investigation was only slightly undersized giving

$$a\ ,\ W - a\ ,\ B \simeq 22.2\ \delta_c$$

Examination of the results given in Figure 8.21 showed that the results obtained by the slightly undersized 10 mm thick specimen would be very close to the conservative K_{IC} value. Consequently, the 10 mm thick COD test specimen was found to be adequate in providing thickness independent "plane strain" fracture toughness data.

The results summarised in Figures 8.22 to 8.25 also showed that with a single exception, the change in fracture mode from cleavage to micro-void coalescence (see Plate 8.6) was accompanied by a rapid rise in fracture toughness, thus supporting the earlier reports that the fracture resistance was sensitive to the type of micro-fracture mechanism in both quasi-static K_{IC} [58, 59] and the impact testings of low strength steels. The exception mentioned earlier was the Hi-AlN Billet Steel which had been subjected to an AlN precipitation heat treatment (see Section 7.1). In the tensile testing of this steel, failure was observed to occur by decohesion at the MnS inclusion particles with the ferrite matrix displaying little or no sign of plastic deformation (see Figure 7.8). It was suspected that the grain refinement effect of the AlN precipitation treatment could have elevated the general yield stress level of the ferrite so that decohesion at MnS inclusions occurred before

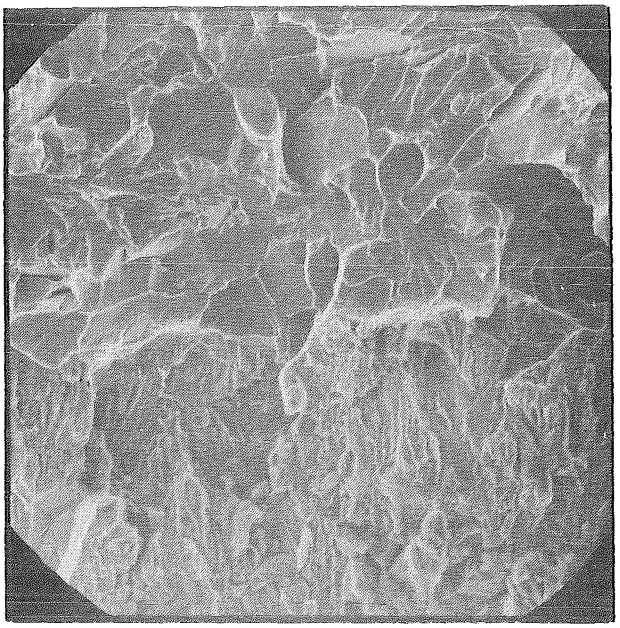

(a) billet steel, separation by cleavage
mag. = ×390 test temp. = -70°C

direction of crack propagation

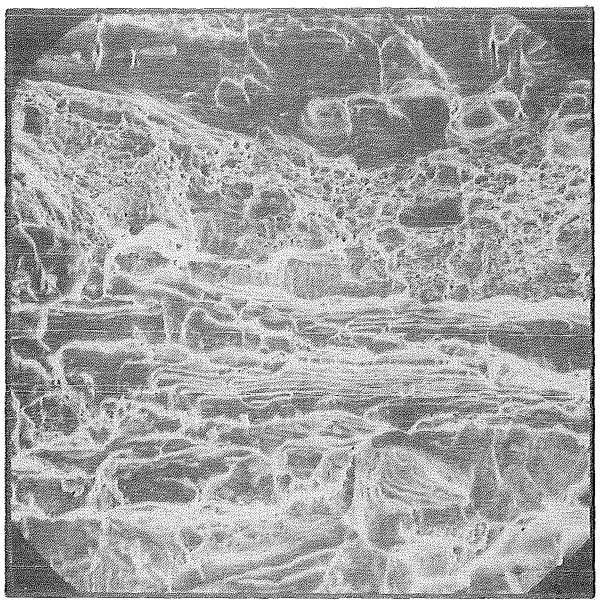

(b) billet steel, separation by micro-void coalescence
mag. = ×390 test temp. = -20°C

PLATE 8·6 SCANNING ELECTRON MICROGRAPHS OF THE FRACTURE SURFACES OF BROKEN COD TEST SPECIMENS.

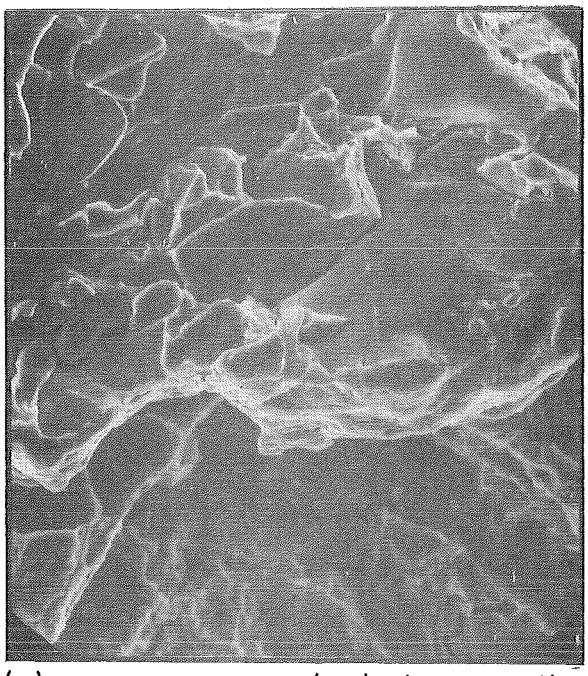

(c) pressure vessel steel separation by cleavage.
mag. = ×1000 test temp. = -70°C

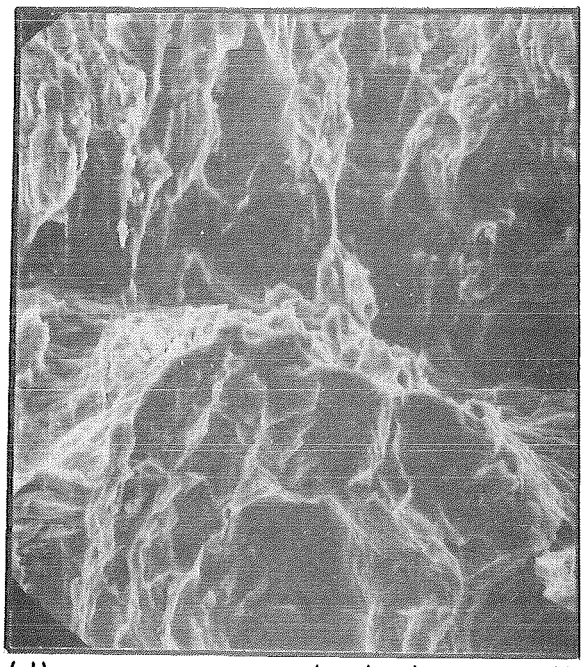

(d) pressure vessel steel separation by microvoid coalescence.
mag. = ×1000 test temp. = -70°C

direction of crack propagation

PLATE 8·6 SCANNING ELECTRON MICROGRAPHS OF THE FRACTURE SURFACES OF BROKEN COD TEST SPECIMENS.

direction of crack propagation.

(e) grade 275 steel separation by cleavage.
mag. = ×390 test temp. -70°C

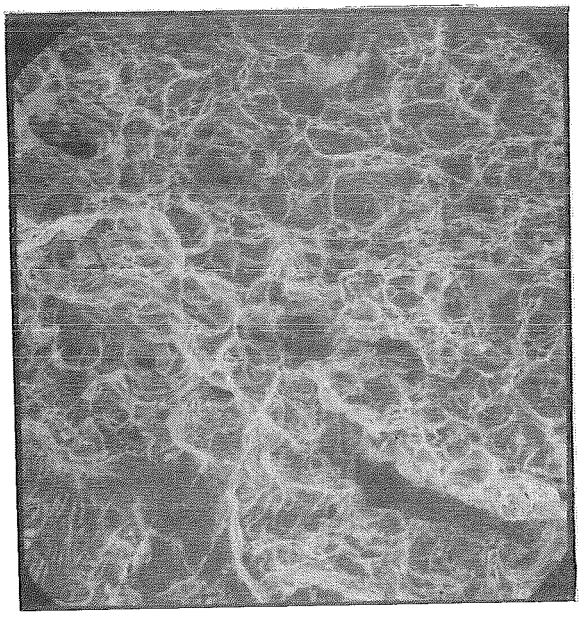

direction of crack propagation.

(f) grade 275 steel separation by microvoid coalescence.
mag. = ×390 test temp -20°C

PLATE 8·6 SCANNING ELECTRON MICROGRAPHS OF THE FRACTURE SURFACES OF BROKEN COD TEST SPECIMENS.

the ferrite matrix had attained its upper yield stress. This suspicion was investigated with tensile specimens orientated in the longitudinal direction to minimise the effect of MnS (see Figure 7.7) and also measuring the average grain diameter of the As-Rolled and the Hi-AlN steels. The results of this investigation are shown in Table 8.2. The results supported the earlier suspicion that the yield stress level of the ferrite matrix was elevated by the grain refinement effect of the AlN precipitation treatment. Consequently, it is reasonable to assume that in the COD testing of this steel, decohesion at the MnS inclusion occurred before the attainment of the upper yield stress level of the ferrite matrix thus resulting in the abnormal "brittle" behaviour of tensile test specimens and also the COD being insensitive to change in fracture mode from cleavage to micro-void coalescence.

The possibility of intergranular fracture caused by the segregation of AlN precipitates to primary ferrite grain boundaries[158] being responsible for the abnormal behaviour of the Hi-AlN steel in COD testing was also investigated. This was prompted by the observed presence of a band of granular fracture area at the crack-tip region of one of the Hi-AlN COD test specimen which is shown in Plate 8.7. The Energy Dispersion Analysis of this area given in Figure 8.26 indicated that it was Al-rich. However, exhaustive Scanning Electron Microscope Examination of the fracture surfaces of several other broken Hi-AlN COD test specimens did not reveal the presence of similar granular fracture areas. Hence, the isolated nature of the occurrence of this abnormal granular

Steel Type	Upper Yield Stress, σ_{UY} ($MN\text{-}m^{-2}$)	Lower Yield Stress, σ_{LY} ($MN\text{-}m^{-2}$)	Ultimate Tensile Stress, σ_{UTS} ($MN\text{-}m^{-2}$)	Fracture Strain, ε_f	Average Grain Diameter, d_g (μm)
Hi-AlN Billet	320	315	520	0.76	26.4
As-Rolled Billet	285	280	476	0.70	31.3

Table 8.2 Properties Of The Billet Steel In The Longitudinal Direction Tested At Ambient Temperature

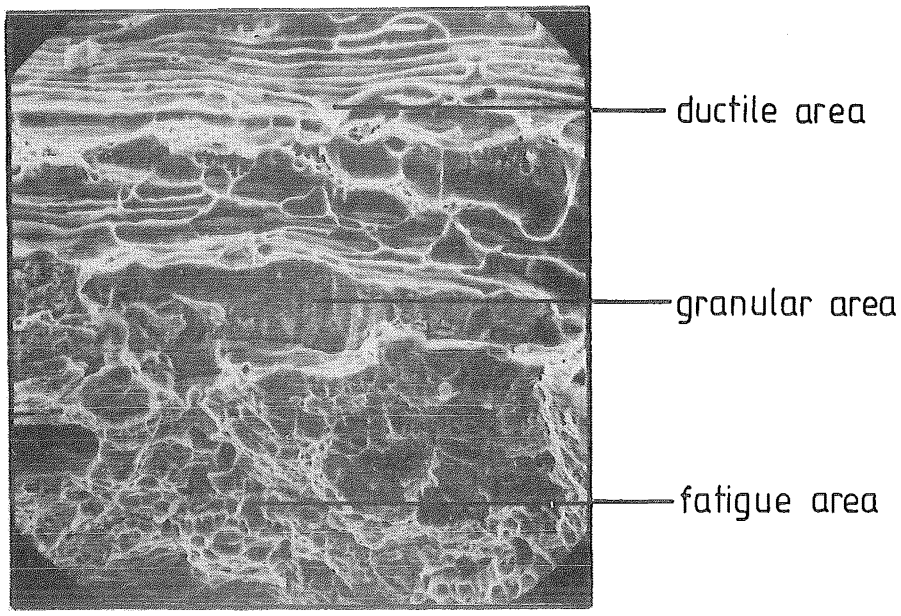

PLATE 8·7 SCANNING ELECTRON MICROGRAPH SHOWING THE PRESENCE OF GRANULAR FRACTURE AREA (×1000)

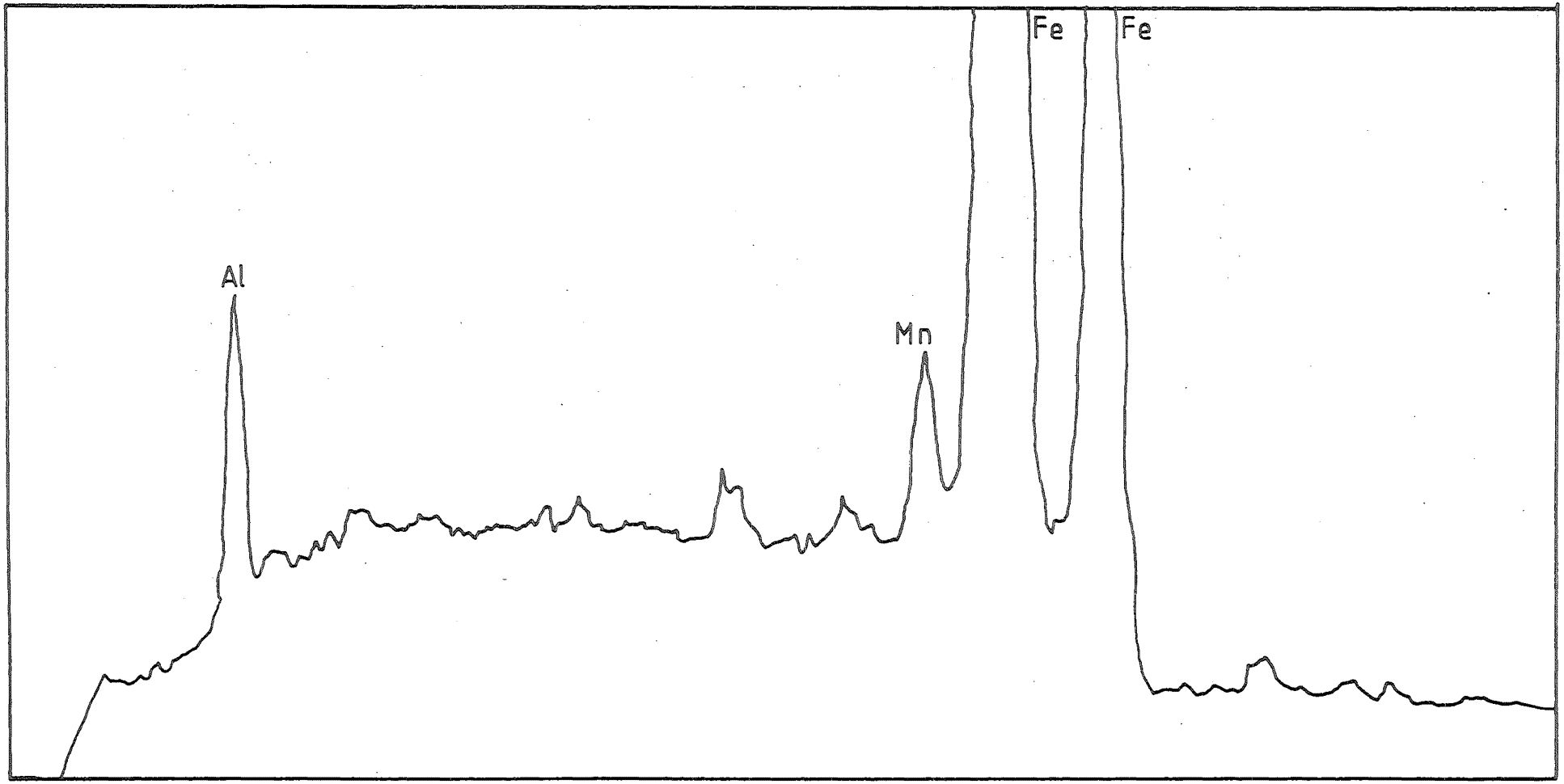

201

FIG 8·26 ENERGY DISPERSION ANALYSIS OF THE GRANULAR FRACTURE AREA OF PLATE 8·7

fracture area meant that it could not have been caused by the segregation of AlN precipitates to the primary ferrite grain boundary during the precipitation heat treatment. Instead, it was likely to have been the legacy of the segregation of Al during the casting process and subsequently being located at the fatigue crack-tip by chance.

An important consequence of this abnormal behaviour of the Hi-AlN Billet Steel was that this steel could not be used in assessing the effect of Nitrogen Strain Ageing of the crack-tip plastic zone. Fortunately, an alternative material was available in the form of the Grade 275 Steel where the active Nitrogen content had been reduced by suitable Titanium addition (see Table 7.1). The results of Figure 8.25 showed that the fracture toughness of the Grade 275 Steel was not affected by the addition of Titanium as a nitride former.

8.4 Relationship Between Fracture Toughness And Micro-Parameters

The results shown in Figures 8.22, 8.24 and 8.25 were compared with the predictions made by the micro-fracture models of cleavage [15, 16, 17] and of micro-void coalescence [18, 19, 20] which were proposed to describe the fracture behaviour of cracked materials. For clarity, the results of this investigation will be presented in two separate sections, viz

(a) Cleavage

(b) Microvoid coalescence

(a) Cleavage

It has been reported that when the magnitude of the yield and fracture stress are comparable, the plane strain Critical Stress Intensity Factor, K_{IC} , can be related to the fracture stress, σ_F , by Equation (4.1.6)[15, 16, 17]

$$K_{IC} = \sigma_F(2\pi X_o)^{\frac{1}{2}}$$

where X_o is known as the "characteristic distance" and was shown to be 1 to 2 times the average grain diameter, d_g .

The experimental works related to the above relationship was performed at -196°C so that quasi-brittle condition could be attained for pure cleavage failure to occur as well as to facilitate the use of the standard ASTM K_{IC} test with small test specimen size[3]. The original reports on the K_{IC}-σ_F relationship of Equation (4.1.6) showed that the relationship X_o = 1 to 2 times d_g became invalid when d_g < 40 μm. However, a later report contradicted this by showing that the relationship remained valid even when d_g was as low as 8.3 μm in steel of strength level similar to that used in the original report[17]. Nevertheless, the difference in the range of application of the relationship given by Equation (4.1.6) could have arisen from the fact that the steel used in the latter of the two reports had been subjected to a spheroidisation heat treatment. More significantly, both

reports arrived at the similar conclusion that

(i) Nucleation of micro-cracks in the first two grains of the crack-tip region is necessary before spontaneous crack propagation can occur.

(ii) The nucleation of micro-cracks at grain boundary carbide particles proposed by Smith[109] can be adopted to provide the nucleation mechanism of micro-cracks at the first two grains of the crack-tip material.

The present experimental results of the standard ASTM fracture toughness and tensile tests of the Pressure Vessel and the Grade 275 Steels measured at $-196^{o}C$ are given in Tables 8.3 and 8.4. The experimental details have been given in Sections 7.2.1 and 7.3.2.c respectively. The comparison between the experimental fracture toughness data and the predictions made by the cleavage fracture model [15, 16, 17] are supplied in Table 8.5. Similar testings of the Billet Steel did not produce meaningful result because of the MnS affected fracture behaviour described earlier in Sections 7.3.2 and 8.2, and therefore had to be discarded. It can be seen that the fracture toughness values predicted by the cleavage fracture models showed good agreement with the experimental data. Thus, the experimental results disagreed with the earlier report that the K_{IC}-σ_F relationship given by Equation (4.1.6) was

Steel Type	Instability Load, P_Q KN	Crack Length a (mm)	Specimen Width W (mm)	Specimen Thickness B (mm)	$\frac{a}{W}$	Compliance Function $Y(\frac{a}{W})$	Apparent Fracture Toughness+ K_Q $(MN\text{-}m^{-\frac{3}{2}})$	Yield Stress* σ_{LY} $(MN\text{-}m^{-2})$	$B>2.5(\frac{K_Q}{\sigma_{LY}})^2$
Pressure Vessel	2.62	10.43	20	9.99	0.520	10.21	19.20	860	Yes
Normal Grade 275	2.90	10.07	20	9.96	0.503	9.609	19.85	830	Yes
Ti-Added Grade 275	2.60	10.37	20	9.97	0.519	10.18	18.80	846	Yes

* See Table 8.4

+ $K_Q = \frac{P_Q}{BW^{\frac{1}{2}}} Y(\frac{a}{W})$; for values of $Y(\frac{a}{W})$ see ref. No.3.

Table 8.3 Experimental Results Of The Standard ASTM K_{IC} Test Conducted At $-196^{\circ}C$

Steel Type	Initial Specimen Diameter D_o (mm)	Diameter At Fracture D_F (mm)	Upper Yield Load P_{UY} (KN)	Lower Yield Load P_{LY} (KN)	Fracture Load P_F (KN)	Lower Yield Stress σ_{LY} ($MN\text{-}m^{-2}$)	Fracture Stress σ_F ($MN\text{-}m^{-2}$)	Fracture Strain ϵ_f
Pressure Vessel Steel	4.99	4.30	18.7	16.8	16.6	859	1143	.29
Normal Grade 275	4.95	4.40	17.6	16.2	17.4	842	1144	.24
	5.01	4.30	18.2	16.2	17.1	822	1184	.30
Ti-Added Grade 275	5.00	4.07	18.6	16.4	14.9	835	1145	.41
	4.91	4.11	18.2	16.2	15.9	856	1198	.36

Table 8.4 Tensile Properties Of The Pressure Vessel And Grade 275 Steels Measured At $-196^{o}C$

Steel Type	Fracture Stress σ_f ($MN\text{-}m^{-2}$)	Average Grain Diameter d_g (μm)	Characteristic Distance $X_o = 2\ d_g$ (μm)	Predicted Fracture Toughness $K_{IC_{predicted}}$ ($MN\text{-}m^{-\frac{3}{2}}$)	Experimental Fracture Toughness $K_{IC_{expt}}$ ($MN\text{-}m^{-\frac{3}{2}}$)
Pressure Vessel	1143	24.6	49.2	20.1	19.7
Normal Grade 275	1164	20.5	41.0	18.7	19.8
Ti-Added Grade 275	1170	17.2	34.2	17.2	18.8

Table 8.5 Comparison Of The Predicted And Experimental Fracture Toughness At $-196^{\circ}C$

valid only when the grain size d_g exceeded 40 μm[15, 16]. In these reports, the grain size dependence of the σ_F-K_{IC} relationship was explained by the argument that suitably sized grain boundary carbides were needed for the Smith's cleavage mechanism[109] and that the probability of the existence of such carbide particles were greatly reduced in fine grain material[15, 16]. However, it should be noted that this argument had omitted the Cottrell's cleavage mechanism which did not require the presence of grain-boundary carbide for the formation of microcracks[107]. Furthermore, the Cottrell's model had also been reported to be applicable in conventional low carbon steels[110]. Hence, it is likely that the limit on grain size may not be necessary because of the availability of an alternative micro-crack nucleation mechanisms.

Although the nucleation of micro-cracks had been implied to be essential for spontaneous crack propagation by the relationship $K_{IC} = \sigma_F(2\pi 2d_g)^{\frac{1}{2}}$, an explicit description of the chain of events at the crack-tip material leading to cleavage fracture had not been given. This may be rectified by examining the sequence of events from the Linear Elastic Fracture Mechanics points of view. The combination of the present experimental data and the results of earlier reports showed that the fatigue crack-tip merely acted as a stress

concentrator by elevating the local crack-tip tensile stress, σ_{local} [15, 16, 17]. When this stress exceeded the material's yield stress, micro-cracks would be generated by possibly a combination of the Cottrell's[107] and the Smith's[109] mechanisms. Experimental evidence on the presence of these micro-cracks had been reported elsewhere for both fracture toughness[51] and uniaxial tensile[159] test specimens which failed by cleavage. Hence, the subsequent elevation of the crack-tip stress so that the fracture stress level was exceeded in the first few grains ahead of the crack-tip would lead to spontaneous crack propagation when the Critical Stress Intensity Factor, K_{IC}, at a suitably sized microcrack, shown experimentally to be 1 to 2 grain diameters was exceeded (see Figure 8.27).

Thus, it can be seen that the fracture toughness measured by the standard ASTM K_{IC} test[3] can be related to the basic concepts of Linear Elastic Fracture Mechanics of a cracked body and that the test method measures the energy required to nucleate and to subsequently propagate the micro-crack ahead of the fatigue crack.

As the temperature was increased from -196°C, increasing degree of plastic deformation would be required to elevate the local crack-tip stress by strain hardening so that the fracture stress which was reported to be temperature independent[160, 161] could be exceeded.

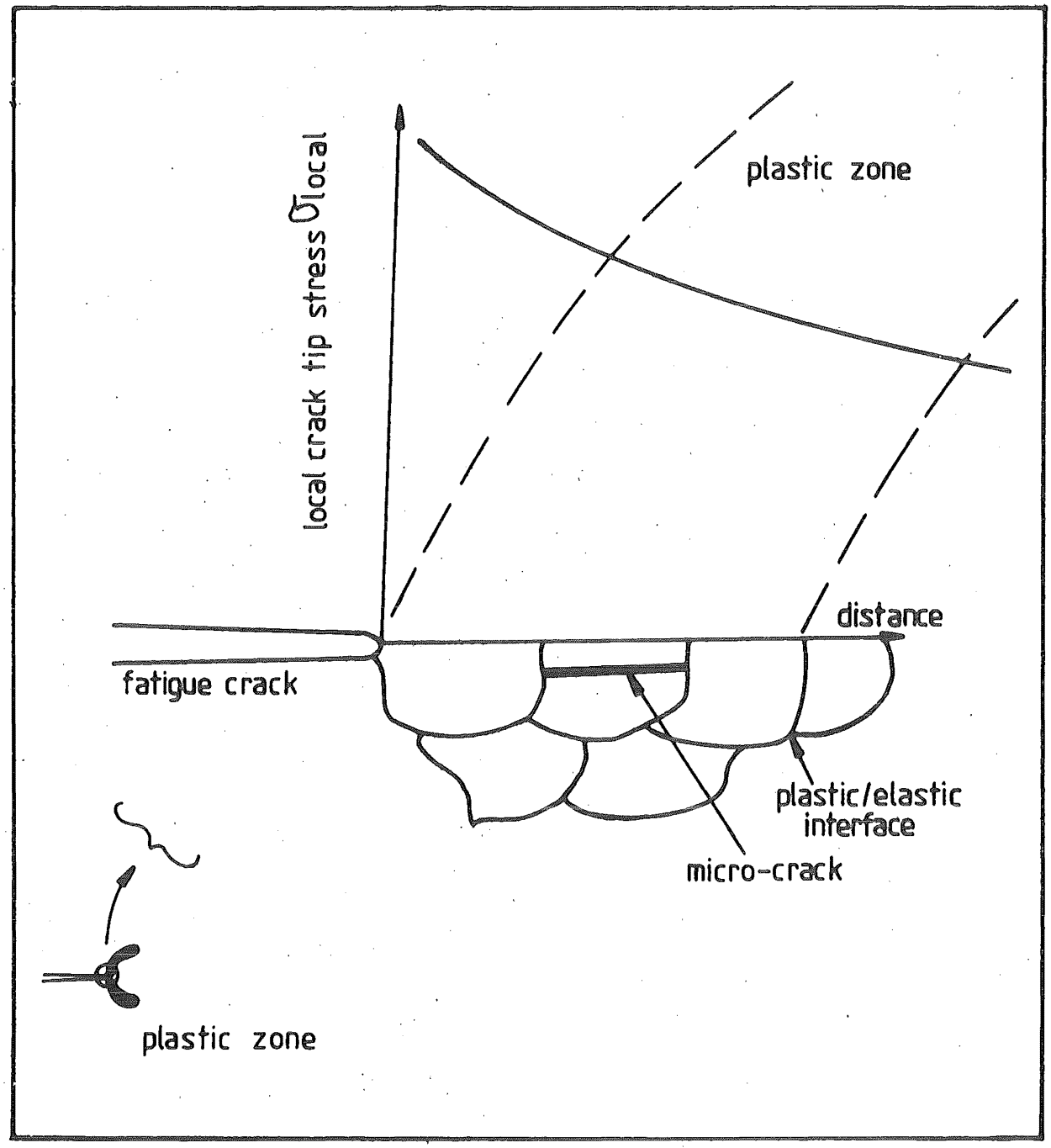

FIG. 8·27 THE SITUATION AT THE FATIGUE CRACK-TIP PRIOR TO CLEAVAGE FRACTURE AT - 196°C

Consequently, the K_{IC}-σ_F relationship may now be inapplicable because a higher proportion of energy will be absorbed by plastic deformation.

(b) Micro-void Coalescence

Recent reports indicated that the values of COD measured at the initial stable crack extension by micro-void coalescence, δ_i , could be predicted from either the mean-free path between non-metallic inclusion particles[18, 19], or from the average grain diameter where grain boundary cementites were assumed to be the primary voiding particles[20].

The non-metallic inclusion model relates the COD at initial crack extension, δ_i , to the average inter-inclusion particle spacing, ℓ_f , by the equation

$$\delta_i = \varepsilon_{fi} \ell_f \qquad (8.4.1)$$

where ε_{fi} is the critical crack-tip strain commonly termed the "notched ductility".

In low carbon steel, ℓ_f was shown to be represented by the average spacing of the MnS inclusion, which was also reported to be the primary voiding particle[18].

The grain size model relates δ_i to the average grain diameter, d_g , by the equation[20]

$$\delta_i = 2\, d_g \exp(0.2\, \varepsilon_f) \qquad (8.4.2)$$

where ε_f is the uniaxial tensile fracture strain.

The applicability of these models to the experimental steels was investigated. The notched ductility results are given in Figure 8.28 and the uniaxial tensile fracture strain data are given in Appendix F. The comparison between the critical COD predicted from the two micro-void coalescence models and the experimental data are shown in Table 8.6. These results showed good agreement between experimental data and the predictions made by the non-metallic inclusion model[18, 19]. However, the values predicted by the Sailor's model[20] displayed large deviation from the experimental data and was therefore inapplicable in the experimental steels. However, it is interesting to note that by redefining the primary voiding particle of the Sailor's model as the MnS inclusion and re-evaluating the inter-particle spacing accordingly, the experimental and predicted COD values showed remarkably improved agreement (see Table 8.6). This is not surprising because the MnS had earlier been shown to be the principal voiding particle in Section 8.2 Thus, the experimental data supported the report that non-metallic inclusions being the primary voiding particles and that a critical crack-tip strain value, viz. the notched ductility must be exceeded before micro-void coalescence of the crack-tip material could occur by an inter-particle "necking" mechanism[19, 119].

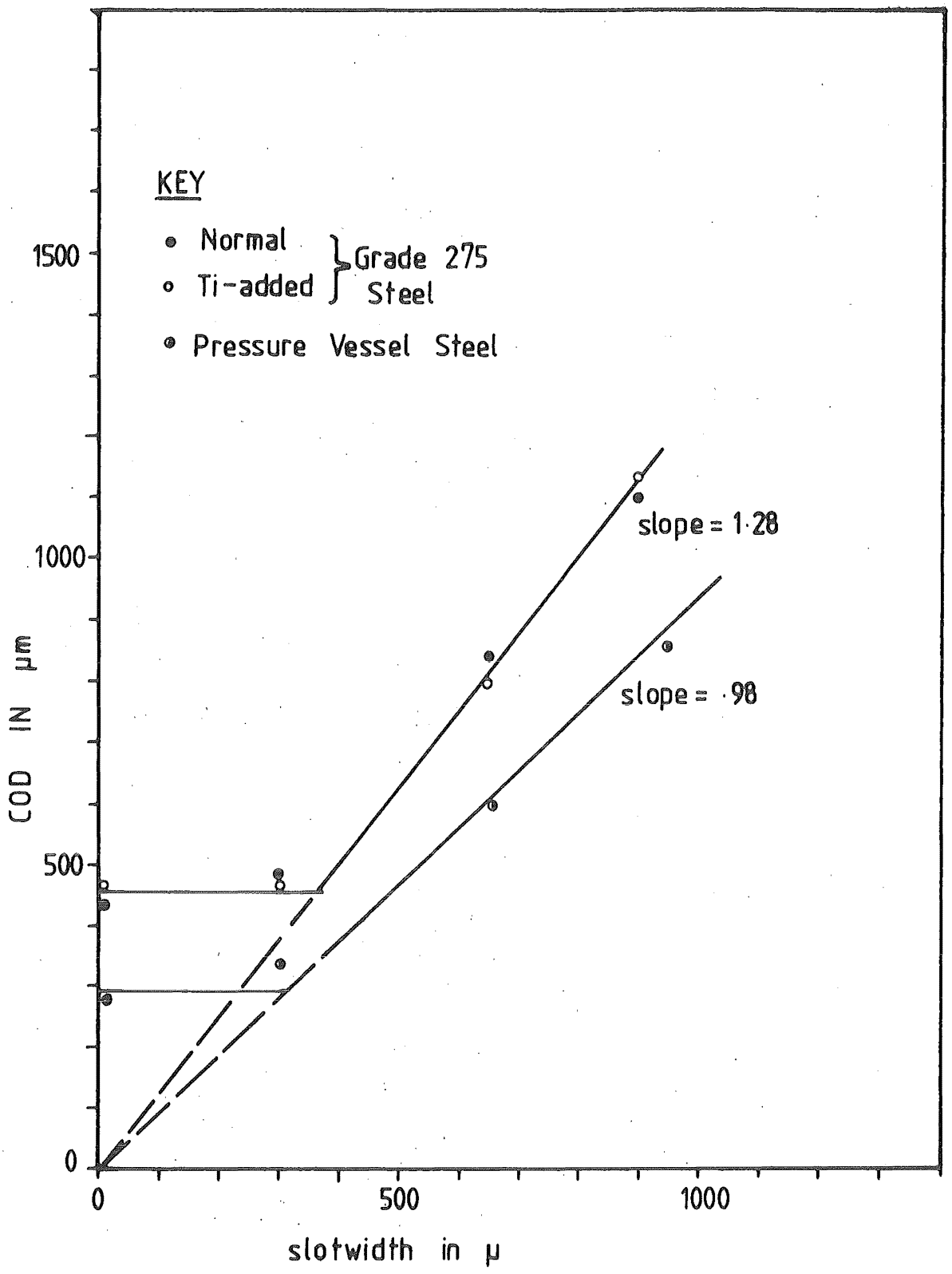

FIG 8.28 GRAPH SHOWING THE EFFECTS OF SLOTWIDTH ON THE SUB-CRITICAL CRACK EXTENSION COD OF THE PRESSURE VESSEL AND GRADE 275 STEELS

Steel Type	Notched Ductility ε_{fi}	Average Inter-MnS Particle Spacing ℓ_f (μm)	Uniaxial Tensile Fracture Strain ε_f	Average Grain Diameter (μm)	COD At Initial Crack-Tip Instability δ_i (μm)			
					Inclusion Model[18, 19]	Sailor's Model[20]	Experimental	Modified Sailor's
Pressure Vessel	0.94	321	0.92	24.6	302	59.1	280	458
Normal Grade 275	1.28	378	0.97	20.5	484	49.8	440	459
Ti-Added Grade 275	1.28	353	0.96	17.2	452	42.5	445	428

Table 8.6 Comparison Of Predicted And Experimental Values Of δ_i At Ambient Temperature

Although reasonably good agreement between the predicted and experimental critical COD values of micro-void coalescence was observed, the statistical significance of the results could not be determined accurately because of the non-uniform nature of the inclusion particles' distribution. Furthermore, examination of the Scanning Electron Micrographs (see Plate 8.6) showed the presence of smaller secondary voids at the periphery of the primary MnS voids. This observation indicates that other micro-structure such as cementite and precipitates may affect the voiding process. Thus, the micro-void coalescence model should be treated as empirical and applied with caution. Nevertheless, it was shown that the existence of the fracture mode transition temperature in fracture toughness testing of low carbon steels could be predicted by theoretical models of micro-fracture behaviour.

8.5 Correlation Between The Plane Strain Critical Stress Intensity Factor (K_{IC}) And The Charpy V-Notched Impact Energy (C_V)

The results of the Charpy v-notched impact tests of the Pressure Vessel and the Grade 275 Steels are given in Figures 8.29 and 8.30. Comparison of these results with the quasi-static fracture toughness test results given earlier in Figures 8.24 and 8.25 showed that the transition temperature obtained by the two test methods did not coincide. This is not unexpected because the two techniques

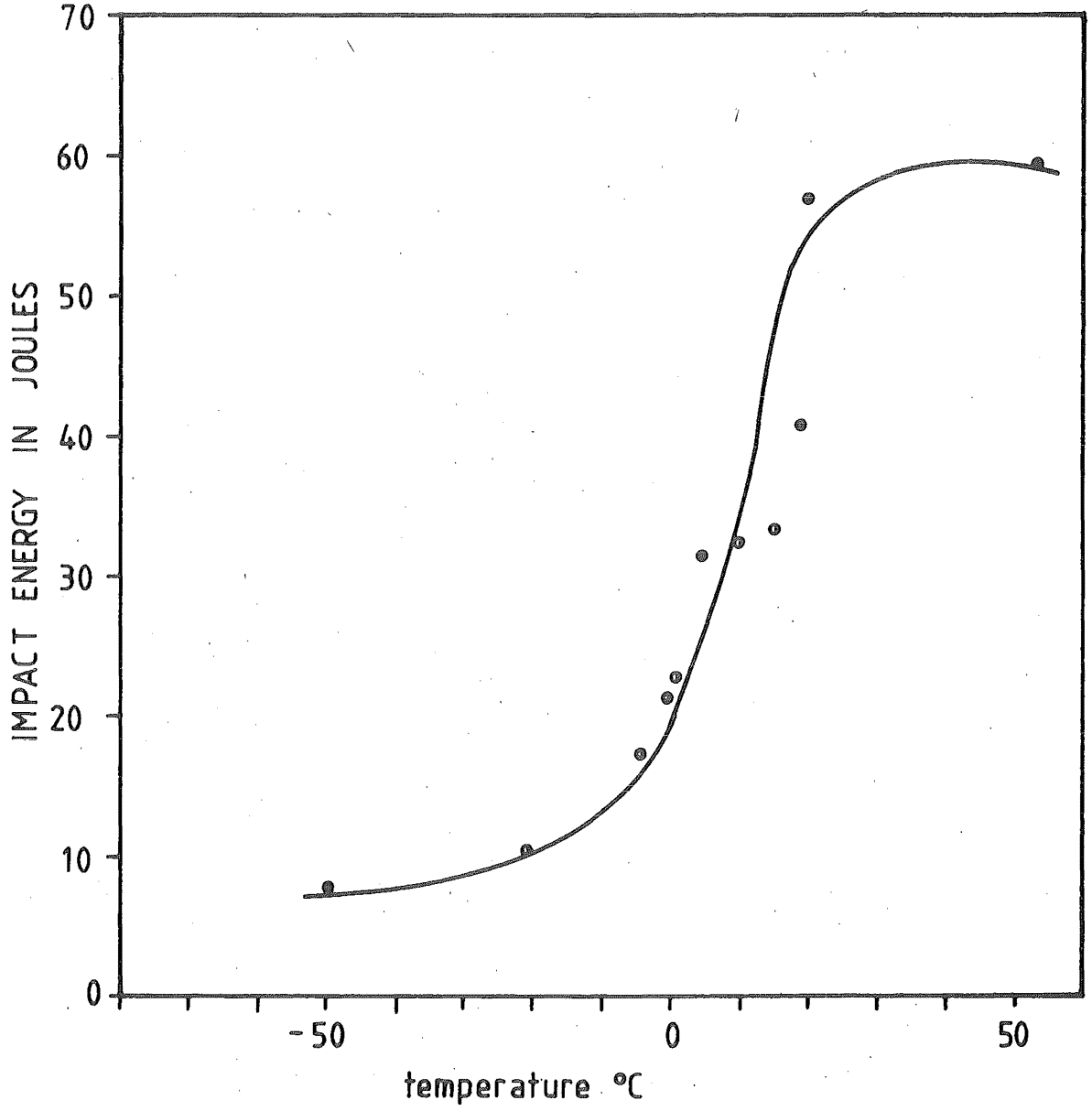

FIG 8.29 THE CHARPY V-NOTCHED IMPACT CURVE OF THE PRESSURE VESSEL STEEL

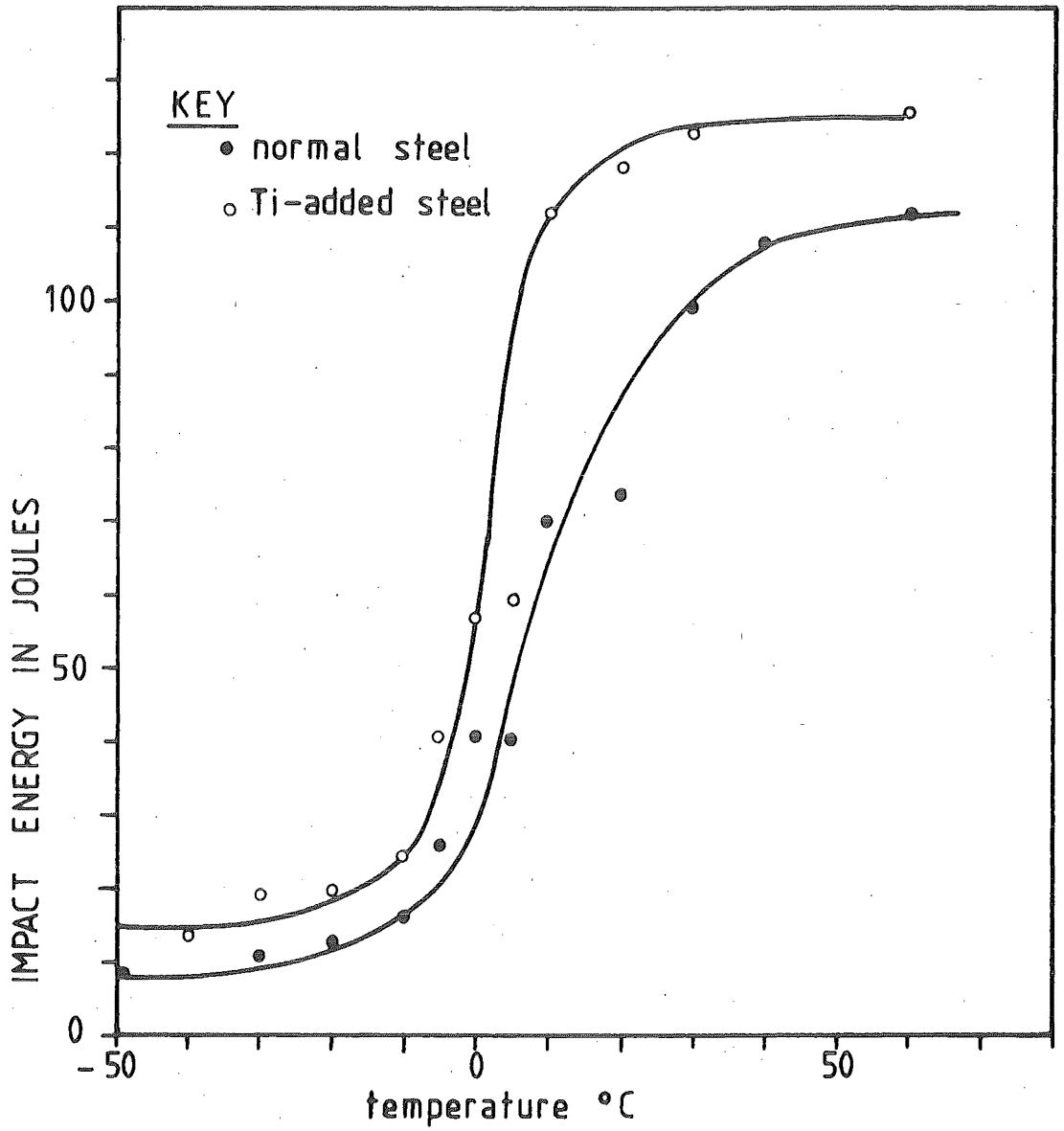

FIG 8.30 THE V-NOTCHED CHARPY IMPACT ENERGY CURVE OF GRADE 275 STEEL

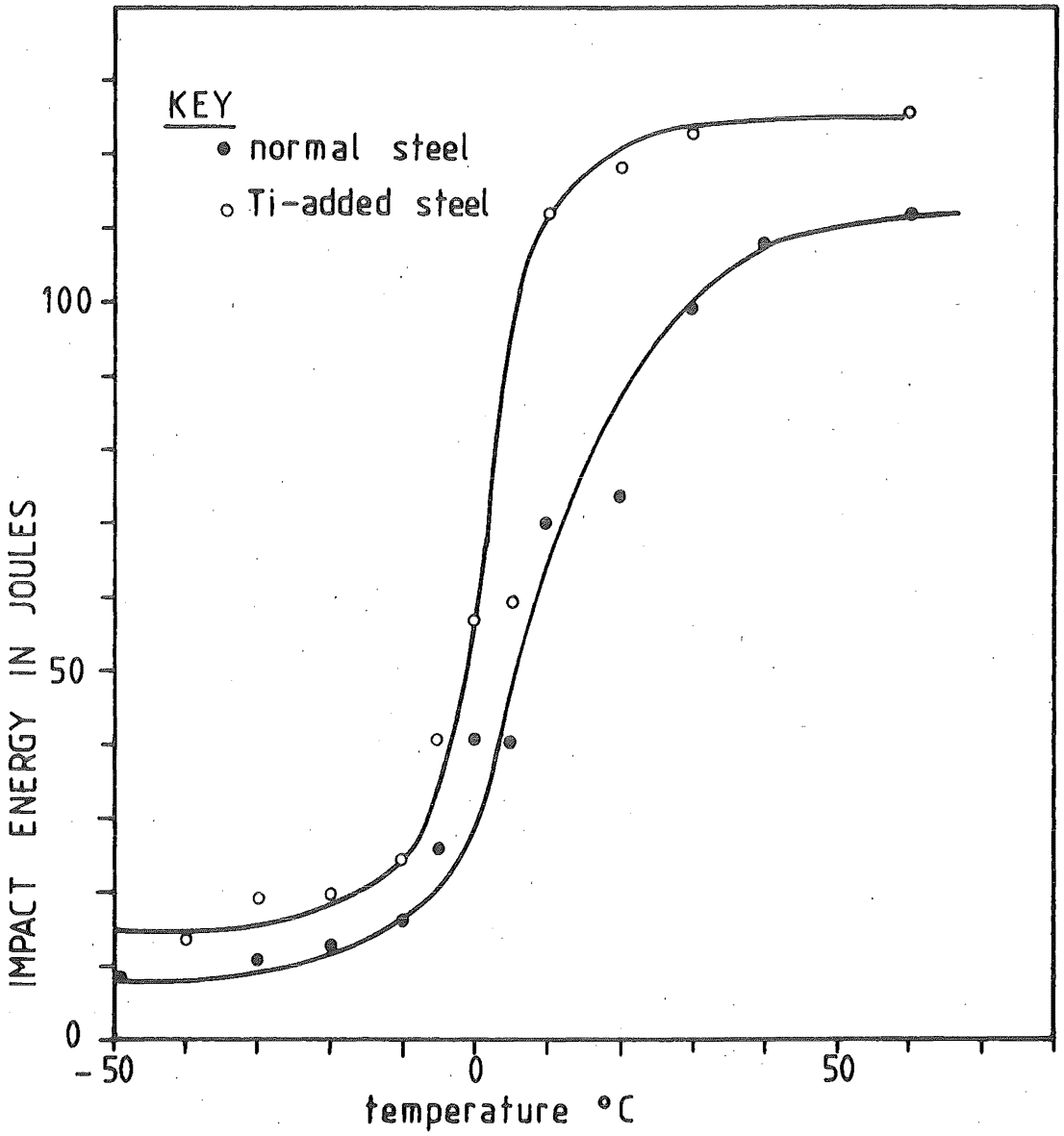

FIG 8.30 THE V-NOTCHED CHARPY IMPACT ENERGY CURVE OF GRADE 275 STEEL

differed significantly in several aspects. Some of the more prominent differences are discussed briefly as follows:

(a) Strain-rate

The COD test was conducted with quasi-static loading condition while the Charpy test had impact loading condition. The effects of strain-rate on fracture toughness had been reported by Radon and Turner who showed that significant changes in fracture toughness occurred when the strain rate was varied from 10^{-2} s^{-1} to 10^{7} s^{-1} (60).

(b) Triaxiality

The COD test specimen size has been shown to be adequately large so that size independent K_{IC} value could be obtained (see Section 8.3). Therefore, the degree of crack-tip triaxiality obtained by the COD test could be expected to be consistent. On the other hand, the Charpy V-notched specimen was arbitrarily specified as 10 mm thick. Consequently, the triaxiality of the crack-tip could vary in specimen of different flow stress levels.

(c) Notch Size

The artificial flaws introduced into the two types of test specimens differed significantly in size. The Charpy test specimen had a machined V-notched of root-radius approximately 0.25 mm whereas the COD test specimen had a fatigue crack. This difference is significant

because the fracture toughness had been reported to be affected by flaw size (see Figure 8.28 and Ref. No. 188).

Apart from the above tangible disparities, the basic concepts of the two tests are also different. The quasi-static fracture toughness test measures the energy required to cause the instability of the crack-tip material regardless of the mechanism of final specimen instability. The Charpy test differed by measuring the energy required to initiate and propagate the crack through the uncracked ligament of the test specimen only when instability is by total cleavage. Consequently, any attempt to generalise the correlation between the two fracture resistance parameters should be treated with caution.

Currently, several empirical correlations between the Charpy Impact Energy (C_v) and the fracture toughness (K_{IC}) had been reported[21, 31, 32, 33, 162, 163]. Some of these correlations are given in Table 8.7. The applicability of these correlations to the experimental steels were investigated by comparing the predictions made by these documentated correlations with the experimental data. The results of this comparison are given in Figures 8.31 to 8.33. Examination of these results will emphasise the empirical nature of these correlations as none of the correlation equations fit the experimental data. This is not unexpected because the empirical correlations were derived for different classes of steel. However, it can be seen that the basic form of the Marandet-Sanz correlation curve[31] was very similar to the

Correlation Equation Between K_{IC} And C_v*	Reference
$K_{IC} = 19(C_v)^{\frac{1}{2}}$ $T_{K_{IC}(100)} = 9 + 1.37\, T_{C_v(28)}$	Marandet and Sanz[31]
$K_{IC} = 30.2(C_v)^{\frac{1}{2}}$ $T_{shift} = 119 - 0.12\, \sigma_Y$	Barsom[32]
$K_{IC} = 3.08 \exp\{ .036(T - T_{40J}) + 100 \} + 36.4$	Chirigos and Meyer[33]

K_{IC} is the plane strain Critical Stress Intensity Factor

C_v is the Charpy V-Notched Impact Energy

Table 8.7 Empirical Correlations Between C_v And K_{IC}

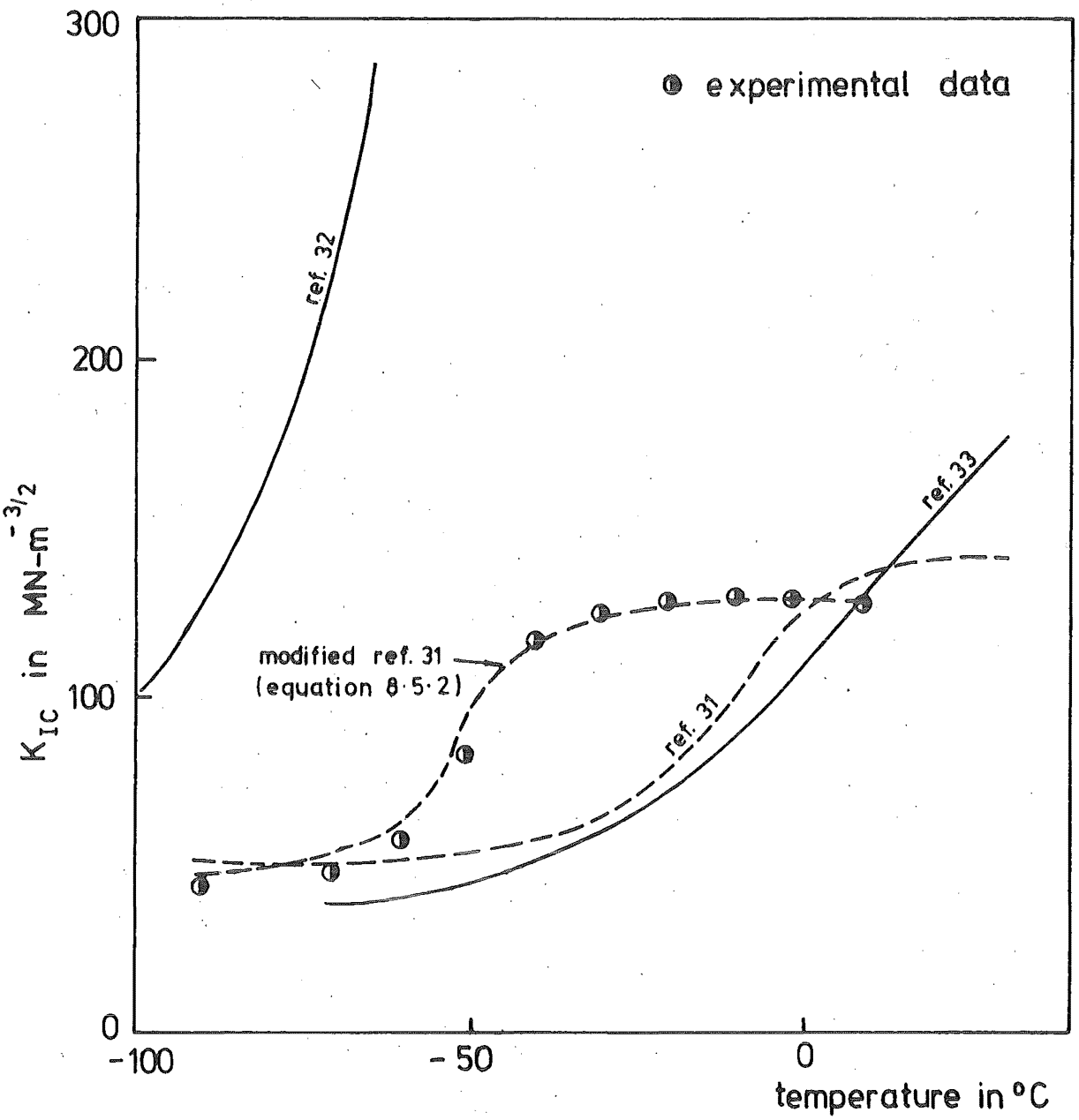

FIG. 8·31 COMPARISON BETWEEN PREDICTED & EXPERIMENTAL K_{IC} OF THE PRESSURE VESSEL STEEL.

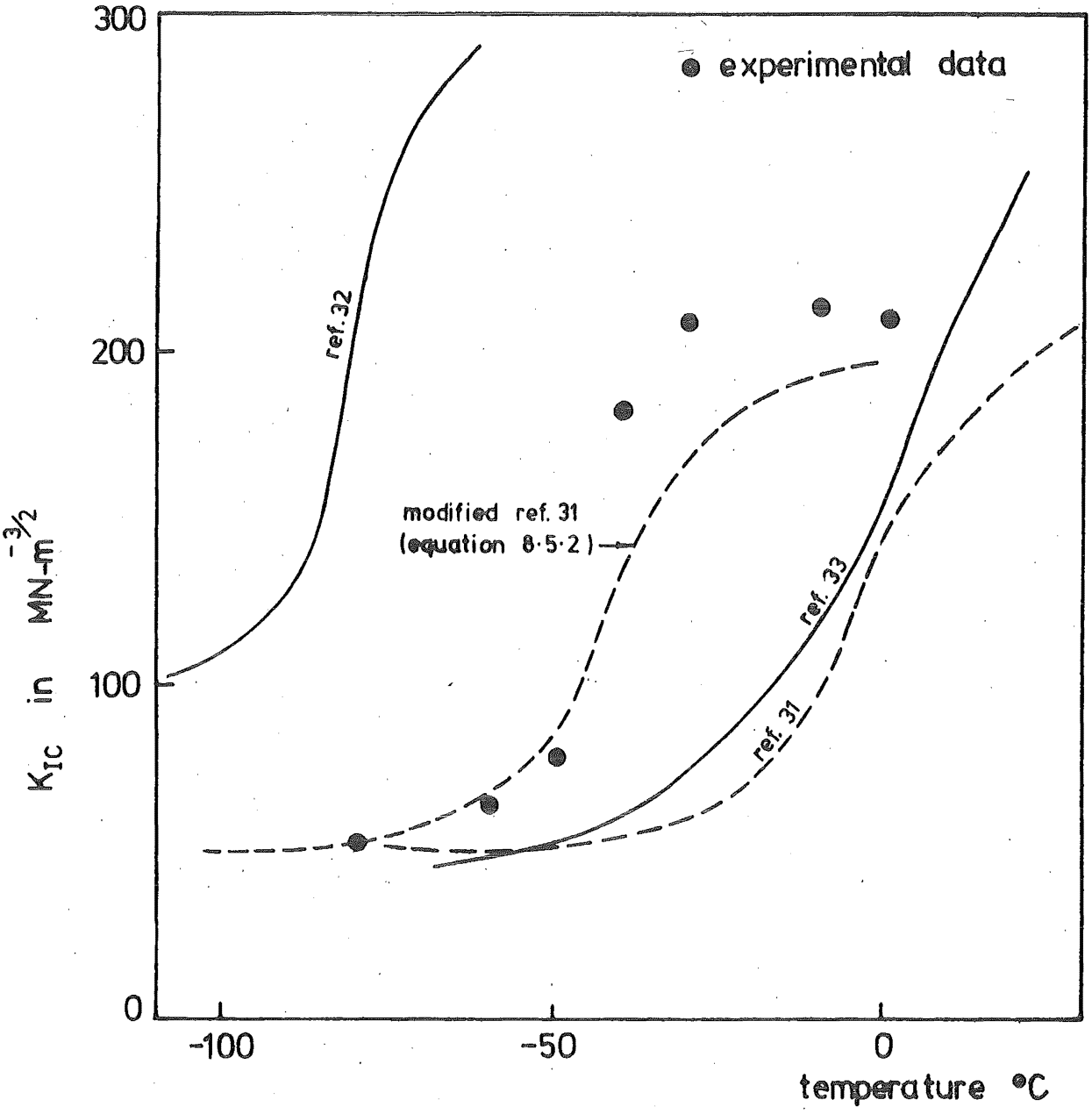

FIG. 8.32 COMPARISON BETWEEN PREDICTED & EXPERIMENTAL K_{IC} OF NORMAL GRADE 275 STEEL.

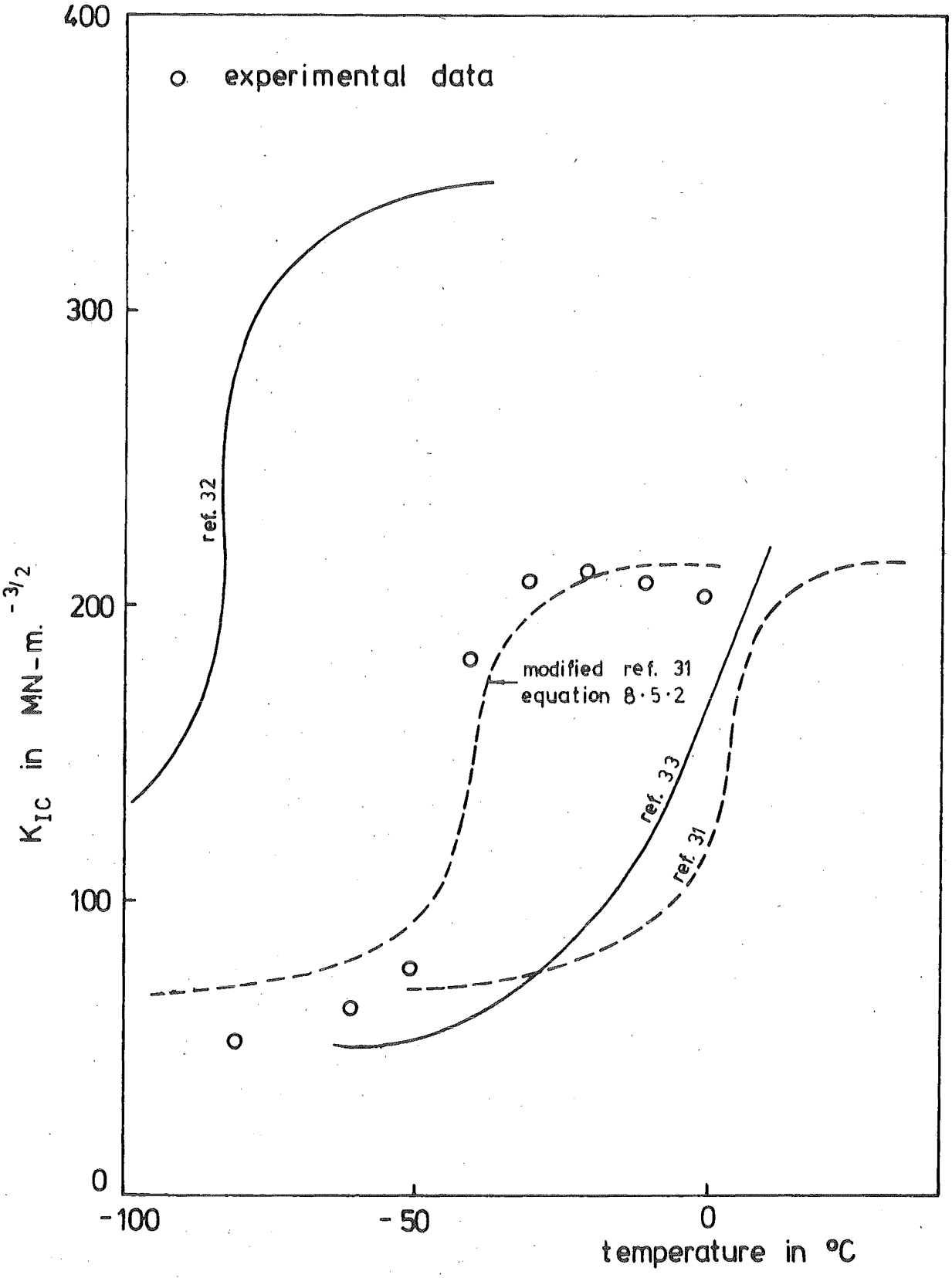

FIG. 8.33 COMPAPARISON BETWEEN PREDICTED & EXPERIMENTAL K_{IC} OF Ti-ADDED GRADE 275 STEEL.

experimental curves. When slight modification was introduced, the basic Marandet-Sanz correlation was found to agree with the experimental data. The modification included the redefinition of the point on the experimental K_{IC} (see Figures 8.24 and 8.25) and C_v (see Figures 8.29 and 8.30) versus temperature curves at which a rapid upswing in fracture resistance occurred. The modified correlation equations are listed in Table (8.8) and their predicted results were added onto Figures 8.31 and 8.33. As the basic Marandet-Sanz correlation equations had been derived from a series of low alloy Carbon-Manganese Steels with yield stress ranging from 215 to1000 $MN\text{-}m^{-2}$, it is not surprising that they could be adapted readily to describe the cleavage K_{IC}-C_v correlation of the experimental steels which were basically of similar chemical composition (see Table 7.1). However, it must be pointed out that the correlation was strictly limited to the cleavage regime with the transition temperature as the upper limit because the impact energy level at the upper shelf level, i.e. at microvoid coalescence, did not provide any meaningful information.

Hence, it was shown that empirical correlation could be established between the cleavage K_{IC} and C_v of the experimental steels. This observation is significant because when the statistical reliability of the correlation equations is determined, the more economical Charpy V-notched Impact test can be used to evaluate the cleavage fracture toughness indirectly when fracture resistance testings are being performed for quality control purposes. However, if the fracture toughness data are required for

Steel Type	Correlation Equation Between Experimental K_{IC} And C_v*	Equation Number
Pressure Vessel (Figure 8.31)	$K_{IC} = 16(C_v)^{\frac{1}{2}}$	8.5.1.a
	$T_{K_{IC}}\ (60\ MN\text{-}m^{-\frac{3}{2}}) = T_{C_v}\ (20J) - 58$	8.5.1.b
Normal And Ti-Added Grade 275 (Figures 8.32 and 8.33)	$K_{IC} = 19(C_v)^{\frac{1}{2}}$	8.5.2.a
	$T_{K_{IC}}\ (80\ MN\text{-}m^{-\frac{3}{2}}) = -(T_{C_v}\ (20J) + 55)$	8.5.2.b

* K_{IC} is the Plane Strain Critical Stress Intensity Factor

C_v is the Charpy V-Notched Impact Energy

Table 8.8 Experimental K_{IC}-C_v Correlation Of The Pressure Vessel And Grade 275 Steels

design analysis, it is felt that the fracture toughness test should always be used since it has been shown that size independent data could be obtained with the use of small test specimens.

8.6 The Fatigue Crack-Tip Plastic Zone

The current popular models of fatigue crack propagation assumed that plastic deformation occurred at the crack-tip[24, 25, 26]. This assumption was supported experimentally by the report that zones of high density tangled dislocations were observed at the fatigue crack-tip area of α-iron specimens[27]. In this project, the presence of this fatigue crack-tip plastic zone was investigated with the use of a special High Nitrogen Low Carbon steel. The details of the experimental technique have been given earlier in Section 7.7. The micrographs of the crack-tip area of the etched specimens are given in Plates 8.8 and 8.9, where the plastically deformed zones at the crack-tip are represented by the dark areas of high etch-pit density. The Scanning Electron Micrograph given in Plate 8.9 gives a close-up view of the individual etch-pit on the surfaces of the grain located adjacent to the crack-tip. The plastic zones were observed to be present as two "lobes" at the crack-tip. The size of each lobe was estimated at approximately 25 to 50 μm ahead, and 100 μm away from the side of the crack-tip. In terms of grain size, the extent of these zones was estimated at 1 to 2 grains ahead, and about 4 grains on either side of the crack-tip. Thus, the plastic zones covered an area of the crack-tip material from which the fracture toughness were being measured by

PLATE 8·8 THE FATIGUE CRACK TIP PLASTIC ZONE (×425)

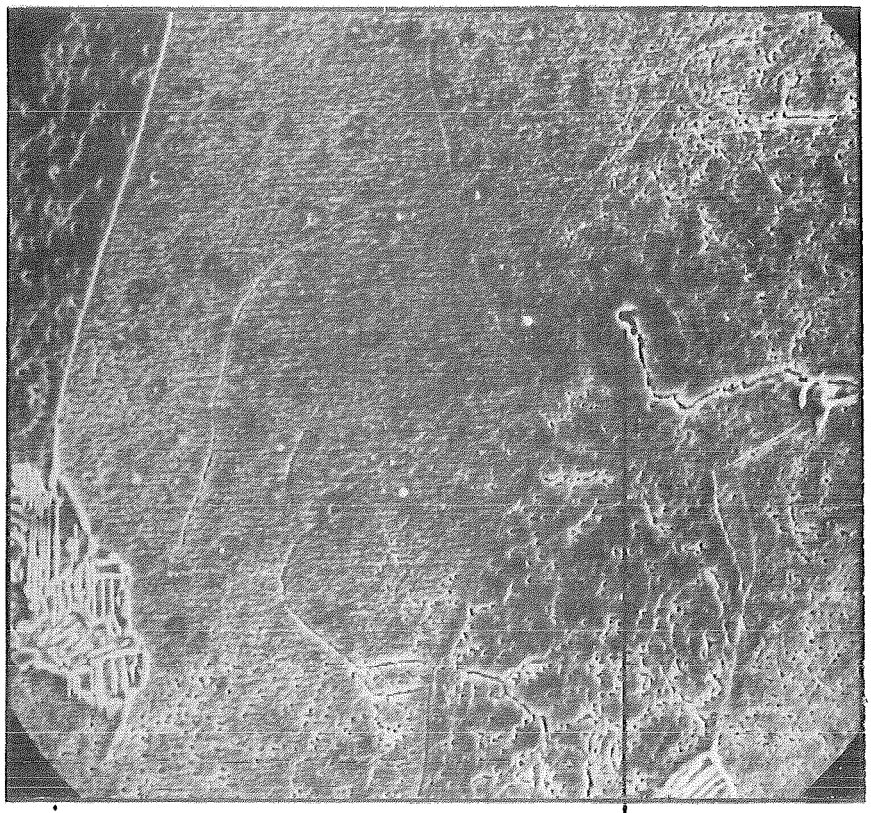

PLATE 8·9 ETCH PITS AT THE FATIGUE CRACK TIP AREA (×2400)

both the standard ASTM K_{IC} and the COD test methods. Consequently, the change in the material properties caused by ageing the fatigue crack-tip plastic zones could produce significant embrittlement effect.

8.7 The Effect Of Ageing Of The Fatigue Crack-Tip Plastic Zone On Fracture Toughness

The Billet and the Grade 275 Steels were originally selected for this investigation because they could be treated to produce different strain ageing propensity. However, it was found that the reduction of active Nitrogen by the AlN precipitation heat treatment had resulted in the unexpected temperature insensitivity of the critical COD (see Section 8.3). Consequently, the Billet Steel was found to be unsuitable. Fortunately, the addition of Titanium in Grade 275 Steel as a nitride former did not affect either the fracture toughness level or its temperature dependence (see figure 8.25), although the active Nitrogen content was reduced by approximately sixteenfold.

The results of this series of tests are given in Figures 8.34 and 8.35. Both figures compared the temperature dependence of the critical COD values of the as-fatigued specimens with those of the specimens that were aged after fatigue cracking - the ageing treatment being soaking at $80^{o}C$ for 30 hours. It can be seen that the ageing treatment produced a small but significant shift in the transition temperature of the Normal steel but did not affect that of the Ti-added steel. However, both the lower and upper shelf

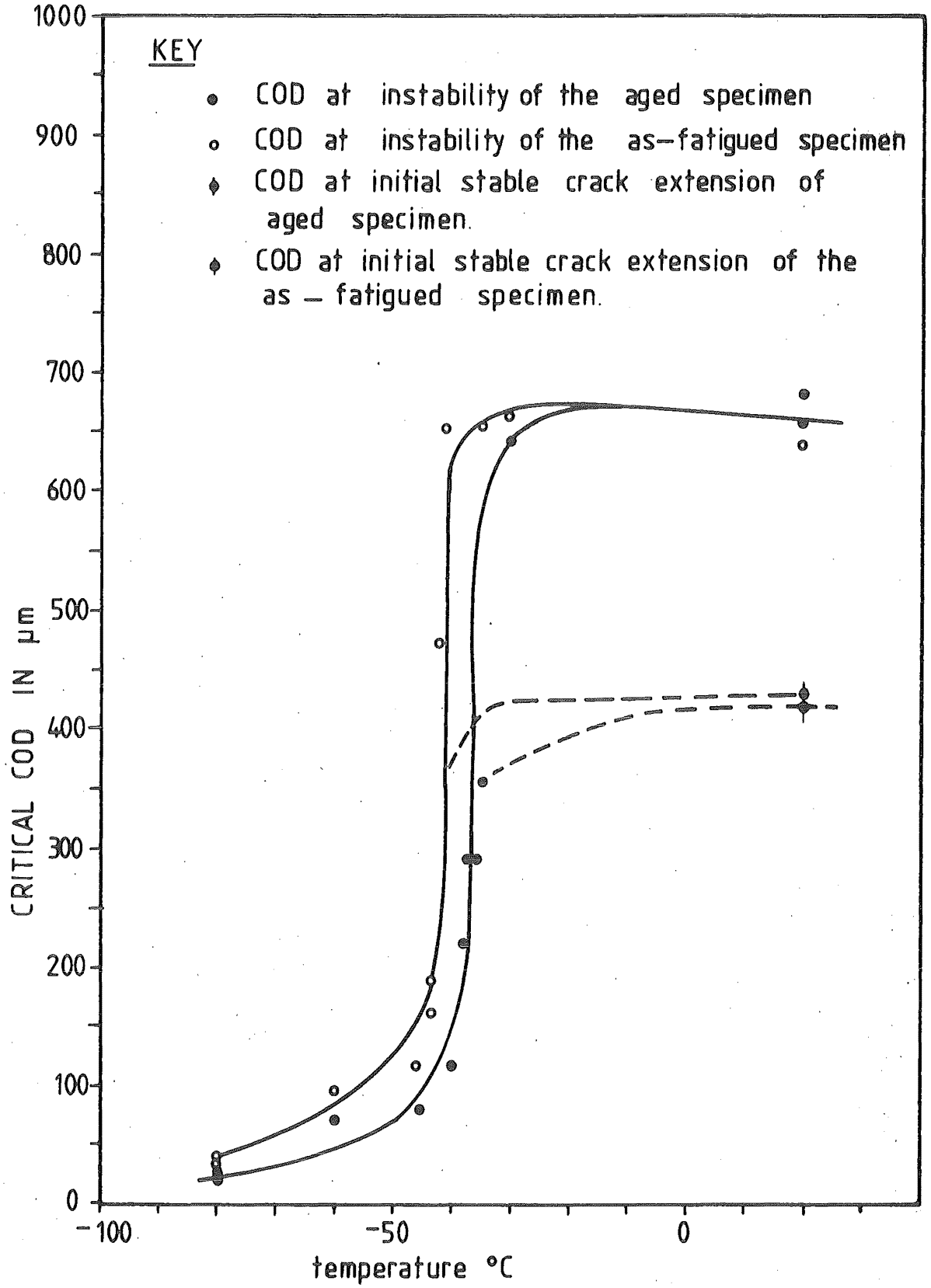

FIG 8·34 VARIATIONS OF CRITICAL COD WITH TEMPERATURE OF NORMAL GRADE 275 STEEL -SHOWING THE EFFECT OF AGEING

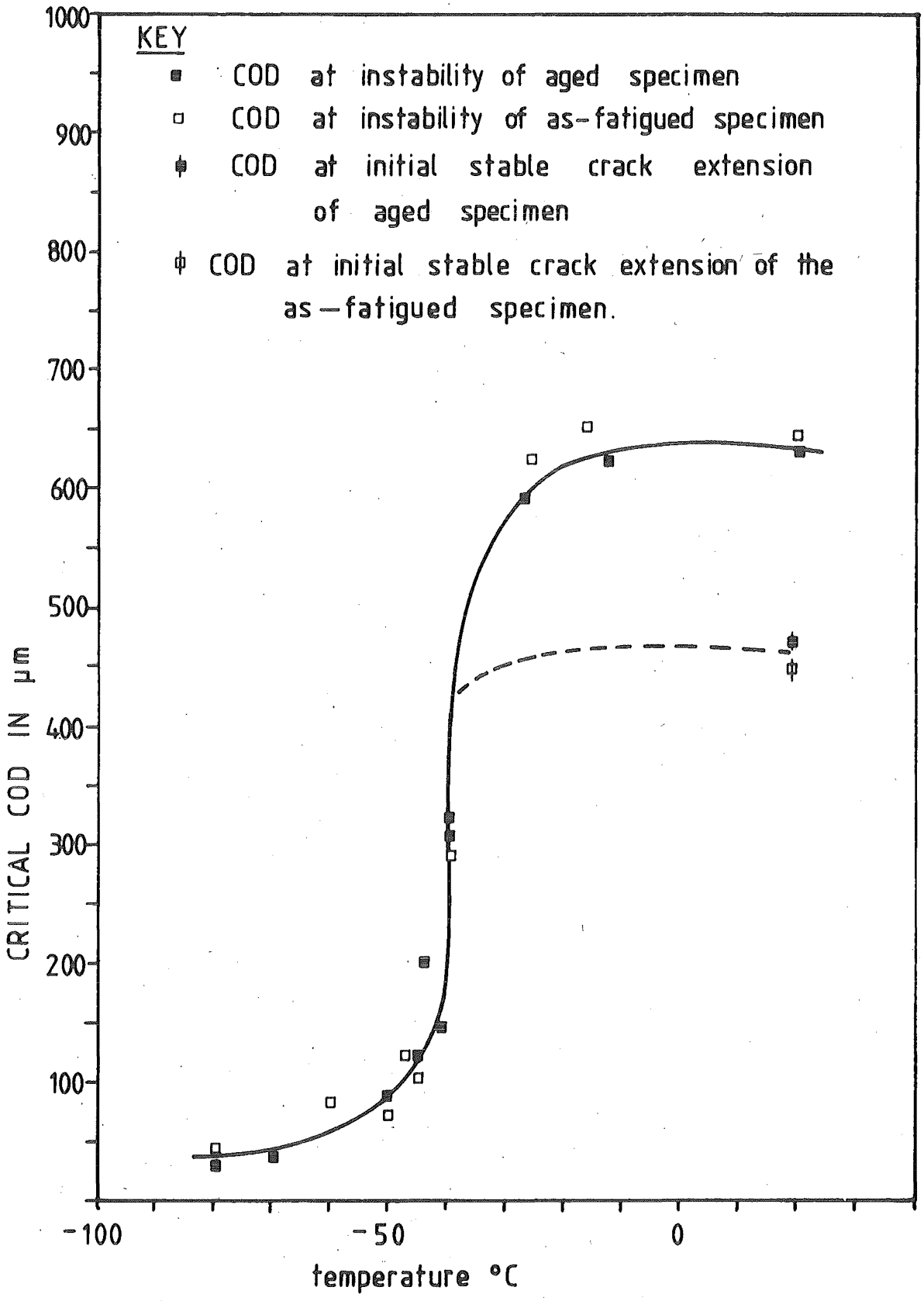

FIG 8·35 VARIATIONS OF CRITICAL COD WITH TEMPERATURE OF Ti-ADDED GRADE 275 STEEL - SHOWING THE EFFECT OF AGEING

levels of the two steels were not affected.

Using the combination of

(i) The COD test results given in Figures 8.34 and 8.35

(ii) The tensile test results given earlier in Figure 8.19

the fracture toughness values were calculated using Equation (7.4.4) given as

$$K_{crit} = 0.4769 \, (\sigma_{LY} \delta_c)^{\frac{1}{2}} \ MN\text{-}m^{-\frac{3}{2}}$$

where K_{crit} is the Critical Stress Intensity Factor

σ_{LY} is the Lower Yield Stress in $MN\text{-}m^{-2}$

δ_c is the critical COD in μm.

These calculated results are summarised in Figures 8.36 and 8.37. The thickness-dependence of these fracture toughness values were evaluated using the size criterion (see Section 8.3)

$$a \ , \ W - a \ , \ B \geq 25 \ \delta_c$$

where a is the crack length

W - a is the uncracked ligament length

B is the specimen thickness

δ_c is the COD at the initial instability of the crack-tip material

It can be seen that except for the highest COD value of the Normal steel, the size criterion was met adequately. The highest COD value

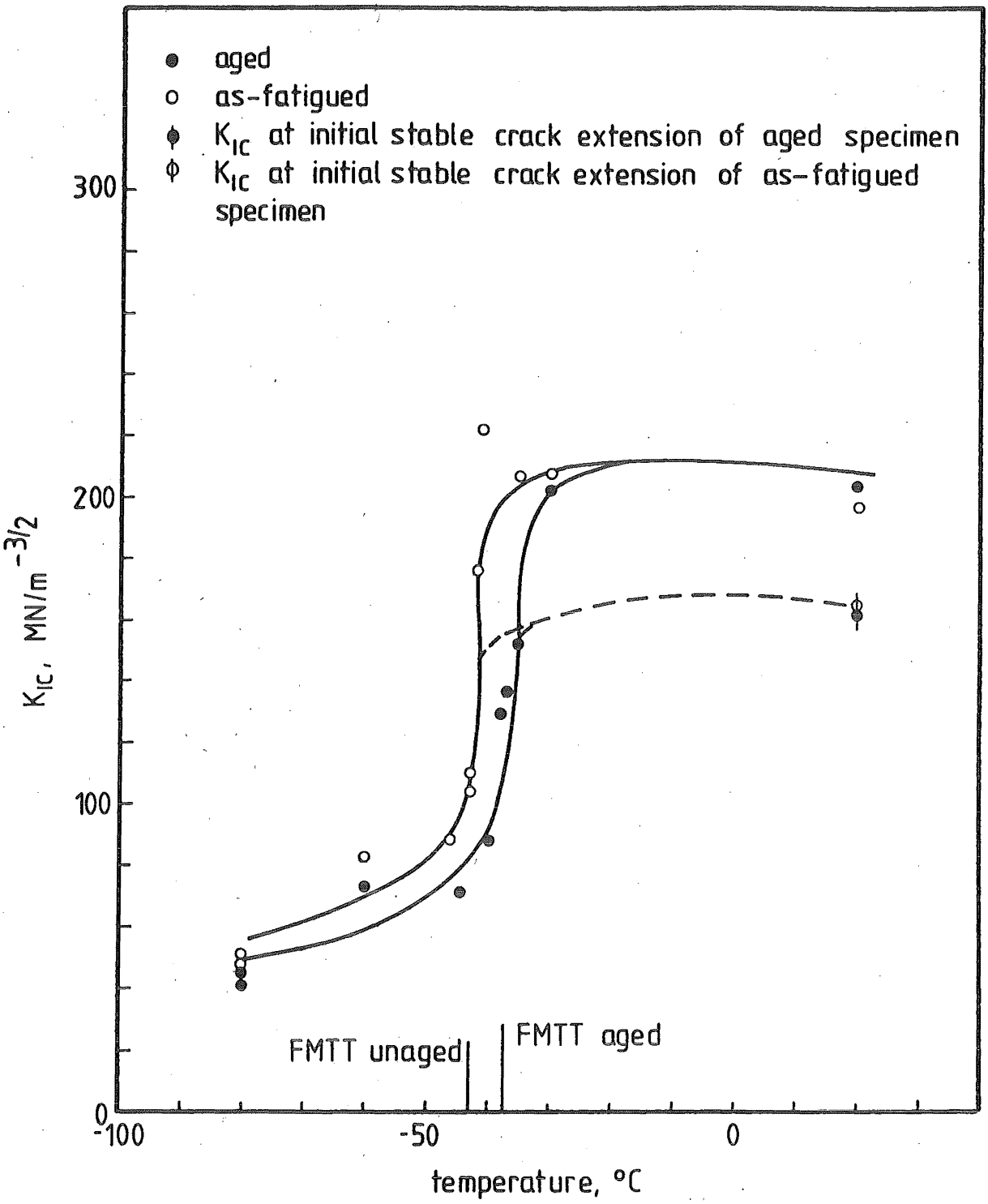

FIG 8·36 VARIATION OF K_{IC} WITH TEMPERATURE OF NORMAL GRADE 275 STEEL - SHOWING THE EFFECT OF AGEING

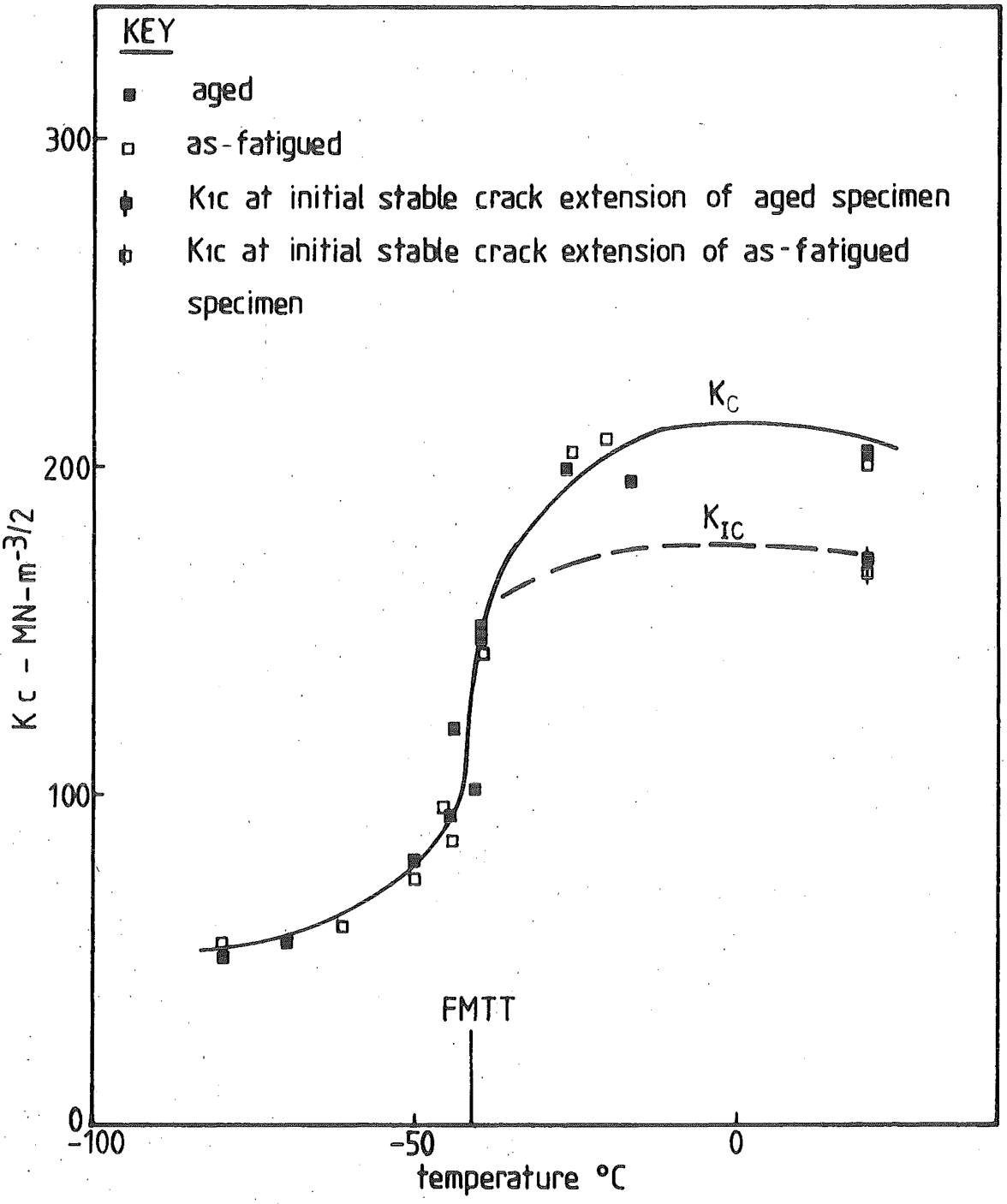

FIG. 8·37 VARIATION OF K_C WITH TEMPERATURE OF TI-ADDED GRADE 275 STEEL - SHOWING THE EFFECT OF AGEING

of the Normal Steel tested at 25°C was 450 μm. The corresponding minimum size for size independent fracture toughness was calculated to be 11.5 mm. This value was slightly higher than the actual nominal specimen size of

$$a = W - a = B = 10 \text{ mm}$$

Hence, it was felt that even in this test, the K_{crit} value should be very close to the size independent value because the ratio $\frac{B}{\delta_c}$ was approximately 22.2 (see Section 8.3). Consequently, the K_{crit} results of this investigation were expected to be size independent and can therefore be regarded as the "plane-strain" K_{IC} values. Once again, from the results given in Figures 8.35 and 8.36, it can be seen that as in the COD test results of Figures 8.34 and 8.35 the ageing treatment affected the fracture toughness in the vicinity of the fracture mode transition temperature of the Normal Steel but not the Ti-added Steel.

Before discussing the experimental results, it is necessary to examine any error arising from the use of the lower yield stress, σ_{LY}, in the calculation of K_{IC} for both the as-fatigued and the aged specimens. It is well established that static strain ageing raises the flow stress level (see Figure 6.1) so that the change in flow stress, ΔY, caused by strain ageing can be written as

$$\Delta Y = \sigma_{Y_{aged}} - \sigma_{flow_{pre\text{-}strained}} \qquad (8.7.1)$$

where $\sigma_{Y_{aged}}$ is the yield stress of the aged material

$\sigma_{flow_{pre\text{-}strained}}$ is the flow stress of the pre-strained material

The effect of Titanium addition on the magnitude of ΔY of Grade 275 Steel with 5% pre-strain and an artificial ageing treatment of 3 hours at 100°C had been reported earlier by Chong and Lim[164] and their results are shown in Figure 8.38. Similar estimate of ΔY measured at -196°C was not performed because it was not feasible to attach the extensometer onto the tensile specimen without elaborate modification. However, from the -196°C tensile test records of both the Normal and Ti-added Steel specimens given in Figures 8.39 and 8.40, it can be seen that

$$\sigma_{flow_{5\%}} \simeq \sigma_{LY_{as\text{-}rolled}} \qquad (8.7.2)$$

where $\sigma_{flow_{5\%}}$ is the flow stress at 5% pre-strain

$\sigma_{LY_{as\text{-}rolled}}$ is the lower yield stress in the as-rolled condition

so that at -196°C

$$\Delta Y \simeq \sigma_{LY_{strain\ aged}} - \sigma_{LY_{as\text{-}rolled}} \qquad (8.7.3)$$

Hence, the magnitude of ΔY at -196°C can be estimated from the results of strain ageing on the tensile properties of the two steels given in Figures 8.41 and 8.42. These results were combined with those measured at ambient temperature to give an estimate of ΔY at the two extremities of the test temperature range, and these combined results are shown in Table 8.9. The error ratio shown by $\frac{\Delta Y}{\sigma_{flow}}$ in Table 8.9 was unlikely to be exceeded in the calculation

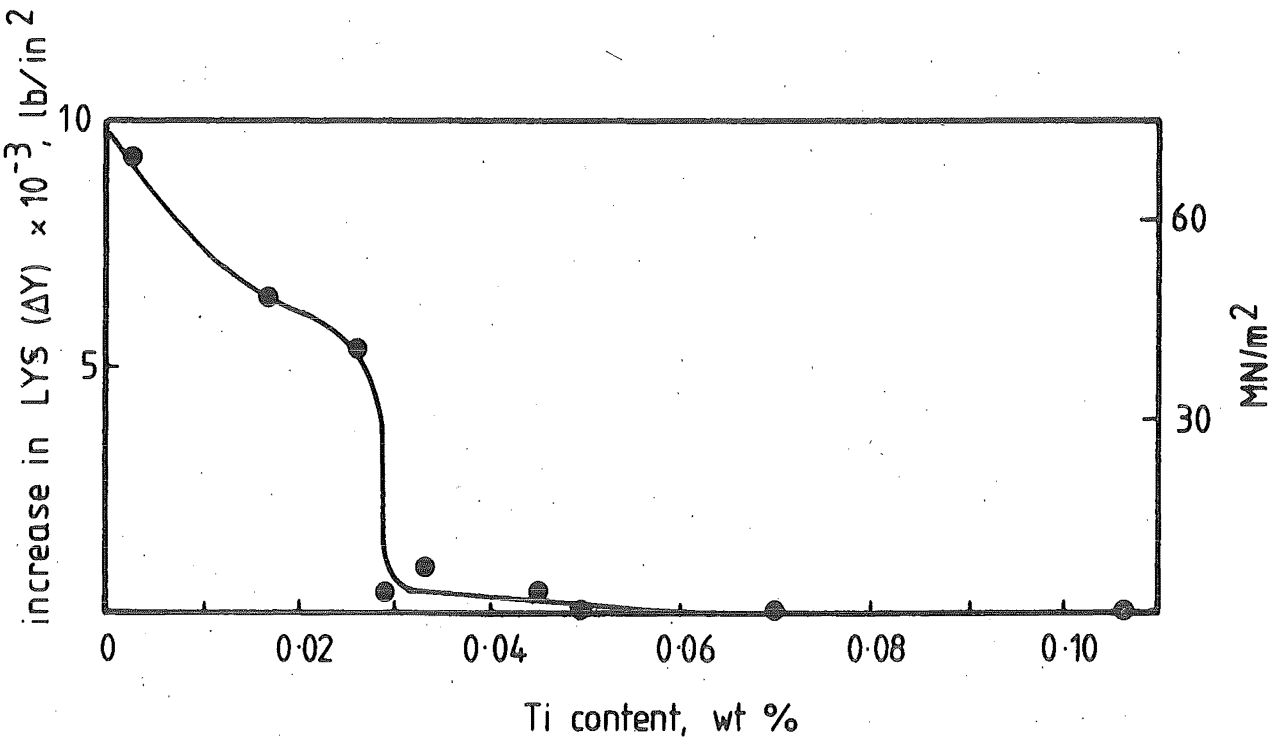

FIG 8·38 EFFECT OF TITANIUM CONTENT ON THE INCREASE IN LOWER YIELD STRESS (ΔY) AFTER STRAIN AGEING. (GRADE 275). (Chong & Lim [164])

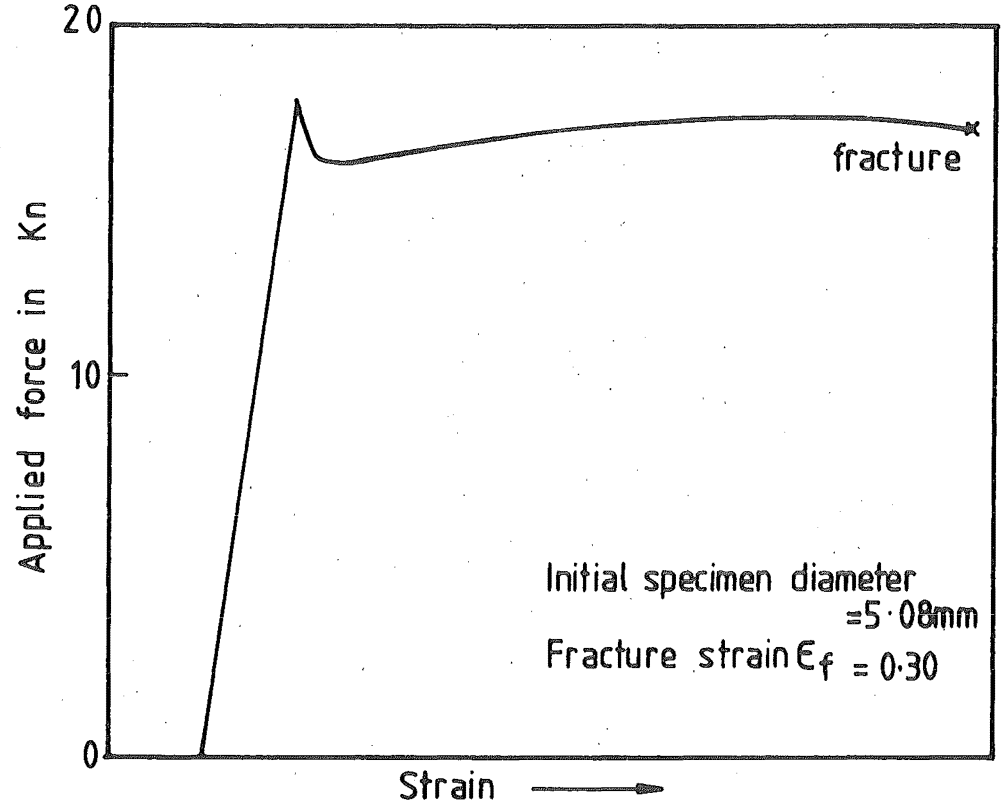

FIG 8·39 TYPICAL TENSILE TEST RECORD OF NORMAL GRADE 275 STEEL AT −196°C

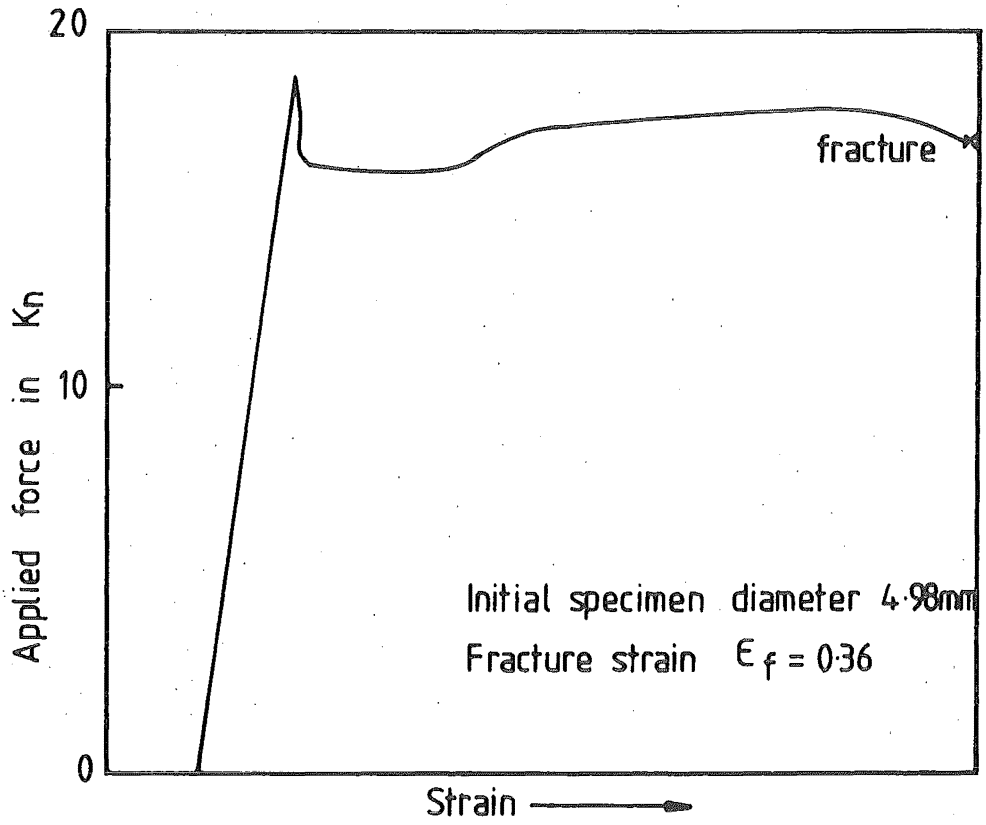

FIG 8·40 TYPICAL TENSILE TEST RECORD OF Ti-added GRADE 275 STEEL AT -196°C

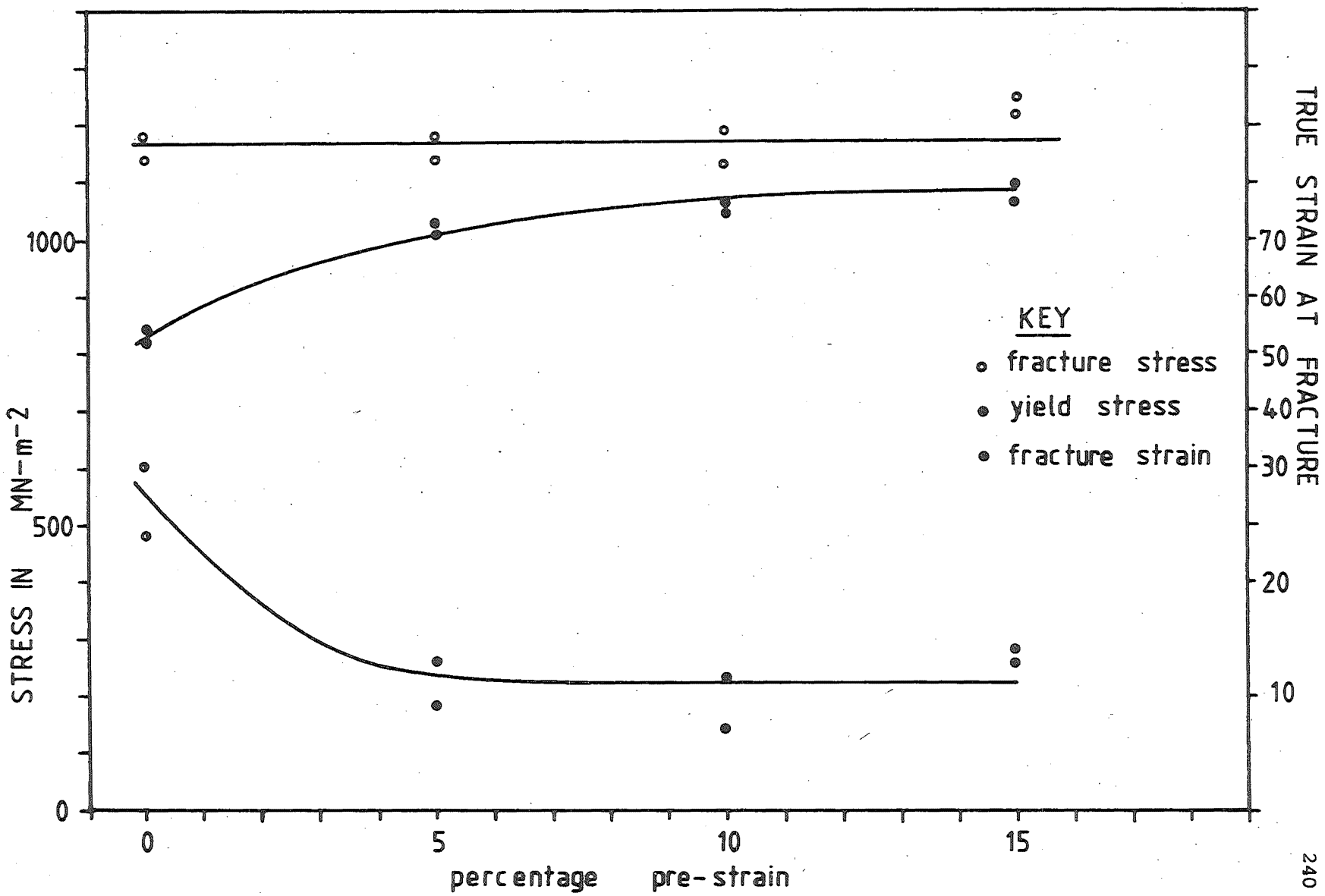

FIG 8-41 EFFECTS OF STRAIN AGEING ON THE TENSILE PROPERTIES OF THE NORMAL GRADE 275 STEEL MEASURED AT -196° CELSIUS

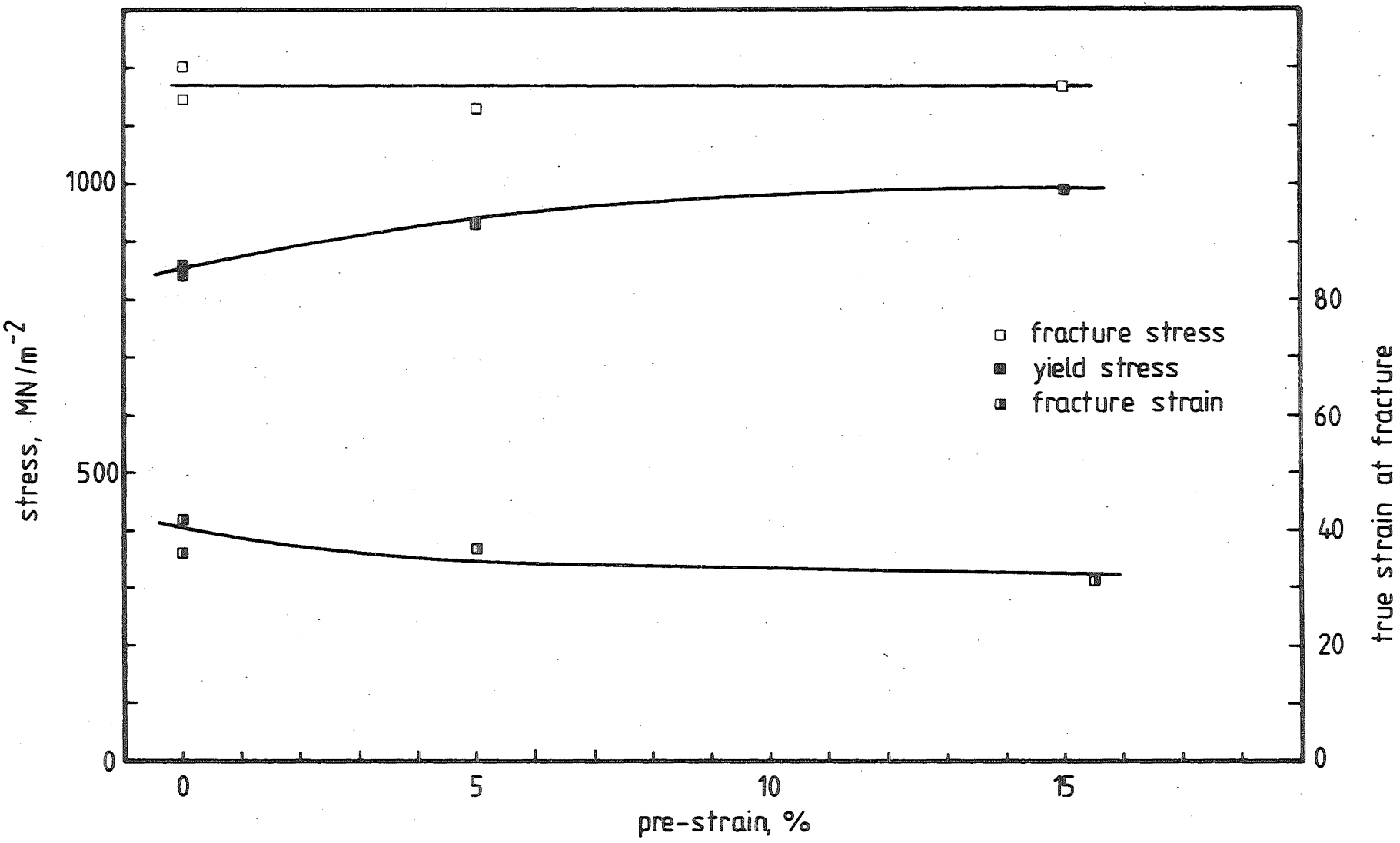

FIG 8·42 EFFECT OF STRAIN AGEING ON THE TENSILE PROPERTIES OF THE Ti-ADDED GRADE 275 STEEL MEASURED AT -196°C.

Steel Type	Temperature (^{o}C)	Flow Stress		Strain Aged Yield Stress $\sigma_{Y_{aged}}$ ($MN\text{-}m^{-2}$)	Change In Flow Stress ΔY ($MN\text{-}m^{-2}$)	$\frac{\Delta Y}{\sigma_{flow}}$
		As-Rolled Yield Stress, $\sigma_{as\text{-}rolled}$ ($MN\text{-}m^{-2}$)	5% pre-strain $\sigma_{5\%\ p.s.}$ ($MN\text{-}m^{-2}$)			
Normal	25	285	379	442	63	0.17
Normal	-196	830	-	915	85	0.10
Ti-Added	25	296	411	414	3	0.01
Ti-Added	-196	850	-	930	80	0.01

Table 8.9 Effect Of Strain Ageing On The Flow Stress Of The Grade 275 Steel

of K_{IC} where the flow stress was taken as the As-Rolled yield stress because the plastic strain at the fatigue crack-tip plastic zone was unlikely to exceed that induced by the 5% pre-strain. Consequently, the ratio of $\frac{\Delta Y}{\sigma_{flow}}$ caused by the strain ageing of the fatigue crack-tip plastic zone was expected to be lower than the estimate given in Table 8.9 because the magnitude of ΔY had been shown to be influenced by the severity of prestraining (see Figures 8.41 and 8.42). Hence, the conservative limit of the uncertainty in the calculation of K_{IC} caused by ignoring the change in flow stress due to strain ageing can be evaluated by the equation

$$\frac{\Delta K_{IC}}{K_{IC}} = \frac{1}{2} \left(\frac{\Delta Y}{\sigma_{flow}}\right) \qquad (8.7.4)$$

Using the data given in Table 8.9, the magnitude of the ratio $\frac{\Delta K_{IC}}{K_{IC}}$ of the Normal Grade 275 Steel was calculated at < 10% while that of the Ti-added Steel was insignificant. Consequently, the shift in Fracture Mode Transition Temperature of the Normal Grade 275 Steel shown in Figure 8.36 could not have been caused by either the uncertainty in the calculation of K_{IC} or in temperature monitoring technique (see Section 8.1) and was therefore caused by strain ageing.

The effect of the ageing of the crack-tip plastic zone on the fracture toughness measured at $-196^{o}C$ was investigated and the results are given in Table 8.10. It can be seen that the quasi-brittle fracture toughness was not affected by the ageing of the

Steel Type	Instability Load P_Q (KN)	Crack Length a (mm)	Specimen Width W (mm)	Specimen Thickness B (mm)	$\frac{a}{W}$	Compliance Function $Y(\frac{a}{W})$	Apparent Fracture Toughness K_Q + ($MN\text{-}m^{-\frac{3}{2}}$)	Yield Stress* σ_{LY} ($MN\text{-}m^{-2}$)	$B>2.5(\frac{K_Q}{\sigma_Y})^2$
Normal (Aged)	2.30	10.80	20	9.97	0.540	10.890	17.9	832	Yes
Normal (As-fatigued)	2.90	10.07	20	9.96	0.503	9.609	19.8	832	Yes
Ti-Added (Aged)	2.20	11.0	20	9.96	0.550	11.26	17.6	846	Yes
Ti-Added (As-fatigue)	2.60	10.37	20	9.97	0.519	10.18	18.8	846	Yes

* See Figures 8.40 and 8.41 + $K_Q = \frac{P_Q}{BW^{\frac{1}{2}}} Y(\frac{a}{W})$; for values of $Y(\frac{a}{W})$ see ref. No.3.

Table 8.10 Effect Of Strain Ageing On The Fracture Toughness Of The Grade 275 Steels Measured At -196°C

fatigue crack-tip plastic zone. This experimental observation further supported the micro-fracture model for cleavage failure [15, 16] discussed earlier in Section 8.4.a. The fracture model's equation of

$$K_{IC} = \sigma_F (4\pi d_g)^{\frac{1}{2}}$$

where K_{IC} is the fracture toughness

σ_F is the fracture stress

d_g is the grain diameter

predicts that the fracture toughness should be independent of strain ageing as the fracture stress, σ_F, had been experimentally found to be independent of strain ageing (see Figures 8.41 and 8.42). This prediction was verified by the results given in Table 8.10.

On the other extremity of the test temperature range, i.e. where fracture occurred by micro-void coalescence, the ductile fracture model [18, 19] predicted that the critical COD at the initial instability of the crack-tip material, δ_i, would depend on the influence of strain ageing on the crack-tip critical strain only since

$$\delta_i = \varepsilon_{fi} \times \ell_f$$

where ε_{fi} is the critical crack-tip strain or notched ductility

and ℓ_f is the average inter-MnS inclusion spacing

Consequently the effect of strain ageing on the critical crack-tip

strain was investigated experimentally. The results of this investigation given in Figures 8.43 and 8.44 showed that the critical crack-tip strain (notched ductility) was apparently independent of strain-ageing. Since the average inclusion spacing should also remain unaltered, the micro-void coalescence model appears to predict δ_i, the critical COD at the initial separation of crack-tip material to be independent of the ageing crack-tip plastic zone. This prediction was supported by the experimental data shown in Figures 8.34 and 8.35. However, these observations are in conflict with earlier reports on the effects of strain ageing on ductility and fracture toughness published elsewhere[28, 130]. This apparent discrepancy is not entirely surprising because the degree of pre-strain at the mechanical notch root is expected to be small, possibly even less severe than that at the fatigue crack-tip. Hence it is likely that the COD test is insufficiently sensitive to detect the effect of strain ageing of these small plastic strains thus producing the above-mentioned discrepancy.

Since the two basic micro-fracture and models were shown to predict the independence of the cleavage and ductile fracture toughness from the ageing of the crack-tip plastic zone, it is logical to assume that the small shift in the transition temperature of the high active Nitrogen Steel (Normal Grade 275) observed in Figure 8.35 can be elucidated by these two fracture models. At $-196^{o}C$, the magnitude of the yield stress and the fracture stress were comparable. Consequently, very small degree of plastic yielding at the crack-tip was required to intensify the local tensile stress level, σ_{local}, to exceed the fracture stress, σ_F. It is reasonable to assume that the as-fatigued Normal Grade 275 Steel specimen has a slightly higher degree of plastic deformation prior to fracture than the aged steel because the latter had a higher flow stress level (see Figures 8.41 and 8.42). Hence, by denoting the applied stress as σ_{app}, the plastic strain

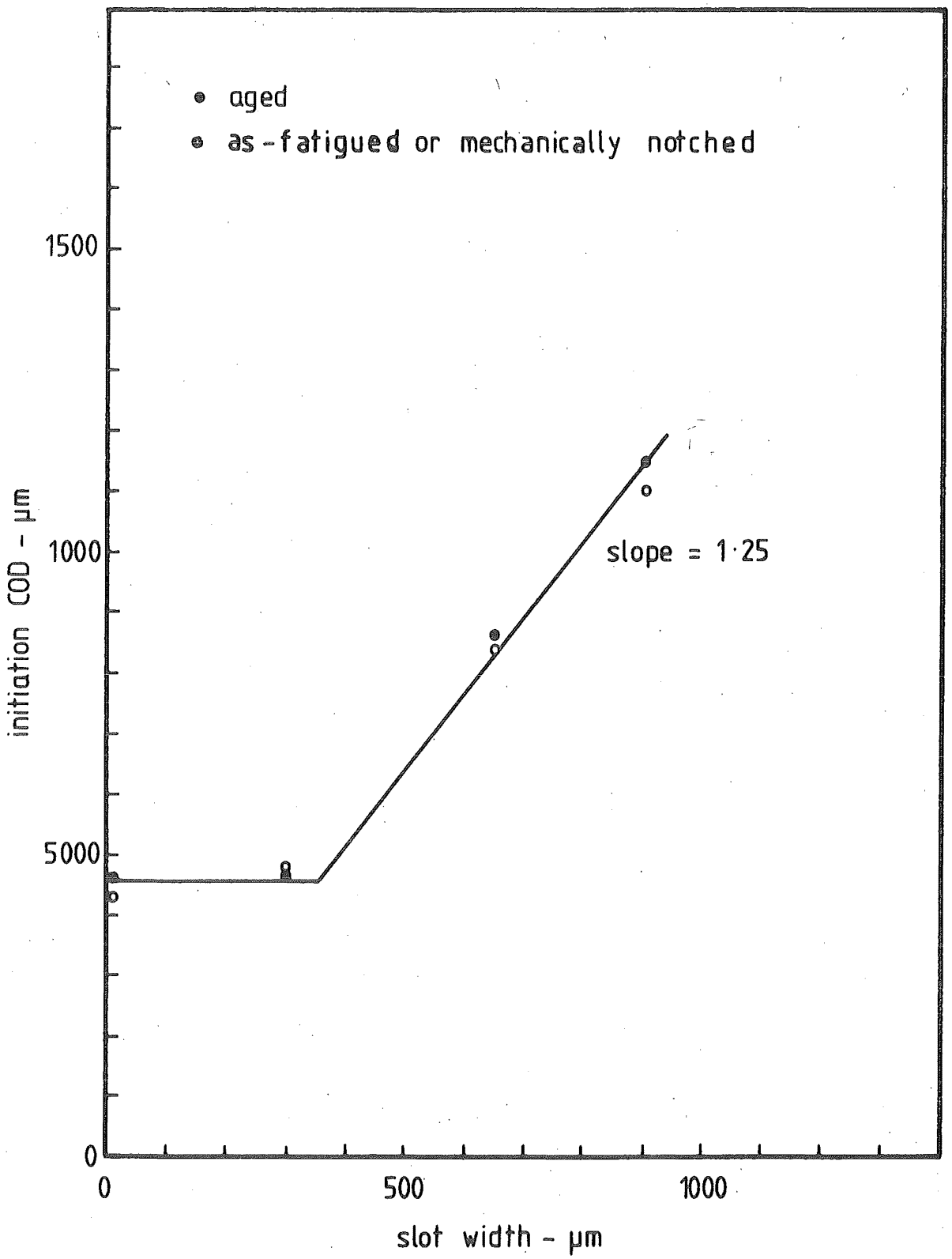

FIG 8·43 NOTCHED DUCTILITY OF NORMAL GRADE 275 STEEL

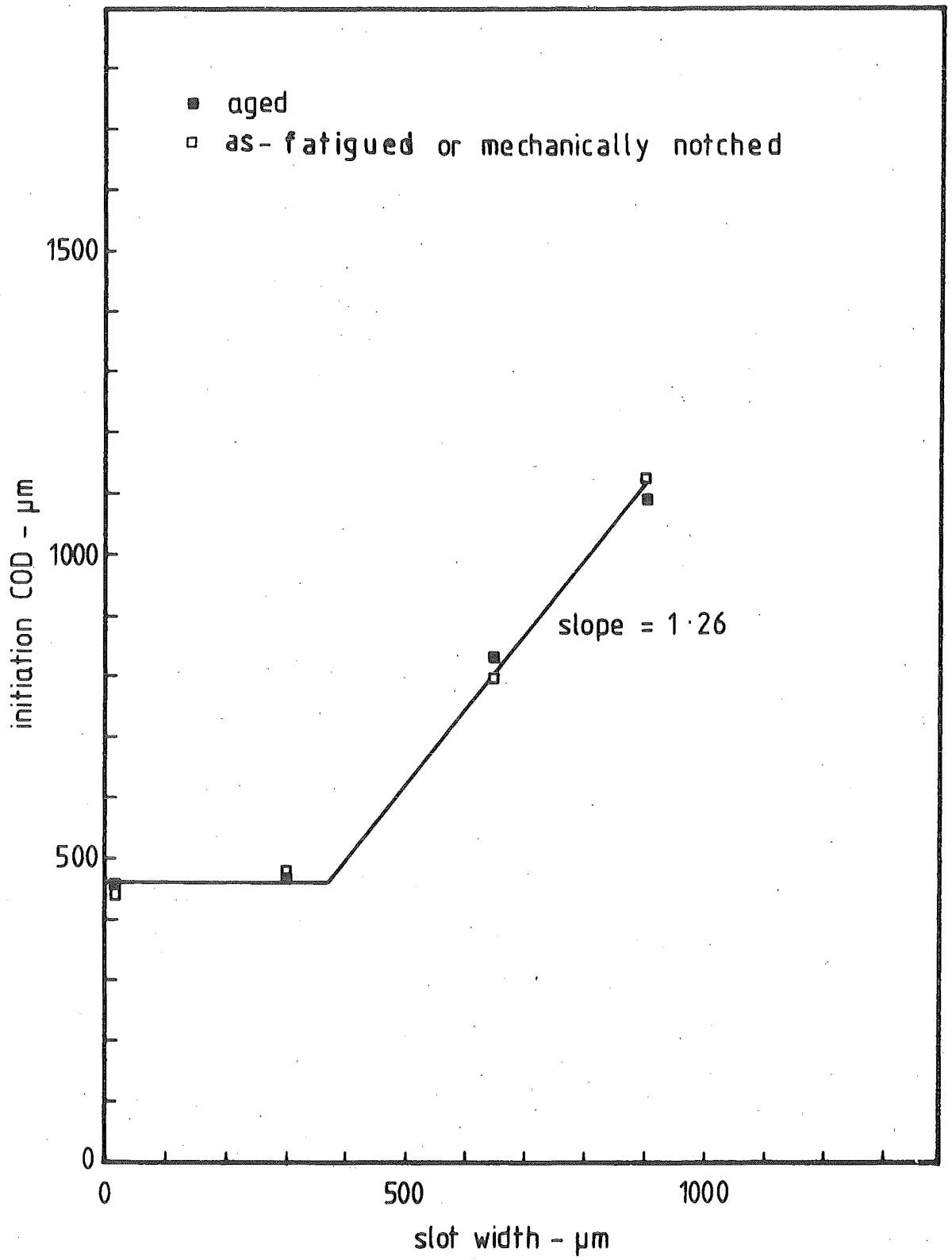

FIG. 8·44 NOTCHED DUCTILITY OF Ti-ADDED GRADE 275 STEEL

as ε_p, the yield stress as σ_Y and the flow stress as σ_{flow}, the local crack-tip tensile stress, σ_{local}, can be expressed as

$$\sigma_{local} = f(\sigma_{app}) \quad \text{when } \sigma_{local} < \sigma_Y \tag{8.7.5.a}$$

$$\sigma_{local} = f(\sigma_{flow}) = f(\varepsilon_p) \quad \text{when } \sigma_{local} > \sigma_Y \tag{8.7.5.b}$$

and the fracture plastic strain, ε_F, of the aged and as-fatigued specimens can be related by the expression

$$\varepsilon_{F_{aged}} < \varepsilon_{F_{as\ fatigued}} \tag{8.7.6}$$

As the temperature increased, the yield stress should decrease. This can be confirmed by comparing the yield stress of the Grade 275 Steel measured at different temperature, as shown in Table 8.11. Hence, increasing degree of stress intensification by plastic strain hardening of the crack-tip material[165] was now required to elevate the local crack-tip stress, σ_{local}, to exceed the fracture stress, σ_F, which was earlier reported to be temperature independent[160, 161]. Hence the condition of cleavage fracture at any temperature T remained as

$$\sigma_{local} \geq \sigma_F \tag{8.7.7}$$

possible with σ_{local} being attained over the characteristic distance of twice the average grain diameter ahead of the crack-tip. Thus, in the cleavage fracture regime in the vicinity of the Fracture Mode Transition Temperature (FMTT), both the local crack-tip stress of the aged and the as-fatigued specimens must exceed the fracture

Temperature (^{o}C)	Yield Stress σ_Y ($MN\text{-}m^{-2}$)	
	Normal	Ti-Added
-196	830	850
-80	374	400
25	285	296

Table 8.11 Temperature Dependence Of The Yield Stress Of The Grade 275 Steel

stress σ_F so that

$$\sigma_{local_{aged}} = \sigma_{local_{as\text{-}fatigued}} \geq \sigma_F \qquad (8.7.8)$$

However, since the yield stress level of the aged specimen, $\sigma_{Y_{aged}}$, was higher than the flow stress level of the as-fatigued specimen $\sigma_{flow_{as\ fatigued}}$ i.e.

$$\sigma_{Y_{aged}} > \sigma_{flow_{as\text{-}fatigued}} \qquad (8.7.9)$$

the degree of plastic strain required in the aged steel would be less than that in the as-fatigued specimen in elevating the local crack-up stress, σ_{local}, to exceed the fracture stress, σ_F so that the fracture plastic strain can still be expressed as in Expression (8.7.6) where

$$\varepsilon_{F_{aged}} < \varepsilon_{F_{as\text{-}fatigued}}$$

This argument was indirectly supported by the fracture strain data of Figures 8.41 and 8.42 which showed that the fracture strain of the strain aged Normal Grade 275 Steel was markedly lower than that of the as-rolled material while strain ageing had little effect on the fracture strain of the low strain ageing propensity Ti-added Grade 275 Steel. It should be noted that although ageing was kept minimal in the as-fatigued specimens, some dislocation locking were still expected to have occurred during the short time required for the preparation of the specimens for COD testing after pre-fatigue

cracking. Thus, it is reasonable to assume that the yield point would re-emerge in these specimens although the magnitude of the change in flow stress given as

$$\Delta Y = \sigma_{Y_{aged}} - \sigma_{flow_{as\ fatigued}}$$

was expected to be insignificant because of the short ageing time[130, 141]. Consequently, the value of $\sigma_{flow_{as\ fatigued}}$ in Expression (8.7.9) can be written as $\sigma_{Y_{as\ fatigued}}$, with $\sigma_{Y_{as\ fatigued}}$ being different from the fully aged yield stress value of $\sigma_{Y_{aged}}$. Expression (8.7.9) can now be re-written as

$$\sigma_{Y_{aged}} > \sigma_{Y_{as\ fatigued}} \qquad (8.7.10)$$

With the rise in temperature, the plastic deformation required for crack-tip stress elevation increased accordingly. When the crack-tip plastic strain, ε_p, exceeded the notched ductility, ε_{fi}, i.e. when

$$\varepsilon_p > \varepsilon_{fi} \qquad (8.7.11)$$

the fracture mode would change from cleavage to micro-void coalescence. Since the plastic strain required for cleavage fracture of the aged specimen was earlier shown to be less than that of the as-fatigued specimen at the similar temperature, it is logical to deduce that the as-fatigued specimen would attain the critical crack-tip strain at a lower temperature than the aged specimen.

Therefore the transition temperature of the as-fatigued steel should be lower than that of the aged steel. Hence, it can be seen that the effect of strain ageing on tensile properties can be combined with the micro-fracture model to predict that

(a) In the high strain ageing propensity steel, the Fracture Mode Transition Temperature (FMTT) of the aged steel is higher than the corresponding transition temperature of the as-fatigued material i.e.

$$(FMTT)_{aged} > (FMTT)_{as\ fatigued}$$

(b) In the low strain ageing propensity steel, the Fracture Mode Transition Temperature is independent of strain ageing.

These predictions were verified by the experimental data given in Figures 8.36 and 8.37. Unfortunately, quantitative analysis is currently unfeasible because of the unavailability of experimental technique for measuring the precise degree of plastic strain at the fatigue crack-tip plastic zone.

The effect of strain ageing on the Charpy V-notched impact toughness of the Grade 275 Steels is shown in Figures 8.45 and 8.46. It can be seen that the shift in transition temperature caused by strain ageing was more prominent than that in the quasi-static fracture toughness test results given earlier in Figures 8.34 and 8.35. The transition temperature shifts of the two test techniques are compared in Table 8.12. The observed different

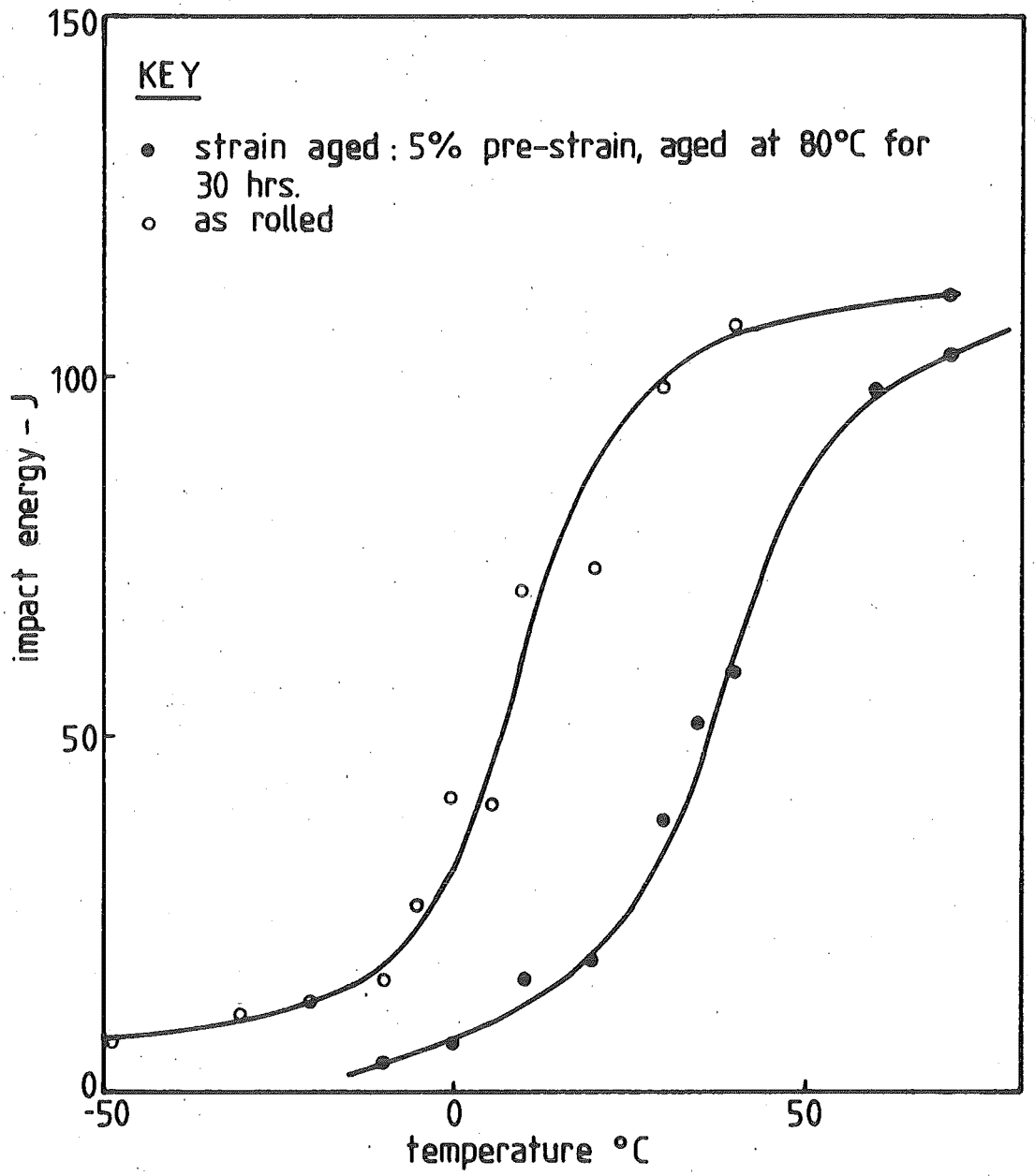

FIG.8·45 THE V-NOTCED CHARPY IMPACT ENERGY CURVE OF NORMAL GRADE 275 STEEL

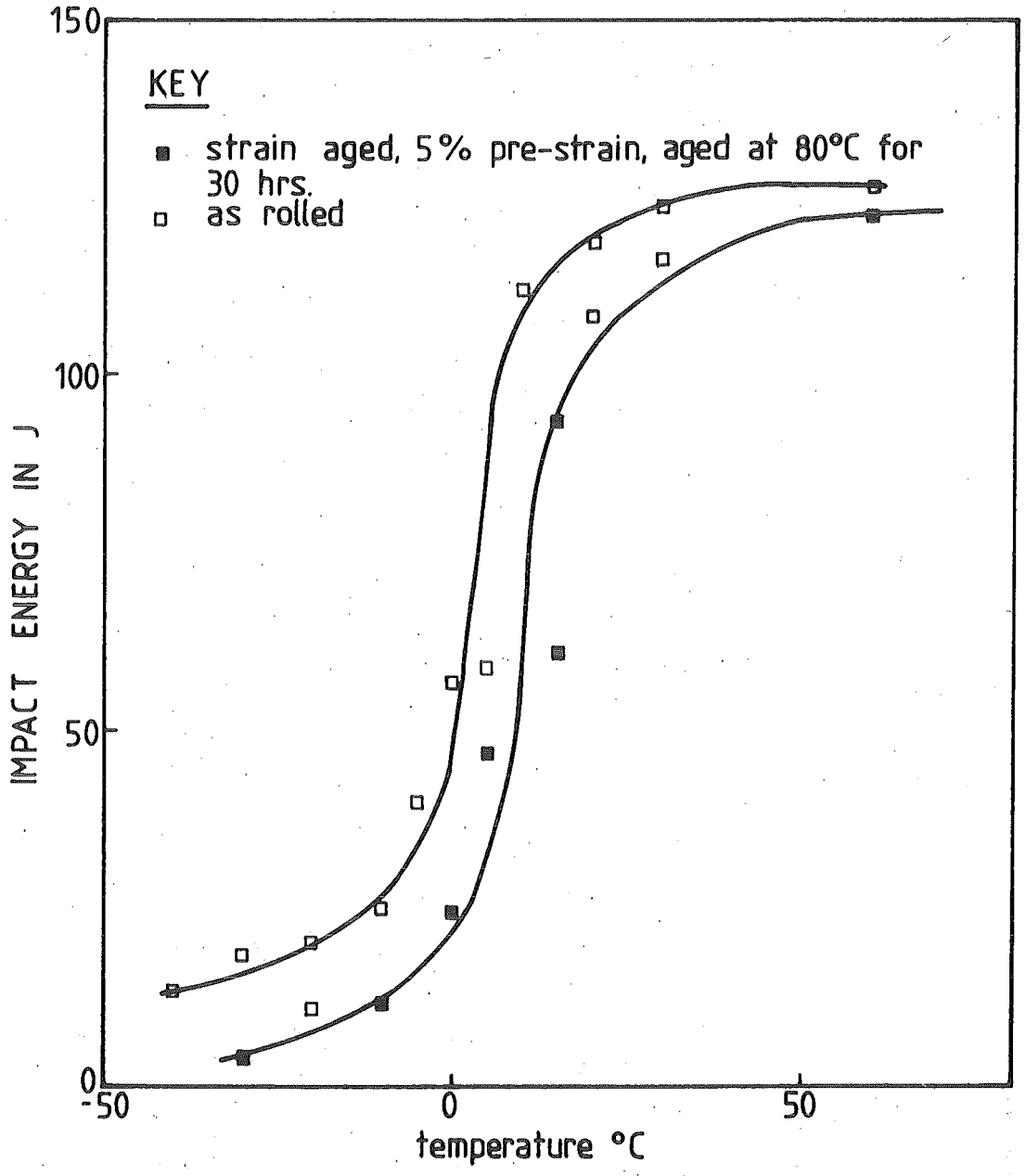

FIG. 8·46 THE V-NOTCHED CHARPY IMPACT ENERGY CURVE OF TI-ADDED GRADE 275 STEEL

Steel Type	Shift In Transition Temperature (^{o}C)	
	Quasi-Static K_{IC}	Charpy Impact (5% pre-strain)
Normal Grade 275	6	30
Ti-Added Grade 275	0	8

Table 8.12 Magnitude Of The Shift In Transition Temperature Of The Quasi-Static And Impact Fracture Toughness Test

magnitude of strain aged induced transition temperature shift was likely to have been caused by

(a) The basic differences in the two test methods discussed earlier in Section 8.5

(b) The difference in the pre-strain severity. In the Charpy V-notched impact test, the steel was tested either in the as-rolled condition or strain aged with 5% pre-strain whereas in the COD test, the steel was either in the as-fatigued or post-fatigue fully aged condition. Consequently, the pre-strain of the Charpy test specimen was markedly more severe than that of the COD test specimen. This difference is significant because the shift in transition temperature was reported to be dependent on the pre-strain severity[139, 141]. Furthermore, it was reported that mere pre-straining would cause a shift in transition temperature from that of the as-rolled material[129].

8.8 Summary

The experimental measurements of Critical Stress Intensity Factor of low carbon steel using the Crack Opening Displacement philosophy were investigated. It was found that the use of 10 mm thick standard compact tension specimen was sufficient to provide size independent, "plane strain" fracture toughness results.

The standard ASTM fracture toughness test method was used to experimentally measure the plane strain Critical Stress Intensity Factor with the aim of comparing the experimental data with the predictions made by the micro-fracture models which were developed to describe the cleavage fracture behaviour of a notched body[15, 16]. It was found that the experimental results showed good agreement with the theoretical prediction; thus implying that the fatigue crack-tip of the fracture toughness specimen merely acted as a stress concentrator and that the test measured the energy needed for the nucleation and subsequent spontaneous propagation of micro-cracks in the fatigue crack-tip region.

Similar comparison of the experimental and theoretically predicted[18, 19, 20] fracture toughness values associated with micro-void coalescence showed that in low carbon steel, the primary voiding particle was the Manganese Sulphide inclusion, and not the grain boundary cementile particles.

Comparison of the quasi-static fracture toughness, K_{IC}, with the Charpy V-notched Impact Energy, C_v, showed that empirical correlation could be obtained. However, the use of these correlations must be treated with caution.

The fatigue pre-cracking process of the fracture toughness specimen was found to have produced two lobes of plastically damaged zone extending to approximately 1 to 2 grain ahead, and approximately 4 grain on either side of the crack-tip. Strain ageing of this area by locking of dislocation by interstitial Nitrogen was

found to have produced a small but significant shift in the Fracture Mode Transition Temperature. However, the two shelf levels of fracture toughness were unaffected by ageing. This behaviour can be qualitatively predicted by introducing the effect of strain ageing on tensile properties into the two micro-fracture models mentioned earlier. Quantitative analysis of this phenomenon is currently unfeasible because of the unavailability of experimental technique for measuring the severity of the fatigue crack-tip plastic zone.

The magnitude of the shifts in transition temperature caused by strain ageing was observed to be different for the Crack Opening Displacement and the Charpy V-notched Impact tests. This disparity was likely to have been caused by a combination of the basic differences of the two test procedure and the different severity of plastic pre-strain of the two types of test specimens.

PART 2

EFFECT OF DYNAMIC STRAIN AGEING ON THE FRACTURE TOUGHNESS OF A LOW CARBON STEEL

CHAPTER NINE

DYNAMIC STRAIN AGEING IN LOW ALLOY STEELS

9.1 General Characteristics

When strain ageing and plastic straining occur simultaneously, the phenomenon is known as "dynamic strain ageing". In the tensile testing of mild steels, dynamic strain ageing manifests itself by:-

(i) serration of the stress strain curve (Figures 9.1.a and 9.1.b)

(ii) decrease in ductility (Figure 9.1.c)

(iii) increase in the rate of work hardening (Figure 9.1.b)

When tested under normal strain rate, this phenomenon occurs at test temperatures ranging from 150^{o}C to 300^{o}C. This temperature range coincides with the "blue heat" zone of the temper colour range. Consequently, dynamic strain ageing in mild steel is often referred to as "blue-brittleness". However, the diminished ductility is not a true brittle behaviour, although the lower elongation at fracture may be detrimental if the steel is worked around these temperatures. Discussions on the engineering aspects of dynamic strain ageing have been summarised elsewhere[166].

Hall[167] had studied the metallography of deformation in iron strained in the blue-brittle temperature range and found that serrated yielding resulted in an extremely regular saw-tooth

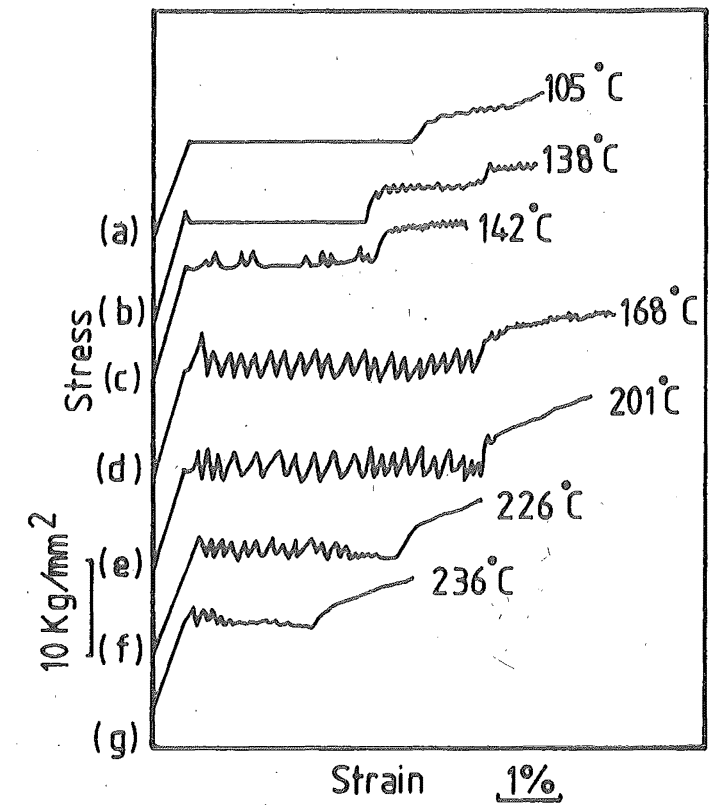

FIG 9·1a SELECTED STRESS-STRAIN CURVES FOR MILD STEEL TESTED IN THE BLUE – BRITTLE RANGE (Ref 174)

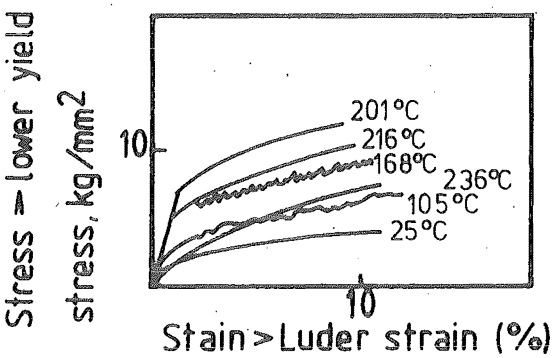

FIG 9·1b SUPERIMPOSED STRESS-STRAIN CURVES BEYOND THE LUDER PLATEAU FOR MILD STEEL TESTED AT VARIOUS TEMPERATURES (Ref 174)

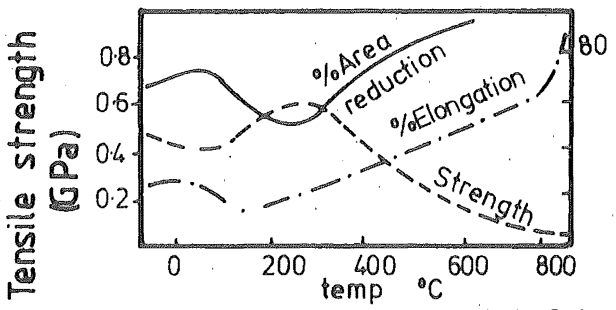

FIG 9·1c EFFECT OF TEMPERATURE ON THE MECHANICAL PROPERTIES OF MILD STEEL (Ref166)

type of stress-strain curve; each rise in stress was associated with primary Luder bands being momentarily locked by strain ageing, and each fall in stress was associated with the Luder band's forward movement. Examinations of surface marks left at each stoppage indicated that the Luders strain was not uniform. The work hardening material behind the Luder band fronts strain aged rapidly, so that beyond the lower yield extension, deformation took place by the movement of secondary Luder bands. These too were stopped by strain ageing and left behind surface marks. Hall suggested that the extent to which serrated yielding and flow effects were observed would depend on the "stiffness" of the testing machines. In "hard" machines, jerky flow would be recorded more clearly than in "soft" machine.

9.2 Factors Affecting Dynamic Strain Ageing

It is well established that dynamic strain ageing can be influenced by several factors. They may be summarised as follows:-

9.2.1 Composition

As in the case of static strain ageing, intersititial carbon and nitrogen atoms had been shown to be responsible for blue-brittleness of mild steels[166, 168, 169, 170].

Baird and Jamieson investigated the effects of carbon, nitrogen and manganese on the tensile properties of strip steel specimens over a range of testing temperatures[168]. All specimens were

annealed in moist hydrogen to facilitate the removal of carbon and nitrogen. Some were tested in this condition while others were recarburised or renitrided before testing. The results (Figures 9.2 and 9.3) showed that the tensile properties of the carbon and nitrogen free-specimens fell on a smooth curve in the temperature range of 20°C and 250°C, whereas pronounced strengthening effects were present in the specimens with free carbon and nitrogen over the temperature range of 100°C and 300°C. Furthermore, serrated yielding was observed in the temperature range of 175°C to 225°C, and jerky flow was present in the temperature range of 125°C to 250°C. These observaitons indicated that the strengthening effect was caused by dynamic strain ageing. The less marked strengthening in the Fe-Mn-C alloy suggested a weak affinity between Mn and C. The results also showed that the most pronounced effect of dynamic strain ageing was the increase in the rate of strain hardening, while the effect on yield strength was less marked. Nitrogen was observed to produce a greater ageing effect than carbon. This can be explained by the higher solubility of nitrogen[129]. The yield stress-temperature curve (Figure 9.2) displayed a single strengthening peak for the steel containing free nitrogen. However, the stress-temperature curve of $\sigma_{0.1}$ (Figure 9.3) displayed three distinct strengthening peaks. Thus, dynamic strain ageing can be expected to be a complex phenomenon with the possibility of several over-lapping strengthening mechanisms.

Glen et al[171] studied the effects of temperature on the yield or proof stress of several normalised commercial steels and found that aluminium-killed steels, where nitrogen had combined with Al,

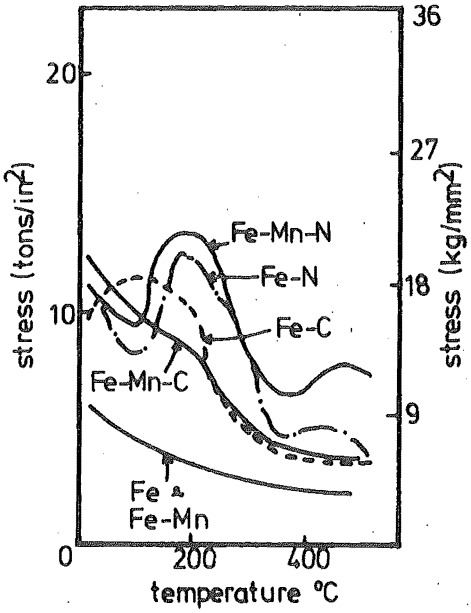

FIG. 9·2 EFFECT OF CARBON, NITROGEN AND MANGANESE ON YIELD OR 0·2% PROOF STRESS OF IRON (REF 168)

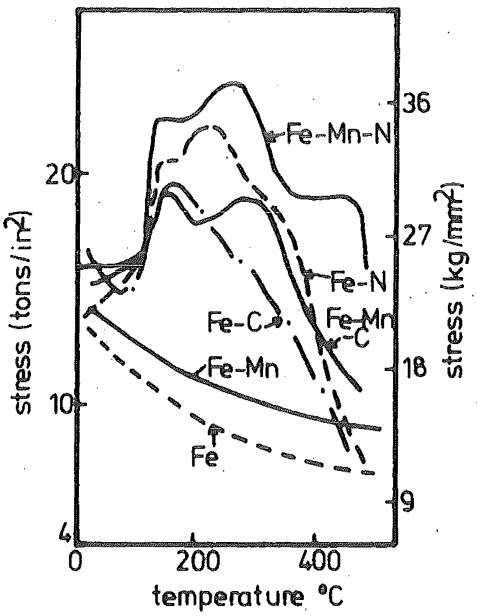

FIG. 9·3 EFFECT OF CARBON, NITROGEN AND MANGANESE ON 10% PROOF STRESS OF IRON (REF 168)

did not exhibit a peak in yield stress in the temperature range of 150°C to 300°C (Figure 9.4). Further evidence supporting the retarding effects of carbide and nitride formers on dynamic strain ageing in commercial steels has been reported by Epstein et al, who showed that serrated yielding could be suppressed by the addition of Vanadium[172].

The presence of substitutional solutes with an affinity for nitrogen and carbon has been shown to be responsible for the extension of strengthening peak to higher temperatures[169, 170] (Figure 9.5). Baird and Jamieson's work showed that peaks in tensile properties were not obtained in Fe-Mn alloys in the absence of carbon and nitrogen[170]. Hence, the broadening of the peaks arises from an interaction between Mn and N interstitials. The detailed mechanisms of substitutional-interstitial interaction are currently imperfectly understood. However, Cottrell suggested that strain-enhanced diffusion of substitutional atoms to dislocations may occur and results in some form of clustering or localised ordering around these dislocations[173]. This localised ordering may be responsible for the observed broadening effects.

9.2.2 Grain Size

Blackmore and Hall investigated the blue-brittle behaviour of mild steels with grain size of 50, 85 and 170 grain/mm^2 and found that grain size did not affect the kinetics of dynamic strain ageing significantly[174]. However, Brindley and Barnby showed that there was a difference in the serration of fine and coarse grained mild

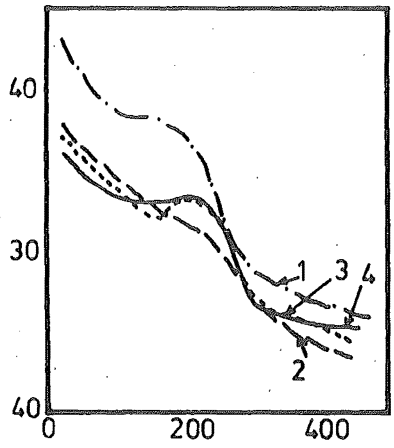

FIG. 9·4 EFFECT OF TEMPERATURE ON YIELD OR 0·2% PROOF STRESS OF FOUR CARBON-MANGANESE STEEL NORMALISED FROM 850°C AND STRESS RELIEVED FOR 3 HRS. AT 600°C (1) SI-KILLED + 0·015% Nb (2) 0·045% SOL·Al (3) SI-KILLED (4) BALANCED (REF 171)

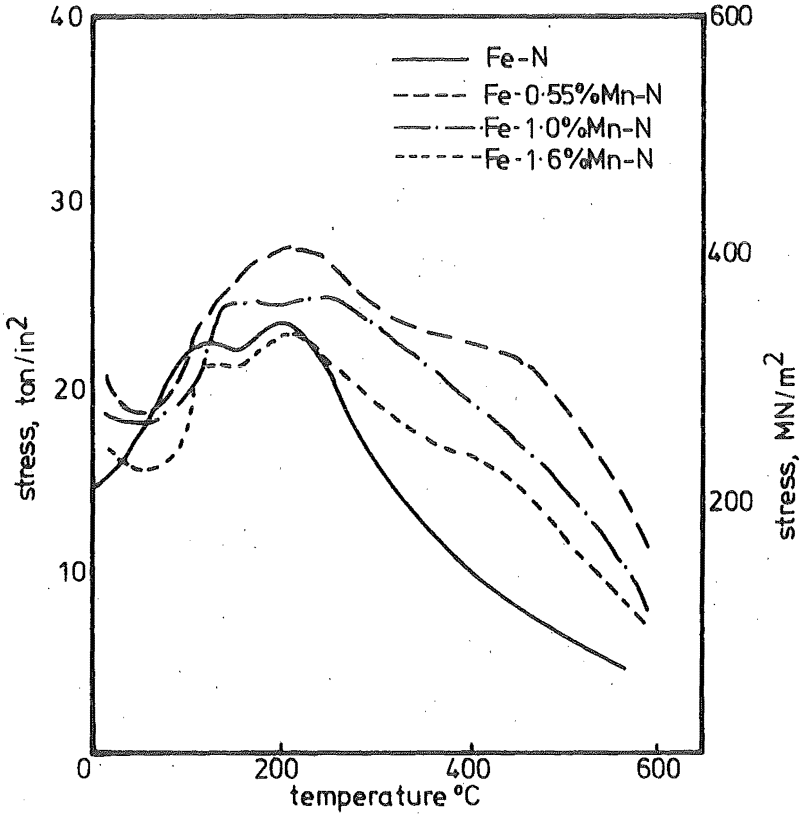

FIG. 9·5 EFFECT OF MANGANESE LEVEL ON TRUE STRESS FOR 10% STRAIN OF IRON CONTAINING 0·01% N (REF 170)

steel specimens with low nitrogen content when tested in tension in the temperature range of 20°C to 400°C[175]. Fine grained specimens showed one type of serration which occurred in the temperature range of 60°C to 200°C and was present at the onset of plastic deformation (Figure 9.6.a). Coarse grained specimens of the same composition showed a second type of serration which only occurred after the specimen had already undergone 8 to 10% of smooth plastic deformation (Figure 9.6.b) in the temperature range of 200°C to 300°C. It was later shown that in such coarse grained specimens, increases in nitrogen content would eliminate the serration and increase the work hardening capacity[176] (Figure 9.6.c)

9.2.3 Strain Rate

It has been well established that varying the strain rate will alter the position of the dynamic strain ageing effects on the temperature scale, but does not change the magnitude of the effects or the pattern of dynamic strain ageing. Manjoine observed that the maximum in yield strength and UTS of a mild steel occurred at about 550°C for a strain rate of 300 s^{-1} compared with 225°C for a strain rate of 8.5×10^{-4} s^{-1} [177].

Based on Manjoine's results, Cottrell deduced that the minimum temperature range at which serration occurs in iron corresponds to that at which the diffusion coefficient of the solute, D, is expressed by [178]:

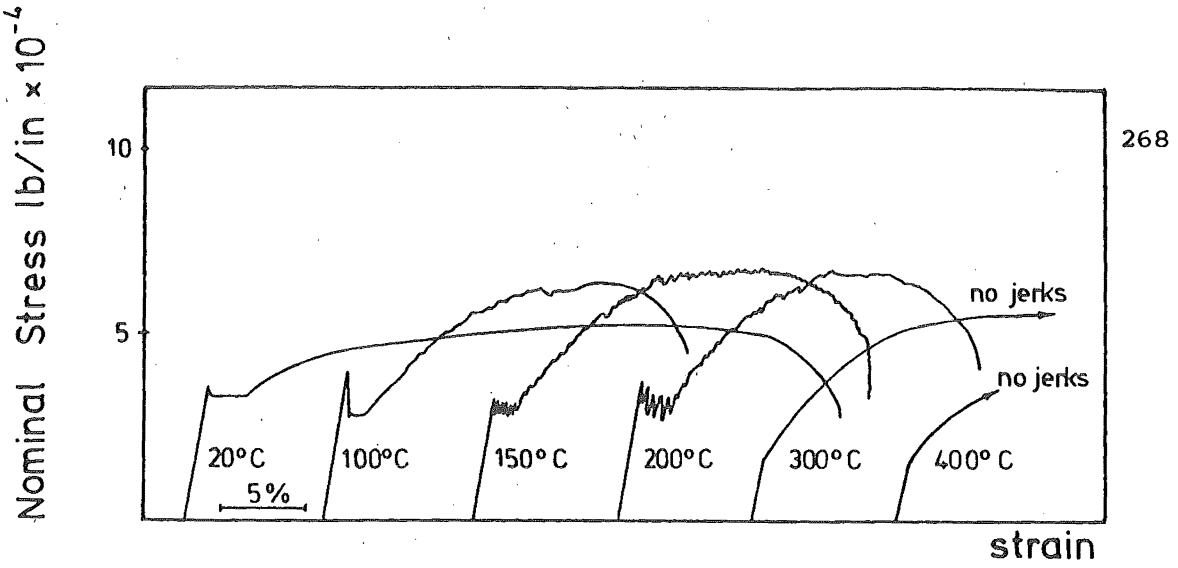

FIG.9·6·A STRESS STRAIN CURVES FOR MILD STEEL, GRAIN SIZE 0·02mm. STRAIN RATE 10^{-4} sec.(REF.175)

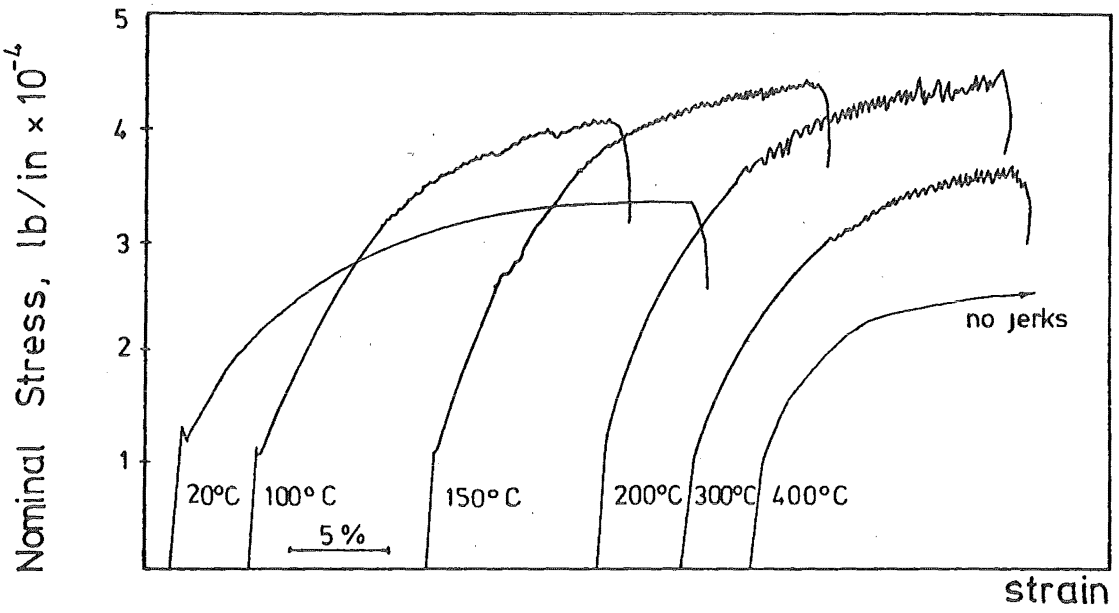

FIG.9·6·B STRESS STRAIN CURVES FOR MILD STEEL, GRAIN SIZE 0·02 mm. (REF.175)

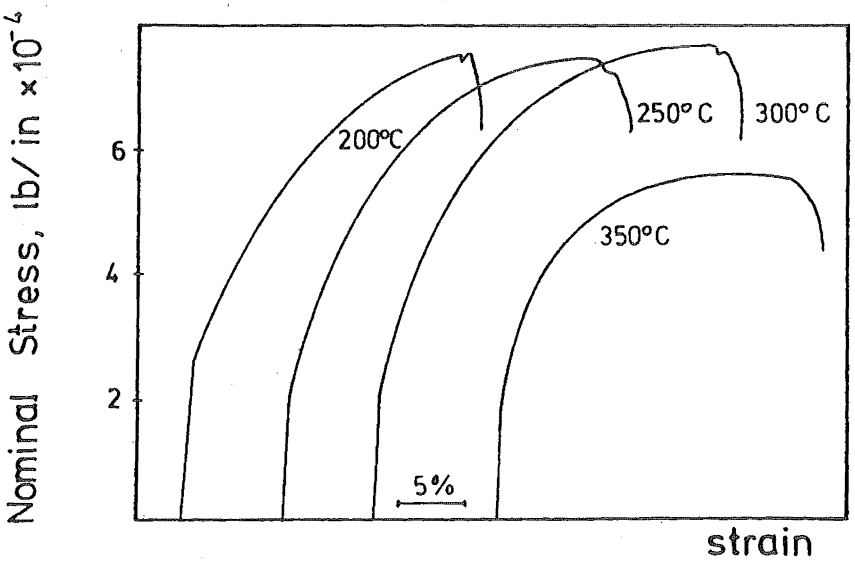

FIG.9·6·C STRESS STRAIN CURVES FOR COARSE GRAINED (0·2mm.) HIGH NITROGEN STEEL.(REF.176)

$$D \simeq \dot{\epsilon} \times 10^{-9} \text{ cm}^2\text{-s}^{-1} \qquad (9.2.1)$$

where $\dot{\epsilon}$ is the applied strain rate

The effects of strain rate may also be described in terms of activation energies obtained from Arrhenius plots. Baird had summarised the results obtained from several other reports and found good agreement amongst them[139]. The activation energy at the low temperature end of dynamic strain ageing where the onset of serration occurs is approximately 20,000 cal/mol , while that for the upper end of the temperature range where serration disappears is 30,000 to 36,000 cal/mol. The value of activation energy for the lower temperature end is approximately equal to that of the diffusion of either carbon or nitrogen in ferrite. Since the lower limit of serration has been found to be very sensitive to interstitial solute level[179], Cottrell's deduction of Equation (9.2.1) needs to be modified to account for the effects of interstitial content.

9.3 Mechanisms Of Dynamic Strain Ageing

The occurrence of multi-strengthening peaks suggests that there is more than one operative strengthening mechanism. Currently, four mechanisms had been proposed to explain the observed strengthening pattern in the blue-brittle temperature range[170]. They are listed in the order of increasing temperature as follows:-

(i) strain induced ordering of solute atoms around

dislocations which have become temporarily blocked by obstacles producing locking,

(ii) strain induced ordering of solute atoms around moving dislocations producing an increased frictional resistance to movement,

(iii) Long range segregation of solute atoms to dislocations temporarily blocked by obstacles producing locking,

(iv) drag exerted on moving dislocations by solute atmospheres diffusing with the dislocations.

Theories predicting the kinetics of the above mechanisms have been proposed. Unfortunately, insufficient accurate knowledge of some of the parameters in these theories leads to the uncertainty of their range of application. Nevertheless, it is possible to infer the operative mechanism from the characteristics of recorded deformation.

The theory of strain induced hardening mechanism by solute ordering had been considered by Wilson, Russel and Eshelby, who observed that the rate of work hardening increased markedly in the temperature range of 20°C to 130°C[180]. This mechanism can thus explain the subsidiary peak in the flow stress at 150°C as observed by Baird and Jamieson[168] (Figure 9.3). It was suggested that this mechanism may be operative up to around 200°C[181].

The long range segregation of solute atoms to blocked dislocations

may become operative at about 130°C with normal tensile strain rate. Examination of Hundy's Equation[133] will reveal that the diffusion rate of interstitials may be sufficiently fast at this temperature. The upper limit of effectiveness can be the temperature at which the dislocations can escape from the segregated solute atoms or the temperature at which the segregated solutes can diffuse with dislocations. This upper limit should approximately correspond to the temperature at which sharp yield point disappears (250°C to 350°C). It is now believed that most dislocations which become locked during deformation in the blue-brittle temperature range are never subsequently unpinned[182].

Carbon and nitrogen atoms continue to segregate to dislocations up to about 500°C. With normal strain rate, these atmospheres may diffuse with the dislocations and cause little drag. However, should the strain rate increase, they may start to lag behind the dislocations, thus exerting a drag. The atmosphere drag effect has been examined by Cottrell and Jawson[183]. Their calculations showed that the solute atmosphere drag mechanism is unlikely to affect the yield stress greatly at normal solute contents, although it may cause sufficient drag to raise the rate of strain hardening appreciably by causing the activation of more dislocation sources during straining. This mechanism could thus partially explain the strengthening due to carbon and nitrogen at temperatures above 300°C[168] (see Figure 9.3)

9.4 Effects Of Dynamic Strain Ageing On Tensile Properties

The effects of temperatures and strain rates on the yield and ultimate tensile stresses were investigated elsewhere[177] and the results are summarised in Figure 9.7. It can be seen that both the yield stress and the strain hardening exponent display increases due to dynamic strain ageing.

The variations of yield stress as expressed in the Hall-Petch relationship[127]

$$\sigma_Y = \sigma_i + k_Y d^{-\frac{1}{2}}$$

in the blue-brittle temperature range has been investigated by Wilson[184]. The results (Figure 9.8) for a rimmed low carbon steel showed that

(i) k_Y decreased from 20°C to 100°C and again from 160°C to 200°C, while remaining constant in the intermediate temperature range.

(ii) σ_i increased slightly from 75°C to 150°C and fell slightly at higher temperature.

In the absence of carbon and nitrogen, σ_i would be expected to fall smoothly above 20°C. Hence, the slight rise at the beginning of the blue-brittle temperature range is probably indicative of an increased frictional drag on the dislocations in this temperature range.

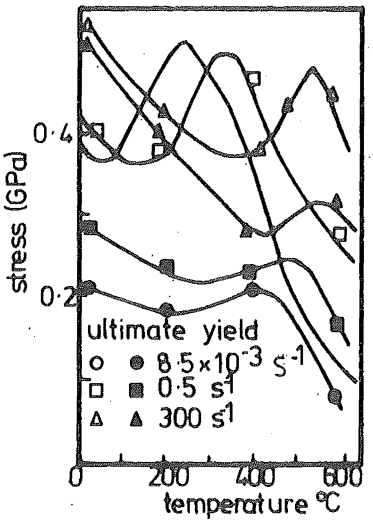

FIG. 9·7 EFFECT OF TEMPERATURE AND STRAIN RATE ON THE YIELD AND TENSILE STRENGTH OF MILD STEEL (REF 177)

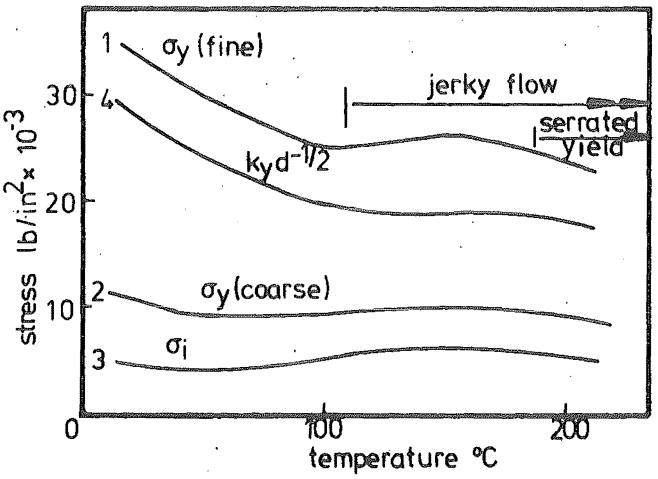

FIG. 9·8 EFFECT OF TEMPERATURE ON TENSILE LOWER YIELD STRESS OF ANNEALED AND FURNACE COOLED LOW CARBON STEEL (REF 184) CURVE 1: σ_y FOR SPECIMENS WITH 8300 GRAINS/MM^2 CURVE 2: σ_y FOR SPECIMENS WITH 16 GRAINS/MM^2 CURVE 3: σ_i CURVE 4: $k_y d^{-1/2}$ FOR FINE GRAINED SPECIMENS

The yield stress-temperature plots of Manjoine[177] and Wilson[184] displayed a similar trend between 20°C and 200°C for normal tensile testing strain rate. Although Manjoine's curve showed a peaking effect at about 500°C, it should be noted that discontinuous yield point had vanished at 400°C.

It is now established that the strain hardening rate and hence the flow stress and the Lower Yield Stress are the properties most affected by dynamic strain ageing (Figure 9.7). Dynamic strain ageing causes a large increase in the strain hardening index n in the relationship[185]

$$\sigma = K_s \varepsilon^n \qquad (9.4.1)$$

where σ is the true stress

ε is the true strain

K_s is the strengthening coefficient

It has also been shown that there is a much greater increase in dislocation density for a given strain in the blue-brittle temperature range than at room temperature[175, 185], and this effect is clearly responsible for much of the enhanced strain hardening rate. This higher dislocation density may be explained by the continual generation and multiplication of fresh mobile dislocations when the existing dislocations become immobilised by precipitate pinning. In addition, the rate of elimination of dislocations by mutual annihilation decreases[185].

The effects of strain rate on yield and flow stresses had

been investigated by Majoine[177] (Figure 9.7). It was found that increasing the strain rate markedly increased the temperature at which the maximum in yield and tensile stresses occurred. More recently, it has been shown that there exists an inverse strain rate dependency of the flow stress, but not the lower yield stress at 100°C[179] (Figure 9.9). The serrations of the flow curve have been proposed as a symptom of negative strain rate sensitivity of flow stress[179], which is a condition sufficient for dynamic plastic instability of the deformed zones.

The ductility as expressed by the fracture elongation has been shown to be dependent on the level of free nitrogen. On straining in the blue-brittle temperature range, localised depletion of nitrogen occurs, resulting in the formation of bands of high deformation which manifests itself in the form of serrations of the flow curve[170] (Figure 9.6.b). If the materials in these bands fail to work-harden sufficiently to compensate for the reduction in area, fracture will occur within these bands with low elongation. Increase in nitrogen level will raise the strain at which this occurs, and thus increases the fracture elongation [170] (Figure 9.10).

9.5 Effects Of Dynamic Strain Ageing On Fracture Toughness

The effects of plastic deformation induced in the dynamic strain ageing temperature range on the ductility, subsequently measured at ambient temperature, have been investigated recently.

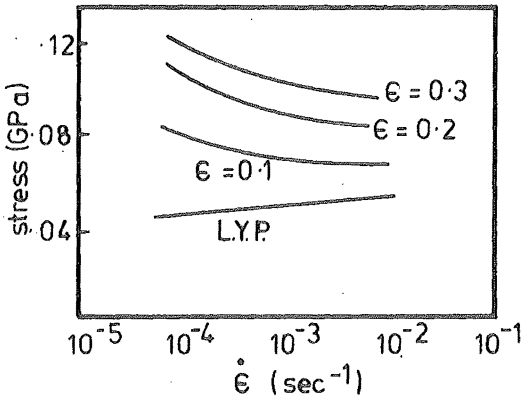

FIG. 9·9 STRAIN RATE DEPENDENCE OF YIELD AND FLOW STRESS (REF 179)

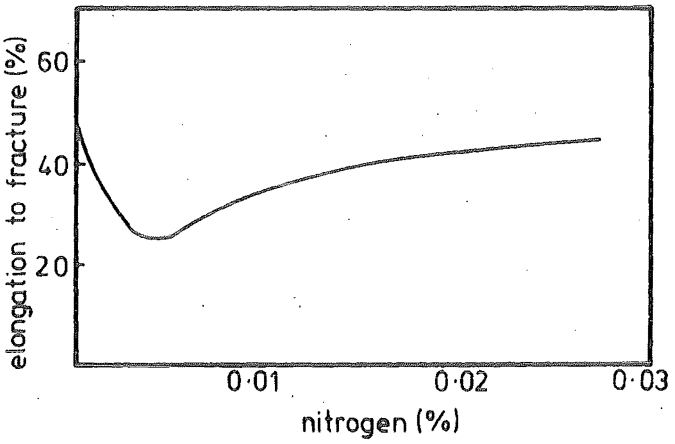

FIG. 9·10 EFFECT OF NITROGEN LEVEL ON ELONGATION TO FRACTURE OF IRON STRAINED AT 225 °C (REF 170)

These investigations have practical relevance because warm pre-stressing is normally employed to improve notched toughness.

Burdekin et al pre-strained mild steel specimens between 150°C and 250°C and then tested them at ambient temperature[186]. The effects of these treatments on the crack opening displacements obtained by slow bend tests are summarised in Figure 9.11. It can be seen that pre-bending at 250°C increased the transition temperature by about 80°C, when compared with pre-bending to a similar degree at ambient temperature and subsequently ageing at 250°C.

The ambient temperature embrittlement by dynamic strain ageing was further supported by an investigation involving a low alloy C-Mn steel[187]. By simulating the service strain cycle in pre-cracked bend specimens at 277°C, brittle fracture was induced at room temperature. The equivalent temperature for brittle fracture of the steel in "as-received' condition was approximately -100°C.

The results of the above investigations are consistent with the observations of high strain hardening rate during dynamic strain ageing which raises the flow stress towards the fracture stress σ_F, thus resulting in brittle fracture occurring more readily at higher temperatures.

The two investigations discussed previously have been involved with embrittlement effects ascertained at ambient temperature. De Morten extended the field on dynamic strain ageing embrittlement by measuring the fracture toughness and the tensile properties

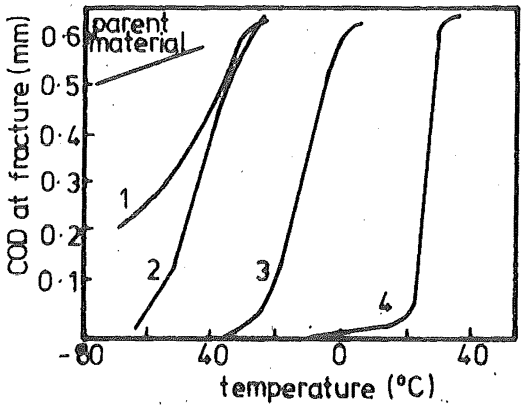

FIG. 9·11 EFFECT OF PRE-STRAIN ON CRITICAL COD FOR 10mm SQUARE NOTCHED SPECIMENS OF NORMALISED MILD STEEL. (1) PRE-BENT AT R.T. AGED 250°C (2) PRE-BENT AT 150°C (3) PRE-BENT AT 350°C (4) PRE-BENT AT 250°C (REF. 186)

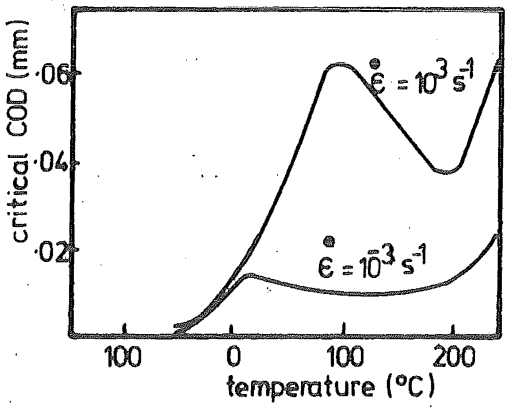

FIG. 9·12 CRACK OPENING DISPLACEMENT AS A FUNCTION OF TEMPERATURE AND STRAIN RATE (REF. 165)

of a mild steel at temperatures ranging from cryogenic to beyond blue-brittleness[165]. The steel was water quenched from 850°C and then tempered at 300°C for one hour so as to simulate weld heat affected zone conditions. The results (Figure 9.12) showed that the normal transition temperature curve could be produced using COD as the toughness parameter. More importantly, they also showed a decrease in toughness at dynamic strain ageing temperatures.

9.6 Summary

Dynamic strain ageing in mild steels is commonly termed blue-brittleness. The phenomenon manifests itself during tensile testing by:-

(i) serrations of the stress-strain curve,

(ii) increase in the rate of work hardening,

(iii) decrease in ductility.

Dynamic strain ageing has been observed to be dependent on several factors. These include:

(i) composition of the steels,

(ii) strain rate,

(iii) grain size.

Currently, it is believed that several overlapping mechanisms are responsible for the strengthening characteristics of dynamic strain ageing. They are:

(i) strain induced ordering of solute atoms around mobile dislocations which are temporarily blocked by obstacles producing
   (a) locking,
   (b) increased frictional resistance to movement.

(ii) long range segregation of solute atoms to dislocations producing
   (a) solute atmospheres which diffuse with the moving dislocations, thus exerting a drag,
   (b) permanent locking by precipitate formation thus causing the generation of new dislocations.

The strengthening effects of dynamic strain ageing may be extended to higher temperatures by the presence of substitutional atoms which have an affinity for carbon and/or nitrogen interstitials.

Dynamic strain ageing raises the yield and flow stresses. The rise in yield stress is mainly caused by an increase in σ_i, indicating an increased frictional drag on the dislocations, although k_Y has been shown to be temperature insensitive between $100^{\circ}C$ and $160^{\circ}C$. The marked rise in flow stress has been shown to have resulted from the large increase in the strain hardening index n. It is now believed that the high value of n is a direct consequence of high dislocation density caused by the rapid generation and multiplication of new dislocations, when permanent locking of existing mobile dislocations by precipitates occurs.

The detrimental aspect of dynamic strain ageing is its embrittling effect. It is well established that tensile fracture elongation decreases significantly in blue-brittle temperature range. More recently, toughness parameters in the form of transition temperatures and crack opening displacements have confirmed this embrittlement effect in several mild steels.

CHAPTER TEN

THE EFFECTS OF DYNAMIC STRAIN AGEING ON THE FRACTURE TOUGHNESS OF A LOW CARBON STEEL

10.1 Introduction

Although the effects of dynamic strain ageing (DSA) on the tensile properties of low carbon steels have been well established, there are relatively few research efforts directed at investigating its influences on the quasi-static K_{IC}. The more recent report has been that of De Morten who measured the critical COD of a mild steel which has been embrittled by quenching and tempering treatment over temperature ranging from cryogenic to blue-brittle[165]. De Morten used double fatigue bend COD specimens and found that the critical COD decreased substantially over the DSA temperature range. It is the aim of this investigation to ascertain the effects of DSA on the COD-related K_{IC} of a low carbon steel in its as-rolled condition.

The Pressure Vessel Steel was selected for this experimental investigation because of the following reasons:-

(a) The maximum load COD has been shown to provide a reasonably accurate measure of the COD at the instance of crack-tip instability (see Section 8.2).

(b) The measurement of the critical COD of the Pressure Vessel steel has been shown to be free of the problems

associated with the presence of large Mns inclusion cluster (see Section 8.2).

The chemical composition and Nitrogen analysis of the Pressure Vessel steel have been summarised earlier in Tables 7.1 and 7.2.

10.2 COD Tests

10.2.1 Experimental Procedure

Standard 10 mm thick compact tension specimens were prepared from the Pressure Vessel Steel (see Figure 7.1). The specimens were subsequently tested over the temperature range of 25°C to 350°C. A Wild-Barfield (1150°C maximum temperature) electric furnace was used to heat the test specimens up to temperature. The temperatures were monitored by a Cr-CrAl thermocouple placed at the crack-tip area through the fatigue crack starter notch. Each specimen was soaked at the desired temperature for 15 minutes for homogeneity. The tests were conducted on the Instron Universal Testing machine at the cross-head displacement rate of 1 mm-sec^{-1}. It was found that the use of the extensometer and its extension arms was impractical without complicated modification to existing equipment. As an alternative, the extensometer displacement, V_g, was prior calibrated against the cross-head displacement V_{ch} and by referring to the V_g-COD calibration of Figure 8.2, the COD-V_{ch} calibration was obtained. The results of this calibration are given in Figure 10.1. The critical COD values were then evaluated

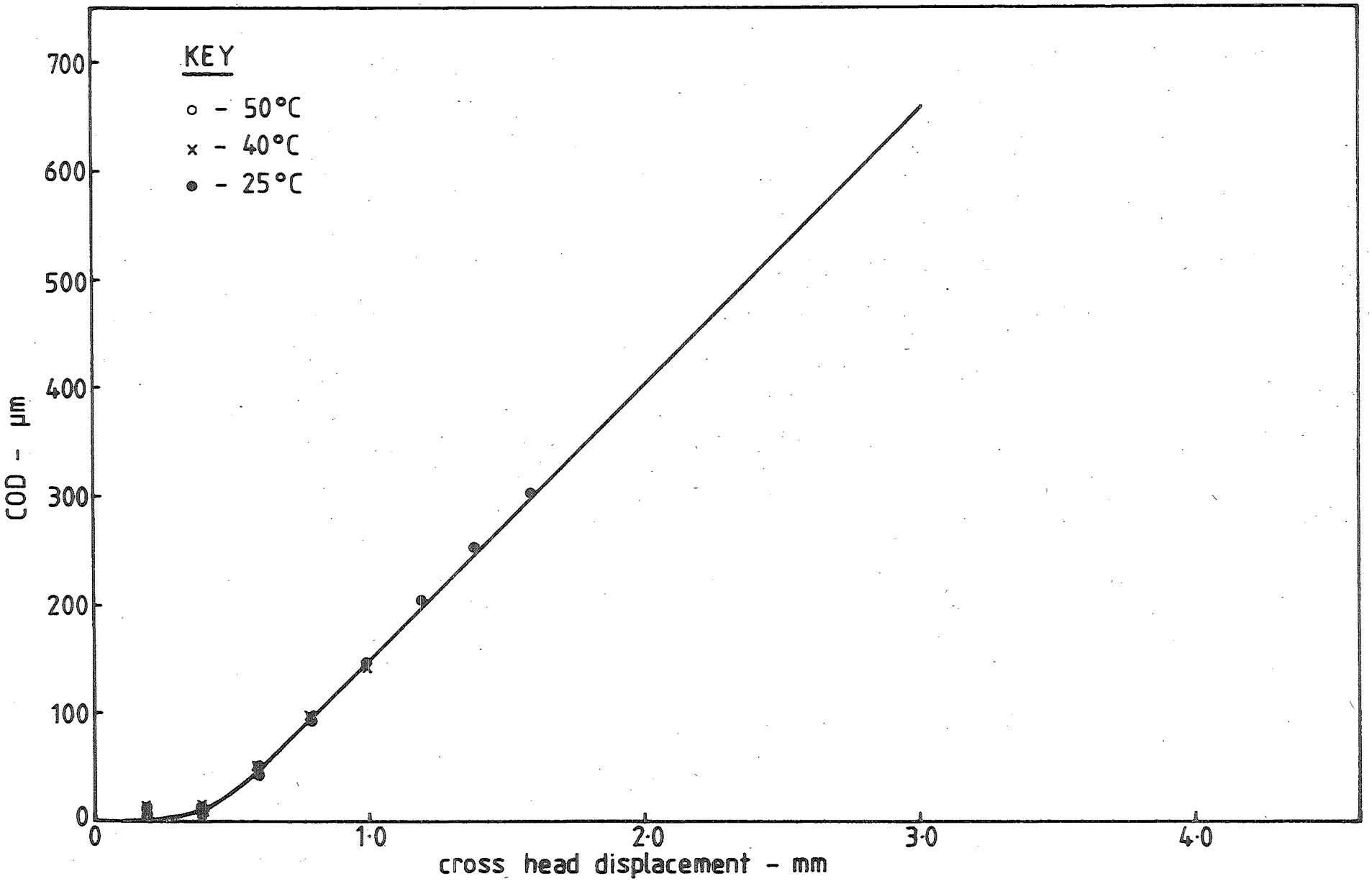

FIG. 10·1 COD–CROSSHEAD DISPLACEMENT CALIBRATION

from the COD value corresponding to the cross-head displacement at maximum load. The effects of static strain ageing were kept to a minimum by keeping the specimens refrigerated in a household freezer after fatigue cracking, and then testing them within the subsequent week. The results in Figure 8.14 were added to the experimental results of this investigation for comparison of the fracture toughness at the blue brittle temperature with that at cleavage. The fracture surfaces of the broken specimens were examined under the scanning electron microscope to determine the mode of separation.

10.2.2 COD Test Results

The COD-V_{ch} calibration has been supplied in Figure 10.1. It can be seen that the cross-head displacement can be used to evaluate the critical COD value.

The applied force-displacement test records generally followed that of Figure 7.5.b where final instability is by ductile separation. However, the record of tests conducted at temperature above 150^{o}C showed "steps" after the attainment of maximum load (see Figure 10.2).

The results of the COD tests are shown in Figure 10.3. It can be seen that the critical COD in the DSA temperature is substantially lower than the ambient temperature critical COD associated with microvoid coalescence.

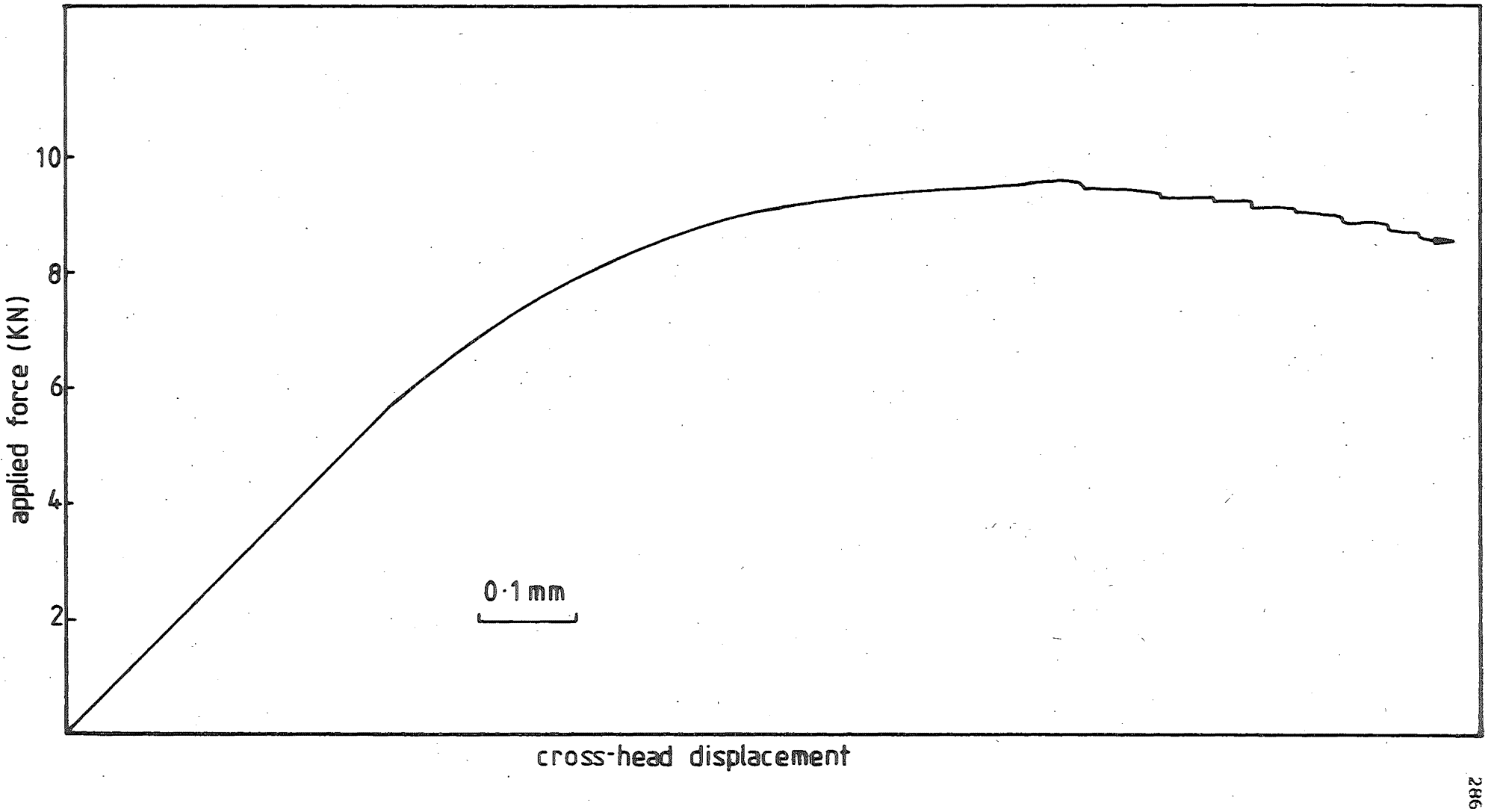

FIG. 10·2 TYPICAL "BLUE BRITTLE" TEMPERATURE COD TEST RECORD (TEMPERATURE = 250°C)

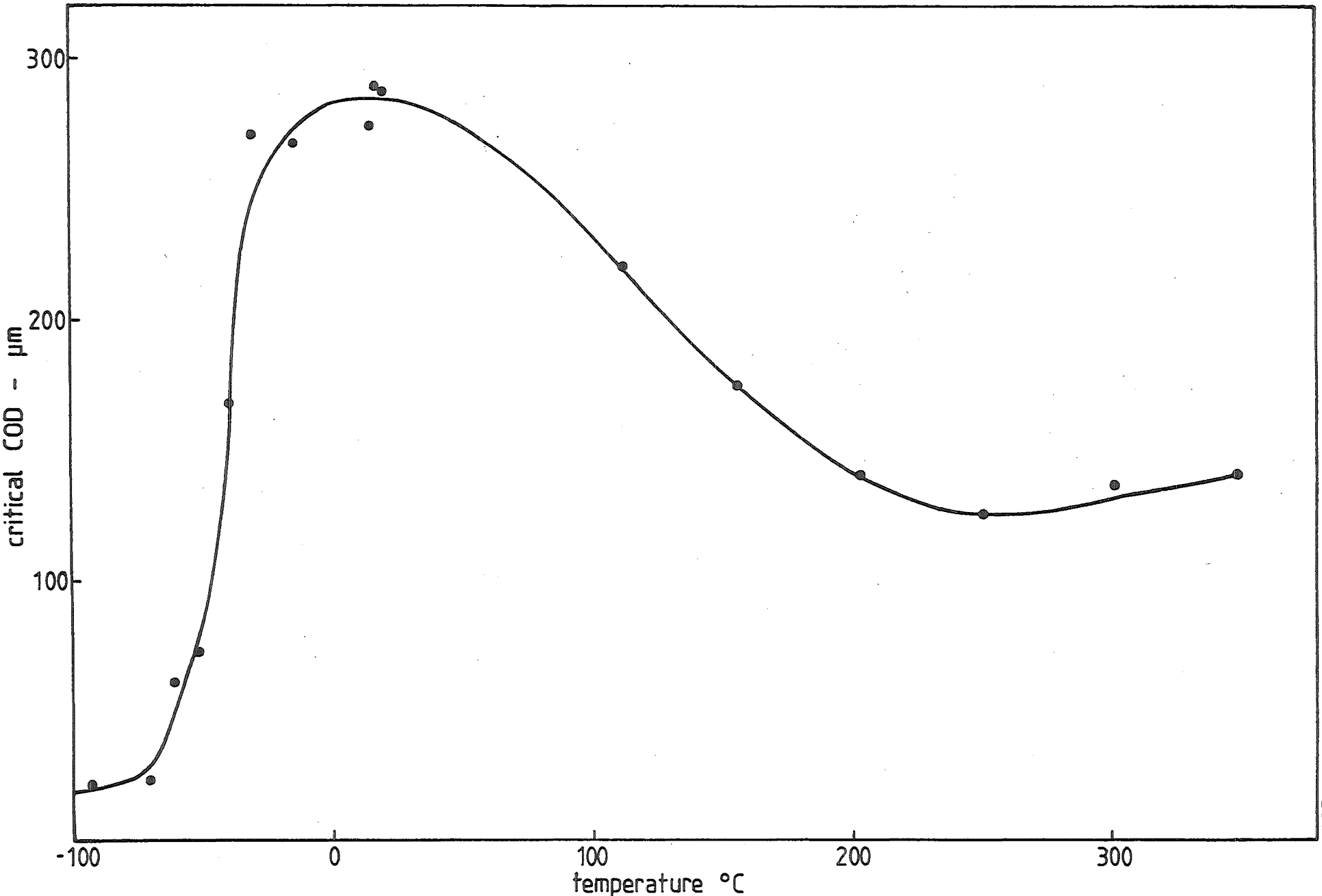

FIG. 10·3 VARIATION OF CRITICAL COD WITH TEMPERATURE OF THE PRESSURE VESSEL STEEL

The notched ductility at 250°C was obtained by using the maximum load COD of specimens with different notch width. The calibration curve of Figure 10.1 can be used to estimate the critical COD of the notched specimens as the COD-V_g calibration has been shown to be relatively unaffected by the difference in slot width (see Figure 8.3). These experimental data were supplemented by the relevant ambient temperature data from Figure 8.24. The combined results are shown in Figure 10.4. It can be seen that the notched ductility has decreased substantially at the DSA temperature of 250°C.

10.2.3 The Fracture Surfaces

The fracture surfaces of selected samples of broken test specimens were examined under the Jeol JSM 35 Scanning Electron Microscope. Typical micrographs of specimens tested at 18°C and 250°C are supplied in Plate 10.1. It can be seen that the separation mode in the DSA temperature is microvoid coalescence although the voids appeared to be shallower than those of the ambient temperature specimen.

10.3 Tensile Tests

Tensile tests were conducted to obtain values of σ_Y for the calculation of K_{IC}. The dimensional and machining specifications of the tensile specimens have been supplied in Section 7.3.1. The tests were conducted on the Instron Universal Testing machine.

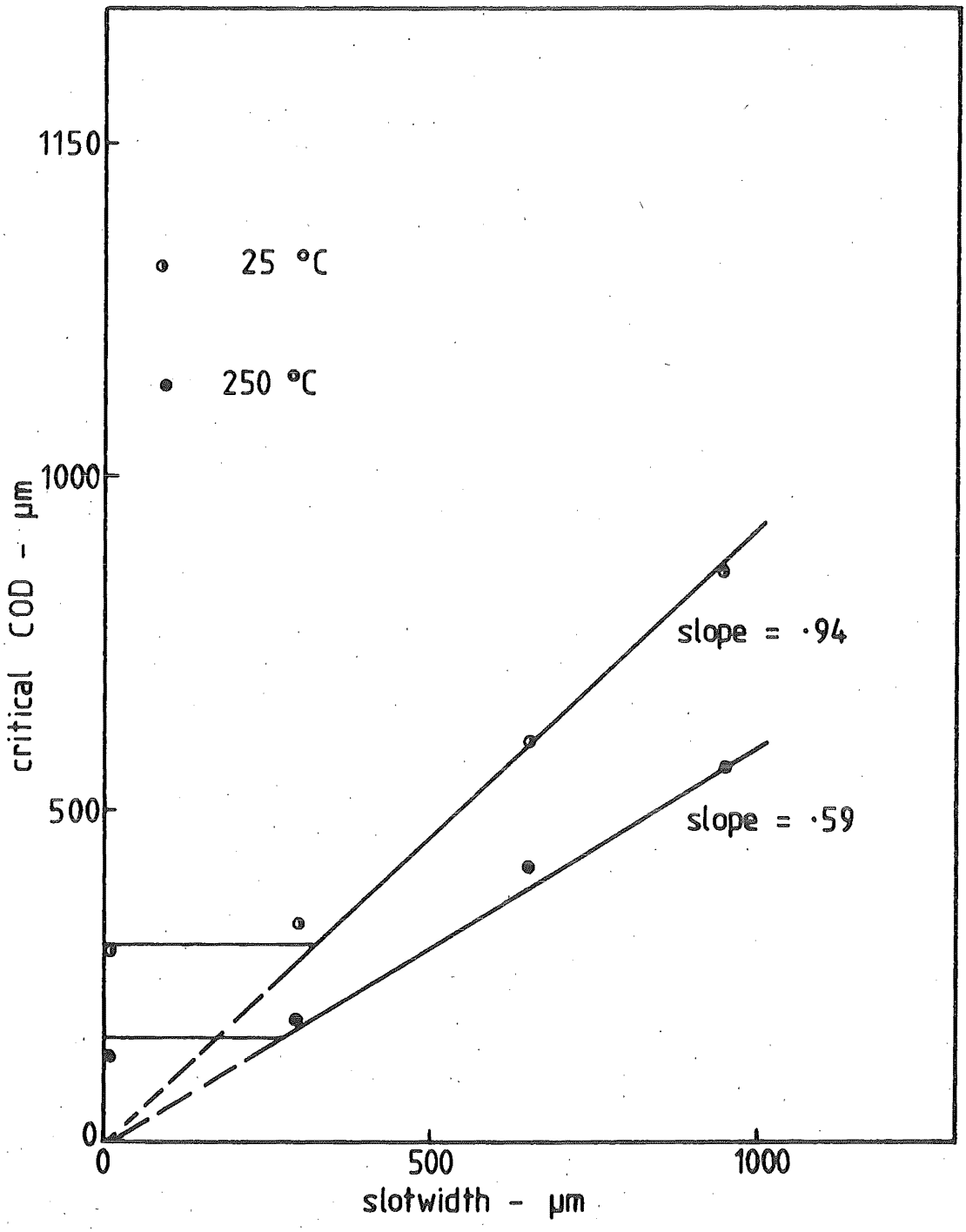

FIG. 10·4 EFFECTS OF DSA ON NOTCHED DUCTILITY OF THE PRESSURE VESSEL STEEL

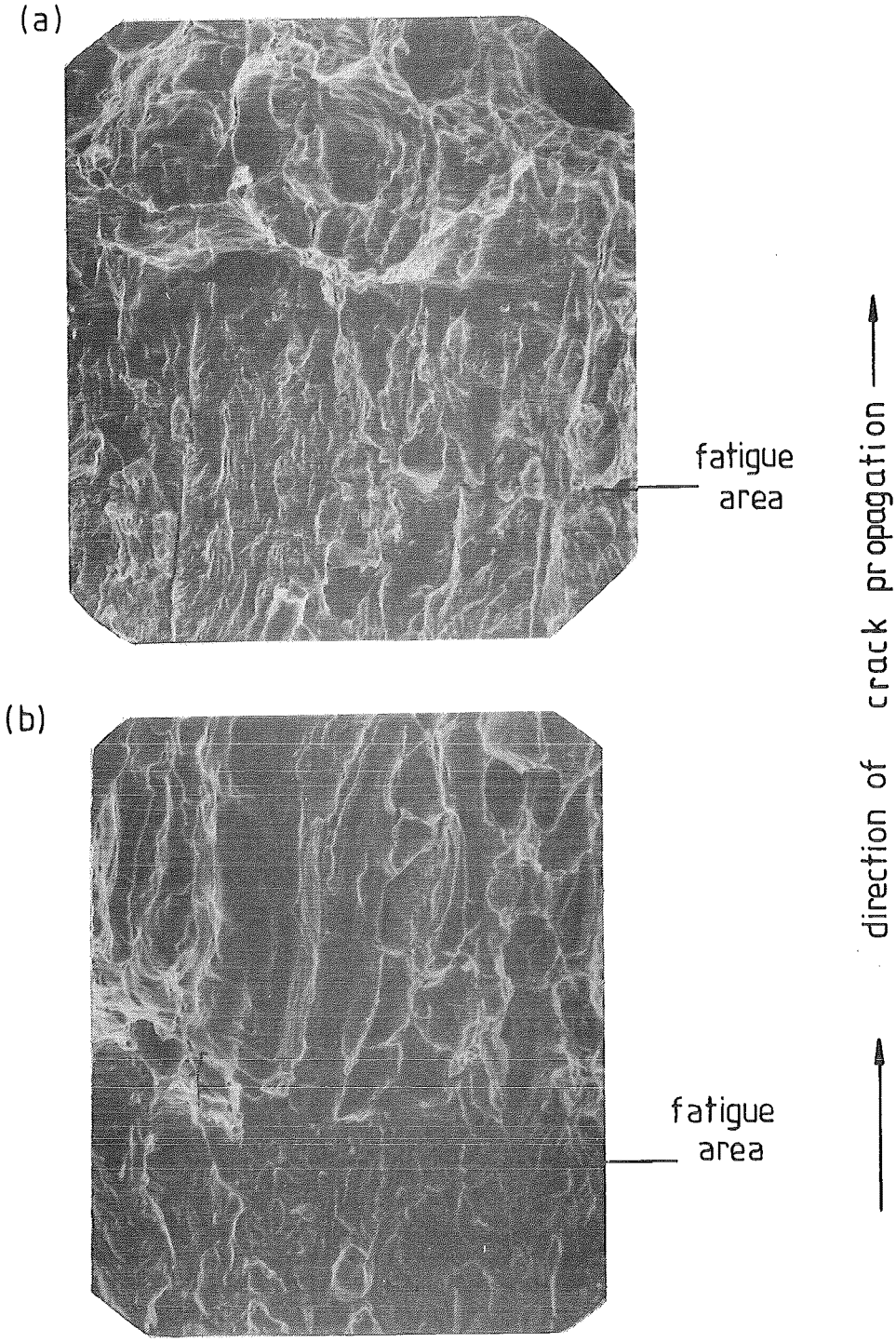

PLATE 10·1 SCANNING ELECTRON MICROGRAPHS OF THE FRACTURE SURFACE OF SPECIMENS BROKEN AT (a) 18° C (b) 250° C (x 390)

The specimens were heated by the Wild-Barfield electrical furnace and the specimen temperatures were monitored by a Cr-CrAl thermocouple. The test record consisted of the applied force-cross-head displacement graphs, and the yield stress values were calculated using the value of applied force at the "plateau" of these records. It should be noted that the yield plateau had disappeared at 350°C. In this case, the value of σ_Y was calculated by estimating the 0.2% proof load. Serrations of the flow curves were observed in specimens tested between 100°C and 250°C. The tensile test results were supplemented by the tensile test results summarised in Figure 8.18. The combined data are supplied in Figure 10.5. Typical tensile test records are also shown in Figure 10.6 for the purpose of estimating the stress-strain relationship of the steel at ambient and DSA temperatures. The stress-strain relationship may be estimated by taking small values of strains and their corresponding stress values from the tensile records so that the engineering stress and strain values may be used as close approximation of the true stress and strain values. By substituting these values into the true stress-true strain relationship

$$\sigma = K_s \varepsilon^n \qquad (10.3.1)$$

the values of K_s and n can then be calculated.

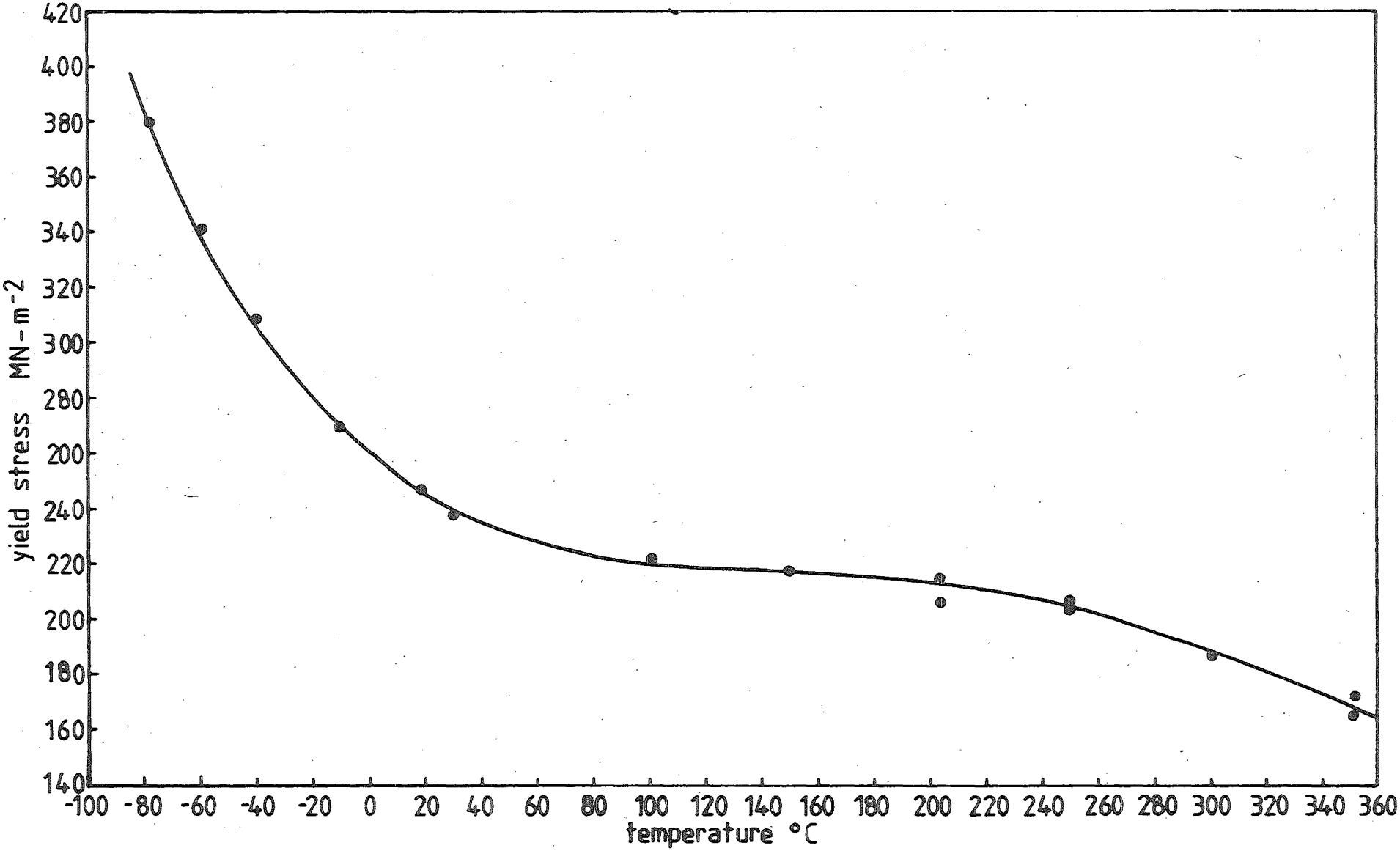

FIG. 10·5 VARIATION OF YIELD STRESS WITH TEMPERATURE

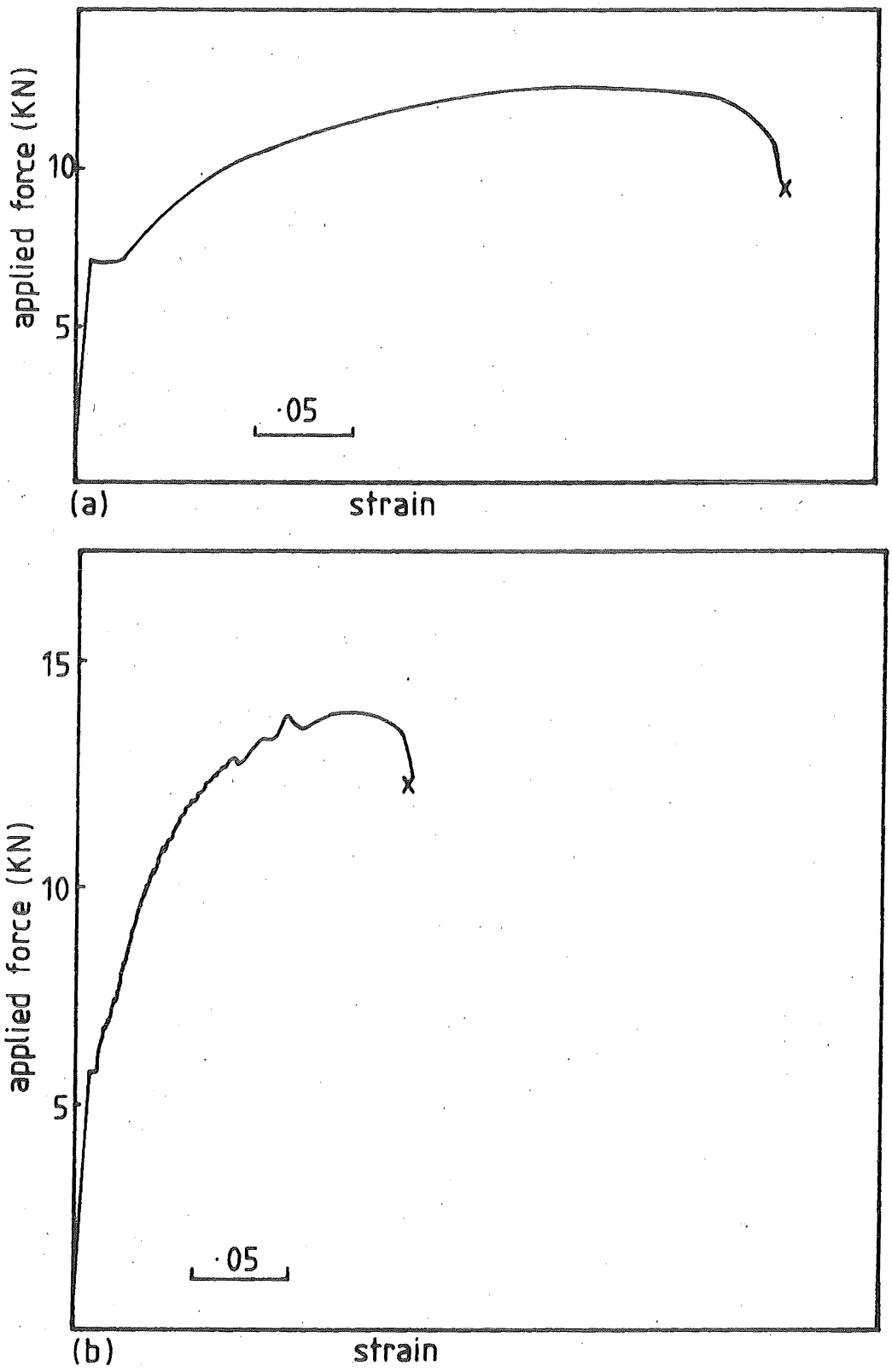

FIG. 10·6 TENSILE TEST RECORDS OF SPECIMENS TESTED AT (a) 25°C, (b) 250°C

Thus,

(a) At $25^{o}C$ (see Figure 10.6.a)

$\varepsilon = 0.025$ $\qquad\qquad$ $\sigma = 297\ MN\text{-}M^{-2}$

$\varepsilon = 0.05$ $\qquad\qquad$ $\sigma = 350\ MN\text{-}M^{-2}$

so that $n = 0.240$

$K_s = 720\ MN\text{-}M^{-2}$

(b) At $250^{o}C$ (see Figure 10.6.b)

$\varepsilon = 0.025$ $\qquad\qquad$ $\sigma = 316\ MN\text{-}M^{-2}$

$\varepsilon = 0.05$ $\qquad\qquad$ $\sigma = 380\ MN\text{-}M^{-2}$

so that $n = 0.265$

$K_s = 840\ MN\text{-}M^{-2}$

Hence, at $25^{o}C$, $\sigma = 720\ \varepsilon^{.240}$ (10.3.2)

at $250^{o}C$, $\sigma = 840\ \varepsilon^{.265}$ (10.3.3)

The accuracy of this approximation method can be verified by comparing the ambient temperature K_s and n values with those obtained by the more accurate true-stress and true-strain test (see Appendix F).

10.4 COD-Related K_{IC} Results

The geometrical criterion for size-independent critical COD and hence K_{IC} values has been supplied in Equation (7.5.3) as

$$a, B, W - a \geq 25\ \delta_c$$

Hence, it can be seen that the standard 10 mm thick CT specimens used in this experimental investigation should satisfy the above criterion. The K_{IC} values were calculated using Equation (7.4.4) where

$$K_{crit} = 0.4769 (\sigma_{LY}\delta_c)^{\frac{1}{2}}$$

and the results are given in Figure 10.7. It can be seen that DSA has reduced the fracture toughness significantly. However, the DSA temperature K_{IC} level is still substantially higher than the cleavage K_{IC} value of 19.2 MN-M$^{-\frac{3}{2}}$ (see Table 8.3)

10.5 Discussions

The extensometer was not used to measure the COD of specimens tested at DSA temperatures because of practical difficulties. Instead, the use of the cross-head displacement V_{ch} as a substitute has been investigated. It was found that satisfactory experimental COD-V_{ch} calibration could be obtained (see Figure 10.1) provided the various specimen dimensions fell within the specified tolerances. The calibration curve in Figure 10.1 was also used in the DSA temperature notched ductility tests. The justification of this method has been supplied in Appendix B.

The DSA temperature COD tests revealed that after the initial crack extension, subsequent crack growth appeared to occur in "bursts". This phenomenon manifested itself in the form of "steps"

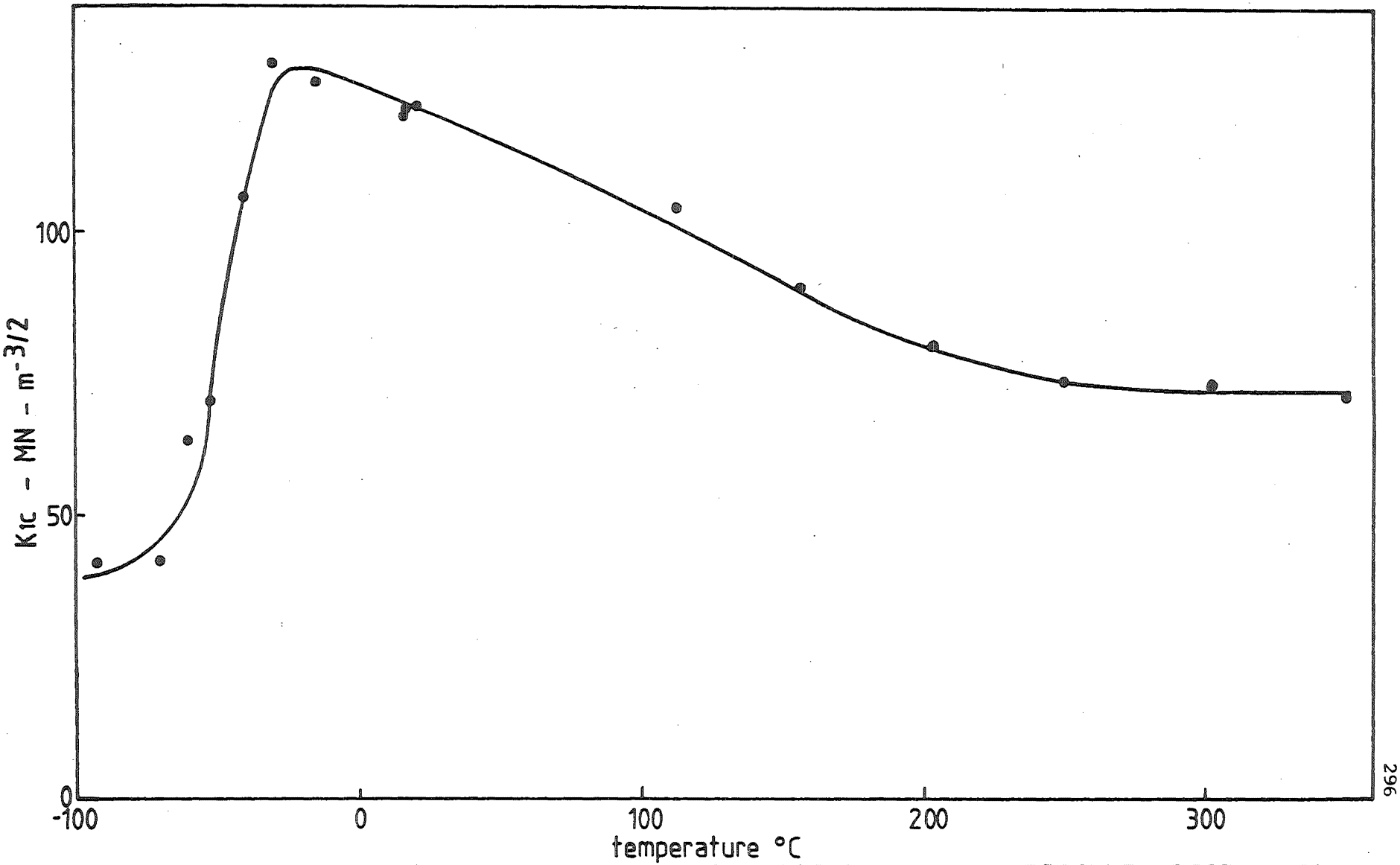

FIG.10·7 VARIATION OF K_{1c} WITH TEMPERATURE OF THE PRESSURE VESSEL STEEL

in the COD test records (see Figure 10.2) at the temperature range approximately similar to that of tensile serration. However, the SEM examination of the fracture surface did not reveal any evidence of cleavage facet (see Plate 10.1.b). Instead, microvoid coalescence with "shallow" dimples was found to be the separation mode, and results from Figures 10.3 and 10.4 showed that the non-metallic inclusion model provides a reasonable estimate of the critical COD at DSA temperatures. The mechanism which causes this "steps" phenomenon is likely to be that which causes the serration of tensile records[170], that is, the localised depletion of Nitrogen and Carbon interstitials at the crack-tip region, caused by the continual dislocation locking associated with DSA. This depletion of interstitials would result in localised areas of high deformation[170]. When the strain in this area exceeded the notched ductility, separation by microvoid coalescence would occur, and the magnitude of the consequential crack extension would be limited by the size of the localised deformation area. This process repeated itself at the new crack front, thus resulting in the observed "steps" in the test records.

The temperature ranges in which the COD "steps" and tensile "serration" phenomena occurred have been summarised in Table 10.1. It can be seen that they are overlapping, with the tensile serration temperature range slightly lower. This difference is likely to be the consequence of different rates of strain at the relevant gauge length areas of the two types of test specimens. The strain rate of the COD test may be estimated by assuming a rotational

Test Method	Unusual Phenomenon	Occurrence Temperature Range	Cross-head Displacement Rate	Gauge Length
COD	"Steps"	150-350^{o}C *	1 mm-s^{-1}	381 μm
Tensile	"Serration"	100-250^{o}C *	0.5 mm-s^{-1}	30 mm

* Highest Test Temperature

Table 10.1 Data Relevant To DSA Temperature COD And Tensile Tests

constant of 0.4[63] and a 'gauge length', represented by the average non-metallic inclusion spacing of 381 μm. The rate of strain of the COD test was calculated at 12.4×10^{-3} s^{-1}. This is much higher than the tensile test strain rate of 0.28×10^{-3} s^{-1} (see Table 10.1). This difference in strain rate is likely to be sufficiently significant in causing the reported strain rate induced shift in DSA along the temperature scale[177].

The marked loss of fracture toughness in the form of a substantial decrease in the critical COD at DSA temperatures (see Figure 10.3) is similar to that reported by De Morten[165]. The cause of this loss in fracture toughness is not well understood, although it has been suggested that the observed increase in the hardening index during DSA[185] can lead not only to an increase in flow stress level, but also to a rapid rise in triaxiality of the stress system at the crack-tip[89]. Based on these reports, De Morten postulated that the new crack-tip stress state will affect the microvoid coalescence mechanism[165].

The present experimental data support these observations in that

(a) The strain hardening rate as defined by

$$\left(\frac{d\sigma}{d\varepsilon}\right)_{\varepsilon = \varepsilon_1} = n\frac{\sigma_1}{\varepsilon_1} \qquad (10.5.1)$$

showed an appreciable increase from 2851 $MN\text{-}m^{-2}$ at 25°C to 3350 $MN\text{-}m^{-2}$ at 250°C when $\varepsilon_1 = 0.025$. However

the rise in the strain hardening index n by 0.025 is much smaller than those reported earlier[185] (see Section 10.3)

(b) The voids formed at 250°C were shallower than those at ambient temperature (see Plate 10.1)

(c) The notched ductility at 250°C was lower than that at ambient temperature (see Figure 10.4).

The effects of DSA on K_{IC} are shown in Figure 10.6. It can be seen that the K_{IC} values decreased substantially at DSA temperature. This decrease is expected to be caused by the embrittlement effect of strain ageing as it has been shown earlier that introduction of a small crack-tip pre-strain by the fatigue pre-cracking process is unlikely to cause a significant error in the calculation of K_{IC} (see Section 8.7).

10.6 Summary

The fracture toughness of a low carbon steel has been shown to decrease substantially even though the basic fracture mechanism remains unaltered as microvoid coalescence. Experimental evidence appears to support the postulation that the decrease in fracture toughness is a consequence of the microvoid coalescence process being affected by the increase in the strain hardening rate associated with Dynamic Strain Ageing.

CHAPTER ELEVEN

CONCLUSIONS

As the standard K_{IC} test method has been originally designed to evaluate the size independent K_{crit} values of high strength quasi-brittle materials, it is not surprising that except at cryogenic temperatures, the test method is inapplicable to low carbon steels.

The COD test method has been a popular alternative in assessing the fracture toughness of low strength materials. However, owing to the lack of a rigorous, standardised procedure, considerable ambiguity still exists in the definition of the critical fracture event when final instability is by:-

(a) Cleavage accompanied by sub-critical crack-extension

(b) Ductile tearing.

In such cases, the BS-DD 19 recommends that the critical event being defined as either

(a) The instance of crack extension so that $\delta_{crit} = \delta_i$

or (b) The instance of instability,

so that $\delta_{crit} = \delta_c$ for cleavage separation

and $\delta_{crit} = \delta_m$ for cases where separation occurs after the attainment of maximum load.

It was found that substantial difference can exist between the two

recommended critical COD values when the initial crack extension was by micro-void coalescence. From the Material Science's points of view, the initiation COD, δ_i , obviously has more significance because it coincides with the physical separation of the crack-tip material. However, this type of crack extension does not lead to structural instability. Therefore, it may be argued that the maximum load COD, δ_m , is a more practical parameter as it corresponds to the instance of instability of the uncracked ligament area. It is obvious that the selection of the appropriate critical COD value will depend entirely on the ultimate aims of the model test. If the model test represents the service application reasonably accurately, then the use of δ_m is justified. However, it is felt that the more conservative initiation COD should be used whenever the relation between model and service application is less well defined.

Testings of specimens with crack planes orientated in the ST direction were hampered by the morphology of the non-metallic inclusions, which is predominently MnS "stringers". In these specimens, the presence of cluster of these inclusion "stringers" at the crack-tip area can invalidate the COD tests by either

(a) Causing the fatigue crack to propagate out-of-plane

(b) Resulting in over-optimistic critical COD values when the "opening" occurred at the inclusion cluster.

This problem plagued the COD testings of the Billet Steel continually and has led to a high rejection rate. Hence, the COD tests of such a material will require a higher degree of precaution to

prevent unduly optimistic conclusions.

Nevertheless, it has been shown that size independent fracture toughness value in the forms of critical COD or K_{IC} can be obtained by the COD test method using the compact tension specimen geometry. From the experimental data, it may be concluded that:-

(a) The transition of fracture mode is accompanied by a rapid change in fracture toughness

(b) Satisfactory predictions of the fracture toughness levels associated with the two distinct modes of separation, namely, cleavage and microvoid coalescence, can be made by the currently popular micro-fracture models

(c) The good agreement between the experimental and theoretically predicted fracture toughness for both cleavage and microvoid coalescence inferred that

  (i) In cleavage fracture, the fatigue crack-tip of the fracture toughness specimen behaved as a stress concentration and that micro-cracks need to be nucleated in the material ahead of the crack-tip before spontaneous crack propagation can occur

  (ii) In microvoid coalescence, the primary voiding particles of low carbon steel were confirmed to be the MnS inclusions.

These observations were also reported by other research programmes using the three-point and four-point bend specimen geometry.

It has also been shown that empirical correlation exists between the quasi-static COD-related K_{IC} and the Charpy Impact Energy values. As the Charpy Impact test is a more economical test method, the empirical correlations may be useful if their statistical reliability can be verified. The obvious advantage will be the cost reduction and the simplicity of the Charpy Impact test, especially for repetitive quality control type of testings for normal production runs. However, since the Charpy Impact test is only applicable as a fail-safe test, it is felt that the quasi-static K_{IC} should always be considered first for establishing parameters for structural design purposes because it can provide information at both cleavage and microvoid coalescence.

The current popular models of fatigue crack propagation assume that plastic damage occurs at the crack-tip. This area has been shown to be present as two "lobes" on either side of the crack-tip; each "lobe" extending over a distance of several grain diameters. Although the size of this plastic zone is small, its location at the crack-tip is critical when favourable ageing conditions prevail. The embrittlement effects of the strain ageing of this plastic zone have been confirmed by the observed increase in the transition temperature of the Grade 275 Steels aged by the locking of dislocations by Nitrogen interstitials. This transition temperature shift can be qualitatively predicted by the micro-fracture models after accounting for the increase in flow stress level associated with strain ageing. Hence, it is felt that the recommended standard COD test procedures should include the

embrittlement effects caused by the strain ageing of the inherent fatigue crack-tip plastic zone in the fracture toughness testings of high strain ageing propensity materials.

The fracture toughness at "blue-brittleness" temperatures decreases substantially although the basic separation mode remains unchanged as micro-void coalescence. Although the cause of this phenomenon is not well understood, experimental observations support the postulation that the increase in hardening rate associated with Dynamic Strain Ageing which alters the void formation mechanism is responsbile for the decrease in fracture toughness.

REFERENCES

1. PLACE, T.A., 1977, "Fracture Mechanics In Engineering Design", Paper presented at the autumn meeting of the Australasian Institute of Metals, Christchurch, New Zealand.

2. GRIFFITH, A.A., 1920, Phil. Trans. Royal Society, A221, p.163

3. ASTM E399-1974

4. BS5447: 1977

5. EGAN, G.R., 1973, Eng. Frac. Mechanics, 5, p.167.

6. WELLS, A.A., 1969, Eng. Frac. Mechanics, 1, p.399.

7. TRACEY, P.G., 1973, Ph.D. Thesis, Brum University, referred to by Sumpter J.D.G. and Turner C.E. in J. Mech. Eng. Science, 1976, 18, p.97

8. RICE J.R., 1968, J. App. Mechanics, 35, p.379.

9. BEGLEY, J.A., Landes J.D., 1972, ASTM STP 514, p.1.

10. SUMPTER, J.D.G., 1976, Metal Science, p.354.

11. ROBINSON, J.M., Tetelman A.S., 1973, "Determination of K_{IC} Values From Measurement of COD At Fracture Initiation", presented at the Third International Conference On Fracture, Munich.

12. WITT, F.J., MAGER J.R., 1971, Nuc. Eng. Design, 17, p.91.

13. CHELL, G.G., MILNE, I., 1976, Mat. Sci. and Engineering, 24, p.249

14. CHELL, G.G., 1977, Metals Technology, p.136.

15. RITCHIE, R.O., RICE, J.R., KNOTT, J.F., 1973, J. Mech. Phy. Solids, 21, p.395.

16. CURRY, D.A., KNOTT, J.F., 1976, Metal Science, p.1.

17. RAWAL, S.P., GURLAND, J., 1977, Metal Trans. A, p.691.

18. SMITH, R.F., KNOTT, J.F., 1971, Conf. on "Practical Application of Fracture Mechanics To Pressure Vessel Technology", Inst. Mech. Eng., p.65.

19. BROWN, L.M., EMBURY, J.D., 1973, Proc. Int. Conf. "Strengthening of Metals And Alloys", Cambridge, p.164

20. SAILOR, R.H., 1976, ASTM STP 605, p.34.

21. FERGUSON, W.G., THORBY, P.N., 1976, Material Science and Engineering, 22, p.177.

22. HAHN, G.T., HOAGLAND, R.G., ROSENFIELD, A.R., 1976, Metals Trans., 7A, p.49.

23. BSI DD19 - 1972

24. LAIRD, C., 1967, ASTM STP 415, p.119.

25. HERTZBERG, R.W., 1967, *ibid*, p.205.

26. FORSYTH, P.J.E., RYDER, D.A., 1961, Metallurgia, 63, p.117.

27. AWATANI, J., KATAGIRI, K., SHIRAISHI, T., 1976, Metal Trans., 7A, p.807.

28. BURDEKIN, F.M., 1967, British Weld. Journal, p.649.

29. LANDES, J.D., BEGLEY, J.A., 1974, ASTM STP 560, p.170.

30. PARIS, P.G., Written discussion to Ref. 9.

31. MARANDET, B., SANZ, G., 1977, ASTM STP 631, p.72.

32. BARSOM, J.M., 1975, Eng. Frac. Mechanics, 7, p.605.

33. CHIRIGOS, J.N., MEYER, T.A., 1978, J. Test. And Evaluation, 6, p.289.

34. GILMAN, J.J., 1963, "Mechanical Behaviour of Crystalline Solids", National Bureau of Standards Monograph, 59, p.79.

35. COTTRELL, A.H., 1953, "Dislocation And Plastic Flow", Oxford Press.

36. COTTRELL, A.H., 1963, Tewksbury Symposium on Fracture, University of Melbourne, p.1.

37. IRWIN, G.R., 1957, J. Appl. Mechanics, 24, p.36.

38. WESTERGAARD, H.M., 1939, *ibid.*, A, p.49.

39. "Fracture Toughness", 1968, ISI Publication 121, p.17.

40. CARTWRIGHT, D.J., ROOKE, D.P., 1971, "Stress Intensity Factor: A Compedium", HMSO, London.

41. IRWIN, G.R., KIES, J.A., SMITH, H.L., 1958, Proc. ASTM, 58, p.640

42. OROWAN, E., 1945, Trans. Inst. Eng. Shipbuilders, Scotland, 89, p.165.

43. IRWIN, G.R., 1957, Nineth Int. Cong. App. Mechanics, VIII, Paper 10, University of Brussels.

44. IRWIN, G.R., 1964, App. Mat. Research, 3, p.65.

45. IRWIN, G.R., WELLS, A.A., 1965, Met. Review, 10, p.38.

46. DUGDALE, D.S., 1960, J. Mech. Phy. Solids, 8, p.100.

47. KRAFFT, J.M., SULLIVAN, A.M., BOYLE, R.W., 1961, Proc. Symp. Crack Propagation, Cranfield, p.8.

48. BROWN, Jnr. W.F., SRAWLEY, J.E., 1965, ASTM STP 381, p.133.

49. TETELMAN, A.S., McEVILY, A.J., 1967, "Frac. Of Structural Materials", Wiley, New York.

50. COTTRELL, A.H., 1963, Proc. Roy. Society, A276, p.1.

51. KNOTT, J.F., 1971, Mat. Sci. Engineering, 7, p.1.

52. BILBY, B.A., COTTRELL, A.H., SWINDEN, K.H., 1963, Proc. Roy. Society, A272, p.304.

53 ASTM Standards, 1977, E561, 10.

54. PELLINI, W.S., SRAWLEY, J.E., 1961, "Procedures For Evaluation of Fracture Toughness of Pressure Vessel Materials", Report 56009, U.S. Naval Lab.

55. BROWN, Jnr. W.F., SRAWLEY, J.E., 1966, ASTM STP 410, p.1.

56. SRAWLEY, J.E., JONES, M.H., BROWN, Jnr. W.F., 1967, "Determination of Plane Strain Fracture Toughness", Materials Research and Standards, June.

57. NEILSON, F.G., SCHILLING, P.E., KAUFMAN, J.G., 1972, Eng. Frac. Mechanics, 4, p.33.

58. WESSEL, E.T., 1969, "Practical Fracture Mechanics For Structural Steels", Paper H. UKAEA, Chapman and Hall.

59 CLARKE, Jnr. W.G., WESSEL, E.T., 1966, ASTM STP 410, p.161.

60. RADON, J.C., TURNER, C.E., 1966, JISI, 204, p.842.

61. WELLS, A.A., 1961, "Proc. Symposium Crack Propagation", Cranfield, p.210.

62. COTTRELL, A.H., 1961, ISI Special Report, 69, p.281.

63. KNOTT, J.F., 1973, "Fundamentals of Fracture Mechanics", Butterworths, London, p.158

64. BURDEKIN, F.M., STONE, D.E.W., 1966, J. Strain Analysis, 1, p.145.

65. BARENBLATT, G.I., 1962, Advances In App. Mechanics, 7, p.55.

66. VITVITSKII, P.M., LEONOV, M.Ya., reported by Heald et al, 1972, Mat. Sci. Engineering, 10, p.129.

67. GOODIER, J.N., FIELD, F.A., 1963, "Fracture of Solids", ed. Drucker and Gilman, Academic Press, New York, p.103.

68. HAHN, G.T., ROSENFIELD, A.R., 1965, Acta Metallurgica, 13, p.293.

69. KNOTT, J.F., 1973, "Fundamentals of Fracture Mechanics", Butterworths, London, p.72.

70. TURNER, C.E., 1975, J. Strain Analysis, 10, p.207.

71. ROBINSON, J.N., TETELMAN, A.S., 1974, ASTM STP 559, p.139.

72. ROBINSON, J.N., 1976, Int. J. Fracture, 12, p.723.

73. HAIGH, J.R., RICHARDS, C.E., reported by Chell et al, 1975, Metals Technology, 2, p.549.

74. SUMPTER, J.D.G., TURNER, C.E., 1976, J. Mech. Eng. Science, 18, p.97.

75. HEALD, P.T., SPINK, G.M., WORTHINGTON, P.J., 1972, Mat. Sci. Engineering, 10, p.129.

76. KNOTT, J.F., 1966, JISI, 204, p.1014.

77. ELLIOT, D., WALKER, E.F., MAY, M.J., 1971, Conf. on "Practical Application of Fracture Mechanics To Pressure Vessel Technology", Inst. Mech. Eng., p.217.

78. INGHAM, T., EGAN, G.R., ELLIOT, D., HARRISON, T.C., *ibid.*, p.200.

79. WELLS, A.A., 1971, Canadian Congress On App. Mechanics, Calgary, Canada, p.59.

80. FIELDS, B.A., MILLER, K.J., 1977, Eng. Frac. Mechanics, 19, p.133.

81. RITTER, J.C., REA, T.W., J. Australian Inst. of Metals, 1977, 22, p.115.

82. KUNA, M., 1976, Int. J. Fracture, 12, p.175.

83. HARRISON, T.C., FEARNEHOUGHT, G.D., 1969, Int. J. Fracture Mechanics, 5, p.348

84. LEIREM, J., EMBURY, J.D., 1979, Eng. Frac. Mechanics, 11, p.161.

85. ESHELBY, J.D., 1956, Solid State Physics, 3, p.79.

86. CHERPANOV, G.P., 1967, J. App. Mechanics, 31, p.503.

87. McLINTOK, E., 1971, "Fracture - An Advance Treatise", ed. Liebowitz H., 2, Academic Press, New York, Chapter 2.

88. HUTCHINSON, J.W., 1968, J. Mech. Phy. Solids, 16, p.13.

89. RICE, J.R., ROSENGRAN, G.F., 1968, *ibid.*, 16, p.13.

90. BUCCI, R.J., PARIS, P.C., LANDES, J.D., RICE, J.R., 1972, ASTM STP 514, p.40.

91. ADAMS, N.J.I., MUNRO, H.G., 1974, Eng. Frac. Mechanics, 6, p.119.

92. RICE, J.R., PARIS, P.L., MERKLE, J.G., 1973, ASTM STP 536, p.231.

93. SUMPTER, J.D.G., TURNER, C.E., 1976, ASTM STP 601, p.3.

94. CLARKE, G.A., 1976, ASTM STP 590, p.27.

95. VITEK, V., CHELL, G.G., 1977, Mat. Sci. Engineering, p.209

96. BEGLEY, J.A., LANDES, J.R., 1973, ASTM STP 536, p.246.

97. WITT, F.J., 1971, Conf. on "Practical Application of Fracture Mechanics To Pressure Vessel Technology", Inst. of Mech. Eng., p.163.

98. CHELL, G.G., SPINK, G.M., 1977, Eng. Frac. Mechanics, 9, p.101.

99. CHELL, G.G., WORTHINGTON, P.J., 1976, Mat, Sci. Engineering, 26, p.95.

100. CHELL, G.G., 1976, *ibid.*, 24, p.233.

101 WITT, F.J., 1971, "The Equivalent Energy Method For Calculating Elastic-Plastic Fracture", U.S. Atomic Energy Commission Report ORNL-TM-3172, Oak Ridge Lab.

102. CHELL, G.G., 1974, Mat. Sci. Engineering, 17, p.227.

103. EWING, D.J.F., RICHARDS, C.E., 1974, J. Mech. Phy. Solids, 22, p.27.

104. OATES, G., 1968, JISI, 206, p.930.

105. WILSHAW, T.R., RAW, C.A., TETELMAN, A.S., 1968, Eng. Frac. Mechanics, 1, p.191.

106. LOW, J.R., 1954, Symp. On "Relation of Properties To Microstructure", ASM, p.163.

107. COTTRELL, A.H., 1958, Trans. AIME, 212, p.192.

108. McMAHON, C.J., COHEN, M., 1965, Acta Metallurgica, 13, p.591.

109. SMITH, E., 1968, Int. J. Frac. Mechanics, 4, p.131.

110. EVENSEN, J.D., 1978, Ph.D. Thesis, McMaster University, Canada.

111. WILSHAW, T.R., 1966, JISI, 204, p.936.

112. KNOTT, J.F., 1976, "Mechanics And Physics Of Fracture", Met. Society, London, p.86.

113. CURRY, D.A., KNOTT, J.F., 1978, Metal Science, p.511.

114. ALMOND, E.A., TIMBRES, D.H., EMBURY, J.D., 1969, "Fracture 1969", Proc. Second Int. Conf. On Fracture, Chapman and Hall, London, p.253.

115. ARGON, A.S., IM, J., NEEDLEMAN, A., 1975, Met. Trans., 6A, p.815.

116. ASHBY, A.S., 1966, Phil. Mag., 14, p.1157.

117. LINDLEY, T.C., OATES, G., RICHARDS, C.E., 1970, Acta Metallurgica, 18, p.1127.

118. McCLINTOK, F.M., 1968, Int. J. Frac. Mechanics, 4, p.101.

119. THOMASON, P.F., 1969, J. Inst. Metals, 54, p.360.

120. CLAYTON, J.Q., KNOTT, J.F., 1976, Metal Science, 10, p.63.

121. CHIPPERFIELD, C.G., KNOTT, J.F., 1975, Metals Technology, 2, p.45.

122. FAHY, F.W., ERASMUS, L.A., SMAILL, J.S., MUSOLFF, C.F., McELROY, P.J., EARL, W.B., 1978, "Engineering Metallurgy", Seminar Notes, University of Canterbury, New Zealand, p.87.

123. COTTRELL, A.H., BILBY, B.A., 1949, Proc. Roy. Society, A62, p.49.

124. HAHN, G.T., 1962, Acta Metallurgica, 10, p.727.

125. DALBY, W.E., 1913, Proc. Royal Society, A88, p.281.

126. HALL, E.O., 1970, "Yield Point Phenomena In Metals And Alloys", MacMillan, London, p.79.

127. PETCH, N.J., 1953, JISI, 174, p.25

128. FISHER, R.M., 1961, Ph.D. Thesis, University of Cambridge, England, referred to by Erasmus L.A. in Ref. 132.

129. BAIRD, J.D., 1963, Iron and Steel Institute, 36, pp. 186, 326, 368, 400, 450.

130. WILSON, D.V., RUSSEL, B., 1960, Acta Metallurgica, 8, pp. 36, 468.

131. NACKEN, M., HELLER, W., 1956, Arch. Eisenh, 27, p.45.

132. ERASMUS, L.A., 1972, Ph.D. Thesis, University of Cape Town, South Africa.

133. HUNDY, B.B., 1954, JISI, 178, p.34.

134. BUTLER, J.F., 1962, Trans. Metal Society, AIME, 224, p.89.

135. LOW, J.R., GESSAMER, M., 1944, Trans. AIME, 58, p.207.

136. STEPHENSON, E.T., 1961, Trans. ASM, 54, p.72.

137. WILSON, D.V., 1968, Acta Metallurgica, 16, p.743.

138. LESLIE, W.C., KEH, A.S., 1962, JISI, 200, p.722.

139. BAIRD, J.D., 1971, Metallurgical Review, 16, p.1.

140. DEKAZINCZY, F., Axnäs, A., 1963, Jerknot. Ann., 147, p.931.

141. PUSSEGODA, L.N., ERASMUS, L.A., 1977, Proc. "Sixth Australasian Conf. on The Mechanics of Structure and Materials", University of Canterbury, Christchurch, New Zealand, p.445.

142. COTTRELL, A.H., 1958, Trans. American Inst. Min. Metall. Petrol Eng., 212, p.192.

143. PETCH, N.J., 1958, Phil. Mag., 3, p.1089.

144. ERASMUS, L.A., 1971, M.Sc. Thesis, University of Cape Town, South Africa.

145. HESLOP, J., PETCH, N.J., 1958, Phil. Mag., 3, p.1128.

146. KOCHENDÖRFER, A., SCHULZE, H.D., RIEDEL, H., 1975, Int. J. Fracture, 11, p.365.

147. BAUSCHER, J.A., MAGOR, J.K., 1963, ISI Special Report, 79, p.34.

148. ENRIETTO, J.F., 1966, JISI, 204, p.252.

149. ROLLASON, E.C., 1973, "Metallurgy For Engineers", (Edwards Arnold), p.157.

150. PUSSEGODA, L.N., 1978, Ph.D. Thesis, University of Canterbury, New Zealand.

151. GLADMAN, T., PICKERING, F.B., 1967, JISI, 205, p.653.

152. The United Steel Companies Ltd, Research and Development Department, Swinden Labs., Moorgate, Rotherham, England, 1962, Ref. No. A 3763/-/62.

153. BEEGHLY, H.F., 1949, Anal. Chem., 21, p.1513.

154. ASTM Standards E 112 - 63, part 3.

155. ABEL, A., 1979, Metals Australasia, March, p.16.

156. CASE, S.L., VAN HORN, K.R., 1953, "Aluminium In Iron and Steel", Wiley, New York, p.57.

157. LEIREM, J., 1978, M.E. Thesis, McMaster University, Canada.

158. LORIG, C.H., ELSEA, A.R., 1947, Trans. Am. Foundrymen's Association, 55, p.160.

159. HAHN, G.T., OWEN, W.S., AVENBACH, B.L., COHEN, M., 1959, Welding Journal Research Supplement, 138, p.367s.

160. KNOTT, J.F., 1966, JISI, 204, p.104.

161. GRIFFITHS, J.R., OWEN, D.R.J., 1971, J. Mech. Phy. Solids, 19, p.419.

162. LOGAN, J.G., CROSSLAND, B., 1971, Conf. on "Practical Application of Fracture Mechanics To Pressure Vessel Technology", Inst. Mech. Eng., p.65

163. SAILORS, R.H., CORTEN, H.T., 1972, ASTM STP 514, p.164.

164. CHONG, C.J., LIM, K.H., 1974, Project Report No. MM/3/74, Department of Mechanical Engineering, University of Canterbury, New Zealand.

165. DE MORTEN, M.E., 1973, Conf. on "Stress And Strain In Engineering", Brisbane, Australia, Inst. of Eng., Australia. p.67.

166. KENYON, R.A., BURNS, R.S., 1939, "Age Hardening Of Metals", ASM, p.262.

167. HALL, E.O., 1952, JISI, 170, p.331.

168. BAIRD, J.D., JAMIESON, A., 1963, N.P.L. Symposium on "The Relation Between Structure And Mechanical Properties of Metals", HMSO, p.361.

169. GLEN, J., 1957, JISI, 186, p.21.

170. BAIRD, J.D., JAMIESON, A., 1966, *ibid*, 204, p.793.

171. GLEN, J., LESSELS, J., BARR, R.R., quoted by Baird in Ref. 129.

172. EPSTEIN, S., CULTER, S., FRAME, J.W., 1950, Trans AIME, 188, p.830.

173. COTTRELL, A.H., 1957, JISI, 187, p.219.

174. BLACKMORE, J.S., HALL, E.O., 1966, *ibid.*, 204, p.817.

175. BRINDLEY, B.J., BARNBY, J.T., 1966, Acta Metallurgica, 14, p.1765.

176. BRINDLEY, B.J., BARNBY, J.T., 1968, *ibid.*, 16, p.41.

177. MANJOINE, M.J., 1944, J. App. Mechanics, 11, p.A211.

178. COTTRELL, A.H., 1953, Phil. Mag., 44, p.829.

179. KEH, A.S., NAKADA, Y., LESLIE, W.C., 1968, "Dislocation Dynamics", McGraw-Hill, New York & London, p.337.

180. WILSON, D.V., RUSSEL, B., ESHELBY, J.D., 1959, Acta Metallurgica, 7, p.628.

181. HAHN, G.T., REID, C.N., GILBERT, A., 1962, *ibid.*, 10, p.747.

182. KEH, A.S., discussion to Ref. 168.

183. COTTRELL, A.H., JAWSON, M.A., 1949, Proc. Royal Society, A199, p.104.

184. WILSON, D.V., 1961, Acta Metallurgica, 9, p.618.

185. DINGLEY, D.J., McLEAN, D., 1967, *ibid.*, 15, p.885.

186. BURDEKIN, F.M., DAWES, M.G., ARCHER, G.L., BONOMO, F., EGAN, G.R., 1968, B. Weld. Journal, 15, p.590.

187. FORMBY, C.L., CLARNOK, W., 1971, Conf. on "Practical Application Of Fracture Mechanics To Pressure Vessel Technology", Inst. of Mech. Eng., p.1.

188. GROSS, J.H., 1970, ASTM STP 466, p.21.

189. TIMOSHENKO, S., 1955, "Strength Of Materials, Vol. 1", Van Nostrand East West Press, pp.5, 53.

APPENDIX A

DETERMINATION OF NITROGEN IN STEEL

The total nitrogen content in steel is considered to be made up of two parts:

(i) Acid-insoluble nitrides, and

(ii) Acid-soluble nitrides, which consist mainly of aluminium nitride and interstitial nitrogen.

It is assumed that

$$\%\ N_{\text{as free interstitial}} = \%\ N_{\text{as soluble nitrides}} - \%\ N_{\text{as AlN}}$$

The procedure is summarised diagramatically in Figure A(1).

(a) METHOD FOR DETERMINING SOLUBLE AND INSOLUBLE NITRIDES

3.5 gm of steel sample (in the form of drillings) is dissolved in about 40-50 ml of 18% sulphuric acid. The mixture is heated over a steam bath to aid the decomposition of metal. After cooling, 2 ml of barium chloride is added, and separation of the soluble and insoluble parts is carried out by centrifuging. (Barium Chloride is added to improve the separation.)

The soluble part is siphoned off and 10 ml of concentrated sulphuric acid is added to the insoluble nitrides. Heat is added until complete dissolution of the 'insoluble' nitrides.

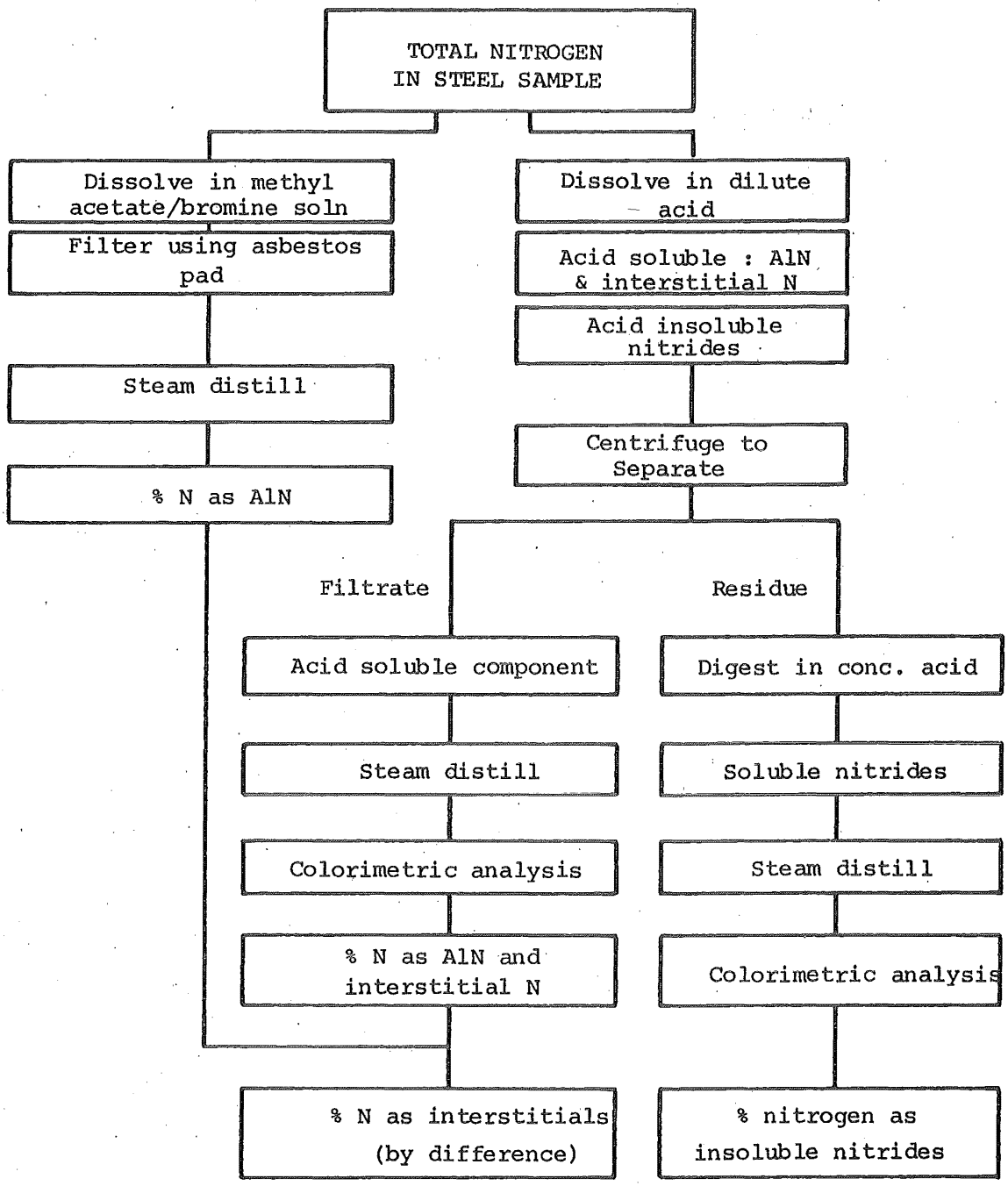

FIGURE A.1: Format for nitrogen analysis of steel

The soluble and 'insoluble' solutions are then separately steam distilled with 40-50 ml of sodium hydroxide and about 40 ml of ammonia free distilled water. The distillation apparatus is as shown in Figure A(2). The distillate is collected in 10 ml of boric acid solution. 2 ml of Nessler reagent is added to the distillates and the solutions are adjusted to equal volume by adding ammonia-free water. The amount of nitrogen present in these solutions may then be determined using colorimetric examination, and the actual nitrogen level obtained from the calibration curve prepared using standard nitrogen solutions. The interstitial (or active) nitrogen is then given by the difference between the nitrogen in soluble nitrides and the nitrogen combined as aluminium nitride.

(b) METHOD OF DETERMINING THE ALUMINIUM NITRIDE

3.5 gm of steel sample (in the form of drillings) is dissolved in 50 ml of Methyl-Acetate plus 10 ml of Bromine. The mixture is dissolved with the aid of a small flame. Aluminium nitride, which is not soluble in these solutions, is filtered off using an asbestos pad. The pad is washed using Methyl-Acetate and then dried. The dried pad is then put into the distillation flask (E in Figure A(2)), and the nitrogen combined as AlN is obtained by steam distillation and determined using colorimetry.

The accuracy of these analyses is in the order of ±0.0005%.

(c) GENERAL PRECAUTION

(i) Care must be taken to ensure that decomposition of steel

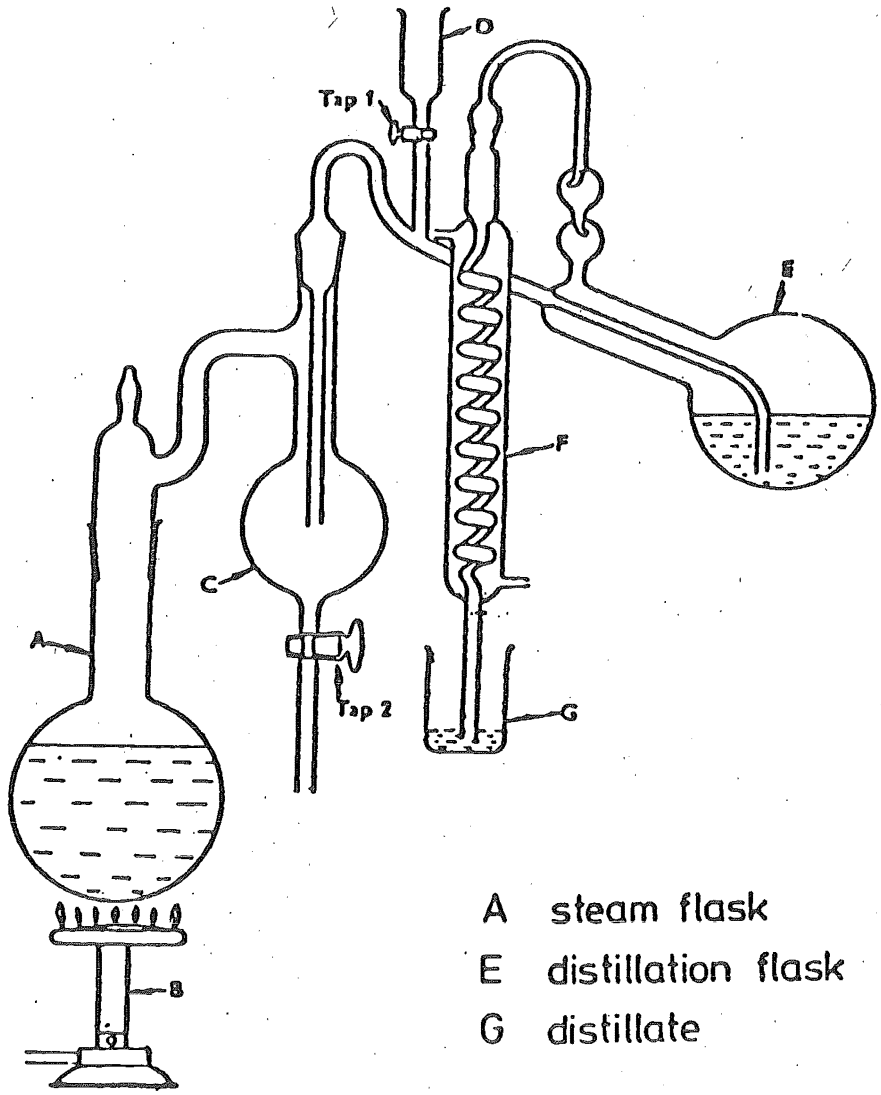

FIG. A.2 STEAM DISTILLATION APPARATUS

samples and the centrifuging separation process is complete.

(ii) Every precaution against contamination with extraneous ammonia must be taken.

(iii) Blank determination should be carried out with each batch of tests to ensure that nitrogen does not come from any other sources other than the steel sample.

APPENDIX B

CALIBRATION OF THE COD EXTENSOMETER

The experimental calibration of the Instron A384-1B clip-on type extensometer was conducted with the aim of providing an accurate relationship between extensometer reading(V_g) and the COD. The calibration was conducted at ambient temperature.

The mounting arrangement of the extensometer has been schematically illustrated in Figure B.1. The calibration technique involved loading the specimen to pre-determined values of V_g and then impregnating the crack with SIL-21 silicon rubber to obtain a replica of the crack-tip profile. The mid-section of the crack-tip was then measured with the use of a Nikon Model 6C type Shadowgraph under a magnification of 20. During the curing of rubber, which took 2 to 3 minutes, the load relaxed by approximately 5% but this should not affect the calibration. In the calibration of the Grade 275 Steel specimens, calibration was conducted beyond the point of initial sub-critical extension. In these cases, the V_g values higher than 4 mm were obtained by extrapolation of the V_g-time plot. This was possible because the V_g appeared to be linearly dependent with time after general yielding.

The results of this experimental calibration are supplied in Figure 8.2. It can be seen that

(a) The COD-V_g relationship of the three 10 mm specimens appeared

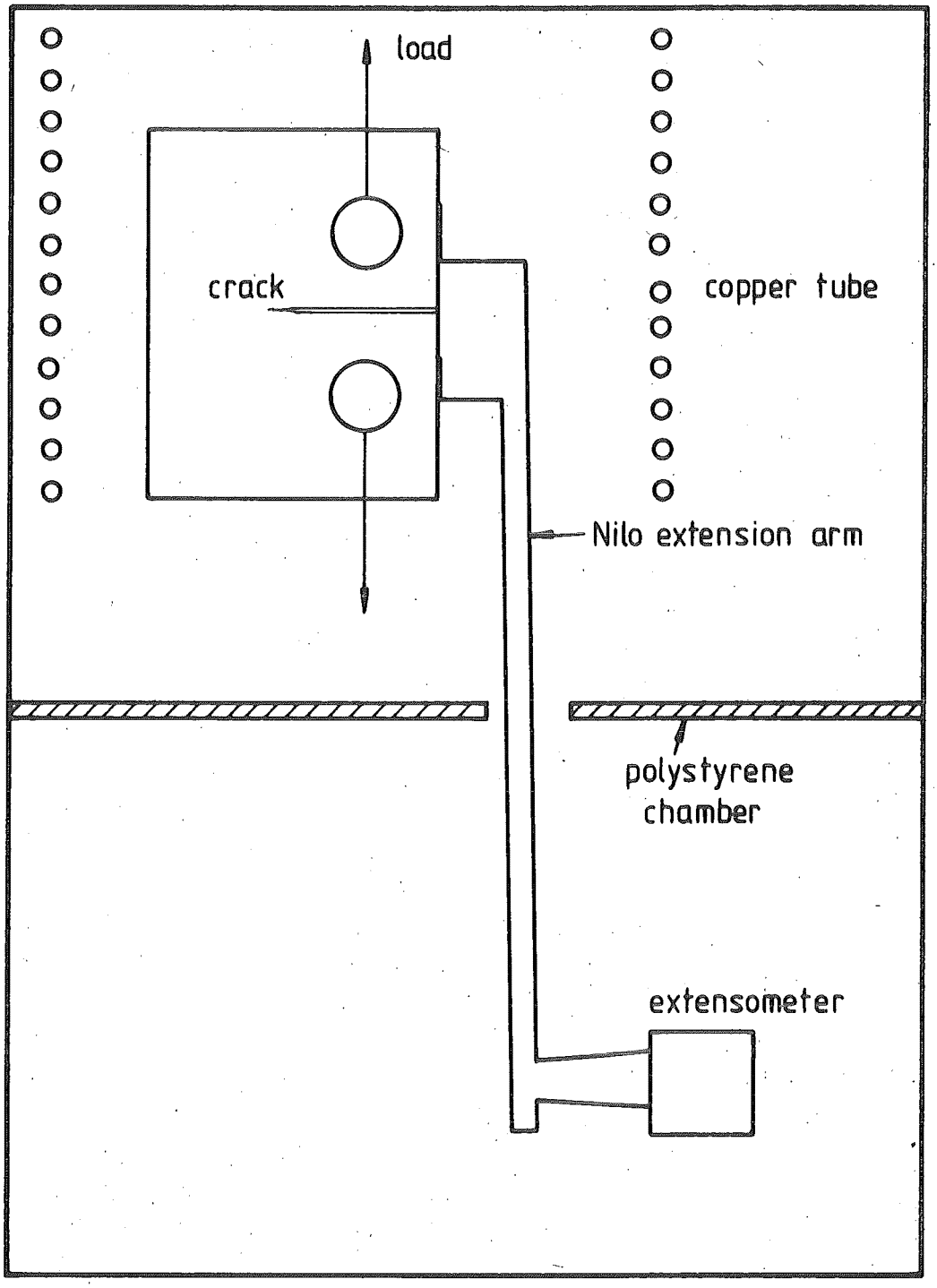

FIG B·1 MOUNTING ARRANGEMENT OF EXTENSOMETER

to be similar.

(b) The location of the neutral axis in the uncracked ligament was initially variable during small scale yielding but appeared to have stabilized at and after general yielding.

The effects of slot-width on the COD-V_g calibration were investigated by ascertaining the COD-V_g relationship of three Ti-added Grade 275 Steel specimens with slot-width of fatigue crack magnitude, 300 and 650 μm. The results have been summarised in Figure 8.3. It can be seen that the calibration curve of Figure 8.3 can be used to estimate the COD-V_g relationship of specimens with notches that are wider than the fatigue crack.

APPENDIX C

ACCURACY OF THE TEMPERATURE MONITORING TECHNIQUE

The desired sub-ambient temperatures of the COD tests were obtained by circulating liquid air through a helical copper tube around the test specimen. Consequently, the possible presence of a through-thickness temperature gradient warranted investigation.

The experimental technique involved the simultaneous measurements of the surface and mid-section temperature. The two surfaces' temperatures were measured by two Phillips PR 64C213/60 Ni-NiCr thermocouples while the mid-section crack-front temperature was measured by inserting a Cr-CrAl thermocouple into a hole drilled at the "back face" of the specimen as shown in Figure C.1. The relative accuracy of the two types of thermocouple had been pre-tested and were found to be satisfactory within the temperature range of -100 to 20^{o}C.

These temperature measurements were conducted with typical samples of the 10, 20 and 30 mm COD test specimens over the COD test temperature range. The results have been supplied in Figure 8.1.

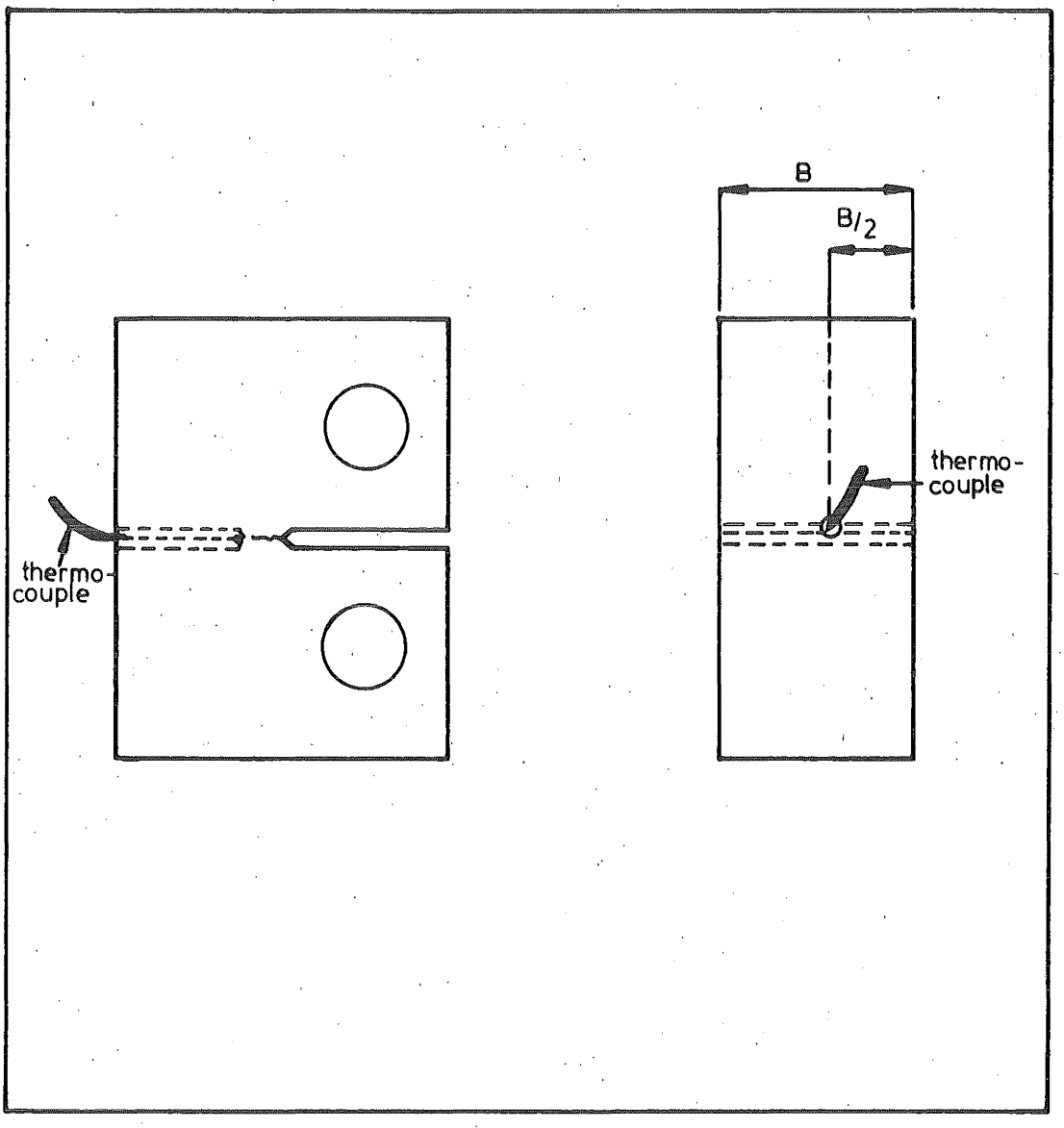

FIG. C·1 MOUNTING OF CR-CRAl THERMOCOUPLE

APPENDIX D

FATIGUE PRE-CRACK HISTORY OF THE COD TEST SPECIMENS

Specimen Identification	Maximum Load (KN)		Number Of Stress Cycles (x 10^3)
	Initial	Final	
PSA6	2.5	1.0	160
PSA12	2.5	1.0	160
PSA2	2.5	1.0	500
PSA5	2.5	1.0	500
PSA13	2.5	1.0	220
PSA4	2.5	1.0	410
PSA1	2.5	1.0	300
PSA8	2.5	1.0	293
PSA7	2.5	1.0	220

Table D. 1 10 mm Thick As-Rolled Billet Steel Specimens

Specimen Identification	Maximum Load (KN)		Number Of Stress Cycles (x 10^3)
	Initial	Final	
PS2A7	10.0	3.0	300
PS2A6	10.0	3.0	250
PS2A2	10.0	3.0	183
PS2A9	9.0	3.0	350
PS2A5	10.0	3.0	155
PS2A12	8.5	3.0	492
PS2A1	10.0	3.0	500
PS2A14	10.0	3.0	450

Table D.2 20 mm Thick As-Rolled Billet Steel Specimens

Specimen Identification	Maximum Load (KN)		Number Of Stress Cycles (x 10^3)
	Initial	Final	
PS3A6	22	5.0	640
PS3A8	22	5.0	820
PS3A4	22	5.0	709
PS3A10	22	5.0	980
PS3A3	21	5.0	866
PS3A2	24	5.0	774
PS3A7	22	5.0	1020
PS3A1	24	5.0	930
PS3A5	21	5.0	760

Table D.3 30 mm Thick As-Rolled Billet Steel Specimens

Specimen Identification	Maximum Load (KN)		Number Of Stress Cycles (x 10^3)
	Initial	Final	
PSHT9	2.5	1.0	341
PSHT1	2.5	1.0	275
PSHT11	2.5	1.0	155
PSHT2	2.5	1.0	343
PSHT7	2.5	1.0	332
PSHT3	2.5	1.0	603
PSHT8	2.5	1.0	210
PSHT4	2.5	1.0	304

Table D.4 10 mm Thick Hi-AlN Billet Steel Specimens

Specimen Identification	Maximum Load (KN)		Number Of Stress Cycles (x 10^3)
	Initial	Final	
PS2HT10	10	3.0	157
PS2HT8	10	3.0	116
PS2HT2	10	3.0	114
PS2HT12	10	3.0	135
PS2HT11	10	3.0	121
PS2HT1	10	3.0	160
PS2HT5	10	3.0	124
PS2HT9	10	3.0	148
PS2HT13	10	3.0	100
PS2HT4	10	3.0	140
PS2HT3	10	3.0	150
PS2HT7	10	3.0	105

Table D.5 20 mm Thick Hi-AlN Billet Steel Specimens

Specimen Identification	Maximum Load (KN)		Number Of Stress Cycles (x 10^3)
	Initial	Final	
PS3HT10	22	5.0	876
PS3HT1	23	5.0	631
PS3HT2	23	5.0	620
PS3HT3	24	5.0	1040
PS3HT8	22	5.0	993
PS3HT4	22	5.0	868
PS3HT7	22	5.0	945
PS3HT5	24	5.0	571
PS3HT12	22	5.0	662

Table D.6 30 mm Thick Hi-AlN Billet Steel Specimens

Specimen Identification	Maximum Load (KN)		Number Of Stress Cycles (x 10^3)
	Initial	Final	
A11	2.0	1.0	133
A19	2.75	1.0	153
A14	3.0	1.0	144
A8	2.2	1.0	170
A10	2.0	1.0	231
A13	2.0	1.0	148
A7	2.5	1.0	115
A6	2.5	1.0	676
A22	2.5	1.0	360
A17	2.5	1.0	690
A12	2.5	1.0	707
A21	2.5	1.0	366
A23	2.5	1.0	342
A24	2.0	1.0	450
A25	2.7	1.0	351
A28	3.0	1.0	296

Table D.7 10 mm Thick Pressure Vessel Steel Specimens

Specimen Identification	Maximum Load (KN)		Number Of Stress Cycles (x 10^3)
	Initial	Final	
C4	2.8	1.0	630
C11	3.0	1.0	450
C3	3.0	1.0	375
C9	2.6	1.0	370
C5	2.8	1.0	620
C6	2.8	1.0	383
C2	3.0	1.0	254
C7	2.8	1.0	560
C8	2.7	1.0	558
C12	2.6	1.0	370
C10	2.6	1.0	436
C22	3.0	1.0	220
C25	3.0	1.0	360
C23	3.0	1.0	250
C18	3.0	1.0	325
C15	3.0	1.0	418
C20	3.0	1.0	270
C21	3.0	1.0	283
C19	3.0	1.0	250
C17	3.0	1.0	330
C16	3.0	1.0	440
C24	3.0	1.0	345

Table D.8 10 mm Thick Normal Grade 275 Steel Specimens

Specimen Identification	Maximum Load (KN)		Number Of Stress Cycles (x 10^3)
	Initial	Final	
T9	2.8	1.0	425
T2	3.0	1.0	592
T4	3.0	1.0	340
T5	2.8	1.0	531
T8	2.8	1.0	521
T15	3.0	1.0	500
T3	3.0	1.0	380
T1	3.0	1.0	420
T6	3.0	1.0	520
T7	2.8	1.0	404
T12	2.8	1.0	510
T24	3.0	1.0	310
T22	3.0	1.0	365
T18	3.0	1.0	360
T19	3.0	1.0	285
T20	3.0	1.0	260
T21	3.0	1.0	310
T17	3.0	1.0	360
T16	3.0	1.0	340
T23	3.0	1.0	300

Table D.9 10 mm Thick Ti-Added Grade 275 Steel Specimens

APPENDIX E

CRACK OPENING DISPLACEMENT TEST DATA

Specimen Identification	Test Temperature (^{o}C)	Instability Extensometer Displacement V_{g_c} (mm)	Instability Determined At	Instability Load (KN)	Fracture Appearance
PSA6	-90	0.34	sf	4.1	cl
PSA12	-70	0.39	sf	4.5	cl
PSA2	-61	0.60	sf	4.9	cl
PSA5	-51	0.64	sf	5.2	cl
PSA13	-45	1.02	sf	4.5	cl
PSA4	-43	1.60	ml	5.1	mc
PSA1	-30	1.98	ml	4.4	mc
PSA8	-10	2.10	ml	4.5	mc
PSA7	25	1.98	ml	4.3	mc

sf Spontaneous fracture

cl Cleavage

ml Maximum Load

mc Micro-void Coalescence

Table E.1 10 mm Thick As-Rolled Billet Steel Specimens

Specimen Identification	Test Temperature (^{o}C)	Instability Extensometer Displacement V_{g_c} (mm)	Instability Determined At	Instability Load (KN)	Fracture Appearance
PS2A7	-80	0.45	sf	27.0	cl
PS2A6	-70	0.48	sf	24.0	cl
PS2A2	-60	0.75	sf	23.3	cl
PS2A9	-50	1.05	sf	27.0	cl
PS2A5	-45	1.38	ml	24.2	mc & cl
PS2A12	-40	1.75	ml	27.0	mc & cl
PS2A1	-30	2.22	ml	23.0	mc & cl
PS2A14	25	2.31	ml	22.0	mc

sf Spontaneous fracture

cl Cleavage

ml Maximum Load

mc Micro-void Coalescence

Table E.2 20 mm Thick As-Rolled Billet Steel Specimens

Specimen Identification	Test Temperature (^{o}C)	Instability Extensometer Displacement V_{g_c} (mm)	Instability Determined At	Instability Load (KN)	Fracture Appearance
PS3A6	-70	0.62	sf	42.0	cl
PS3A8	-60	0.89	sf	41.0	cl
PS3A4	-50	0.95	sf	40.0	cl
PS3A10	-41	1.20	ml	40.0	mc & cl
PS3A3	-39	1.72	ml	44.0	mc & cl
PS3A2	-35	1.97	ml	42.0	mc & cl
PS3A7	-31	2.20	ml	42.5	mc & cl
PS3A1	-20	2.45	ml	39	mc & cl
PS3A5	25	2.52	ml	41.0	mc

sf Spontaneous fracture

cl Cleavage

ml Maximum Load

mc Micro-void Coalescence

Table E.3 30 mm Thick As-Rolled Billet Steel Specimens

Specimen Identification	Test Temperature (^{o}C)	Instability Extensometer Displacement V_{g_c} (mm)	Instability Determined At	Instability Load (KN)	Fracture Appearance
PSHT9	-81	0.42	sf	5.5	cl
PSHT1	-75	0.44	sf	5.2	cl
PSHT11	-70	0.52	sf	4.0	cl
PSHT2	-65	0.50	sf	5.1	cl
PSHT7	-61	0.47	sf	5.6	cl
PSHT3	-55	0.45	sf	5.4	cl
PSHT8	-43	0.45	ml	4.9	mc
PSHT4	-34	0.47	ml	5.0	mc

sf Spontaneous fracture

cl Cleavage

ml Maximum Load

mc Micro-void Coalescence

Table E.4 10 mm Thick Hi-AlN Billet Steel Specimens

Specimen Identification	Test Temperature (^{o}C)	Instability Extensometer Displacement V_{g_c} (mm)	Instability Determined At	Instability Load (KN)	Fracture Appearance
PS2HT10	-71	0.74	sf	29.2	cl
PS2HT8	-61	0.56	sf	24.6	cl
PS2HT2	-60	0.43	sf	26.4	cl
PS2HT12	-57	0.67	sf	26.5	cl
PS2HT11	-55	0.67	sf	26.5	cl
PS2HT1	-51	0.70	sf	25.8	cl
PS2HT5	-45	0.68	ml	27.0	mc
PS2HT9	-45	0.67	ml	28.0	mc
PS2HT13	-40	0.67	ml	23.5	mc
PS2HT4	-40	0.63	ml	25.5	mc
PS2HT3	-30	0.63	ml	23.0	mc
PS2HT7	-20	0.68	ml	23.0	mc

sf Spontaneous fracture
cl Cleavage
ml Maximum Load
mc Micro-void Coalescence

Table E.5 20 mm Thick Hi-AlN Billet Steel Specimens

Specimen Identification	Test Temperature (^{o}C)	Instability Extensometer Displacement V_{g_c} (mm)	Instability Determined At	Instability Load (KN)	Fracture Appearance
PS3HT10	-60	0.92	sf	49.2	cl
PS3HT1	-59	0.90	sf	45.0	cl
PS3HT2	-51	0.80	ml	44.0	mc
PS3HT3	-40	0.92	ml	43.5	mc
PS3HT8	-40	0.84	ml	43.5	mc
PS3HT4	-30	0.90	ml	46.5	mc
PS3HT7	-30	0.90	ml	39.8	mc
PS3HT5	-20	0.90	ml	40.5	mc
PS3HT12	0	0.88	ml	40.2	mc

sf Spontaneous Fracture

cl Cleavage

ml Maximum Load

mc Micro-void Coalescence

Table E.6 30 mm Thick Hi-AlN Billet Steel Specimens

Specimen Identification	Test Temperature (^{o}C)	Instability Extensometer Displacement V_{g_c} (mm)	Instability Determined At	Instability Load (KN)	Fracture Appearance
A11	-92	0.31	sf	4.1	cl
A19	-70	0.35	sf	4.8	cl
A14	-60	0.56	sf	4.7	cl
A8	-52	0.68	sf	4.7	cl
A10	-40	1.25	sf	4.3	cl
A13	-29	1.95	ml	4.7	mc & cl
A7	-15	1.90	ml	5.0	mc
A6	+16	2.04	ml	4.1	mc
A22	18	2.15	ml	4.0	mc
A17	20	1.96	ml	4.1	mc
A12	110	1.52	ml	4.3	mc
A21	150	1.25	ml	4.7	mc
A23	203	1.00	ml	4.4	mc
A24	250	0.95	ml	4.4	mc
A25	300	1.00	ml	4.6	mc
A28	350	1.02	ml	4.9	mc

sf Spontaneous fracture
cl Cleavage
ml Maximum Load
mc Micro-void Coalescence

Table E.7 10 mm Thick Pressure Vessel Steel Specimens

Specimen Identification	Test Temperature (^{o}C)	Instability Extensometer Displacement V_{g_c} (mm)	Instability Determined At	Instability Load (KN)	Fracture Appearance
C4	-80	0.34	sf	6.3	cl
C11	-80	0.28	sf	6.1	cl
C3	-60	0.62	sf	7.0	cl
C9	-45	0.64	sf	6.0	cl
C5	-40	0.88	sf	6.1	cl
C6	-38	1.53	sf	6.0	cl
C2	-37	1.96	sf	6.5	cl
C7	-35	2.39	sf	7.2	mc & cl
C8	-30	4.20	ml	7.7	mc & cl
C12	25	4.30	ml	7.0	mc & cl
C10	25	4.80	ml	7.1	mc & cl

sf Spontaneous fracture

cl Cleavage

ml Maximum Load

mc Micro-void Coalescence

Table E.8 10 mm Thick Normal Grade 275 Steel Specimens - Aged

Specimen Identification	Test Temperature (°C)	Instability Extensometer Displacement V_{g_c} (mm)	Instability Determined At	Instability Load (KN)	Fracture Appearance
C22	-80	0.34	sf	4.5	cl
C25	-80	0.26	sf	4.2	cl
C23	-60	0.76	sf	6.4	cl
C18	-46	0.89	sf	6.0	cl
C15	-43	1.16	sf	6.4	cl
C20	-43	1.30	sf	6.3	cl
C21	-42	3.14	sf	6.0	mc & cl
C19	-41	3.14	sf	6.6	mc & cl
C17	-35	4.30	sf	6.8	mc & cl
C16	-30	4.40	ml	7.5	mc & cl
C24	25	4.20	ml	7.1	mc & cl

sf Spontaneous Fracture

cl Cleavage

ml Maximum Load

mc Micro-void Coalescence

Table E.9 10 mm Thick Normal Grade 275 Steel Specimens - As Fatigued

Specimen Identification	Test Temperature (°C)	Instability Extensometer Displacement V_{g_c} (mm)	Instability Determined At	Instability Load (KN)	Fracture Appearance
T9	-80	0.36	sf	6.8	cl
T2	-70	0.41	sf	7.0	cl
T4	-50	0.66	sf	6.6	cl
T5	-45	0.90	sf	7.6	cl
T8	-44	1.35	sf	7.3	cl
T15	-41	1.07	sf	6.9	cl
T3	-40	2.17	sf	6.9	cl
T1	-40	2.08	sf	8.1	cl
T6	-27	3.90	sf	8.4	mc & cl
T7	-17	3.85	ml	7.9	mc & cl
T12	25	4.50	ml	8.1	mc & cl

sf Spontaneous Fracture

cl Cleavage

ml Maximum Load

mc Micro-void Coalescence

Table E.10 10 mm Thick Ti-Added Grade 275 Steel Specimen: - Aged

Specimen Identification	Test Temperature (^{o}C)	Instability Extensometer Displacement V_{g_c} (mm)	Instability Determined At	Instability Load (KN)	Fracture Appearance
T24	-80	0.33	sf	7.1	cl
T22	-60	0.66	sf	7.7	cl
T18	-50	0.66	sf	7.1	cl
T19	-46	0.92	sf	6.2	cl
T20	-45	0.78	sf	6.0	cl
T21	-40	1.98	sf	7.0	cl
T17	-26	4.11	ml	7.3	mc & cl
T16	-20	4.53	ml	7.8	mc & cl
T23	25	4.56	ml	7.9	mc & cl

sf Spontaneous Fracture
cl Cleavage
ml Maximum Load
mc Micro-void Coalescence

Table E.11 10 mm Thick Ti-Added Grade 275 Steel Specimens - As Fatigued

APPENDIX F

THE TRUE STRESS - TRUE STRAIN RELATIONSHIP OF THE EXPERIMENTAL STEELS

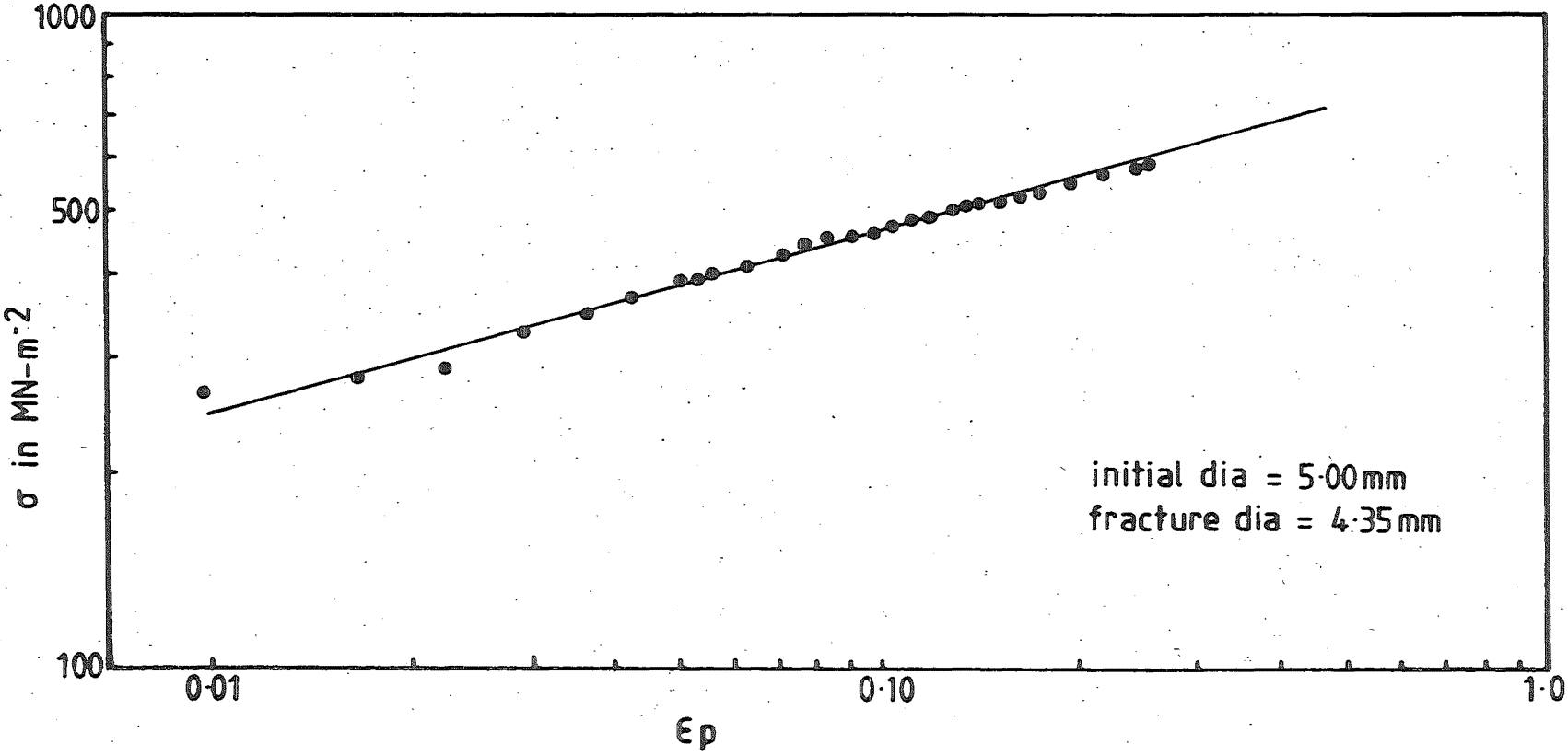

FIG. F·1 TRUE STRESS-TRUE STRAIN RELATIONSHIP OF THE AS-ROLLED BILLET STEEL

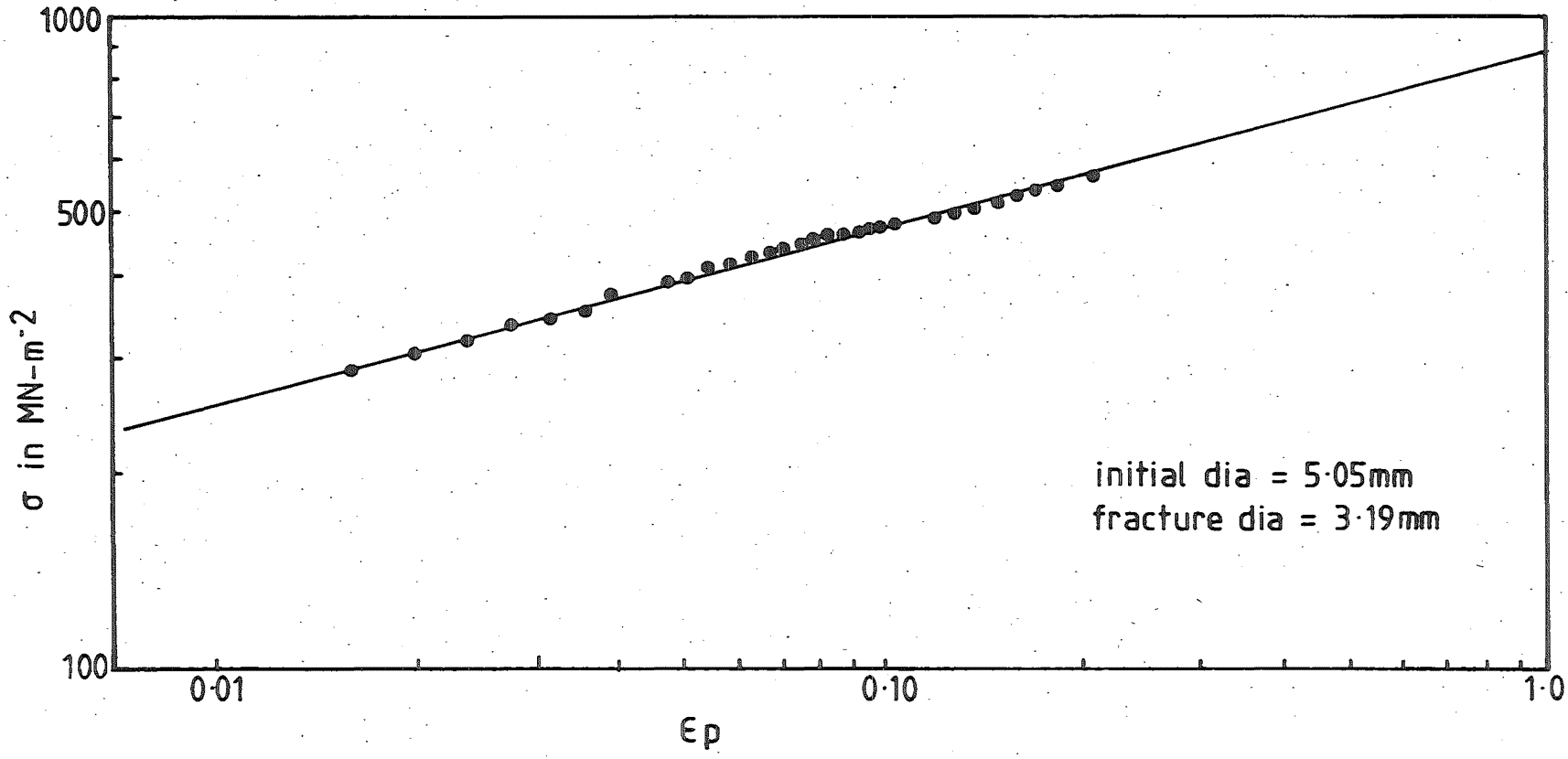

FIG. F·2 TRUE-STRESS- TRUE STRAIN RELATIONSHIP OF THE PRESSURE VESSEL STEEL

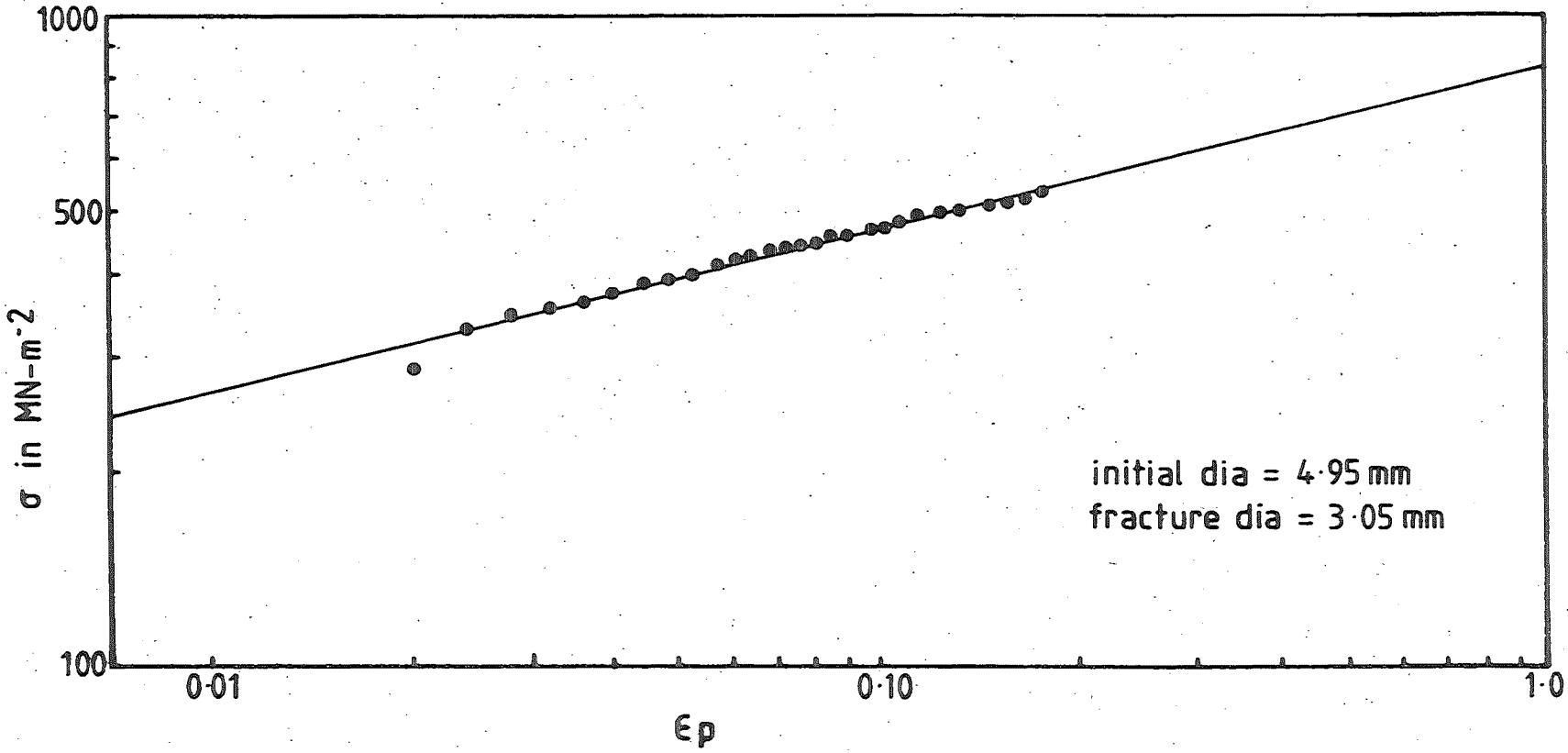

FIG. F·3 TRUE STRESS - TRUE STRAIN RELATIONSHIP OF THE NORMAL GRADE 275 STEEL

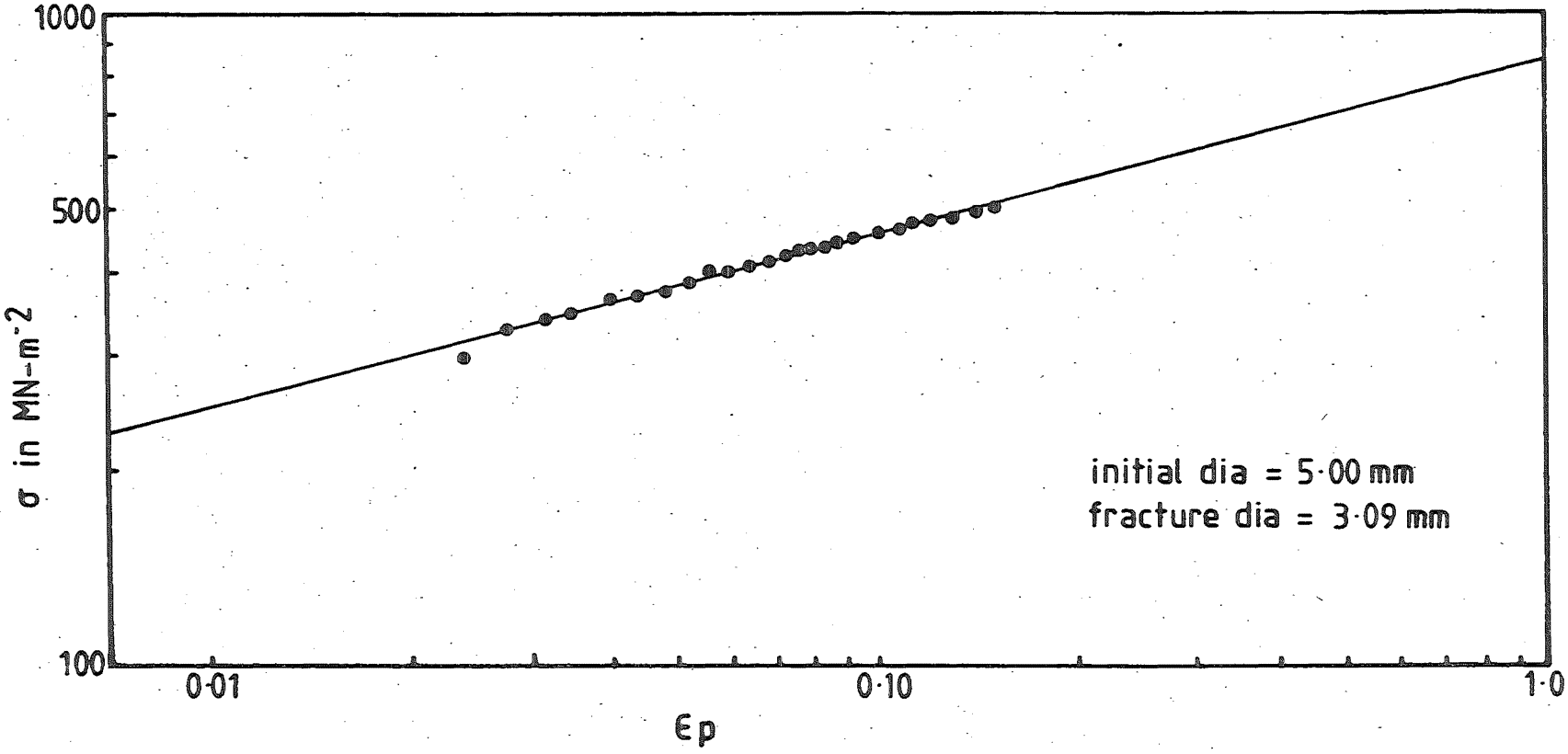

FIG. F·4 TRUE STRESS- TRUE STRAIN RELATIONSHIP OF THE TI-ADDED GRADE 275 STEEL

APPENDIX G

CHARPY V-NOTCHED IMPACT TEST RESULTS

Test Temperature (^{o}C)	Impact Energy C_v (J)
-70	7.0
-50	8.0
-20	10.2
-4	17.6
0	21.7
1	23.0
5	31.9
10	32.5
15	33.1
19	40.7
20	56.7
53	59.4
100	63.0
140	58.0 , 50.2
200	54.2

Table G.1 Pressure Vessel Steel

Test Temperature (^{o}C)	Impact Energy C_v (J)
-50	8.0
-30	10.8
-20	12.2
-10	15.6
-5	25.8
0	40.7
5	40.0
10	69.8
20	73.2
30	98.3
40	107.1

Table G.2 As Rolled Normal Grade 275 Steel

Test Temperature (^{o}C)	Impact Energy C_v (J)
-10	4.1
0	6.8
10	15.6
20	18.3
30	38.0
35	51.5
40	58.2
60	97.6
70	103.0

Table G.3 5% Pre-Strained And Aged Normal Grade 275 Steel

Test Temperature (^{o}C)	Impact Energy C_v (J)
-40	13.6
-30	18.3
-20	19.7
-10	24.4
-5	40.0
0	56.3
5	59.0
10	111.8
20	118.0
30	123.4
60	126.1

Table G.4 As Rolled Ti-Added Grade 275 Steel

Test Temperature (^{o}C)	Impact Energy C_v (J)
-30	4.7
-20	10.8
-10	11.5
0	24.4
5	46.8
15	61.0 , 93.5
20	108.5
30	115.9

Table G.5 5% Pre-Strained And Aged Ti-Added Grade 275 Steel